Modelling wave breaking in envelope type models



Yuxuan Liu

Green Templeton College

University of Oxford

A thesis submitted for the degree of

Doctor of Philosophy

Trinity 2024

This thesis is dedicated to:

Feng Liu and *Wen Jiang* for always supporting my education, *Shuya Liu* for her love and support, and *Michael Allshouse* for igniting my passion for academic research.

Modelling wave breaking in envelope type models

A thesis submitted for the degree of
Doctor of Philosophy at the University of Oxford

By Yuxuan Liu, Green Templeton College, Trinity 2024

Wave breaking in the ocean is a phenomenon crucial for understanding energy transfer, erosion processes, and climate modelling, and has an essential role in marine and coastal dynamics. This thesis seeks to build surrogate models to enable fast breaking-wave prediction in non-linear Schrödinger-type (i.e., envelope-based) equations. We begin by revisiting four established models in the field, providing an evaluation of their methodologies, strengths, and limitations. Building on this foundation, we introduce the Modified Kato & Oikawa model, a novel approach that integrates key aspects of the existing Kato & Oikawa (1995, *Journal of the Physical Society of Japan*, 64(12), pp. 4660–4669) model while incorporating innovative mechanisms to more accurately represent the complexities of wave breaking. To further advance the study of wave breaking dynamics, this thesis develops a machine learning (ML) model to capture the inherent nonlinearity of the process. Our early ML experiments—based on a synthetic dataset that is created using the Modified Kato & Oikawa model—suggest that the ML model can capture the dissipation from breaking waves. In the next milestone, this thesis applies RANS (Reynolds-Averaged Navier–Stokes) simulations to generate a dataset that encompasses a wide range of wave breaking scenarios. This large dataset provides the foundation for training our ML model, ensuring that it is robust and capable of generalising across different conditions. Training of the ML model with the RANS dataset is the key contribution of this thesis, demonstrating the synergy between high-fidelity simulations and the ML model. The trained model demonstrates excellent agreement with the simulations and experiments, offering a performance that surpasses existing models.

Acknowledgements

First and foremost, I owe a huge debt of gratitude to Professors Thomas A. A. Adcock and Ton S. van den Bremer. My time at the University of Oxford under their careful and committed supervision has been nothing short of transformative. They have both been pillars of wisdom and support, guiding me through the intricacies of my DPhil studies with a patience I am deeply thankful for.

Dr. Debbie Eeltink also deserves a special mention for her role as a co-supervisor. The quality of my work has benefited immensely from her astute and incisive feedback. Debbie brought a fresh perspective and invaluable insights that have profoundly shaped my approach to research, and for that, I am immensely grateful.

I must also thank my colleagues and friends—Zhenhao Li, William Wei, Tim Tang, Tuo Wang, Judy Li, and so on—whose support has stretched far beyond the academic realm. Their camaraderie, tolerance, and constant encouragement have enriched my experience immeasurably. A particular shoutout to Tim Tang, whose generous life advice and companionship have been a great comfort and inspiration.

Before my journey at Oxford began, I spent nine months at Laboratoire de Mécanique des Fluides de Lille under the guidance of Professor John Christos Vassilicos. Those days in France were a test of endurance and adaptability—challenging on every front as the world teetered on the brink of the COVID-19 outbreak. Christos was instrumental in ensuring that these challenges did not interrupt my research. His dedication helped lay a solid foundation for my doctoral pursuits.

My academic journey is peppered with memorable interactions, like my first meeting with Professor Michael Allshouse. I had reached out to him with hopes of joining his research group, and despite my apparent lack of knowledge in fluid dynamics during our initial conversation, Michael saw potential. His engaging class on the subject and his mentorship thereafter shaped the researcher I am today. Michael's guidance introduced me to a community of earnest, kind-hearted, and diligent individuals, constantly pushing their limits. I am forever grateful for his influence in my life.

Lastly, I must express my deepest appreciation for my family and my girlfriend, who have been my steadfast support system. My parents have been unwavering in their encouragement, and I carry my late grandmother's love and care with me every day. Their collective strength has been my foundation, and I am eternally blessed to have them by my side.

Contents

1 Introduction **1**

1.1 Thesis Outline 1

1.2 Synopsis of Thesis Chapters 3

1.3 List of Publications 6

2 Literature Review **9**

2.1 A Century of Ocean Surface Wave Modelling and Forecasting 10

2.2 Modelling Non-Breaking Waves with Potential Flow Theory 12

2.3 Weakly Nonlinear Formulation of Waves in Deep Water 14

2.4 MNLS Simulations of Surface Wave Groups 15

2.5 Wave Breaking: A Critical Challenge in Nonlinear Wave Theory . . . 16

2.6 Mathematical Formulation: Navier–Stokes Equations 17

2.7 Machine Learning in Fluid Dynamics and Oceanography 19

2.7.1 Machine Learning in Wave Prediction and Analysis 21

2.7.2 A Convolutional-Recurrent Neural Network Model 23

2.8 Conclusions 24

3 Comparison of breaking models in envelope-based surface gravity wave evolution equations **25**

3.1 Introduction 26

3.2 Theoretical and Experimental Methodology 28

3.2.1 Envelope-Based Evolution Equation 29

3.2.2 Four Reduced-Form Breaking Models 30

3.2.3 Laboratory Experiments 33

3.2.4 Initial Conditions for the MNLS Simulations 34

3.3 Perturbed Plane Waves 35

3.3.1 Initial Conditions 36

3.3.2 Comparison of Breaking Models 37

3.4 Focused Wave Groups 40

3.4.1 Effects of Breaking 40

3.4.2 Comparison of Breaking Models 42

3.5 Breaking Model Optimisation and Modification 45
3.5.1 Breaking Criteria 48
3.5.2 Parameter Optimisation 49
3.5.3 Model Modification 51
3.5.4 Performance of the Modified Kato & Oikawa (M-KO95) Model 52
3.6 Conclusions 55

4 A machine learning architecture for including wave breaking in envelope-type wave models 58
4.1 Introduction 59
4.2 Methods 62
4.2.1 Envelope-Based Evolution Equation 62
4.2.2 Reduced-Form Breaking Model 64
4.2.3 Initial Conditions for the MNLS Simulations 65
4.2.4 Simulation Settings 67
4.3 Neural Network Model 67
4.4 Focused Wave Cases 70
4.4.1 Synthetic Data Generation 70
4.4.2 Training History 71
4.4.3 Model Analysis 74
4.4.4 Prediction for Focused Wave Groups 74
4.5 Modulated Plane and Random Waves 78
4.6 Conclusion 81

5 Numerical simulation of wave breaking using RANS: comparison with experiments 84
5.1 Introduction 85
5.2 Methodology 88
5.2.1 Navier–Stokes Equations 88
5.2.2 The $\varkappa - \omega$ Turbulence Model 88
5.2.3 Adaptive Mesh Refinement 90
5.2.4 Wave Parameters 91
5.2.5 Numerical Configuration 94
5.3 Validation of the RANS Turbulence Model 98
5.3.1 Non-Breaking Stokes Waves 98
5.3.2 Breaking Focused Wave Group 101
5.4 Numerical Results 104
5.4.1 Comparison to the Experiments of Eeltink et al. (2022) 106
5.4.2 Random Periodic Domain Simulations 107
5.5 Conclusions 110

6 Using machine learning based on RANS to model deep-water wave breaking in envelope-type wave models **112**
6.1 Introduction . . . 113
6.2 Methods . . . 115
6.2.1 Envelope-Based Evolution Equation . . . 115
6.2.2 Initial Conditions for the MNLS Simulations . . . 116
6.2.3 Simulation Settings . . . 117
6.2.4 Nerual Network Model . . . 118
6.2.5 Data Preparation and Training Strategy . . . 120
6.2.6 Aix-Marseille University Wave Tank Experiment . . . 120
6.2.7 Reduced-Form Breaking Model . . . 121
6.3 Results . . . 121
6.3.1 Wave Type I: Prediction for Focused Wave Groups . . . 121
6.3.2 Wave Types II and III: Modulated Plane Wave and Random Waves . . . 122
6.3.3 Comparision to Existing Breaking Models . . . 129
6.3.4 Comparison to Aix-Marseille University Wave Tank Experiment (Eeltink et al., 2022) . . . 130
6.3.5 Model Efficiency . . . 131
6.4 Discussion . . . 133

7 Discussions and Conclusions **136**

References **141**

A ConvLSTM neural network architecture **162**

B Appendices for Chapter 3 **164**
B.1 Comparison for Additional Perturbed Plane Wave Cases . . . 164
B.2 Performance of Other Modified Models . . . 166
B.3 Dissipation Elements in Watertank Experiments . . . 170

C Appendices for Chapter 4 **174**
C.1 Simple Variants of the ConvLSTM Model . . . 174
C.2 Additional Results for Plane Wave and Random Waves . . . 178

D Appendices for Chapter 6 **183**
D.1 MNLS+ML Experiments on the Test Dataset . . . 183
D.2 MNLS+ML Experiments on the Non-Breaking Cases . . . 183
D.3 Training History . . . 183
D.4 Data-Processing Details . . . 188
D.5 NMSE and NMAE of the Absolute Magnitude of the Envelope . . . 190

List of Figures

3.1 The gauge layout in the Multi-function Towing Tank at Shanghai Jiao Tong University. The gauges in the 4×2 array are labelled as 1-8. Wave groups travel from left to right. 34

3.2 Surface elevations and amplitude spectra at different gauge locations for perturbed plane waves (case 1 in Table 3.2). Black solid lines correspond to experimental data and coloured dashed lines to MNLS simulations (a) without a breaking model and (b) with the breaking model of TD90. For the wave spectra, we use $\Omega = \omega/\omega_0 - 1$. 39

3.3 Spatial evolution of perturbed plane waves for different reduced-from breaking models including no breaking model (NBM), showing a) the carrier wave normalised by its value at the first gauge, $a_c/a_{c,0}$; b) the normalised lower sideband $a_-/a_{c,0}$; c) the normalised upper sideband, $a_+/a_{c,0}$; d) the spectral peak, $\Omega_{\text{peak}} = \text{argmax}_\Omega \hat{A}$ with $\hat{A}$ the amplitude spectrum of η and $\Omega = \omega/\omega_0 - 1$; e) spectral mean or centroid, $\Omega_{\text{center}} = \int \Omega(\omega)\hat{A}(\omega)\mathrm{d}\omega / \int \hat{A}(\omega)\mathrm{d}\omega$; f) the energy measure $E = \int |B|^2 \,\mathrm{d}t$ normalised by its value at the first gauge E_0. The black squares show the experimental data from Eeltink et al. (2022) (case 1 from Table 3.2). 41

3.4 Surface elevations and amplitude spectra at different gauge locations for focused wave groups (case 1 in Table 3.1). Black solid lines correspond to experimental data and coloured dashed lines to MNLS simulations (a) without a breaking model and (b) with the breaking model of TD90. For the wave spectra, we use $\Omega = \omega/\omega_0 - 1$. 43

3.5 Surface elevations at different gauge locations for focused wave groups (case 1 in Table 3.1). Black solid lines correspond to experimental data and coloured dashed lines to MNLS simulations (a) with the model of KO95; (b) with the SL model; (c) with the model of H11; and (d) with the M-KO95 model. 44

3.6 Comparison of amplitude spectra before and after breaking of a focused wave group (see Table 3.1) for different reduced-form breaking models including no breaking model (NBM), showing experiments (black solid/dashed lines), with grey shaded region corresponding to ± 1 standard deviation from repeated experiments, and MNLS simulations with different breaking models (coloured dashed lines with markers). 46

3.7 Phase difference between consecutive gauges for case 1 (a) and case 2 (b) for focused wave groups in Table 3.1 (with the labels corresponding to the gauge with the largest x), comparing experiments (black lines), MNLS simulations with no breaking model (NBM, red dashed lines) and with the breaking models (coloured dashed lines). In case 1, breaking occurred between gauge x = 3.04 m and x = 6.50 m. In case 2, a weak breaking event occurred between x = 3.04 m and x = 6.50 m, and a second strong breaking event occurred between x = 6.50 m and x = 9.82 m. 47

3.8 Optimal spectral dissipation strength parameter $\hat{\beta}$ as a function of $\lambda = k/k_0 - 1$ for the modified Kato and Oikawa (1995) model (M-KO95) for three different breaking criteria. The open circles are the actual control points, and any values in between two points are reconstructed by linear interpolation. 52

3.9 Spatial distribution of the normalised dissipation term $\tilde{D} = 2\epsilon k_0/\omega_0 D$ (top panels) aligned with the envelope for simulations with no breaking model (NBM) and with the M-KO95 model (bottom panels), for which the dissipation term is examined in the top panels, at the start (or just before, left) and at the end (or just after, right) breaking for a focused wave group (case 1 in Table 3.1). The dashed black line corresponds to the surface elevation from MNLS simulations with no breaking model, the red dotted line is the envelope from MNLS simulations with no breaking model (NBM), and the brown solid line in the bottom panels is envelope from MNLS simulations with the M-KO95 model. 54

3.10 Temporal evolution before, during and after breaking according to MNLS simulations with the M-KO95 model for focused wave groups (Table 3.1), showing activation of the dissipation term (top left), the normalised spectral mean $\lambda_{\text{center}} = \int \lambda(k)\hat{A}(k)\,\mathrm{d}k / \int \hat{A}(k)\,\mathrm{d}k$ (top right), the energy measure $E = \int |B|^2 \mathrm{d}x$ normalised by its initial value (bottom left) and the energy flux defined as $W = \int B^*(\partial B/\partial x) - B(\partial B^*/\partial x)\,\mathrm{d}x$, which is normalised by $W_0 = E_0 k_0/2\pi$ (bottom right). 55

4.1 Schematic of the structure and computing diagram of a neural network model composed of four layers in vertical: an input layer accepting a pair of real numbers (the magnitudes of the real and imaginary part of the complex envelope), a ConvLSTM layer, a convolution layer, and an output layer. τ is the timestep. The model accepts input $\hat{B}_n$ and model states H_{n-1}, C_{n-1} from the previous timestep and predicts the change in ΔB_n and model states H_n, C_n between timesteps. 68
4.2 In this figure, the cell state C for each filter channel is represented in a spatial-temporal plot where space axis is horizontal and time axis is vertical, arranged in panels from top to bottom and left to right. The color scale of the plots is normalised to [-1, 1] for each panel, where brighter colors indicate higher values, darker colors represent lower values and color with decreased saturation for values close to zero. The scaling factor for the color range in each plot is denoted in the annotation at the top-left corner of each panel. 75
4.3 The evolution of the 'energy' (for each channel) of the cell state. The channels are sorted in descending order based on the energy level of the channel. 76
4.4 The figures consists of two subplots. In subplot (a), panels (i), (ii) and (iii) show the evolution of the absolute value of the complex envelope using different models, while panels (iv), (v), and (vi) show the evolution of the absolute value of the wavenumber spectrum of the complex envelope. Specifically, panel (i) and (iv) show the NBM result, panel (ii) and (v) show the MNLS+ML result, and panel (iii) and (vi) show the ground truth generated by the M-KO95 model. In subplot (b), panel (i) plots the mean squared error (MSE) of the absolute value of the complex envelope. Panels (ii), (iii), and (iv) compare the energy evolution $E = \int \|B\|^2 \, \mathrm{d}t$ normalised by its value at the first time step E_0, wavenumber spectral mean or centroid, $\Lambda_{\text{center}} = \int k\tilde{B}(k)\mathrm{d}k / \int \tilde{B}(k)\mathrm{d}k$, and evolution of steepness. All panels share the same legend, which is placed on the top of subplot (b). In the legend, the green solid line represents the ground truth, the blue dashed line represents the MNLS+ML result or MSE of MNLS+ML compared to the ground truth, and the orange dotted line represents the NBM result or MSE of NBM result compared to the ground truth. 77

4.5 The figure depicts profiles of a specific case from the test dataset at different gauge locations x. The case is randomly selected from the test dataset. The solid green line is ground truth, the blue dashed line is the MNLS+ML simulation and the orange dotted line is the NBM simulation. Panel (a) plots the surface elevation η normalised by the characteristic wave amplitude a_0 and panel (b) represents the frequency spectrum of normalised surface elevation, where $\Omega = \omega/\omega_0 - 1$ is the normalised modulational frequency. 78

4.6 This figure plots the MSE error distribution across the test dataset. Panel (a) shows the evolution of MSE of MNLS+ML and NBM simulations as a function of time, where the blue line with the shaded region corresponding to $\pm 1\sigma$ indicates the MSE of the MNLS+ML simulations and the orange line with the shaded region corresponding to $\pm 1\sigma$ indicates the MSE of the NBM simulations. Panel (b) illustrates the distribution of the MSE for the MNLS+ML and the NBM simulations at the final time step, where blue bars stand for MNLS+ML and orange bars for NBM. 79

4.7 The figure depicts (a) the surface elevation profile of a modulational plane wave case;(b) the corresponding frequency spectrum; (c) the surface elevation profile of a random wave case and (d) the corresponding frequency spectrum. The case was randomly selected from the test dataset. Solid green line is ground truth, blue dashed line is MNLS+ML and orange dotted line is NBM simulation. The time series of random wave case is not shifted by group speed. 80

4.8 The figure plots the evolution of maximum breaking parameter u/c (Barthelemy et al., 2018) in nonbreaking zone averaged over test cases for (a) modulated plane wave and (b) random waves. Solid green line is ground truth, blue dashed line with errorbars is MNLS+ML and orange dotted line is NBM simulation. The errorbars indicate maxima and minima of maximum breaking parameter throughout the test cases. 82

5.1 A snapshot of the mesh during breaking. The mesh is refined adaptively based on the local error of the velocity and volume fractions. The interface and the bottom boundary is enforced to be at maximum resolution at all time. The maximum resolution of this simulation is $0.0032\lambda_0$, where λ_0 is the carrier wave length. 92

5.2 Validation of the RANS turbulence model, showing the evolution of TKE and turbulent eddy viscosity of a Stokes wave and comparing the approximate analytical solution of decaying turbulence, eqns. (5.28) and (5.29), in still water and RANS simulations. 98
5.3 Validation of the RANS turbulence model, showing the energy budget for a Stokes wave. Top panels compare the energy budget for three different Reynolds numbers, Re = 60,000, 600,000, 1,000,000. Middle panels display the energy budget for Re = 1,000,000 with different grid resolutions, $\delta/\Delta x = 1, 2, 4$, where δ is the boundary layer thickness. Bottom panels plot the energy budget for Re = 1,000,000 with CFL numbers CFL = 0.025, 0.05 and 0.1. In all panels, E_k, E_p and $E_d(t)$ are kinetic energy, potential energy and viscous dissipation integrated over the water phase and the time, respectively. 99
5.4 This figure contains a space-time plot and wave height profiles at different locations for case FGW2 in Table 5.2. On the left (a), a space-time plot displays the evolution of surface elevation for RANS simulation with maximum refine level $L = 14$. The red dotted lines indicate the positions of the gauges. The right side contains three separate plots (b–d) at specific x locations (23.50 m, 19.50 m, 16.50 m), comparing the surface elevation over time as predicted by RANS simulations with different maximum refine level. The red dashed line is RANS simulation with maximum refine level $L = 14$, $L = 15$ for the green dot-dashed line and $L = 16$ for the blue dotted line. 102
5.5 This figure plots the surface elevation profiles at multiple gauge positions for all focused wave cases in Table 5.2 and compares the experimental measurements, RANS simulation and 'No RANS' (simulation with turbulence model disabled) at different gauge positions. The top panels (a, b) are for case FGW1 and the bottom panels (c, d) are for case FGW2. 103
5.6 This figure plots the surface elevation profiles at multiple gauge positions for all modulated plane wave cases in Table 5.1 and compares the experimental measurements, RANS simulation and 'No RANS' (simulation with turbulence model disabled) at different gauge positions. Panels (a) and (b): case MPW1; Panels (c) and (d): case MPW2; Panels (e) and (f): case MPW3; Panels (g) and (h): case MPW4. 104

5.7 This figure plots the surface elevation profiles at multiple gauge positions for all random wave cases in Table 5.2 and compares the experimental measurements, RANS simulation and 'No RANS' (simulation with turbulence model disabled) at different gauge positions. Panels (a) and (b): case RDW1; Panels (c) and (d): case RDW2; Panels (e) and (f): case RDW3; Panels (g) and (h): case RDW4. 105
5.8 The evolution of interface and turbulent visocity $\nu_{t,w}$ in water domain. Waves propagate from left to right, with breakings occurring between snapshots, creating several slowly drifting patches of underwater turbulence. 108
5.9 This figure plots the evolution of kinetic energy E_k, potential energy E_p and total energy E_t of the periodic RANS simulation of a focused group wave case. 109
5.10 This figure plots breaking parameter b against the max linear slope ϵ. Blue solid line is a semi-empirical formula (Romero et al., 2012). Red dot-dashed line is an exponential fit $b = 0.4(\epsilon - 0.08)^q$ to the RANS data where $q = 2.62$. Grey shaded region is standard deviation $\pm 1\sigma_b$ on the scaling for b. Black dots indicates calculated parameter b of RANS data. 110

6.1 **Schematic of the structure and computing diagram of the neural network model.** 119
6.2 **Test result for the temporal evolution of a Type I (focused wave group) case. a–c** Space domain. Colorbar shows the absolute value of the wave envelope B. **d–f** Wavenumber domain. Colorbar shows the absolute value of the wavenumber spectrum $\hat{B}$. Specifically, **a** and **d** show the NBM result, **b** and **e** show the MNLS+ML result, and **c** and **f** show the ground truth which is RANS simulation. **g** Mean squared error (MSE) of the absolute value of the complex envelope. **h–j** Energy evolution $E = \int \|B\|^2 \, \mathrm{d}x$ normalised by its value in the first time step E_0, the spectral mean or centroid, $\Lambda_{\text{centre}} = \int k\tilde{B}(k)\mathrm{d}k / \int \tilde{B}(k)\mathrm{d}k$, and evolution of steepness. **g–j** share the same legend, the black solid line represents the ground truth, the orange dashed line represents the MNLS+ML result or MSE of MNLS+ML compared to the ground truth, and the green dotted line represents the NBM result or MSE of NBM result compared to the ground truth. The coordinates x, k and t are normalised by (4.3). . . 123

6.3 **The figure plots surface elevation profile of a focused wave group (Type I) case at equally distributed gauge locations.** **a** Surface elevation profile. The surface elevation η is normalised by the characteristic wave height a_0. **b** Frequency spectrum. The spectrum is normalised and $\Omega = \omega/\omega_0 - 1$ is the normalised modulational frequency. Solid black line is ground truth, orange dashed line is MNLS+ML and green dotted line is NBM simulation. The coordinates t and Ω are normalised by (4.3). 124

6.4 **Test result for the temporal evolution of a modulated plane wave (Type II) case. a–c** Space domain. Colorbar shows the absolute value of the wave envelope B. **d–f** Wavenumber domain. Colorbar shows the absolute value of the wavenumber spectrum $\hat{B}$. Specifically, **a** and **d** show the NBM result, **b** and **e** show the MNLS+ML result, and **c** and **f** show the ground truth which is RANS simulation. **g** Mean squared error (MSE) of the absolute value of the complex envelope. **h–j** Energy evolution, the spectral mean or centroid, and evolution of steepness. **g–j** share the same legend, the black solid line represents the ground truth, the orange dashed line represents the MNLS+ML result or MSE of MNLS+ML compared to the ground truth, and the green dotted line represents the NBM result or MSE of NBM result compared to the ground truth. The coordinates x, k and t are normalised by (4.3). 125

6.5 **Test result for the temporal evolution of a random wave (Type III) case. a–c** Space domain. Colorbar shows the absolute value of the wave envelope B. **d–f** Wavenumber domain. Colorbar shows the absolute value of the wavenumber spectrum $\hat{B}$. Specifically, **a** and **d** show the NBM result, **b** and **e** show the MNLS+ML result, and **c** and **f** show the ground truth which is RANS simulation. **g** Mean squared error (MSE) of the absolute value of the complex envelope. **h–j** Energy evolution, the spectral mean or centroid, and evolution of steepness. **g–j** share the same legend, the black solid line represents the ground truth, the orange dashed line represents the MNLS+ML result or MSE of MNLS+ML compared to the ground truth, and the green dotted line represents the NBM result or MSE of NBM result compared to the ground truth. The coordinates x, k and t are normalised by (4.3). 126

6.6 **The figure plots surface elevation profile of a modulated plane wave (Type II) and a random wave (Type III) case. a,c** Normalised surface elevation profile. **b,d** Normalised Frequency spectrum. $\Omega = \omega/\omega_0 - 1$ is the normalised modulational frequency. **a,b** Modulated plane wave case. **c,d** Random wave case. Solid black line is ground truth, orange dashed line is MNLS+ML and green dotted line is NBM simulation. The coordinates t and Ω are normalised by (4.3). 128

6.7 **This boxplot shows the MSE error distribution in the testset for all three wave types. a** Focused wave groups (Type I). The shaded region is composed of overlapping transparent gray intervals that indicate the breaking activities in each case. **b** Modulated plane wave (Type II). **c** Random waves (Type III). **a**–**c** Evolution of MSE of MNLS+ML prediction, M-KO prediction and NBM prediction with respect to time where minimums and maximums are indicated by caps, and the boxes indicate the interquartile ranges of the MSEs, where orange dotted boxes for MNLS+ML prediction, blue backslash boxes for M-KO prediction and green slash boxes for NBM prediction. t is normalised by (4.3). 128

6.8 **Comparison to AMU wave tank experiment. a** MSE for focused wave group (Type I) cases. **b** MSE for modulated plane wave (Type II) cases. **c** MSE for random waves (Type III). The plots **a** and **b** include six gauges positioned in 6.64 m, 11.63 m, 16.11 m, 21.83 m, 26.96 m and 31.10 m. Minimums and maximums are indicated by caps, and the boxes indicate the interquartile ranges of the MSEs. Orange dotted boxes for MNLS+ML prediction, blue backslash boxes for M-KO prediction, and green slash boxes for NBM prediction. For the plot **c** the solid lines show a Type III case with a significant wave height of 80 mm, and the dotted lines display another Type III case with a significant wave height of 40 mm. Orange downward triangle marker for MNLS+ML prediction, blue circles for M-KO prediction, and green squares for NBM prediction. 132

B.1 Similar to Figure 3.3 but for case 2 from Table 3.2: spatial evolution of perturbed plane waves, showing a) the carrier wave normalised by its value at the first gauge, $a_c/a_{c,0}$; b) the normalised lower sideband $a_-/a_{c,0}$; c) the normalised upper sideband, $a_+/a_{c,0}$; d) the spectral peak, $\Omega_{\text{peak}} = \text{argmax}_\Omega \hat{A}$ with $\hat{A}$ the amplitude spectrum of η and $\Omega = \omega/\omega_0 - 1$; e) spectral mean or centroid, $\Omega_{\text{center}} = \sum \Omega_i \hat{A}_i / \sum \hat{A}_i$; f) the energy measure $E = \int |B|^2 \, \mathrm{d}t$ normalised by its value at the first gauge E_0. The black squares show the experimental data from Eeltink et al. (2022)). 165
B.2 Similar to Figures 3.3 and B.1 but for case 3 from Table 3.2. 165
B.3 Similar to Figures 3.3 and B.1 but for case 4 from Table 3.2. 166
B.4 For the reduced-form breaking models with optimised parameters, surface elevations at different gauge locations for focused wave groups (case 1 in Table 3.1). Black solid lines correspond to experimental data and coloured dashed lines to MNLS simulations with (a) the model of TD90; (b) the KO95 model with fixed-interval breaking criterion; (c) the SL model with fixed-interval breaking criterion; and (d) the H11 model with kinematic breaking criterion. 169
B.5 For the case with optimised parameters, comparison of amplitude spectra before and after breaking of a focused wave group (case 1 and case 2 in Table 3.1) for different reduced-form breaking models including no breaking model (NBM), showing experiments (black solid/dashed lines), with grey shaded region corresponding to ± 1 standard deviation from repeated experiments, and MNLS simulations with different breaking models (coloured dashed lines with markers). 171
B.6 For the modified models, comparison of amplitude spectra after breaking of a focused wave group (case 1 and case 2 in Table 3.1) for different modified reduced-form breaking models with different breaking criteria and the case with no breaking model (NBM), showing experiments (black solid/dashed lines), with grey shaded region corresponding to ± 1 standard deviation from repeated experiments, and MNLS simulations with different modified breaking models and breaking criteria (coloured dashed lines with markers). 172

C.1 Various measurements taken from a randomly selected test cases of focused wave, simulated by w3f16 model. The parameters for this case are $\gamma = 4.5027$, $a_0 = 0.0561$ m, $f_0 = 0.6100$ Hz, $L_f = 23.8265$ m and $\sigma_s = 1.2857$. 175

C.2 Depictions of various measurements taken from a randomly selected test case of modulated plane wave, simulated by w3f16 model. The parameters for this case are $f_0 = 1.3769$ Hz, $a_0k_0 = 0.2322$, $b_F = 0.0355$, $\delta\omega = 0.9984$, $\psi = \pi$ and $\alpha = 0$. 176
C.3 Various measurements taken from a randomly selected test cases of random wave, simulated by w3f16 model. The parameters for this case are $\gamma = 2.5328$, $a_0 = 0.0383$ m, $f_0 = 1.2343$ Hz and $\sigma_s = 1.2857$. 177
C.4 This figure depicts four simple variants of the ConvLSTM model. . . 178
C.5 The figure depicts various measurements taken from a randomly selected modulated plane wave case simulated by w9f64 model. In subplot (a), panels (i), (ii) and (iii) show the evolution of the absolute value of the complex envelope using different models, while panels (iv), (v), and (vi) show the evolution of the absolute value of the wavenumber spectrum. Specifically, panel (i) and (iv) show the NBM result, panel (ii) and (v) show the MNLS+ML result, and panel (iii) and (vi) show the ground truth generated by the M-KO95 model. In subplot (b), panel (i) plots the mean squared error (MSE) of the absolute value of the complex envelope.Panels (ii), (iii), and (iv) compare the energy evolution, wavenumber spectral mean or centroid, and evolution of steepness. All panels share the same legend, which is placed on the top of the subplot (b). In the legend, the green solid line represents the ground truth, the blue dashed line represents the MNLS+ML result or MSE of MNLS+ML compared to the ground truth, and the orange dotted line represents the NBM result or MSE of NBM result compared to the ground truth. 179

C.6 The figure depicts various measurements taken from a randomly selected random wave case simulated by w9f64 model. In subplot (a), panels (i), (ii) and (iii) show the evolution of the absolute value of the complex envelope using different models, while panels (iv), (v), and (vi) show the evolution of the absolute value of the wavenumber spectrum. Specifically, panel (i) and (iv) show the NBM result, panel (ii) and (v) show the MNLS+ML result, and panel (iii) and (vi) show the ground truth generated by the M-KO95 model. In subplot (b), panel (i) plots the mean squared error (MSE) of the absolute value of the complex envelope.Panels (ii), (iii), and (iv) compare the energy evolution, wavenumber spectral mean or centroid, and evolution of steepness. All panels share the same legend, which is placed on the top of the subplot (b). In the legend, the green solid line represents the ground truth, the blue dashed line represents the MNLS+ML result or MSE of MNLS+ML compared to the ground truth, and the orange dotted line represents the NBM result or MSE of NBM result compared to the ground truth. 180

C.7 This figure plots the MSE error distribution across the modulated plane wave test cases. Panel (a) shows the evolution of MSE of MNLS+ML prediction and NBM with respect to time where blue line with $\pm 1\sigma$ error bar indicates the MSE of MNLS+ML prediction and orange line with $\pm 1\sigma$ error bar indicates the MSE of NBM prediction. Panel (b) illustrates the MSE of MNLS+ML prediction and NBM at the final time step where blue bar stands for MNLS+ML and orange bar for NBM. 181

C.8 This figure plots the MSE error distribution across the random wave test cases. Panel (a) shows the evolution of MSE of MNLS+ML prediction and NBM with respect to time where blue line with $\pm 1\sigma$ error bar indicates the MSE of MNLS+ML prediction and orange line with $\pm 1\sigma$ error bar indicates the MSE of NBM prediction. Panel (b) illustrates the MSE of MNLS+ML prediction and NBM at the final time step where blue bar stands for MNLS+ML and orange bar for NBM. 182

D.1 **Test results for the temporal evolution of 8 test cases of focused wave group.** 184

D.2 **Test results for the temporal evolution of 8 test cases of modulated plane wave.** 185

D.3 **Test results for the temporal evolution of 8 test cases of random waves.** 186

D.4 **Test results for the temporal evolution of a non-breaking focused wave group.** 187
D.5 **Training history of the neural network.** 188

List of Tables

3.1 Input parameters for the focused wave groups. 34
3.2 Input parameters of the perturbed plane wave cases from Eeltink et al. (2022). 36
3.3 Results from parameter optimisation and modification of the reduced-form breaking models (NBM denotes the case with no breaking model). The L2 loss is normalised by its value for the case with no breaking model. 51

4.1 Overview of the training, validation and prediction losses of the models considered. The MNLS equation without a breaking model (NBM) and with a fully connected LSTM model (Hochreiter and Schmidhuber, 1997) are evaluated as baseline. All losses are computed by (4.20), divided by a universal upper bound of magnitude of ΔB, which is 0.04 for all types of waves considered in this study. 73

5.1 Input parameters for the modulated plane wave cases. 93
5.2 Input parameters for the focused wave groups and random waves based on the JONSWAP spectrum. Cases for which a focussing distance x_f is given correspond to focused wave groups, others to random waves. 94

6.1 A comprehensive overview of the prediction losses of the models taken into consideration. MNLS without a breaking model (NBM) are evaluated as a baseline. All losses are calculated using (6.11) and (6.12) averaged over the entire time span $t \in [0, 100T_0]$ for the surface envelope η. The missing values marked by 'NaN' means the model encounter numerical issues and has failed to provide results in one or more test cases. 130

B.1 Results from modification of the reduced-form breaking models (NBM denotes the case with no breaking model). The L2 loss is normalised by its value for the case with no breaking model. 168

D.1 A comprehensive overview of the prediction losses of the models taken into consideration. MNLS without a breaking model (NBM) are evaluated as a baseline. All losses are computed by (6.11) and (6.12) averaged over the entire time span $t \in [0, 100T_0]$ for magnitude of the envelope $|B|$. Missing values marked by 'NaN' means the model encounter numerical issues and has failed to provide results in one or more test cases. 190

Chapter 1

Introduction

1.1 Thesis Outline

Wave breaking is important for a variety of reasons, such as the energy balance in the ocean, ocean mixing, connecting the atmosphere and the ocean, short-term wave dynamics and statistics, and impacts on maritime structures. The use of envelope-based wave equations, such as the Modified Nonlinear Schrödinger (MNLS) equation (Trulsen et al., 2000), is an effective way to model wave evolution for non-breaking waves in deep water and capture essential nonlinear and dispersive effects.

The MNLS extends the classical Nonlinear Schrödinger Equation (NLS) by incorporating higher-order terms and corrections that account for more complex interactions within the wave field. This makes it especially useful for modelling situations where the standard NLS falls short, such as in the presence of strong nonlinearity or when higher-order dispersion plays a significant role (i.e., for more broad-banded spectra). Applications of the MNLS include predicting rogue waves in deep water (Dudley et al., 2019), studying wave-currents interaction (Liao et al., 2023), modelling pulse propagation in optical fibers (Agrawal, 2013), and understanding wave packet dynamics in plasma physics (Infeld and Rowlands, 2000).

Despite its advanced capabilities, the MNLS lacks an inherent mechanism to model wave breaking—a critical phenomenon where waves reach a steepness threshold and begin to overturn, leading to energy dissipation and turbulence. Wave

breaking is an important phenomenon for waves in the ocean, affecting energy distribution and system stability. Existing breaking models often introduce empirical parameters or ad-hoc modifications to account for this process (Trulsen and Dysthe, 1990; Kato and Oikawa, 1995; Majda and Wang, 2001; Hwung et al., 2011), but they may not fully capture the underlying physics or may lack general applicability across different wave conditions.

This gap highlights the need for more robust, that is, generally applicable and externally validated, breaking models that can be used within the framework of envelope-type wave models such as the MNLS. This thesis addresses this need by focusing on enhancing the modelling of wave breaking dissipation in envelope-based wave equations by leveraging both conventional and machine-learning approaches.

The four specific objectives are:

- *To improve existing breaking dissipation models for envelope-based wave equations using both conventional and machine-learning approachs.*
- *To explore the feasibility of generating large-scale synthetic training data for machine learning of wave breaking using envelope-based wave equations.*
- *To investigate the potential of using RANS simulations to produce higher-fidelity training data for machine learning models of wave breaking.*
- *To evaluate and compare the performance of conventional and deep-learning-based breaking dissipation models for envelope-based wave equations.*

By addressing these objectives, the thesis seeks to overcome the limitations of existing breaking models and provide a more accurate and universally applicable tool for modelling wave dynamics. The integration of machine learning techniques and high-fidelity simulation data represents a novel approach to understanding and predicting wave breaking phenomena.

1.2 Synopsis of Thesis Chapters

The contents of the thesis chapters are described here in brief.

Chapter 2. Literature review

This chapter is an overview of the fundamentals of wave theory, wave equations for fast wave simulation, basics of numerical simulation of breaking wave, and machine learning applications.

Chapter 3. Comparison of breaking models in envelope-based surface gravity wave evolution equations

This chapter reviews four existing models for estimating the effect of breaking dissipation in envelope-based wave equations. A nonlinear optimisation approach is proposed to find optimal parameters for these models. We also propose a new reduced-form model that achieves better performance than existing models.

Specific Outcomes:

O3.1 Use of Modified Nonlinear Schrödinger Equation for Simulations.

O3.2 Evaluation of four existing reduced-form breaking models.

O3.3 Methodology for comparing experimental data and simulations.

O3.4 Proposed nonlinear optimisation approach to find optimal parameters for reduced-form breaking models.

O3.5 Discovered a new parameterisation method that improves the performance of existing breaking models.

O3.6 Implemented a specific modification to an existing breaking model that achieves the highest level of performance.

Chapter 4. A machine learning architecture for including wave breaking in envelope-type wave models

In this chapter, we propose a neural network architecture (Shi et al., 2015) that is capable of capturing the highly nonlinear effect of wave breaking and making accu-

rate predictions in envelope-based wave equations. The specific architecture learns and predicts locally. We apply the new wave breaking model proposed in Chapter 3 to generate the synthetic wave breaking dataset. The results show that the neural network architecture can learn wave breaking dissipation from focused wave groups and generalise to arbitrary wave types such as modulated plane wave and random waves based on the JONSWAP (Joint–North–Sea–Wave–Project, see in Hasselmann et al. (1973)) spectrum.

Specific Outcomes:

O4.1 Implemented a neural network framework for training and testing with wave data.

O4.2 Implemented a unified framework to sample wave parameters in parameter space and generate initial conditions for both envelope-type wave equations and direct numerical simulations.

O4.3 Implemented the proposed Convolutional-Long-Short-Term-Memory (ConvLSTM, Shi et al. (2015)) neural network architecture.

O4.4 Created large synthetic dataset for three types of waves: focused wave group, modulated plane wave and random waves with a JONSWAP spectrum.

O4.5 Trained neural network models with different configurations to search the optimal hyperparameters such as kernel number and kernel width.

O4.6 Proposed a training paradigm to learn wave breaking dissipation from only focused wave group cases, then generalised to arbitrary wave types.

O4.7 Calculated the prediction error of model over time and across waves of different types.

Chapter 5. Numerical simulation of wave breaking using RANS: comparison with experiments

In this chapter, we report the application of Reynolds-averaged numerical simulation (RANS) to simulate wave breaking. We implement and validate the stabilised RANS model (Larsen and Fuhrman, 2018) in the open-source software package Basilisk (Popinet, 2015). We run RANS simulations for a large number of breaking wave

cases to build a large high-fidelity RANS dataset.

Specific Outcomes:

O5.1 Use of an open-source software package Basilisk to perform breaking surface gravity wave simulations with adaptive mesh refinement.

O5.2 Implemented the stabilised turbulence model that is dedicated for large density-ratio surface wave simulations.

O5.3 Validated the convergence of the RANS simulations under different mesh resolutions, Courant–Friedrichs–Lewy (CFL) and Reynolds numbers.

O5.4 Compared the RANS results with experimental measurements from Eeltink et al. (2022) to validate the RANS simulations.

O5.5 Studied energy conservation and energy evolution by running simulations with periodic boundaries.

O5.6 Investigated the parametrisation of breaking dissipation as a function of slope (Drazen et al., 2008) through analysing a large number of breaking wave simulations.

Chapter 6. Using machine learning based on RANS to model deep-water wave breaking in envelope-type wave models

In this chapter, we train the previously proposed neural network model with the large RANS dataset we discussed in Chapter 5. We show that the neural network model is able to learn breaking dissipation from RANS data directly. Thus, we have established a machine learning model that can be trained on RANS simulations and integrated into envelope-based wave equations.

Specific Outcomes:

O6.1 Trained neural network model on data generated from RANS simulations.

O6.2 Made minor modifications to the training process to deal with the noise and bias in RANS data.

O6.3 Studied the evolution of the surface elevation, wavenumber/frequency spectrum, energy, wavenumber/frequency downshift, and the steepness for the neural network model predictions.

O6.4 Verified that the neural network model is able to generalise to unseen wave

types.

O6.5 Compared the performance of the neural network model and the existing breaking models with optimised/literature parameters.

O6.6 Compared the prediction of the neural network model to wave tank experiment data directly.

This thesis is submitted as an "integrated thesis", meaning each chapter is a standalone paper. As such, each chapter has its own introduction and literature review.

1.3 List of Publications

The contents of Chapters 3, 4 and 5 have been published as peer-reviewed journal articles. Chapter 6 will be submitted soon. The list of papers reads as follows.

CHAPTER 3 (published)

Liu, Y., Eeltink, D., Tang, T., Barratt, D., Li, Y., Adcock, T. A. A., van den Bremer, T. S., 2023. Comparison of breaking models in envelope-based surface gravity wave evolution equations. *Phys. Rev. Fluids* 8, 054803. `https://doi.org/10.1103/PhysRevFluids.8.054803`

Credit authorship contribution statement

Yuxuan Liu: Writing – original draft, Validation, Software, Methodology, Investigation, Formal analysis, Conceptualisation. Debbie Eeltink: Writing – review & editing, Supervision. Tianning Tang: Experiments, Experiment methodology. Dylan Barratt: Experiments, Experiment methodology. Ye Li: Experiments, Experiment methodology, Writing – review & editing. Thomas A.A. Adcock: Writing – review & editing, Supervision. Ton S. van den Bremer: Writing – review & editing, Supervision. Tianning Tang, Dylan Barratt and Ye Li performed the water tank experiment at Shanghai Jiao Tong University and I used their experimental data in the paper.

CHAPTER 4 (published)

Liu, Y., Eeltink, D., van den Bremer, T. S., Adcock, T. A. A., 2024. A machine learning architecture for including wave breaking in envelope-type wave models. *Ocean Engineering* 305, 118009. https://doi.org/10.1016/j.oceaneng.2024.118009

Credit authorship contribution statement

Yuxuan Liu: Writing – original draft, Validation, Software, Methodology, Investigation, Formal analysis, Conceptualisation. Debbie Eeltink: Supervision. Ton S. van den Bremer: Writing – review & editing, Supervision. Thomas A.A. Adcock: Writing – review & editing, Supervision.

CHAPTER 5 (published)

Liu, Y., van den Bremer, T. S. and Adcock, T. A. A., 2024. Numerical simulation of wave breaking using RANS: comparison with experiments. *European Journal of Mechanics-B/Fluids.* https://doi.org/10.1016/j.euromechflu.2024.08.003

Credit authorship contribution statement

Yuxuan Liu: Writing – original draft, Visualisation, Software, Methodology, Investigation, Formal analysis, Conceptualisation. Ton S. van den Bremer: Writing – review & editing, Supervision. Thomas A.A. Adcock: Writing – review & editing, Supervision.

CHAPTER 6 (to be submitted)

Liu, Y., Eeltink, D., Adcock, T. A. A. and van den Bremer, T. S., 2024. Using machine learning based on RANS to model deep-water wave breaking in envelope-type wave models.

Credit authorship contribution statement

Yuxuan Liu: Writing – original draft, Validation, Software, Methodology, Investigation, Formal analysis, Conceptualisation. Debbie Eeltink: Supervision. Thomas A.A. Adcock: Writing – review & editing, Supervision. Ton S. van den Bremer:

Writing – review & editing, Supervision.

Chapter 2

Literature Review

Wave breaking plays an important role in air-sea interaction, playing multiple roles including the regulation of wave heights, creation of vorticity and turbulence, maintaining the wave energy budget as a energy sink, generation of currents, and enhancement of gas transfer at the sea surface (Melville, 1996). Offshore structures and marine activities can benefit from improved wave forecasting by successfully modelling breaking dynamics. Solving envelope-based models (systems using a mathematical representation that approximates the overall shape of waveforms) (Trulsen and Dysthe, 1996; Trulsen et al., 2000) provides a way of accurate and fast prediction of wave evolution until breaking onset. However, wave breaking significantly affects the evolution of the wave in a strongly nonlinear way, making it difficult to include in envelope-based models. It is of great interest to improve on predicting wave evolution after breaking. In this review of the literature, we present introductory material which different parts of this thesis build on: envelope-based wave equations, Reynolds averaged turbulence model applied to surface gravity waves, and the neural network structure we use to build the reduced-form wave breaking model in envelope-based wave equations.

2.1 A Century of Ocean Surface Wave Modelling and Forecasting

The study of linear wave theory can be traced back to the nineteenth century, with Stokes' 1847 publication (Stokes, 1847) marking the first study on weakly nonlinear surface waves. Since then, a substantial body of both theoretical and experimental work has been developed to investigate the weakly nonlinear behaviour of non-breaking waves, as highlighted by Benjamin and Feir (1967) and Lake et al. (1977). These efforts laid the groundwork for further studies into the instability of deep-water waves (Melville, 1982) and subsequent works of breaking waves.

Twentieth-century studies have shown that linear wave theory cannot predict wave evolution reliably. Early studies on narrow-banded weakly nonlinear waves rely on the nonlinear Schödinger equation (Zakharov and Shabat, 1972) and its variants. Dysthe (1979) proposed a high-order (fourth-order) NLS, which was later applied to study wave groups in deep water (Lo and Mei, 1985). The bandwidth—describes well by Dysthe (1979)'s equation—was improved by Trulsen and Dysthe (1996) with a new higher-order truncated linear dispersion operator, and soon Trulsen et al. (2000) replaced the truncated operator with its exact version. Gramstad and Trulsen (2011) derived a Hamiltonian form of the modified NLS on arbitrary water depth.

Numerical models are routinely used for wave modelling and forecasting. For wave modellers, many computational tools are available. In wave modelling, phase-averaged models such as SWAN (Booij et al., 1999) and WAM (WAMDI, 1988; Komen et al., 1994) focus on modelling the statistical (or wave-avaraged) properties of the wave field, such as significant wave height, mean wave direction, and wave period or, in some cases, model the spectrum directly. Phase-averaged models are efficient tools for large-scale and long-term wave predictions. On the other hand, phase-resolved models simulate the actual surface elevation of the waves, capturing the details of individual wave phases at higher computational cost, making these models suitable for small-scale studies where understanding of individual wave behaviour is crucial. These models are based on solving the governing equations of fluid

motion or reduced-form versions thereof (the Navier–Stokes equations or simplifications such as the Boussinesq or NLS equations) that describe the wave dynamics in detail.

Phase-averaged models allow prediction on regional (10–100 kilometers), national (100–1,000 kilometers), and global (1,000–10,000 kilometers) scales, with a temporal scale ranging from hours to decades. They use grid resolutions from 100 meters (local coastal studies) to 55 kilometers (global scale). These models are widely used in applications such as long-term climate modelling (Semedo et al., 2011; Brus et al., 2021) and ocean energy budget studies (Ardhuin et al., 2010). They are also crucial for predicting large-scale wave patterns and energy distribution, which can inform coastal protection (Reeve et al., 2018), marine navigation routes (Zhang et al., 2023), and planning for offshore structures (Amaechi et al., 2022). Additionally, phase-averaged models are applied in resource management, such as estimating the potential of wave energy generation over vast areas (Neill et al., 2018), and in risk assessments for maritime operations and coastal infrastructure (Muis et al., 2016).

In comparison to phase-averaged models, phase-resolved models provide more detailed, wave-by-wave forecasting on a finer scale, ranging from 10 meters to 1 kilometers, with resolutions ranging from 0.1 to 1 meter (when applied to ocean waves in the field), and are applicable for time scales of seconds to a few hours. Phase-resolved models are routinely applied to study rogue waves (Zheng et al., 2020; Li et al., 2021). Phase-resolved models have many industrial applications such as improving the control of surface vessels (Liu et al., 2024b), floating platforms (Liu et al., 2024a), offshore wind turbines (Ma et al., 2018), wave energy converters (Li et al., 2012), and other maritime devices. Enhancing phase-resolved models also improve the prediction of operational conditions for submerged structures, such as wave-induced forces acting on pillars (Chen et al., 2018), hydrodynamic loads on ship hull (Ley and El Moctar, 2021) and scour around foundations (Kulkarni et al., 2023). Recent advances in wave field reconstruction algorithms (Ehlers et al., 2023) and real-time wave field capture technologies, utilising X-band radars (Previsic et al., 2021) and lidar devices (Grilli et al., 2011; Nouguier et al., 2014), have further

increased the use of phase-resolved forecasting and the applicability of phase-resolved models in industrial application.

Different phase-resolved models have different advantages and disadvantages. For breaking wave simulation, Navier–Stokes simulations are physically correct (i.e., they resolve all the relevant physical processes) and can resolve the evolution of the breaking process directly (Lubin and Glockner, 2015; Mostert et al., 2022). However, solving the Navier–Stokes equations is extremely computationally expensive and inefficient. Potential flow models are accurate for non-breaking waves, as well as breaking waves until the overturning crest touches the interface, although many implementations cannot deal with waves after the over-turning point unless a breaking model is added (Engsig-Karup et al., 2009; Bihs et al., 2020). Potential flow models are cheaper and faster than Navier–Stokes. Envelope-based models are derived from Taylor expansions of potential flow equation. Envelope-based models can simulate non-breaking waves, but require additional modelling to account for wave-breaking dissipation (Eeltink et al., 2022; Liu et al., 2023). Amongst all the phase-resolved modelling techniques, envelope-based models are the most efficient ones. Problems involving the evolution of slowly varying wave envelopes—especially narrow-banded, modulated wave groups where nonlinear effects like modulational instability and envelope dynamics are important—are best handled by envelope-based methods. In contrast, Navier–Stokes simulations (DNS, LES, RANS) are more suited for problems requiring detailed resolution of the wave field, including turbulence, viscous effects, and complex boundary interactions. We will walk through all these models in detail in the following sections.

2.2 Modelling Non-Breaking Waves with Potential Flow Theory

Non-breaking waves are modelled well by the potential-flow equations. By introducing the assumptions of irrotationality ($\nabla \times \mathbf{u} = 0$), zero viscosity ($\mu = 0$) and incompressibility ($\nabla \cdot \mathbf{u} = 0$), the governing equations for potential flow can be ob-

tained from the Navier–Stokes equations:

$$\nabla^2\phi = 0 \quad \text{for} \quad -\infty < z < \eta, \tag{2.1}$$

$$\frac{\partial\phi}{\partial t} + g\eta + \frac{1}{2}\nabla\phi\cdot\nabla\phi = 0 \quad \text{at} \quad z = \eta, \tag{2.2}$$

$$\frac{\partial\eta}{\partial t} + \nabla\phi\cdot\nabla\eta = \frac{\partial\phi}{\partial z} \quad \text{at} \quad z = \eta, \tag{2.3}$$

$$\frac{\partial\phi}{\partial z} \to 0 \quad \text{as} \quad z \to -\infty, \tag{2.4}$$

where (2.1) describes the potential-flow equation for an inviscid fluid, assuming the flow is irrotational and incompressible. The variable ϕ represents the velocity potential, which satisfies Laplace's equation in the region below the free surface, $z < \eta$, where z is the vertical coordinate and η is the free surface elevation. The dynamic boundary condition at the free surface is given by (2.2). Equation (2.3) represents the kinematic boundary condition, which ensures that particles on the free surface remain on that surface over time. In the context of deep water, (2.4) corresponds to the no-normal-flow condition at the domain's bottom boundary.

Potential equations (2.1)–(2.4) capture the full nonlinearities until viscous effects become important such as when a wave crest impacts the surface. However, solving fully non-linear potential flow equations is computationally expensive. One approach to accelerating (2.1)–(2.4) is to 'linearise' by ignoring higher-order terms and evaluate the boundary conditions at the still water level (Mei, 1989). By taking a perturbation expansion around the free surface it is possible to capture 'weak' non-linearity, which models waves well up to wave breaking. Wave breaking is considered a 'strong' non-linearity and requires solving the more complex Navier–Stokes equations. Much of this thesis looks at how we can capture strong non-linearity in the far simpler models used to analyse weakly non-linear waves.

2.3 Weakly Nonlinear Formulation of Waves in Deep Water

Numerous authors use envelope-based equations derived from potential flow assumptions because solving protential-flow equations directly is not efficient (Lo and Mei, 1985; Henderson et al., 1999; Shemer et al., 2002; Clamond et al., 2006; Shemer and Dorfman, 2008; Toffoli et al., 2010b; Adcock and Taylor, 2016a,b; Barratt et al., 2021). These equations are obtained by assuming a narrow bandwidth (the limits of which are considered in Adcock and Taylor (2016b)). There are many variants of envelope-based equations, such as the NLS equation (Zakharov and Shabat, 1972), the modified Nonlinear Schrödinger equation (MNLS79) (Dysthe, 1979), the broader-band modified Nonlinear Schrödinger equation (BMNLS) (Trulsen and Dysthe, 1996) and the modified Nonlinear Schrödinger equation (MNLS) (Trulsen et al., 2000) enhanced with exact linear operator, and the viscous Dysthe equation (Carter et al., 2019b). Dysthe (1979) introduced higher-order correction terms to the NLS equation using perturbation analysis. In comparison to Dysthe (1979), the equations by Trulsen and Dysthe (1996) and Trulsen et al. (2000) improved resolution in bandwidth. The viscous Dysthe equation is derived from the potential flow equation but incorporates the effects of viscosity. In the present study, we use the equation by Trulsen et al. (2000) as this does not suffer from the 'leakage' issues (Lake et al., 1977)—spectral wave energy leaks into higher frequency components due to approximation errors in the dispersion relation—of the earlier equations but is computationally as efficient as Trulsen and Dysthe (1996).

The MNLS equation introduced above is suitable for infinitely deep water. To adapt the MNLS equation to finite water depth, Finite-depth MNLS equation formulation is needed for sufficiently large water depth (Lo and Mei, 1985; Barratt et al., 2021). Gramstad and Trulsen (2011) provided a Hamiltonian formulation of the MNLS for arbitrary water depth, along with asymptotic formulas for infinitely deep water and sufficiently large water depth.

2.4 MNLS Simulations of Surface Wave Groups

As one of the early studies that used wave groups, Lo and Mei (1985) performed numerical simulations to study the evolution of a bell-shaped envelope with different maximum heights. A non-dimensional version of the Dysthe (1979) equations is used to carry out the numerical study.

Subsequently, Adcock and Taylor (2016a,b) studied 2D and 3D MNLS simulations and compared with fully nonlinear potential-flow results. These simulations used the truncated MNLS equation (Trulsen and Dysthe, 1996). The bound harmonics, which are coupled to the primary wave through nonlinear interactions and modify its shape and characteristics, are reconstructed up to the third order. All individual parts of the envelope—first-order wave and higher-order bound waves—match the fully nonlinear potential flow results well. In both articles, we observe oscillations before the wave group in MNLS simulations, in contrast to the fully nonlinear potential flow result. The oscillations are caused by the unphysical behaviour of the truncated MNLS equation (Trulsen and Dysthe, 1996).

Barratt et al. (2021) investigated the simulation of directionally spread surface gravity wave groups in both deep and finite-depth waters using the MNLS equation, comparing these results against those from a fully-nonlinear potential-flow code. Their findings reveal that the MNLS model, with both the truncated and exact versions of the dispersion operator, yields accurate simulations when the carrier wave's direction and wavenumber are aligned with the wave group's propagation and spectral peak, respectively. The exact dispersion operator is less sensitive to deviations from these conditions, maintaining accuracy even when the carrier wave's parameters do not match the wave group's properties. This robustness enhances the model's ability to simulate steep wave groups and improves the resolution of four-wave interactions while minimising energy leakage. The study also extends the application of the MNLS equation to finite-depth scenarios, demonstrating good agreement with the potential-flow model for a range of depths. This alignment suggests that the MNLS model, particularly with the exact dispersion operator, can

accurately represent the complex dynamics of wave groups across different water depths.

2.5 Wave Breaking: A Critical Challenge in Nonlinear Wave Theory

It turns out that breaking, once triggered, locally dominates wave evolution, and weakly nonlinear theory no longer applies. Numerous experimental investigations of wave breaking have been conducted (Melville, 1982; Rapp and Melville, 1990; Tulin and Waseda, 1999; Banner and Peirson, 2007; Drazen et al., 2008; Perlin et al., 2013), providing insights into the nature of breaking dissipation. Following the work of Phillips (1985), Drazen et al. (2008) proposed an inertial scaling law that quantifies the relationship between the energy dissipation rate and the geometric dimensions of the breaking waves. Subsequently, Romero et al. (2012) suggested an empirical formula for the inertial scaling law, which links breaking intensity to wave steepness. The inertial scaling law estimates the energy dissipated during wave breaking, but it does so without detailing the specific physical mechanisms responsible for the dissipation process. Therefore, satisfying the scaling law can be regarded as a necessary but not sufficient condition for any dissipation models applied in NLS simulations. On the numerical side, potential flow-based methods have theoretical difficulties at breaking onset, because the behaviour of the surface is undefined when the breaking crest overturns and interacts with itself (Dommermuth et al., 1988). Potential-flow simulations are very accurate at simulating fully nonlinear non-breaking waves (Ma and Yan, 2006), and can provide information about the breaking criterion (McAllister et al., 2023). But potential-flow simulations cannot resolve breaking waves, as the breaking process generates energetic vortex structures (Lim et al., 2015) near the free surface, and the velocity field is no longer irrotational—a total violation of the fundamental assumptions of potential flow theory. NLS-based simulations also rely on the potential-flow assumption, and they therefore produce non-physical results during breaking. One way to continue

the simulation of envelope-based equations beyond breaking onset is to add a dissipation term to model the breaking effect. Various empirical dissipation models have been developed (Trulsen and Dysthe, 1990; Kato and Oikawa, 1995; Majda and Wang, 2001; Hwung et al., 2011; Tian et al., 2012; Liu et al., 2023) to approximate breaking dissipation in NLS-based simulations. In these studies, comparison between NLS-based simulations and gauge measurements in experiments are made, showing the inconsistency between NLS breaking wave simulations and experiments, and how much that is improved by including proposed dissipation models. These are examined in detail in Chapter 3.

2.6 Mathematical Formulation: Navier–Stokes Equations

The evolution of breaking waves can be described by two-phase Navier–Stokes equations in 2D or 3D. In this thesis, we focus on the 2D breaking waves and neglect the surface tension. Therefore, the governing equations can be written as (e.g., Mostert et al. (2022)):

$$\frac{\partial \rho}{\partial t} + \nabla \cdot (\rho \mathbf{u}) = 0, \tag{2.5}$$

$$\rho \left(\frac{\partial \mathbf{u}}{\partial t} + \mathbf{u} \cdot \nabla \mathbf{u} \right) = -\nabla p + \nabla \cdot (2\mu \mathbf{D}) + \rho \mathbf{g}, \tag{2.6}$$

$$\nabla \cdot \mathbf{u} = 0, \tag{2.7}$$

where ρ is the fluid density, $\mathbf{u}$ is the velocity vector, μ is the dynamic viscosity, $\mathbf{D}$ is the deformation tensor, and $\mathbf{g}$ is the gravitational acceleration vector, respectively. In these simulations, the density and viscosity parameters can be a function of volume fraction. The volume fraction is zero in regions corresponding to the gas phase and ranges from arbitrarily small non-zero values up to one in regions where the cell contains the liquid phase. Therefore, (2.5) is a statement of conservation

of mass, (2.6) describes the advection and diffusion of momentum, according to the velocity, and (2.7) states the conservation of volume.

Modern numerical methods based on the Navier–Stokes equations include direct numerical simulation (DNS) in 2D (Deike et al., 2015) or 3D (Deike et al., 2016; Mostert et al., 2022), large-eddy simulation (LES) (Derakhti et al., 2018), or Reynolds-averaged numerical simulation (RANS) with stabilised turbulence models (Larsen and Fuhrman, 2018; Li and Fuhrman, 2021). These simulations solve the two-phase Navier–Stokes equation with or without a turbulence model, achieving high fidelity in resolving breaking waves, but the computation is often very expensive and inefficient, as a variety of physical phenomena occurring at different scales need to be resolved. These features vary in size, with sea sprays, jets, and droplets typically ranging from 0.1 micrometers to 1 millimeter, bubbles from 1 micrometer to 10 millimeters, breaking waves from 0.1 to 10 meters, and large-scale wave patterns from 10 meters to 1 kilometer (Deike, 2022). DNS captures fluid motion across all scales down to the Kolmogorov (1941) length scale, fully resolving turbulence and dissipating it via molecular viscosity. In contrast, LES models subgrid-scale turbulence, allowing for a coarser grid resolution. Although more efficient than DNS, LES introduces turbulence modelling, which reduces its fidelity. RANS, on the other hand, only resolves the bulk fluid motion, with turbulence modelled through RANS turbulence models. As a result, RANS is the most efficient but also the least accurate approach compared to DNS and LES. Other novel numerical methods such as Lattice Boltzmann Method (Li et al., 2016) or Smooth Particle Hydrodynamics (Ma et al., 2016) are also applied by researchers to solve the fluid motion in the context of air-water multiphase flow. To stay within the scope of this discussion, we will not introduce these numerical methods in detail. In addition, we will not investigate the difference between 2D and 3D turbulence generated by wave breaking, but we note that turbulence in 2D differs from 3D, as 2D turbulence exhibits an inverse cascade (Boffetta and Ecke, 2012).

2.7 Machine Learning in Fluid Dynamics and Oceanography

Machine learning has played a discernible role in advancing the understanding of fluid dynamics and oceanography, tracing a rich history of contributions in these fields. The objective of machine learning is to build a model that learns from data and generalises to unseen data (Samuel, 1959; Koza et al., 1996). Conventional machine learning methods applied in oceanography include statistical techniques such as curve fitting (Romero et al., 2012), Support Vector Machines for ship classification (Mahjoobi and Adeli Mosabbeb, 2009; Xu et al., 2013), and Random Forests for data assimilation in wave forecasting (Campos et al., 2021). In fluid dynamics, widely used techniques such as kriging (Gaussian process regression) (Krige, 1951) have also found applications in ocean dynamics. Brunton et al. (2020) provides a comprehensive review of machine learning approaches in fluid dynamics, highlighting their applications and potential integration with emerging deep learning technologies. Conventional machine learning methods typically yield interpretable results, enabling a clear understanding of how input features influence the output. This makes them well-suited for applications where explainability and transparency are crucial. However, these methods often suffer from limitations in model expressiveness and are subject to the "curse of dimensionality" (Bellman, 1957), which restricts their ability to model complex non-linear relationships or handle large-scale, high-dimensional data effectively.

Deep learning is a subset of machine learning that uses three or more layers of perceptrons to learn from raw input progressively (LeCun et al., 2015). Artificial Neural Networks (ANN) are one of the most common architectures in deep learning (Schmidhuber, 2022). In the context of ocean applications, Deo and Sridhar Naidu (1998) were the first researchers who demonstrated the superiority of ANNs over conventional methods in forecasting ocean wave heights. Subsequently, Deo and Jagdale (2003) applied ANNs to predict breaking wave height as well as the breaking position over an inclined bottom. There are many more ocean applications of ANNs.

We refer the reader to Portillo Juan and Negro Valdecantos (2022) for a detailed literature review.

While traditional empirical methods often rely on linear equations or assumptions to predict outcomes, neural networks can model complex and dynamic patterns through their layered architecture and interconnected neurons. Neural networks are very powerful and versatile, due to their modularity and structural flexibility. Each neuron receives input, applies an activation function to process it, and then transmits the output to subsequent neurons or produces a final result (Brunton et al., 2020). Neurons can also be arbitrarily stacked, linked and programmed to adapt to different tasks.

Beyond ANN networks, several other architectures are employed by researchers in oceanography studies:

- Convolutional Neural Networks (LeCun et al., 2015) are typically applied to visual tasks, such as ship detection (Liu et al., 2021), ocean surface reconstruction (Zhao et al., 2023) and wave segmentation (Chao et al., 2024).

- Recurrent Neural Networks (Schmidt, 2019) are applied to analyse time series profiles and make sequential predictions, such as ship maneuvering (D'Agostino et al., 2022) and real-time control of offshore devices (Zhang et al., 2024b).

- Transformers (Vaswani et al., 2017) utilise self-attention mechanisms to capture long-range dependencies in data sequences. Transformers can be applied to spatial-temporal predictions such as sea water temperature forecasting (Chen et al., 2024) or ship trajectory prediction (Xue et al., 2024).

- Variational Autoencoders (VAEs) (Kingma and Welling, 2013) have the potential to derive reduced-order representation for chaotic systems in its latent space. In fluid mechanics, VAEs are applied to reduce the dimensionality of fluid flows (Solera-Rico et al., 2024).

- Generative Adversarial Networks (GANs) (Goodfellow et al., 2014) are a kind of generative model, useful for generating synthetic data and learning data

distributions. Zhang et al. (2024a) applied GANs to reconstruct bathymetry data, showing superior performance when comparing to simple interpolation. Gao et al. (2024) conducted unsupervised anomaly detection study of underwater thrusters using GANs.

- Graph Neural Networks (GNNs) (Scarselli et al., 2009) are a class of deep learning models designed to handle data that is structured as graphs. Unlike CNNs, GNNs do not require the data to be uniformly gridded. In the context of ocean modelling, Zhang et al. (2024c) combined GNNs with the Smoothed Particle Hydrodynamics approach to study wave-structure interactions.

The number of deep learning architectures is vast and constantly growing. Researchers create new networks on a daily basis, while existing architectures can be modified, combined, tuned, or linked together, much like neurons in a biological network. This flexibility allows for endless customisation, enabling the design of models that can be tailored to specific tasks and optimised for performance.

2.7.1 Machine Learning in Wave Prediction and Analysis

Long Short Term Memory (LSTM) Network (Hochreiter and Schmidhuber, 1997) has important applications in processing time series data. In the context of ocean wave forecasting, Eeltink et al. (2022) applies the LSTM network to predict the evolution of breaking waves. The LSTM network is embedded into a high order time-NLS framework, where the time-NLS equations predict the envelope of the non-breaking wave. When breaking occurs, the LSTM network provides correction to the time-NLS prediction to cope with the breaking dissipation. Eeltink et al. (2022) present a comprehensive framework for predicting wave breaking and its impact on wave evolution. They classify wave conditions into three distinct categories: modulated plane waves, focused wave groups, and random waves, to address the complexity and diversity of wave phenomena. For each category, they train and evaluate an LSTM network, demonstrating the network's ability to adapt to different wave dynamics. The accuracy of the machine learning model is quantita-

tively assessed using the mean squared error of the envelope, comparing the machine learning predictions against experimental measurements. This approach highlights the significant improvement in predicting breaking waves achieved by the machine learning model, showcasing its potential in enhancing wave forecasting accuracy. However, the study also acknowledges a limitation: the model's inability to retrieve phase information of the wave field. This limitation is attributed to the constraints of the time-NLS framework used in the study.

The other direction of machine learning physics modelling is using Physics-Informed Neural Network (PINN) (Raissi et al., 2019), or incorporating physics-informed loss into the training phase. To our best knowledge, there is no successful study on deep water breaking wave with PINN. Despite that, PINN has shown its capability in learning wave physics and fluid dynamics.

In the context of wave physics, Ehlers et al. (2024) proposes using a PINN network to reconstruct wave fields between measurement points. They integrate the hydrodynamic nonlinear Schrödinger equation into the PINN's loss function to ensure physical consistency in the wave fields. The results showed that the PINN framework successfully reconstructed wave surface envelopes from limited measurement points, with improved quality when equation coefficients were treated as trainable variables.

For learning fluid dynamics, specfically multiphase flow with large density ratio, Qiu et al. (2022) explores the use of PINN to model two-phase flow using the phase-field method. The authors focus on developing a model that integrates the Cahn–Hilliard equation and Navier–Stokes equations into the framework of PINNs, addressing the challenge of capturing complex fluid interfaces in immiscible incompressible two-phase flow. The authors tested the effectiveness of their model in two scenarios: a reversed single vortex and a rising bubble in large density ratio flows. The results showed that the PINN-based phase-field model could accurately capture the interface and dynamics of two-phase flow, with the ability to handle large density ratios effectively. They demonstrated that the model preserves mass conservation and captures the essential features of the flow dynamics, such as the shape

and rising velocity of bubbles. Their study suggests that the PINN-based approach can potentially be applied to simulate surface waves.

2.7.2 A Convolutional-Recurrent Neural Network Model

A convolutional recurrent architecture (ConvLSTM hereinafter) that uses the existing LSTM (Hochreiter and Schmidhuber, 1997) network structure is introduced by Shi et al. (2015). For the equations representing the ConvLSTM network structure, see Appendix A. ConvLSTM network has been adopted in various applied ocean studies. In recent studies, researchers use ConvLSTM network to predict the significant wave height. Choi et al. (2020) estimated real-time significant wave height from raw ocean images using 2D and 3D deep neural networks. Han et al. (2022) and Song et al. (2022) predicted significant wave height in the South China Sea and Beibu Gulf respectively using ConvLSTM-based networks, achieving close agreement with field measurements. These studies demonstrate that ConvLSTM is able to predict the nonlinear evolution of wave statistics under various coarse-grain levels.

In conclusion, promising results to model wave breaking with LSTM are provided in Eeltink et al. (2022)'s study. However, LSTM is versatile model that lacks physical constraints. Therefore, LSTM does not guarantee quality of prediction of wave breaking dissipation. PINNs are important neural architectures for capturing physics, but they require closed-form analytic expressions of the physical model to calculate the loss during training. Modelling wave breaking with PINNs is a potential solution, but there are many forseeable difficulties, and, to our best knowledge, no promising results with PINNs have yet been obtained. ConvLSTM, on the other hand, exhibits many advantages when compared to LSTM, with more flexibility and less stringent constraints on the problem formulation than PINNs. ConvLSTM performs convolution operations, enabling it to learn and predict locally. With convolutions, ConvLSTM also embeds the translation invariance of physics naturally into the architecture. ConvLSTM provides promising results in wave breaking prediction and shows better generalisability to unseen wave types when compared to LSTM. These are examined in detail in Chapters 4 and 6.

2.8 Conclusions

In summary, the literature review has illuminated several key themes, including nonlinear wave theory, wave breaking effects, computational fluid dynamics, and machine learning models, each contributing uniquely to this thesis. While existing research has made significant contributions to our understanding of wave breaking, there remain notable gaps in the literature, particularly in wave breaking models in envelope-based equations. This thesis aims to address these gaps by training neural network models using a RANS simulation-based dataset. By doing so, it contributes to the field by improving the prediction of breaking waves. This research has the potential to build efficient operational wave prediction models, thereby advancing our knowledge of oceanography and informing future research endeavors.

Chapter 3

Comparison of breaking models in envelope-based surface gravity wave evolution equations

Abstract

Wave breaking is the main mechanism that dissipates energy from ocean waves by wind. Its effects on the frequency spectrum cause a downshift of the spectral peak and dissipation of the total energy of the spectrum. Various reduced-form wave breaking models have been developed to capture wave breaking in envelope-based wave evolution equations for perturbed plane wave systems, but their applicability to waves with a continuous spectrum has not been examined. In this chapter, we perform Modified Nonlinear Schrödinger equation simulations to study four existing wave breaking models and compare the results with new experimental data for breaking unidirectional wave groups. We first compare the different wave breaking models for perturbed plane wave simulations and then examine their potential extension to waves with a continuous spectrum. We find that most existing models are able to model breaking in perturbed plane waves but none produce the correct spectral dissipation for focused wave groups. We propose a modification to the breaking model by Kato & Oikawa (1995, *Journal of the Physical Society of Japan*, 64(12),

pp. 4660–4669) in order to model breaking in focused wave groups. The modified model incorporates both a breaking criterion, which activates and de-activates the dissipation term proposed by Kato & Oikawa (1995, *Journal of the Physical Society of Japan*, 64(12), pp. 4660–4669), and a heuristic spectral weighting function that is obtained by fitting to experimental data. The modified model also predicts breaking in perturbed plane waves well.

3.1 Introduction

Surface gravity wave breaking is a familiar phenomenon to those observing the ocean (Babanin, 2011). Yet, a good understanding capturing the fundamental physics of wave breaking has proved difficult for scientists and engineers. Understanding breaking is important for multiple reasons including energy balance in the ocean (Hasselmann, 1974), ocean mixing, air-sea interactions (Melville, 1996; Deike, 2022), influencing short-term wave statistics (Toffoli et al., 2010a), and loading on maritime structures (Peregrine, 2003).

Understanding the problem of wave breaking on a wave-by-wave basis (as opposed to a phased-averaged sea-state analysis) can be crudely broken down into understanding when waves break and then understanding the subsequent evolution. Wave breaking criteria typically use the wave steepness, wave speed and water depth to provide a threshold above which waves would break. The post-breaking behaviour is a complex multi-scale process. Both parts of the problem are active areas of research.

Another problem in ocean wave physics is modelling the evolution of non-breaking waves, which is considered a (weakly) non-linear process. A widely used model for deep-water waves is the non-linear Schödinger (NLS) equation and its higher-order, or 'Modified' (MNLS) (Dysthe, 1979), variants (see Dysthe and Trulsen (2001) for an account of how these have developed). They model the evolution of a wave envelope, which must be multiplied by a carrier wave to obtain the free surface elevation. Due to their underlying assumptions, the validity of these models is restricted to

spectra of limited bandwidth. Generally, these equations can predict the evolution of ocean waves well, although prediction of the largest waves remains challenging due to the non-linear physics driving a local broadening of the spectrum (Adcock and Taylor, 2016a). The great benefit of these equations is that they are computationally fast and thus are ideal for performing long-duration random simulations. However, in any random simulation there will be some wave breaking, which is not captured in the basic MNLS equations. Thus, it is necessary to modify the standard equations in order to capture this process by adding a reduced-form or data-driven breaking term (e.g., (Eeltink et al., 2022)). Such a model can never be perfect—wave breaking is highly complex, turbulent and three dimensional—but even if the model is imperfect locally it is important that the dominant spectral changes are quantitatively captured. This is the topic of the present chapter.

A number of existing breaking models can be added to the MNLS equation as a dissipation term D (cf. 3.3, discussed in detail in 3.2.2). We will examine four. Trulsen and Dysthe (1990) developed a damping term that switches on when the amplitude of the waves reaches above a threshold. Kato and Oikawa (1995) modified the return-current term in the MNLS equation to capture breaking, with breaking essentially turning on when the spectrum broadens. Similarly, applying a selective Laplacian term Majda and Wang (2001) dampens frequency components above a certain threshold. Alternatively, the energy balance equation can be used to derive a breaking module from first principles (Hwung et al., 2011; Tulin and Waseda, 1999).

Our aim is to examine how well these four reduced-form breaking models capture wave breaking and subsequent (nonlinear) wave evolution in different scenarios. We begin by examining perturbed plane wave—this scenario has been studied extensively in the literature (Benjamin and Feir, 1967; Lake et al., 1977), and the discrete nature of the problem makes an investigation of the non-linear energy transfers straightforward, resulting in a form of Fermi–Pasta–Ulam–Tsingu (FPUT) recurrence (Fermi et al., 1955; Dauxois, 2008) in the absence of breaking. Classically, perturbed plane waves have been used to study the impact of breaking (Tulin and Waseda, 1999; Melville, 1982). However, ocean waves are formed by a continuous

spectrum so, secondly, we consider breaking of focused wave groups, which can be used to model the expected shape of an extreme event in a random sea.

In this study, firstly, we review four existing breaking models for plane waves and investigate their ability to predict post-breaking wave fields for focused wave groups. To do so, we make a direct comparison between numerical simulations of the MNLS equation with an added reduced-form breaking and experimental observations. Secondly, we examine how existing breaking models may be modified. While the breaking signature is clear for nonlinearly steepening plane waves (the permanent frequency downshift), our study aims at better understanding wave breaking for focused wave groups. While it is clearly not possible to capture the detailed physics of wave breaking in a simple envelope-based model, a correct prediction of the post-breaking wave field indicates the most important physical features are captured.

Wave breaking is a 3D phenomena in nature. This is true both for breaking inception and for the subsequent physical processes (Mostert et al., 2022). However, 2D simulations are routinely used and our goal here is to understand how well the real 3D process is captured in such 2D models where we are not explicitly modelling such 3D physics as vortex filaments, crescent wave or directionally spread waves.

This chapter is organised as follows. §3.2 introduces our theoretical and experimental methodology. §3.3 examined the performance of four existing reduced-form breaking models for the canonical case of perturbed plane waves. §3.4 then examines the performance of these four models for focused wave groups by comparing to experiments we have performed. §3.5 examines how the existing models can be optimised or modified. §3.6 concludes.

3.2 Theoretical and Experimental Methodology

For our wave simulations, we use the Modified Nonlinear Schrödinger (MNLS) equation proposed by Trulsen et al. (2000). This model solves the linear part of the envelope evolution exactly and approximates the effects of nonlinearity. Four different

existing reduced-form breaking models are then added in turn as a dissipation term to the MNLS equation.

3.2.1 Envelope-Based Evolution Equation

The harmonic expansions for the velocity potential ϕ and the surface elevation η can be written as:

$$\phi = \bar{\phi} + \frac{1}{2}(Ae^{i(k_0x-\omega_0t)+k_0z} + A_2e^{2i(k_0x-\omega_0t)+2k_0z} + ... + \text{c.c.}), \tag{3.1}$$

$$\eta = \bar{\eta} + \frac{1}{2}(Be^{i(k_0x-\omega_0t)} + B_2e^{2i(k_0x-\omega_0t)} + ... + \text{c.c.}), \tag{3.2}$$

where c.c. denotes the complex conjugate, k_0 and ω_0 are the wavenumber and angular frequency of the carrier wave, $A(x,z,t)$ and $B(x,t)$ are complex envelopes, and $\bar{\phi}$ and $\bar{\eta}$ are the mean-flow potential and the wave-averaged free surface, respectively. The envelope $B(x,t)$ is described by the MNLS equation (Trulsen et al., 2000) (given here in two dimensions or for unidirectional wave propagation):

$$\frac{\partial B}{\partial t} + \mathcal{L}(\partial x)B + \frac{i\omega_0k_0^2}{2}|B|^2B + \frac{3\omega_0k_0}{2}|B|^2\frac{\partial B}{\partial x} + \frac{\omega_0k_0}{4}B^2\frac{\partial B^*}{\partial x} + ik_0\frac{\partial\bar{\phi}}{\partial x}B + D = 0, \tag{3.3}$$

$$\frac{\partial\bar{\phi}}{\partial z} = \frac{\omega_0}{2}\frac{\partial}{\partial x}|B|^2 \quad \text{at } z = 0, \tag{3.4}$$

$$\nabla^2\bar{\phi} = 0 \quad \text{for } -\infty < z < 0, \tag{3.5}$$

$$\frac{\partial\bar{\phi}}{\partial z} = 0 \quad \text{for } z \to -\infty, \tag{3.6}$$

where B^* denotes the complex conjugate of B, and D is the dissipation term that will be used to incorporate the reduced-form breaking models into the MNLS. In Fourier wavenumber space, the linear operator $\mathcal{L}(\partial x)$ can be written as Trulsen et al. (2000):

$$\frac{\partial\hat{B}}{\partial t} + i[\omega(k_0+\lambda) - \omega_0]\hat{B} = 0, \tag{3.7}$$

where λ is the modulation wavenumber.

We solve (3.3) using a spectral method in space and a 4th-order Runge–Kutta

method to advance in time. The complex envelope $B(x, t = 0)$ is required as an initial condition for the solver. We either compute the envelope directly or reconstruct it from the linearised Hilbert transform of the surface elevation profile.

The first-order surface elevation is obtained by shifting the complex envelope to the carrier frequency and taking the real part:

$$\eta_1 = \mathrm{Re}\left(Be^{i(k_0x-\omega_0t)}\right). \tag{3.8}$$

To achieve better agreement with experimentally measured surface elevation η, second-order sub-harmonic η_{2-}, second-order super-harmonic η_{2+} and third-order super-harmonic η_3 bound waves are reconstructed according to Trulsen et al. (2000); Toffoli et al. (2010b):

$$\eta_{2-} = \mathrm{Re}\left(\frac{1}{2\omega_0}\frac{\partial\bar{\phi}}{\partial x} - \frac{1}{16k_0}\frac{\partial^2|B|^2}{\partial x^2}\right), \tag{3.9}$$

$$\eta_{2+} = \mathrm{Re}\left(\left[\frac{k_0B^2}{2} - \frac{iB}{2}\frac{\partial B}{\partial x}\right]e^{2i(k_0x-\omega_0t)}\right), \tag{3.10}$$

$$\eta_3 = \mathrm{Re}\left(\frac{3}{8}k_0^2B^2e^{3i(k_0x-\omega_0t)}\right), \tag{3.11}$$

and we compute $\eta = \eta_1 + \eta_{2-} + \eta_{2+} + \eta_3$.

We use a 1D uniform mesh, and the 1D computational domain is configured to ensure that the wave group does not interact with the end of the domain or collide with itself during dispersion. The length of the computing domain spans $[-100\lambda_0, 100\lambda_0]$ in the wave propagation direction, and the resolution is $0.04\lambda_0$, where λ_0 is the carrier wavelength. The left and right-hand sides of the domain are periodic boundaries.

3.2.2 Four Reduced-Form Breaking Models

We will investigate the following four existing reduced-form breaking models: the damping term introduced by Trulsen and Dysthe (1990) (TD90 hereinafter); the modified return-current term introduced by Kato and Oikawa (1995) (KO95 hereinafter); the selective Laplacian (SL hereinafter) proposed by for example Majda

and Wang (2001); and the model introduced by Hwung et al. (2011) (H11 hereinafter) based on the downshifting theory developed by Tulin and Waseda (1999). The modified Kato & Oikawa (1995) (M-KO95 hereinafter) we propose in this chapter will be introduced in §3.5. We also include in our comparison MNLS simulations with no breaking model (labelled NBM). In this section, we list the values of the parameters suggested in the literature, which we adopt when studying the perturbed plane wave cases. For focused wave groups, we use both these parameter values as well as different values, which we obtain through optimisation (see §3.5).

Trulsen & Dysthe (1990) (TD90)

To model breaking, Trulsen and Dysthe (1990) (TD90) introduced a damping term that turns on when the envelope is steeper than a defined threshold. It is controlled by three parameters:

$$D = -\frac{\omega_0}{2\tau} B \left[\left(\frac{|B|}{B_0} \right)^r - 1 \right] H(S - S_0) \quad \text{with} \quad H(x) = \begin{cases} 0 & x < 0, \\ 1 & x \geq 0, \end{cases} \tag{3.12}$$

where we set the nondimensional relaxation time $\tau = 0.125$ (TD90), the breaking strength r is fixed to $r = 2$, and the breaking threshold $S_0 = 0.35$ with $S = k_0|B|$ following TD90; B_0 (> 0) is the critical value of $|B|$ when breaking starts, which we obtain from $B_0 = S_0/k_0$. The dissipation terms grows the more $|B|$ exceeds the critical value B_0.

Kato & Oikawa (1995) (KO95)

Kato and Oikawa (1995) (KO95) model breaking by modifying the return-current term:

$$D = \beta k_0 \frac{\partial \bar{\phi}}{\partial x} B, \tag{3.13}$$

where we set $\beta = 0.2$ according to KO95. KO95 showed that a positive value of β leads to energy dissipation and an energy flux from higher to lower wavenumbers. The dissipation term proposed by KO95 (i.e., (3.13)) increases in magnitude with

larger gradients of the envelope (squared), which also drive the return flow (cf. (3.4)), and will therefore generally be larger after spectral broadening has occurred.

Selective Laplacian (SL)

Majda and Wang (2001) proposed a dissipation term based on a selective Laplacian (SL). In Fourier space, the selective Laplacian can be written as:

$$\hat{D} = \begin{cases} -\beta \frac{\omega_0}{k_0^2} \left(|k| - k^*\right)^2 \hat{B}(k) & \text{for} \quad |k| > k^*, \\ 0 & \text{for} \quad |k| \leq k^*, \end{cases} \tag{3.14}$$

where we set $\beta = 0.01$, k is the wavenumber, k^* is the adjustable threshold value, and we set the $k^* = 1.2k_0$. The selective Laplacian reduces higher-wavenumber modes above the threshold value k^*, which leads to energy dissipation and a frequency downshift. Therefore, as the spectrum broadens, dissipation will increase.

Hwung et al. (2011) (H11)

Hwung et al. (2011) (H11) introduced a model based on Tulin's downshifting theory (Tulin and Waseda, 1999), which starts from the energy balance of a three-wave system with energy dissipation caused by a plunging breaker, including an explicit parametrisation of the shape of the jet formed to determine the energy dissipation. The dissipation term in H11 adds a steepness-based breaking threshold similar to TD90 to the theory to give Tulin and Waseda (1999):

$$D = B\left(\frac{D_a}{g|B|^2} + i4\gamma \int \frac{k_0 D_a}{g|B|^2} \mathrm{d}x\right) H(S - S_0), \tag{3.15}$$

where $D_a = \beta\omega_0|B|^4k_0^2/2$ (Tulin and Waseda, 1999; Hwung et al., 2011), we set $\beta = 0.01$, γ is a breaking strength parameter ranging from 0.4 to 0.7, and we set $\gamma = 0.7$, g is the gravitational constant, the characteristic wave steepness $S_0 = B_0k_0$ (H11 use $S = \sum a_ik_i$ instead, which is obtained from the discrete Fourier transform of the free surface η), and S_0 is the threshold value of the Heaviside function as in TD90.

3.2.3 Laboratory Experiments

To assess the ability of the four different reduced-form breaking models to model breaking in focused wave groups, we have performed laboratory experiments in the Multi-function Towing Tank at Shanghai Jiao Tong University, as illustrated schematically in Figure 3.1. Waves are generated using a flap-type wavemaker. The tank is 300 m long, 16 m wide and the depth $d = 7.33$ m. The study was restricted to wave breaking in unidirectional waves. Four pairs of resistance-type wave gauges are used, as illustrated in Figure 3.1. A sampling frequency of 100 Hz ensures sufficient temporal resolution. As each laterally positioned pair of gauges gives equivalent results, we will henceforth report only four spatial measurements along the length of the flume. The gauges are labelled according to their relative positions to the first gauge: $x = 0$ m (gauges 1 & 2), 3.04 m (gauges 3 & 4), 6.50 m (gauges 5 & 6) and 9.82 m (gauges 7 & 8).

Focused wave groups were generated from a Gaussian surface elevation variance density spectrum:

$$S(f) = \left(\frac{H_s}{4}\right)^2 \frac{1}{\sigma\sqrt{2\pi}} \exp\left[-\frac{(f-f_0)^2}{2\sigma^2}\right], \tag{3.16}$$

where H_s is the significant wave height, and σ is the spectral bandwidth. We generate waves using the 'reverse dispersion method' (Chaplin, 1996) so that under linear evolution all the phases would focus at a specified point in the wave tank. The parameters of the two cases investigated experimentally are listed in Table 3.1. The focus distance L_f was based on linear theory, as shown in Table 3.1. However, breaking happens before this theoretical distance, namely around at 77 m from the wavemaker for both cases, and the measurement carriage was placed at this location. The steepness ϵ is defined as $\epsilon = k_0 H_s/2$. The bandwidth parameter $\nu = \sqrt{m_2 m_0/m_1^2 - 1}$, where m_n is the nth moment of the variance density spectrum; for the Gaussian spectrum (3.16), $\nu = \sigma/f_0$. Cases 1 and 2 differ in their spectral bandwidth (and focus distance), with case 2 being more broadbanded. Both cases 1 and 2 are repeated 10 times.

In case 1, breaking occurred (repeatedly) between gauge pair 3 & 4 ($x = 3.04$

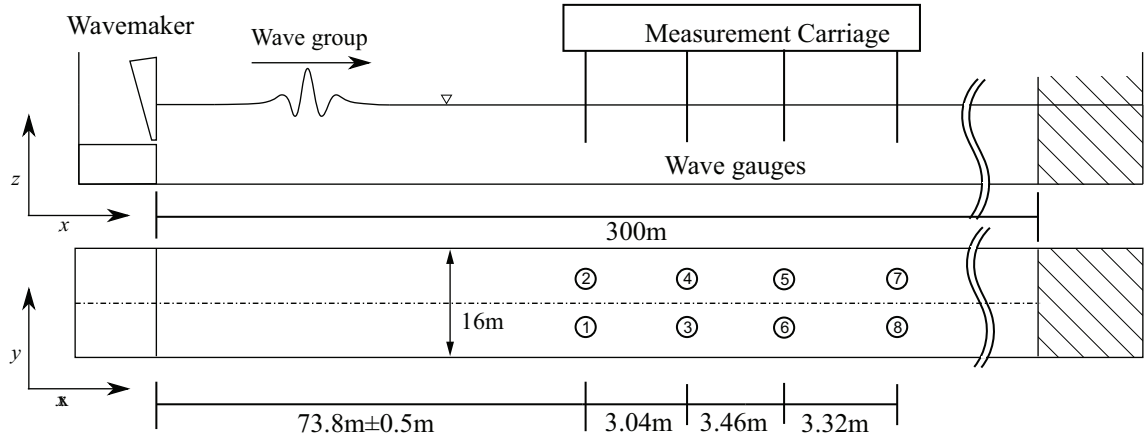


Figure 3.1: The gauge layout in the Multi-function Towing Tank at Shanghai Jiao Tong University. The gauges in the 4×2 array are labelled as 1-8. Wave groups travel from left to right.

m) and gauge pair 5 & 6 (x = 6.50 m). In case 2, a weak breaking event occurred (repeatedly) between gauge pair 3 & 4 (x = 3.04 m) and gauge pair 5 & 6 (x = 6.50 m), and a second strong breaking event occurred (repeatedly) between gauge pair 5 & 6 (x = 6.50 m) and gauge pair 7 & 8 (x = 9.82 m).

Case	f_0 **[Hz]**	H_s **[m]**	σ **[Hz]**	L_f **[m]**	$k_0 d$	ϵ	ν
Case 1	0.5	0.35	0.06	144	7.374	0.176	0.12
Case 2	0.5	0.35	0.15	87	7.374	0.176	0.3

Table 3.1: Input parameters for the focused wave groups.

3.2.4 Initial Conditions for the MNLS Simulations

In order to compare experiments and MNLS simulations, we 'initialise' the simulations using the gauge recordings at the first gauge (gauge pair 1 & 2) instead of starting from the wavemaker position. Accordingly, we set $x = 0$ to correspond to the first gauge (gauge pair 1 & 2).

To convert our surface elevation time series at the first gauge (i.e., $\eta = \eta(x = 0, t)$, a boundary condition) to an initial condition suitable to solve the MNLS equation (3.3) (i.e., $\hat{B}(k, t = 0)$), we proceed as follows. First, we apply a Fourier transform to the measured surface elevation profile $\eta = \eta(x = 0, t)$ and apply a low-pass filter at $f = 1.86 f_0$ and a high-pass filter at $f = 0.25 f_0$ to remove bound waves. In doing so, we

obtain $\hat{B}(x = 0, \omega)$. Second, we use the linear dispersion relation $\omega^2 = gk\tanh(kd)$ to convert the frequency spectrum $\hat{B}(x = 0, \omega)$ to a wavenumber spectrum $\hat{B}(k, t = 0)$. We note that water wave dispersion is non-linear (indeed this is what the non-linear terms of the MNLS model) and so this step is an approximation. However, we find that this works acceptably in practice given the agreement between experiment and numerics found in this chapter. Third, we set up a linear zone to introduce the wave train. The simulation is configured so that all non-linear terms including breaking dissipation term are turned off for $x < 0$. The wave field to the left of the first gauge ($x < 0$) evolves linearly, and the wave field to the right of the first gauge ($x > 0$) evolves non-linearly. This approach is a pragmatic adaptation of the code previous developed in the group enabling us to flux waves into the nonlinear part of the simulation. Fourth, we evolve $\hat{B}(k, t = 0)$ in time to $\hat{B}(k, t = t_f)$. Fifth, we perform a fully nonlinear backward MNLS simulation to evolve $\hat{B}(k, t = t_f)$ to $\hat{B}(k, t = 0)$, where the latter is the initial condition we need.

3.3 Perturbed Plane Waves

In this section, we will compare all four models described in §3.2 with parameters used in the literature as reported in §3.2 for the canonical case of perturbed plane waves, where the dynamics are dominated by three modes: a carrier wave and two sidebands. As all four models were developed to explain the key features of wave breaking, namely a downshift in the mean frequency and energy dissipation, we will focus on these properties. We will compare to recent laboratory experiments of wave breaking for perturbed plane waves in Eeltink et al. (2022) obtained independently from the theoretical models we compare to.

3.3.1 Initial Conditions

Theoretically, in the experiment of Eeltink et al. (2022) the wave maker provided following boundary condition for perturbed plane waves:

$$\eta(0,t) = \frac{H_s}{2}\left[\sqrt{b_c}\sin(-\omega_0 t) + \sqrt{b_+}\sin(-\omega_+ t + \psi) + \sqrt{b_-}\sin(-\omega_- t + \psi)\right], \qquad (3.17)$$

where the upper and lower sideband frequencies are set according to $\omega_\pm = \omega_0 \pm \delta\omega$ with $\delta\omega$ the modulational frequency, and ψ is the phase shift of the sidebands compared to the carrier wave. The sideband wavenumbers $k_\pm$ are calculated using the linear dispersion relationship $\omega_\pm^2 = gk_\pm \tanh(k_\pm d)$. The amplitudes of the carrier wave and the upper and lower sidebands are set according to $a_c = H_s\sqrt{b_c}/2$, $a_+ = H_s\sqrt{b_+}/2$ and $a_- = H_s\sqrt{b_-}/2$, where $b_c = 1 - b_F$, $b_+ = (1 - b_c)/2$, and $b_- = (1 - b_c)/2$, respectively, and b_F is sideband fraction. The water depth $d = 0.8$ m. The parameters of the four breaking cases from Eeltink et al. (2022) we consider are listed in Table 3.2. In these experiments, the wave maker is located at $x = 0$ m and the gauges are labelled based on their relative positions to the wave maker. We compare MNLS simulation with time series data recorded from 6 gauges: $x = 3.79$ m, 8.82 m, 13.73 m, 18.78 m, 24.53 m and 29.10 m.

In practice, instead of using (3.17) the initial wave field for MNLS simulation is recovered from the measurement of the first gauge following step 1 and step 2 described in §3.2.4 so that the surface elevation profile of the first gauge is reproduced exactly. Then we perform the MNLS simulation with linear zone and boundary condition specified above.

Case	f_0 **[Hz]**	H_s **[m]**	$\delta\omega$ **[rad/s]**	b_F	ψ	$k_0 d$	ϵ
Case 1	1.4	0.051	0.98	0.09	π	6.31	0.20
Case 2	1.5	0.031	1.05	0.06	π	7.24	0.14
Case 3	1.5	0.055	1.05	0.01	π	7.24	0.25
Case 4	1.6	0.039	1.60	0.05	π	8.24	0.20

Table 3.2: Input parameters of the perturbed plane wave cases from Eeltink et al. (2022).

3.3.2 Comparison of Breaking Models

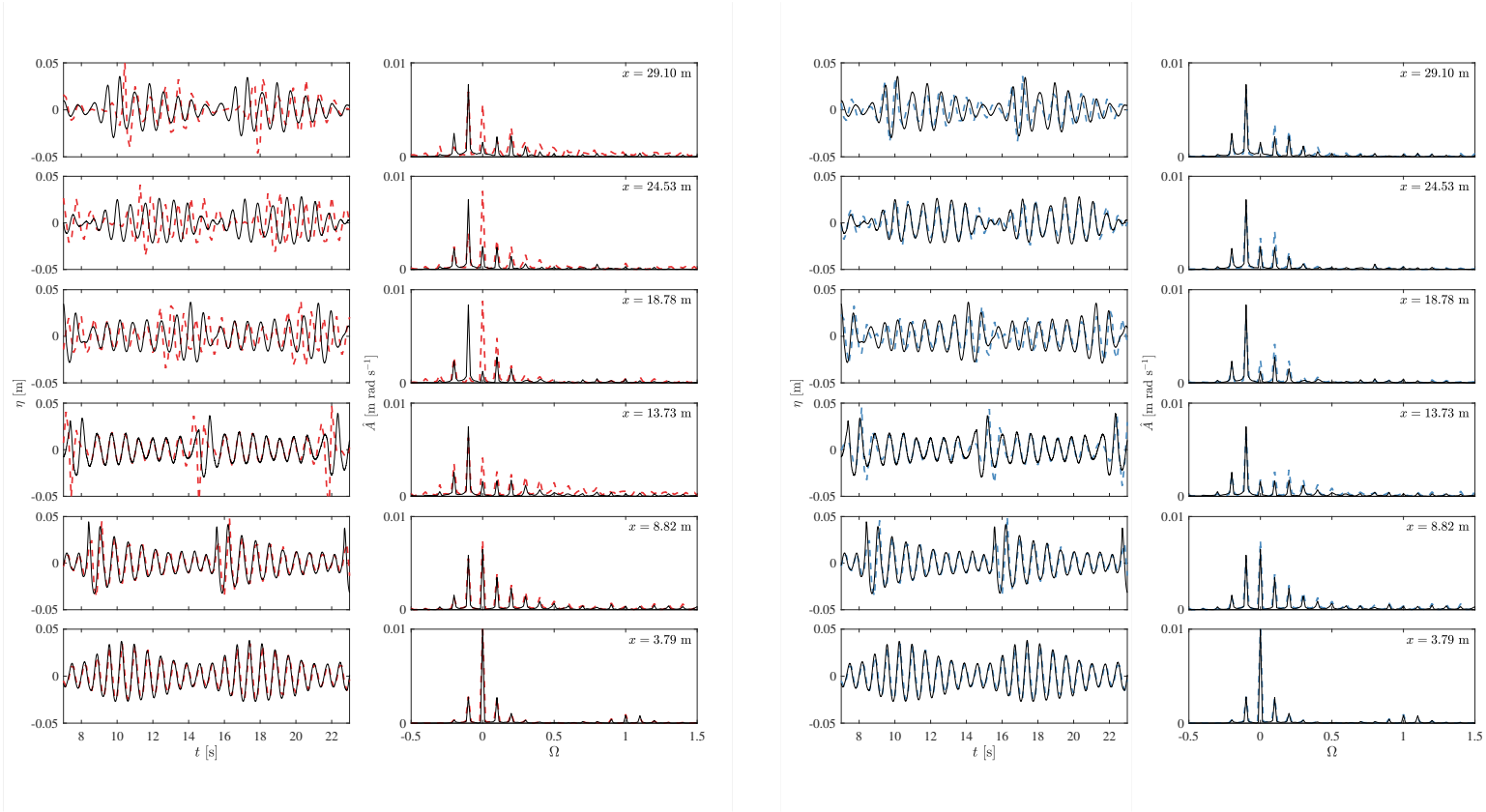
Figure 3.2 shows the surface elevation for case 1 in Table 3.2 at the different gauge locations, where we have moved into the reference frame of the group by shifting in time by $x/c_{g,0}$ with x the gauge location and $c_{g,0} = \omega_0/(2k_0)$ the group speed, comparing experimental data of Eeltink et al. (2022) to (a) MNLS solutions without breaking model and (b) MNLS solutions with the breaking model of TD90. The figure illustrates that the wave train experiences a partial modulation-demodulation cycle as expected for a perturbed plane wave. The MNLS simulation without a breaking model produces an excessively tall focused wave as is evident from the surface elevation profile and fails to predict a downshift in the frequency spectrum. Instead, the MNLS simulation with the breaking model of TD90 predicts a frequency downshift with a slight overestimation of the effect on the upper side band, and the predicted surface elevation profile and frequency spectrum closely match the experimental results.

To examine all four reduced-form breaking models, Figure 3.3 compares MNLS simulations for each model to experimental data for case 1 in Table 3.2. Figure 3.3 examines the evolution of the three modes of the perturbed plane wave, spectral properties and energy conservation. Panel (a)–(c) respectively show the evolution of the carrier wave, the lower sideband and the upper sideband. The TD90 (and the modified Kato & Oikawa model (M-KO95), which will be introduced in §3.5) gives the best prediction for the spatial evolution of the carrier wave amplitude. TD90, SL and M-KO95 model give a reasonably good prediction for the lower sideband. The SL model gives the best prediction for the upper sideband.

In panel d, TD90, SL and M-KO95 model give a good match for the evolution of the spectral peak $\Omega_{\text{peak}} = \text{argmax}_\Omega \hat{A}$ with $\Omega = \omega/\omega_0 - 1$ and $\hat{A}(\Omega)$ the amplitude spectrum, where we note only three values of Ω_{peak} are possible: -0.1, 0, and 0.1, corresponding to the lower sideband, the carrier wave and the upper sideband, respectively.

In panel e, the SL model matches best to experiments in terms of the evolution of spectral mean, $\Omega_{\text{center}} = \sum \Omega_i \hat{A}_i / \sum \hat{A}_i$, while all other models have an upward

bias compared to experiments. For energy conservation (panel f), although the experimental data shows considerable variability, it seems that the TD90 model (and the M-KO95 model) gives the most reasonable prediction of the energy evolution in experiments with the other models underestimating the amount of energy lost due to breaking. The reader is referred to Appendix B.1 for similar figures for the other three cases in Table 3.2, which lead to qualitatively similar conclusions.



(a) No breaking model

(b) TD90 model

Figure 3.2: Surface elevations and amplitude spectra at different gauge locations for perturbed plane waves (case 1 in Table 3.2). Black solid lines correspond to experimental data and coloured dashed lines to MNLS simulations (a) without a breaking model and (b) with the breaking model of TD90. For the wave spectra, we use $\Omega = \omega/\omega_0 - 1$.

3.4 Focused Wave Groups

In this section we will compare the experiments obtained herein for dispersively focused wave groups (see §3.2.3) with MNLS simulations using the breaking models with parameter values taken from the literature as given in §3.2.2. We will examine optimised parameter values in §3.5.

3.4.1 Effects of Breaking

Figure 3.4 shows the surface elevation for case 1 in Table 3.1 at the different gauge locations, comparing experimental data to (a) MNLS solutions without breaking model and (b) MNLS solutions with the breaking model of TD90. Breaking occurs between x = 3.04 m and x = 6.50 m. At x = 6.50 m, the first (left-most) large crest is neither described well by the MNLS simulations without breaking model nor by those with the breaking model of TD90. Both underestimate the surface elevation of the crest compared to experiments. We note that this crest did not actually break in experiments; the difference between simulations and experiments very probably arises because of the inherent limitation of the MNLS equation to model only relatively narrow-banded highly nonlinear waves, as demonstrated in previous work (Trulsen and Dysthe, 1996). It is only the second (from the left) crest (between t = 102 s and t = 105 s) at x = 6.50 m in Figure 3.4 that actually breaks, as can be confirmed from video recordings. Here, the MNLS without breaking model predicts an excessively high crest (panel a), which is not observed in experiments. The TD90 model predicts the reduction of the excessively high crest reasonably well in the time domain.

In the amplitude spectra in Figure 3.6, breaking manifests itself as an effect on the right-hand side 'shoulder' of the spectrum (i.e., at approximately $\Omega = 0.22$). Such phenomena has been observed and discussed in the past literature (Gibson and Swan, 2007; Adcock and Taylor, 2016b). Comparing the magnitude of the spectra between x = 3.04 m (before breaking) and x = 6.50 m (after breaking), a clear reduction of the spectral shoulder is evident, which is neither correctly predicted by

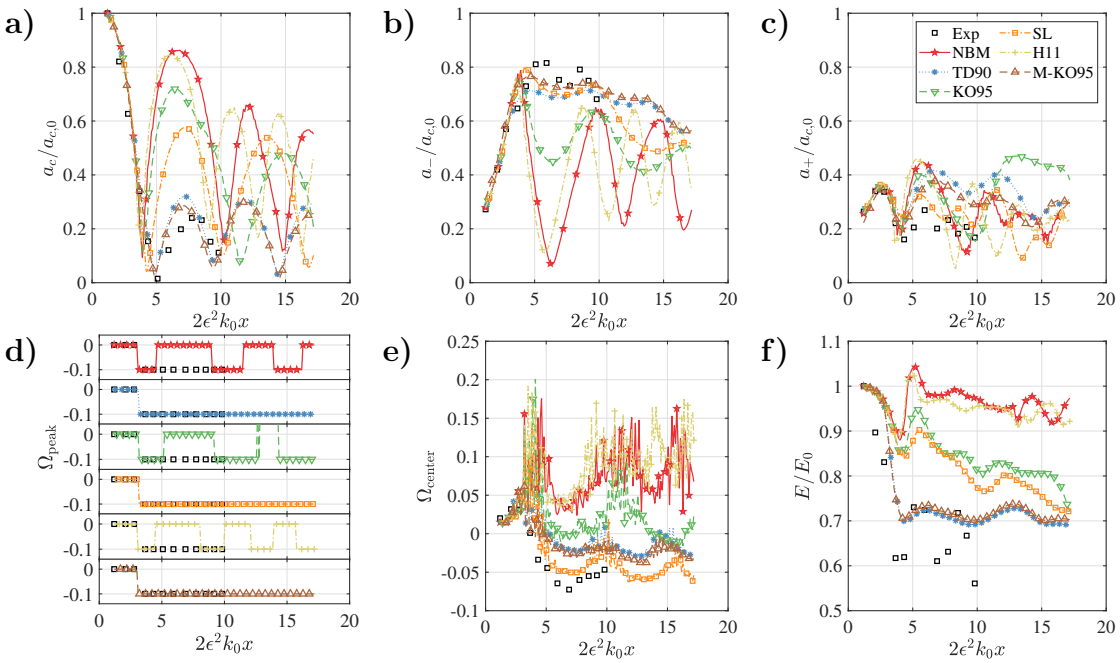


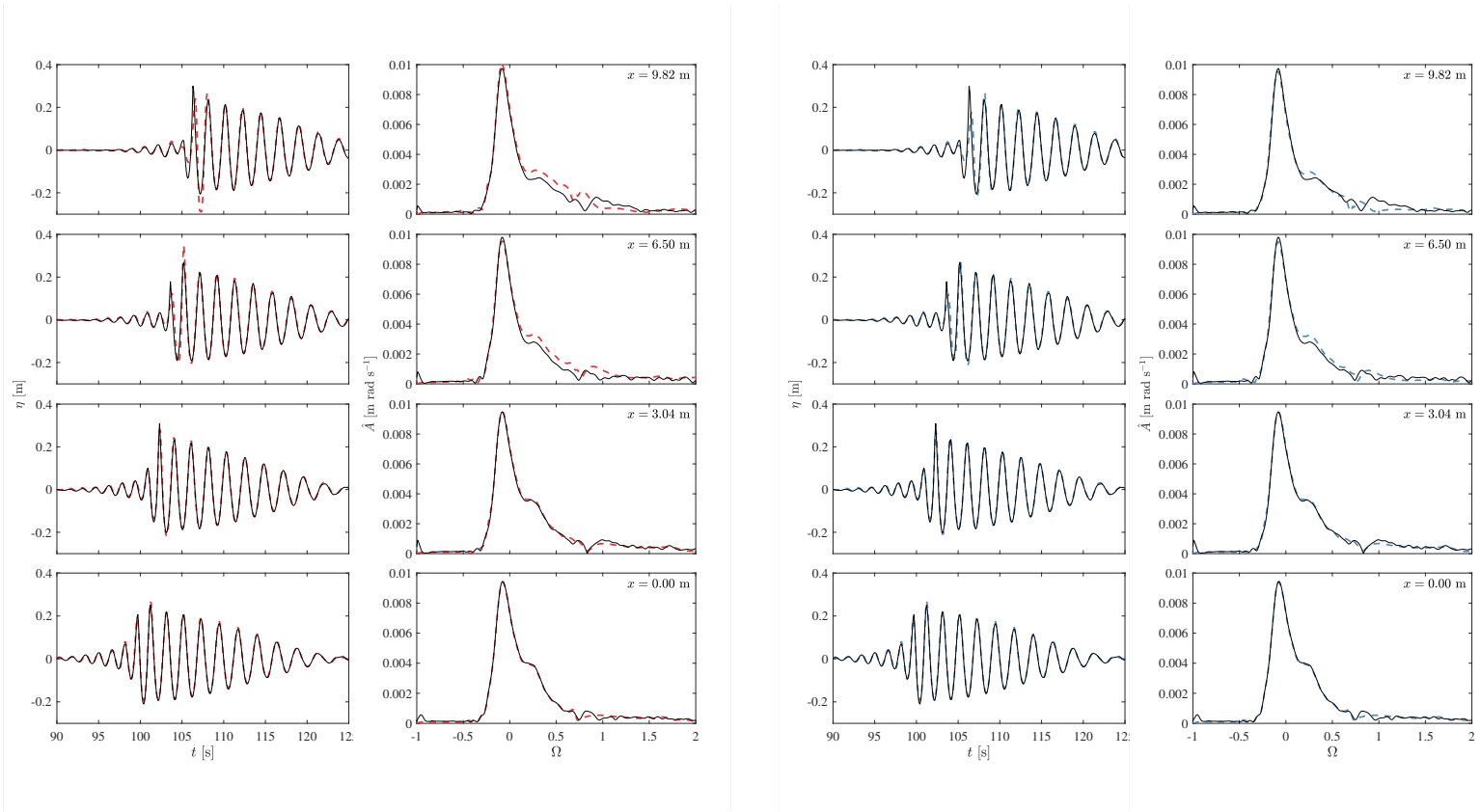
Figure 3.3: Spatial evolution of perturbed plane waves for different reduced-from breaking models including no breaking model (NBM), showing a) the carrier wave normalised by its value at the first gauge, $a_c/a_{c,0}$; b) the normalised lower sideband $a_-/a_{c,0}$; c) the normalised upper sideband, $a_+/a_{c,0}$; d) the spectral peak, $\Omega_{\text{peak}} = \text{argmax}_\Omega \hat{A}$ with $\hat{A}$ the amplitude spectrum of η and $\Omega = \omega/\omega_0 - 1$; e) spectral mean or centroid, $\Omega_{\text{center}} = \int \Omega(\omega)\hat{A}(\omega)\mathrm{d}\omega / \int \hat{A}(\omega)\mathrm{d}\omega$; f) the energy measure $E = \int |B|^2 \,\mathrm{d}t$ normalised by its value at the first gauge E_0. The black squares show the experimental data from Eeltink et al. (2022) (case 1 from Table 3.2).

the MNLS simulations without a breaking model nor by those with the breaking model of TD90.

3.4.2 Comparison of Breaking Models

Comparison based on the time domain

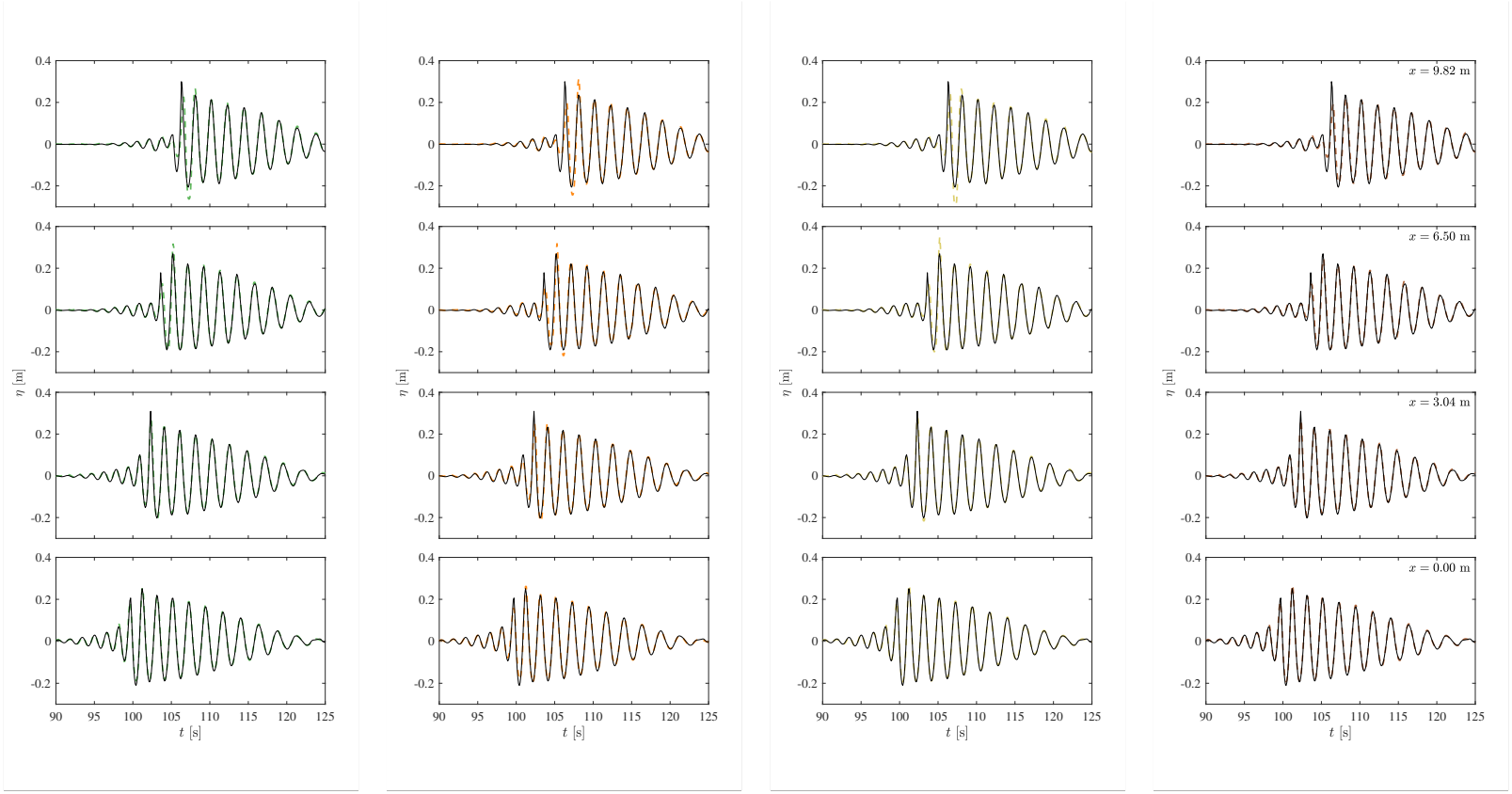
Figure 3.5 shows the surface elevation predicted by the four reduced-form breaking models. The major difference between the models is whether the second steepest crest at x = 6.50 m is suppressed. In MNLS simulations without breaking model, the second steepest crest after breaking is overestimated by 10% compared to experiments. Unlike TD90 in Figure 3.4, all three other models, KO95, SL and H11, do not lead to significantly improved agreement with the experimental data compared to the case with no breaking model (cf. Figure 3.4).



(a) No breaking model

(b) TD90 model

Figure 3.4: Surface elevations and amplitude spectra at different gauge locations for focused wave groups (case 1 in Table 3.1). Black solid lines correspond to experimental data and coloured dashed lines to MNLS simulations (a) without a breaking model and (b) with the breaking model of TD90. For the wave spectra, we use $\Omega = \omega/\omega_0 - 1$.



(a) KO95 model (b) SL model (c) H11 model (d) M-KO95 model

Figure 3.5: Surface elevations at different gauge locations for focused wave groups (case 1 in Table 3.1). Black solid lines correspond to experimental data and coloured dashed lines to MNLS simulations (a) with the model of KO95; (b) with the SL model; (c) with the model of H11; and (d) with the M-KO95 model.

Comparison Based on the Frequency Domain

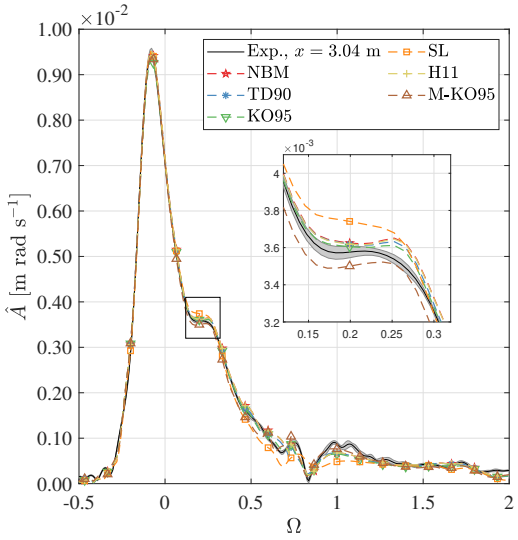
By examining the amplitude spectrum before and after breaking, Figure 3.6 examines the ability of the different reduced-form breaking models to capture the effect of breaking on the spectrum of a wave group (for both case 1 and case 2). By showing confidence bands (grey shaded regions) corresponding to one standard deviation either side of the mean obtained from 10 repeated experiments, the figure first shows that dissipation of the right-hand side spectral shoulder is a robust feature of breaking. Although most models (except for SL) reproduce this shoulder before breaking (x = 3.42 m) and most models predict some kind of reduction in its magnitude after breaking (x = 6.50 m) (except for SL), all of the models underestimate the amount of energy dissipated in the shoulder by breaking.

Comparison Based on Phase

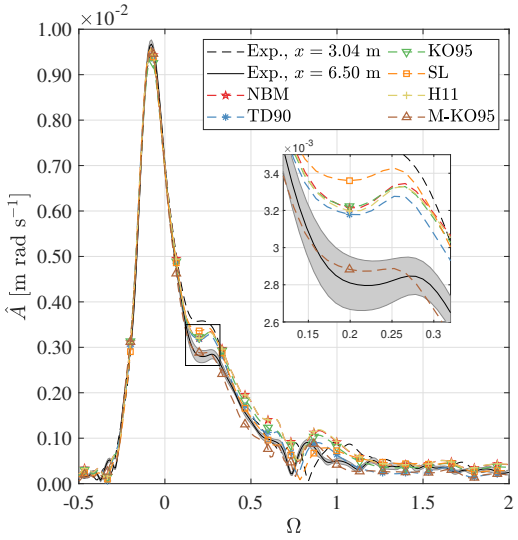
Having examined the effect of breaking on the magnitude of the spectrum, Figure 3.7 examines whether breaking affects phase. In Figure 3.7 we show the phase difference between two consecutive gauges, where we have accounted for linear phase change $k\Delta x$ with Δx the distance between gauges. Although nonlinearity causes a consistent phase shift, we are not able to find any obvious phase distortion caused by wave breaking. The large amplitude oscillations in Figure 3.7 for small Ω in the narrow-banded case arise because of the very small amplitudes of the spectrum for small Ω, will be affected by bound waves, and are therefore ignored here.

3.5 Breaking Model Optimisation and Modification

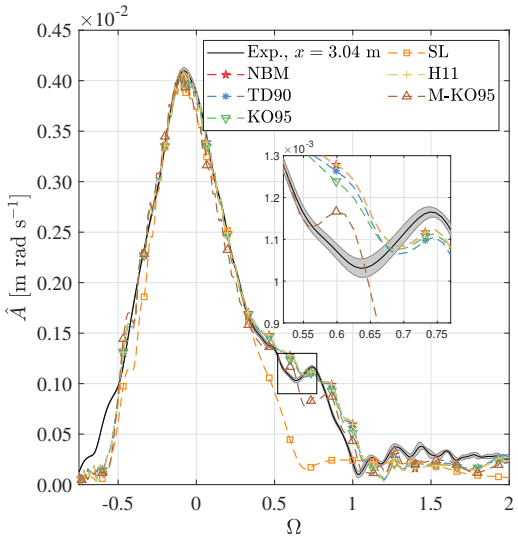
In §3.4, we have used parameter values for the four reduced-form breaking models suggested in the literature for perturbed plane waves (given in §3.2.2) to model breaking in focused wave groups. To examine whether the performance of these models for focused wave groups can be improved, we will select parameters that



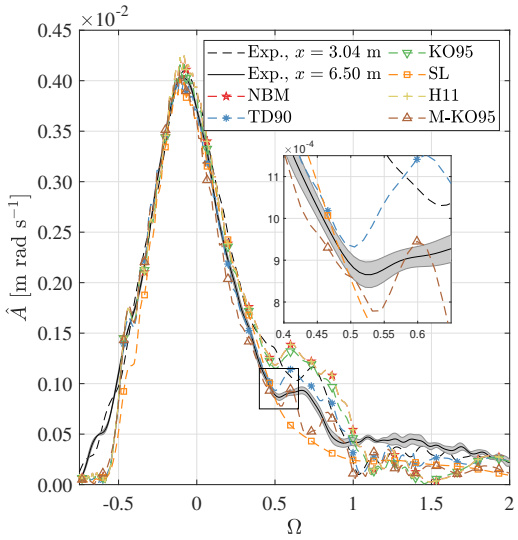
(a) Case 1, Before breaking (x = 3.04 m).



(b) Case 1, After breaking (x = 6.50 m).

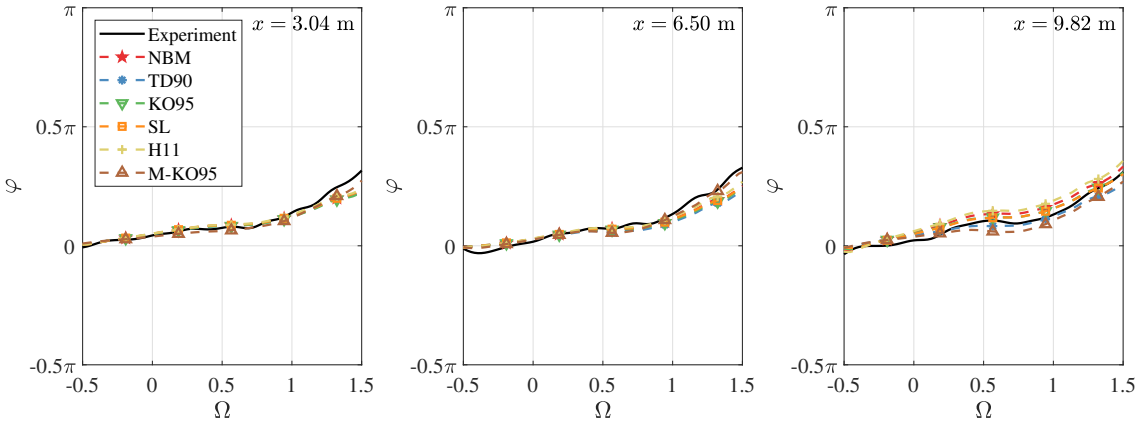


(c) Case 2, Before breaking (x = 3.04 m).

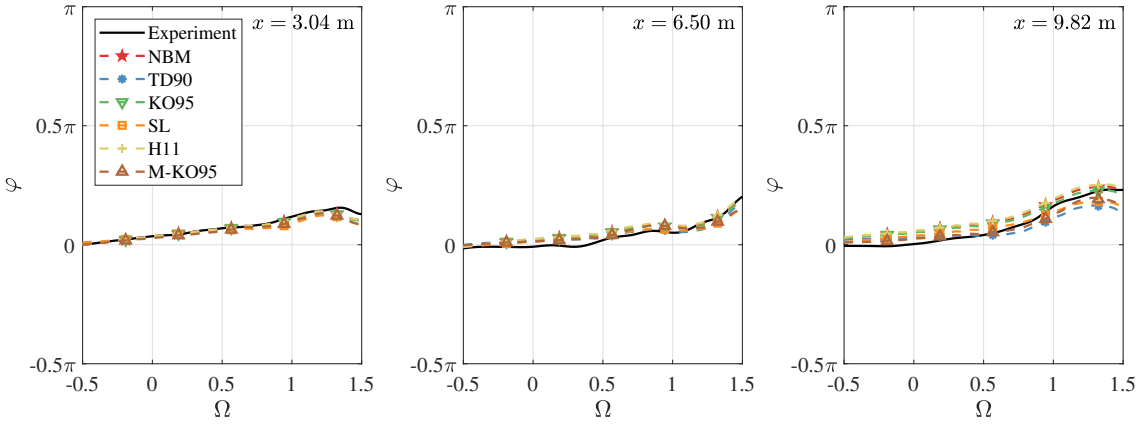


(d) Case 2, After breaking (x = 6.50 m).

Figure 3.6: Comparison of amplitude spectra before and after breaking of a focused wave group (see Table 3.1) for different reduced-form breaking models including no breaking model (NBM), showing experiments (black solid/dashed lines), with grey shaded region corresponding to ± 1 standard deviation from repeated experiments, and MNLS simulations with different breaking models (coloured dashed lines with markers).



(a) Case 1 (narrow-banded).



(b) Case 2 (broad-banded).

Figure 3.7: Phase difference between consecutive gauges for case 1 (a) and case 2 (b) for focused wave groups in Table 3.1 (with the labels corresponding to the gauge with the largest x), comparing experiments (black lines), MNLS simulations with no breaking model (NBM, red dashed lines) and with the breaking models (coloured dashed lines). In case 1, breaking occurred between gauge x = 3.04 m and x = 6.50 m. In case 2, a weak breaking event occurred between x = 3.04 m and x = 6.50 m, and a second strong breaking event occurred between x = 6.50 m and x = 9.82 m.

minimise the least-squares difference between predictions and experiments we have carried out. In doing so, we will also examine the performance and additional benefit of incorporating three different breaking criteria, which we apply to each of the four reduced-form breaking models (noting that TD90 and H11 already include breaking criteria). Finally, we will examine what type of (heuristic) modification of the breaking models can further improve agreement with experimental data.

3.5.1 Breaking Criteria

Three breaking criteria are implemented: a local geometric criterion, a local kinematic criterion, and a global kinematic criterion with a fixed-duration active breaking interval:

1. The local geometric breaking criterion, $H(S > S_0)$, is based on wave steepness S and is equivalent to the criterion already included in the breaking models of TD90 and H11. Steepness $S = k_0|B|$ is defined by the magnitude of the envelope multiplied by the carrier wavenumber. For perturbed plane waves we have set $S_0 = 0.35$, but for focused wave groups we had to adjust S_0 to match the onset of breaking in video recordings of the experiments. We do this by inspecting video recordings of the wave-tank experiments and recording the time at which white-capping starts to develop. We then choose S_0 in MNLS simulations so that the breaking onset occurs at the same time. We thus set $S_0 = 0.24$ and $S_0 = 0.19$ for cases 1 and 2, respectively.

2. The local kinematic breaking criterion, $H(u/c > 0.88)$ from Barthelemy et al. (2018), is based on the ratio of the horizontal fluid speed u and the crest speed c. The former is obtained from the potential (cf. $u = \partial\phi/\partial x$), which is reconstructed up to $\mathcal{O}(\epsilon^3)$ according to Carter et al. (2019a):

$$\phi(x,z,t) = \left[\frac{i\epsilon\omega_0}{k_0}\tilde{B} + \frac{\epsilon^2\omega_0}{2k_0^2}\tilde{B}_x + \epsilon^3\left(-\frac{ik_0\omega_0}{2}|\tilde{B}|^2\tilde{B}_x - \frac{3i\omega_0}{8k_0^3}\tilde{B}_{xx}\right)\right]e^{i(k_0x-\omega_0t)+k_0z} + \text{c.c.}, \tag{3.18}$$

where $\tilde{B} = Be^{k_0 z}$, we set $z = \eta_1$, and c.c. represents the complex conjugate. We ignore the effect of bound waves on the velocity. The breaking crest speed c is approximated by $0.8\omega_0/k_0$. The breaking criterion is local, meaning it is applied only at those locations where $u/c > 0.88$.

3. The global kinematic breaking criterion, $H(u/c > 0.88)$, will turn on globally for a fixed time interval T_b whenever the kinematic breaking criterion is triggered at any location as detailed in Derakhti et al. (2018). The active breaking time interval $T_b = 0.75 \times (2\pi/(k_b c_b))$ (Derakhti et al., 2018), where we set $c_b = 0.8\omega_0/k_0$ and we assume $k_b = k_{\text{local}}$ with the latter obtained from Kurnia and Groesen (2014):

$$k_{\text{local}}(x,t) = \frac{1}{\eta^2 + \mathcal{H}^2(\eta)} \left(\eta \frac{\partial}{\partial x} \mathcal{H}(\eta) - \mathcal{H}(\eta) \frac{\partial}{\partial x} \eta \right), \tag{3.19}$$

where $\mathcal{H}$ is a Hilbert transform. Choosing k_b when the kinematic breaking criterion $H(u/c > 0.88)$ is satisfied at multiple locations, we take the maximum value and apply it globally. Such treatment works for all the cases in this study as only one breaking event is ever active at the same time.

3.5.2 Parameter Optimisation

Comparing the surface elevation profile before ($x = 3.04$ m) and after ($x = 6.50$ m) breaking in Figure 3.4, it is evident that the MNLS simulations agree well with the experimental data before but not after breaking. Thus, in order to improve performance of the different models, we use the experimental data to obtain a value of the pre-factor β in the dissipation terms (or τ in the case of TD90) that leads to better agreement. In particular, we choose a pre-factor β, which we henceforth term the dissipation strength parameter, that minimises the squared difference between the MNLS prediction (with breaking model and breaking criterion) and the measured

surface elevation at the gauge(s) after breaking, which we term the L2 loss:

$$\beta^* = \underset{\beta}{\operatorname{argmin}} \sum_t \left(\eta_{\mathrm{MNLS}}(t, x = (6.50\ \mathrm{m}, 9.82\ \mathrm{m}); \beta) - \eta_{\mathrm{experiment}}(t, x = (6.50\ \mathrm{m}, 9.82\ \mathrm{m}))\right)^2, \tag{3.20}$$

where the sum is taken over the discrete sampling times t and we use fixed experimental durations of 60 s. We use case 1 to obtain β^*, combining gauges at $x = 6.50$ m and $x = 9.82$ m.

Table 3.3 shows the L2 loss for case 1 after optimisation according to (3.20) for the four different reduced-form breaking models with different breaking criteria (described in §3.5.1), as well as the corresponding dissipation strength parameter β^* (or τ^* in the case of TD90). Also shown is the L2 loss for case 2, which is evaluated using the dissipation strength parameter β^* obtained by optimisation for case 1. It is evident that existing models achieve significantly better performance with optimised parameters for case 1. In general, the L2 loss in the time domain for both focused wave cases with optimised parameters decreases compared to the same two cases with values from the literature (for perturbed plane waves). While the optimisation is performed for case 1, the L2 loss for case 2 is also improved, albeit to a lesser extent. We do not observe consistent differences in performance of the different breaking criteria between the different reduced-form models, although inclusion of a breaking criterion generally reduces the L2 error.

Figure B.4 in Appendix B.2 shows the time-domain comparison with experiments for the four reduced-form breaking models with optimised parameters, where we show only the breaking criterion that corresponds to the lowest L2 error in Table 3.3 for each. Compared to the case with values of the parameters from the literature, only modest improvements in the agreement of the surface elevation of the breaking crests with experiments is obtained with the optimised parameters. In the frequency domain, none of the four models with optimised parameters can correctly predict the dissipation of the shoulder of the spectrum that we have observed in Figure 3.6 (see Figure B.5 in Appendix B.2, where we show only the breaking criterion that corresponds to the lowest L2 error in Table 3.3 for each).

Model	Optimised (Y/N)	Breaking criterion	L2 loss (case 1)	L2 loss (case 2)	Parameter (τ, β)
NBM	N	None	1.00	1.00	-
TD90	N	Geometric	0.85	0.90	0.125
TD90	Y	Geometric	0.83	0.92	1.425
TD90	Y	Kinetic	0.85	0.94	0.138
TD90	Y	Fixed Interval	0.83	0.92	1.375
KO95	N	None	0.99	0.94	0.2
KO95	Y	None	0.98	0.96	0.116
KO95	Y	Geometric	0.84	0.92	1.485
KO95	Y	Kinetic	0.89	0.94	6.504
KO95	Y	Fixed Interval	0.82	0.88	1.384
SL	N	None	1.01	0.95	0.01
SL	Y	None	0.97	0.98	0.003
SL	Y	Geometric	0.93	0.97	0.0148
SL	Y	Kinetic	0.92	0.97	0.0663
SL	Y	Fixed Interval	0.67	0.94	0.0475
H11	N	Geometric	0.97	1.00	0.01
H11	Y	Geometric	0.97	1.00	0.0676
H11	Y	Kinetic	0.65	0.99	1.323
H11	Y	Fixed Interval	1.00	1.00	0.001
M-KO95	Y	Geometric	0.68	0.90	Fig. 3.8
M-KO95	Y	Kinetic	0.52	0.92	Fig. 3.8
M-KO95	Y	**Fixed Interval**	**0.52**	**0.80**	**Fig. 3.8**

Table 3.3: Results from parameter optimisation and modification of the reduced-form breaking models (NBM denotes the case with no breaking model). The L2 loss is normalised by its value for the case with no breaking model.

3.5.3 Model Modification

To examine whether still better agreement with experimental data can be obtained, we take the following heuristic approach. We replace the dissipation strength parameter β in D by a spectral dissipation strength parameter $\hat{\beta}(k)$, which is a function of wavenumber k and allows a different weight to be placed on different wavenumbers contributing to the dissipation term. For the Kato and Oikawa (1995) (KO95) model (henceforth the modified Kato & Oikawa model, M-KO95), this modification takes the form:

$$D = k_0 B \mathcal{F}^{-1}\left\{\hat{\beta}(k)\mathcal{F}\left\{\frac{\partial\bar{\phi}}{\partial x}\right\}\right\}H, \tag{3.21}$$

where $\mathcal{F}$ denotes a Fourier transform, and H is the Heaviside function corresponding to one of the three breaking criteria. We require all the components of $\hat{\beta}(k)$ to be

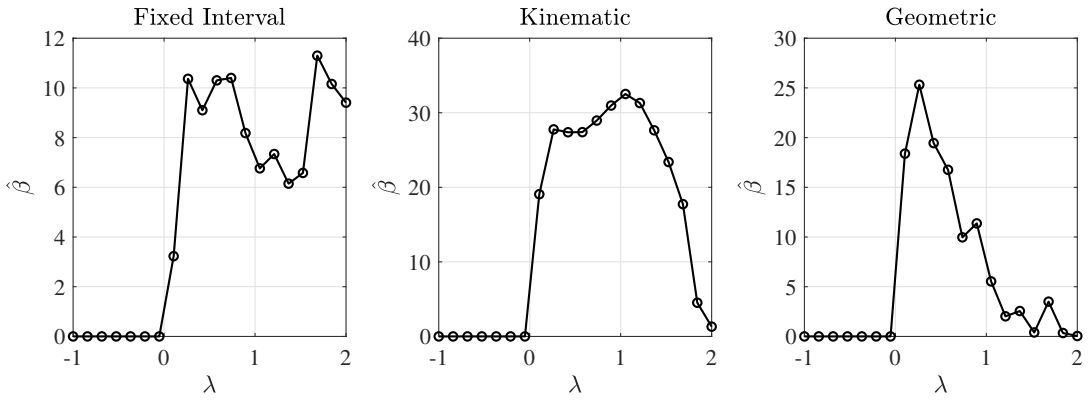


Figure 3.8: Optimal spectral dissipation strength parameter $\hat{\beta}$ as a function of $\lambda = k/k_0 - 1$ for the modified Kato and Oikawa (1995) model (M-KO95) for three different breaking criteria. The open circles are the actual control points, and any values in between two points are reconstructed by linear interpolation.

real. Equations for the three other modified models are given in Appendix B.2.

We use MATLAB's Trust Region Reflective Algorithm to obtain $\hat{\beta}(k)$ according to (3.20). Specifically, we use 20 control points to define $\hat{\beta}(k)$ between $k = 0$ and $k = 3k_0$ and then interpolate linearly to reconstruct the curve in order to reduce computational cost. The result is not sensitive to spatial and temporal resolution of the MNLS solver or the number of control points. We only present the results for the modified Kato & Oikawa model (M-KO95) with a fixed-interval breaking criterion and note that only modified models with a fixed-interval breaking criterion can predict the dissipation near 'shoulder' in spectrum correctly. We choose the M-KO95 model as it achieves the lowest L2 loss for case 2. The optimal spectral dissipation strength parameter $\hat{\beta}(k)$ for the M-KO95 model is shown in Figure 3.8 for the three different breaking criteria. From this figure, it is clear that dissipation should generally be even stronger for higher wavenumbers, noting that the effect of wavenumbers greater than $2k_0$ ($\lambda = 1$) will be weak, as there is little energy at such high frequencies.

3.5.4 Performance of the Modified Kato & Oikawa (M-KO95) Model

In this section we will examine performance of the modified Kato & Oikawa (M-KO95) model with the fixed-interval breaking criterion for perturbed plane waves

and focused wave groups.

Perturbed Plane Waves

Although we have obtained values of the spectral dissipation strength by fitting to experiments for focused wave groups, the M-KO95 model also performs remarkably well for the perturbed plane waves we have considered in §3.3. In Figure 3.3, we find that the M-KO95 model gives the closest prediction of the amplitude of the carrier wave. For the lower and upper sidebands, the performance of the M-KO95 model is as good as existing models. For all other metrics in Figure 3.3 the M-KO95 model also gives reasonable predictions, suggesting a certain robustness and generality of the modified model.

Focused Wave Groups

Starting with the time domain, it is clear from Figure 3.5 that the M-KO95 model captures the reduction of the amplitude of the breaking crests in the experiments very well. In Figure 3.6, we can compare the performance of M-KO95 model to the original (non-modified and with parameter values from the literature) reduced-form breaking models. Only the M-KO95 model predicts the correct dissipation of the shoulder of the frequency spectrum.

Figure 3.9 examines how the M-KO95 models breaking by showing the spatial distribution of the dissipation term and its effect on the envelope at the start and end of the breaking event. Also shown is the reconstructed surface elevation as an indicator of the phase of the surface elevation. From the top panels, it is clear that dissipation is strongest at the front of the wave groups, where the envelope is suppressed by the breaking term (see bottom panels). In Figure 3.10 we further examine the behaviour of the M-KO95 model. It is evident that breaking is only activated for three discrete events as a result of the implementation of the breaking criterion. It is evident that a downshift of the spectral mean takes place, when MNLS simulations with no breaking model would predict an increase due to nonlinear wave interactions. A total of 10-15% of energy is dissipated during breaking. The energy

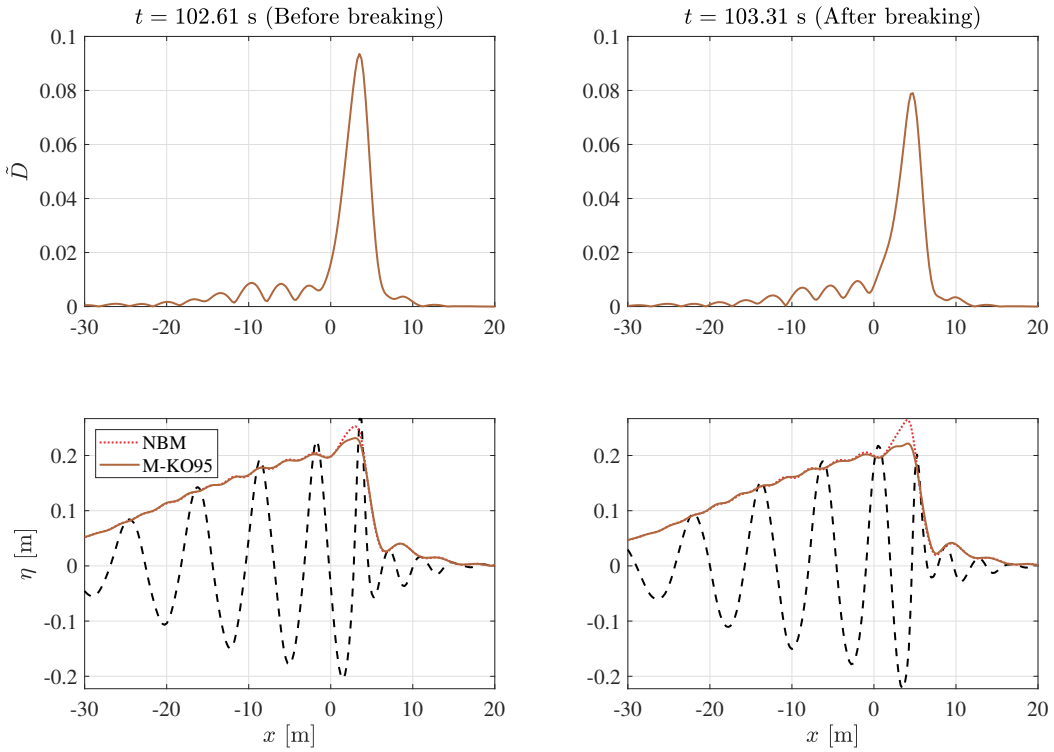
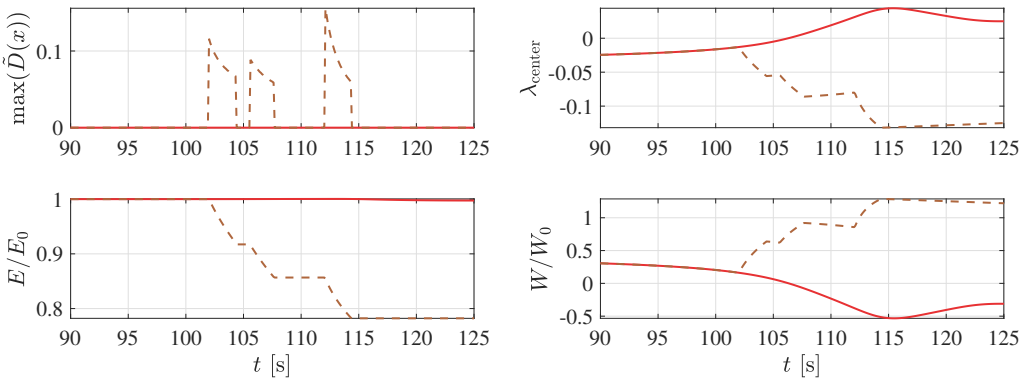
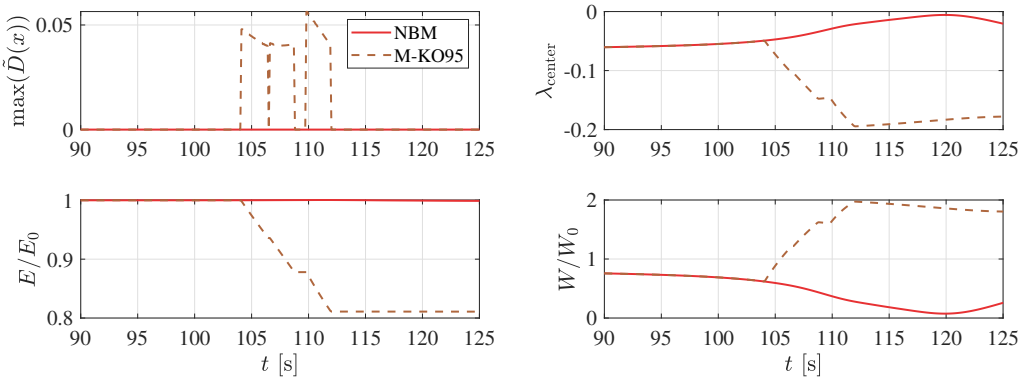


Figure 3.9: Spatial distribution of the normalised dissipation term $\tilde{D} = 2\epsilon k_0/\omega_0 D$ (top panels) aligned with the envelope for simulations with no breaking model (NBM) and with the M-KO95 model (bottom panels), for which the dissipation term is examined in the top panels, at the start (or just before, left) and at the end (or just after, right) breaking for a focused wave group (case 1 in Table 3.1). The dashed black line corresponds to the surface elevation from MNLS simulations with no breaking model, the red dotted line is the envelope from MNLS simulations with no breaking model (NBM), and the brown solid line in the bottom panels is envelope from MNLS simulations with the M-KO95 model.



(a) Case 1: narrow-banded.



(b) Case 2: broad-banded.

Figure 3.10: Temporal evolution before, during and after breaking according to MNLS simulations with the M-KO95 model for focused wave groups (Table 3.1), showing activation of the dissipation term (top left), the normalised spectral mean $\lambda_{\text{center}} = \int \lambda(k)\hat{A}(k)\,\mathrm{d}k / \int \hat{A}(k)\,\mathrm{d}k$ (top right), the energy measure $E = \int |B|^2 \mathrm{d}x$ normalised by its initial value (bottom left) and the energy flux defined as $W = \int B^*(\partial B/\partial x) - B(\partial B^*/\partial x)\,\mathrm{d}x$, which is normalised by $W_0 = E_0 k_0/2\pi$ (bottom right).

flux reflects the symmetry of the wave spectrum, and a positive flux indicates that the energy flows from high to low frequencies (cf. Kato and Oikawa (1995)).

3.6 Conclusions

In this chapter, we have reviewed the performance of existing reduced-form breaking models that can be added as a dissipation term to the Modified Nonlinear Schrödinger (MNLS) equation, which together describe the envelope evolution of breaking deep-water waves. In particular, we have examined the breaking models by Trulsen and Dysthe (1990), Kato and Oikawa (1995), Hwung et al. (2011) and the selective Laplacian (used for example in Majda and Wang (2001)). We have reviewed their performance for two wave types: perturbed plane waves and focused

wave groups.

Perturbed plane waves initially consist of three distinct modes: the carrier wave and two side-bands. During propagation, nonlinear modulation causes the spectrum to broaden. The point of maximum steepness corresponds to the point of maximum spectral width. Wave breaking induces a permanent downshift by dissipating the energy of the upper side-band and thereby the total energy and causing the lower side-band to grown. We have found that for perturbed plane waves, the four models can qualitatively and quantitatively predict these effects of breaking.

For focused wave groups, the maximum steepness is obtained primarily through alignment of the phases. We observe that wave breaking modifies 1 to 2 crests at the front of the wave group. The high-frequency part of the spectrum is selectively dissipated during breaking, taking the form of a distinct high-frequency shoulder that loses energy due to breaking in our experiments. For these waves with a continuous spectrum, all models fail to produce the correct spectral dissipation, both when values of the parameters suggested in the literature for perturbed plane waves and values obtained by optimisation in the time domain based on wave group experiments are used.

As all the reduced-form breaking models 'activate' when the spectrum broadens (or the wave group narrows), this explains their effectiveness for perturbed plane waves. For focused wave group, spectral broadening is not equally effective at 'detecting' wave breaking, although the use of breaking criteria can help. Combining the ideas of the different breaking models, we introduce a heuristic approach to modify existing models to predict breaking in wave groups.

Specifically, we propose to add a breaking criterion (a global kinematic criterion that turns on for a finite time interval works best) to the model of Kato and Oikawa (1995) and make the dissipation strength parameter wavenumber dependent, resulting in what we term the modified Kato & Oikawa model (M-KO95). Optimised on focused wave groups and with a large number of free parameters included in the spectral dissipation strength parameter, unsurprisingly, this model is able to correctly approximate the spectral dissipation observed in our experiments. More

insightful is that it generalises well to perturbed plane waves. Indeed, the M-KO95 model outperforms existing breaking models for both the perturbed plane waves and focused wave groups. The selective dissipation of even higher wavenumbers compared to the non-modified models that is required for this result should inform the development of new reduced-form wave breaking models for wave groups and random seas in the future.

Chapter 4

A machine learning architecture for including wave breaking in envelope-type wave models

Abstract

Wave breaking is a complex physical process about which open questions remain. For some applications, it is critical to include breaking effects in phase-resolved envelope-based wave models such as the non-linear Schrödinger. A promising approach is to use machine learning to capture breaking effects. In the present chapter we develop the machine learning architecture to model breaking proposed by Eeltink et al. (2022, *Nature Communications*, 13(1), p. 2343) further, potentially enabling more detailed breaking physics to be captured. We show that this model can be trained on focused wave groups but can also capture breaking in random waves and modulated plane waves. Analysis of the model suggests that the machine learning has broken the problem into two—one part which detects whether the wave is breaking and another which captures the subsequent behaviour, consistent with the way human scientists routinely understand the breaking problem.

4.1 Introduction

Despite being a phenomenon commonly witnessed by ocean observers (Babanin, 2011), the fundamental physics of surface gravity wave breaking remains elusive to scientists and engineers. A deep understanding of wave breaking is crucial due to its significant impact on various oceanic and atmospheric processes. It plays a vital role in the energy balance of the ocean (Hasselmann, 1974), contributes to ocean mixing mechanisms (Melville et al., 1998), and influences air-sea interactions (Melville, 1996; Deike, 2022). Additionally, wave breaking affects short-term wave statistical properties (Toffoli et al., 2010b) and imposes loading on maritime structures (Peregrine, 2003).

The problem of wave-breaking in the ocean is multi-scale. Wave breaking must be represented in phase-average sea-state models which typically have the scale of $\mathcal{O}$(10-100 km) but ultimately these are trying to capture energy dissipation processes which occur at $\mathcal{O}$(1 μm-10 m) (Deike, 2022). Understanding the problem of wave breaking on a wave-by-wave basis (as opposed to a phased-averaged sea-state analysis) is frequently broken down into understanding when waves break and then understanding the subsequent evolution. Both parts of the problem are active areas of research.

Wave breaking criteria typically use the wave steepness, wave speed and water depth to provide a threshold above which waves would break. Various formulations for breaking criteria exist. Recent developments on this is the concept of breaking inception introduced in Derakhti et al. (2020), which describes the initiation of an irreversible process within the crest that leads to breaking and occurs prior to the stage of breaking onset. The breaking inception indicator proposed by Derakhti et al. (2020) is based on the diagnostic parameter B_{thresh} used in the kinematic breaking criterion (Barthelemy et al., 2018). In Barthelemy et al. (2018), a threshold value $B_{\text{thresh}} \approx 0.855$ is suggested, and this experimental threshold value is verified in laboratory experiments and numerical studies for a variety of wave packet types.

The post-breaking behaviour is a complex multi-scale process. The breaking

process generates turbulence, which is chaotic and complex. In simplified potential flow-based models this complexity can never (fully) be captured. However, we can attempt to model the key energy changes that occur when waves break. Liu et al. (2023) demonstrate that the cumulative dissipation effect of breaking itself is less chaotic and can be approximated. This suggests that prediction of the evolution of breaking waves (and thus wave forecasting) could be enhanced through improved physics-based models, data-driven methods, or other suitable techniques.

In addition to the strong non-linear process of wave breaking, weakly non-linear processes also play a role in water-wave evolution. One computationally fast model that captures this for narrowbanded deep-water waves is the 'Modified non-linear Schödinger' (MNLS) equation (Dysthe, 1979) or variants of it (see also Dysthe and Trulsen (2001)). The MNLS equation models the evolution of the wave's complex envelope. Generally, these equations can predict the evolution of ocean waves well, although prediction of the largest waves remains challenging even for initially narrowbanded spectra due to the non-linear physics driving a local contraction of a wavegroup in space and which can also be thought of as a broadening of the spectrum (Adcock and Taylor, 2016a). In random wave simulation there will always be some wave breaking, which is not captured in the basic MNLS equations. Thus, it is necessary to modify the standard equations in order to capture this process by adding a reduced-form (e.g., Trulsen and Dysthe (1990); Kato and Oikawa (1995); Hwung et al. (2011); Majda and Wang (2001); Tian et al. (2012)) or data-driven breaking term (e.g., Liu et al. (2023)). Liu et al. (2023) showed that envelope-based reduced-form breaking models can capture elements of wave breaking in the MNLS, but this remains a challenging problem.

One approach to improving on envelope-based reduced-form breaking models is to use data-driven models and machine learning. In particular, we focus here on Artificial Neural Networks (ANN), highly efficient tools to capture the evolution of non-linear physics (Raissi et al., 2019; Kochkov et al., 2021). ANNs have been applied to study ocean waves in various ways (Qi and Majda, 2020; Eeltink et al., 2022). Attempts have been made to predict the evolution of significant wave height

in the real ocean (Fan et al., 2020; Choi et al., 2020). Attempts have also been made to predict properties of the turbulence arising from wave breaking (Manucharyan et al., 2021) or the evolution of the interface in a two-phase system (Deo et al., 2023). Of particular importance here are applications to wave breaking. In Eeltink et al. (2022), the authors applied a blended model to predict wave breaking dissipation using the (temporal) MNLS equation (Dysthe, 1979; Shemer et al., 2010) combined with a long-short-term memory (LSTM) model (Hochreiter and Schmidhuber, 1997) to capture the effect of breaking dissipation.

In this study, we extend the work of Eeltink et al. (2022). We propose a novel blended model utilizing a convolutional LSTM cell (ConvLSTM) (Shi et al., 2015) in conjunction with the spatial MNLS equation (Trulsen et al., 2000) to predict the evolution of focused wave-induced breaking dissipation in time. We aim at implementing a 'per-step' model to produce highly spatially resolved prediction in space. Synthetic focused wave data generated the envelope-based reduced-form breaking model of Liu et al. (2023) is applied to train this model. The long-term objective would be to train on highly spatially resolved Computational Fluid Dynamics (CFD) simulations or experimental measurements (if possible). We then analyse the performance of the trained model for focused waves, modulated plane waves and random waves.

The new approach has a number of advantages over Eeltink et al. (2022) due to the introduction of the convolutional-recurrent architecture. We found that the ConvLSTM model learns breaking features locally, which enables the model to learn from a smaller set of representative samples before generalizing these to arbitrary wave fields with flexible domain width and duration. The ConvLSTM model is able to predict the 'per-step' evolution of the wave breaking dissipation for highly spatially resolved wave field. Comparing this with the LSTM model, the behaviour of the ConvLSTM model is easier to interpret. In this study, we will show that our model is not limited to a single type of wave condition but can be effectively applied across various conditions even if not directly trained on these.

The present chapter is part of a wider programme of work in which researchers

are trying to use machine learning to capture multi-scale interactions with improved fidelity. In the present chapter, we base our analysis on envelope-based models. The inability of these to capture wave breaking is one reason why their use has primarily been for academic research rather than as operational models. An reason for improving breaking characterisation is to make such a model more applicable to the real world and thus more useful operationally.

This chapter is organised as follows. In §4.2 we introduce the method we use to generate the synthetic data. In §4.3 we introduce the model and training details. In §4.4 we evaluate the performance of the model using a test dataset not used for training. In §4.5 we analyse the performance of the for different types of waves, before summarising in the conclusions.

4.2 Methods

Our base model in the present chapter is the Modified Nonlinear Schrödinger (MNLS) equation proposed by Trulsen et al. (2000); it solves the potential-flow equations and does not account for wave breaking. This model solves the linear part of the envelope evolution exactly and approximates the effects of weak nonlinearity under the assumption that the waves are narrowbanded. In the present work we assume the fluid is deep but not infinitely so, thus accounting for finite depth in the linear dispersion relation and in the return current but not in the coefficients of the non-linear terms which are only weakly influenced by depth for the depth range considered here (Barratt et al., 2021).

4.2.1 Envelope-Based Evolution Equation

The velocity potential ϕ and the surface elevation η are given by:

$$\phi = \bar{\phi} + \frac{1}{2}\big(\Theta e^{i(k_0 x - \omega_0 t) + k_0 z} + \Theta_2 e^{2i(k_0 x - \omega_0 t) + 2k_0 z} + ... + \text{c.c.}\big), \tag{4.1}$$

$$\eta = \bar{\eta} + \frac{1}{2}\big(B e^{i(k_0 x - \omega_0 t)} + B_2 e^{2i(k_0 x - \omega_0 t)} + ... + \text{c.c.}\big), \tag{4.2}$$

where c.c. denotes the complex conjugate, k_0 and ω_0 are the dimensional wavenumber and angular frequency of the carrier wave, $\Theta(x,z,t)$ and $B(x,t)$ are complex envelopes, and $\bar{\phi}$ and $\bar{\eta}$ are the mean-flow potential and the wave-averaged free surface, respectively. The envelope $B(x,t)$ is described by the MNLS equation (Trulsen et al., 2000) (given here in two dimensions or for unidirectional wave propagation). In equations (4.1) and (4.2), all variables are dimensional, and the primes as superscripts denoting their dimensionality are omitted here. It is more convenient to work with a non-dimensional system. The variables below are used as follows (Lo and Mei, 1985; Gramstad and Trulsen, 2011):

$$\begin{cases} \epsilon = A_0 k_0', \\ L_0 = \dfrac{1}{2\epsilon^2 k_0' \tanh(k_0' d')}, \quad T_0 = \dfrac{1}{\epsilon \omega_0'}, \\ k_0 = k_0' L_0, \quad \omega_0 = \omega_0' T_0, \\ \phi = \dfrac{\phi'}{A_0^2 \omega_0'}, \\ B = B'/A_0, \quad d = d'/L_0, \\ x = x'/L_0, \quad z = z'/L_0, \quad t = t'/T_0, \end{cases} \tag{4.3}$$

where ϵ is the characteristic steepness, A_0 is the characteristic wave height, L_0 is the length scale, T_0 is the time scale, k_0 is the non-dimensional carrier wavenumber, ω_0 is the non-dimensional carrier angular frequency and d is the non-dimensional water depth. Variables with a prime indicating the corresponding dimensional variables. Variables without a prime are always non-dimensional (except for scaling variables A_0, L_0 and T_0). Thus, we solve the following equations:

$$\frac{\partial B}{\partial t} + \mathcal{L}(\partial x)B + \frac{i\epsilon}{2}|B|^2 B + 3\epsilon^3 |B|^2 \frac{\partial B}{\partial x} + \frac{\epsilon^3}{2} B^2 \frac{\partial B^*}{\partial x} + 2i\epsilon^3 \frac{\partial \bar{\phi}}{\partial x}\bigg|_{z=0} B + D = 0, \tag{4.4}$$

$$\frac{\partial \bar{\phi}}{\partial z} = \frac{1}{2}\frac{\partial}{\partial x}|B|^2 \quad \text{at } z = 0, \tag{4.5}$$

$$\nabla^2 \bar{\phi} = 0 \quad \text{for } -d \le z \le 0, \tag{4.6}$$

$$\frac{\partial \bar{\phi}}{\partial z} = 0 \quad \text{for } z = -d, \tag{4.7}$$

where B^* denotes the complex conjugate of B, and D is the dissipation term that will be used to incorporate the reduced-form breaking models into the MNLS. In Fourier wavenumber space, the linear operator $\mathcal{L}(\partial x)$ can be written as (Trulsen et al., 2000):

$$\frac{\partial \hat{B}}{\partial t} + i[\omega(k_0 + \lambda) - \omega_0]\hat{B} = 0, \tag{4.8}$$

where λ is the modulation wavenumber. The variables ω and k follows the linear dispersion relationship:

$$\omega^2 = kg\tanh(kd), \tag{4.9}$$

where $g = g'T_0^2/L_0$ is the non-dimensional gravitational constant ($g' = 9.81\,\mathrm{m^2\,s^{-1}}$).

Equation (4.4) is solved using a spectral method in space and time-marched using a fourth-order Runge–Kutta scheme. The complex envelope $B(x, t = 0)$ is required as an initial condition for the solver. We either compute the envelope directly or reconstruct it from the Hilbert transform of the linearised surface elevation profile. In our simulation, we fix the steepness $\epsilon = 0.35$, so that A_0 depends on the choice of carrier wavenumber.

The first-order surface elevation is obtained by shifting the complex envelope to the carrier frequency and taking the real part:

$$\eta = \mathrm{Re}\left(Be^{i(k_0 x - \omega_0 t)}\right). \tag{4.10}$$

4.2.2 Reduced-Form Breaking Model

We use the modified Kato & Oikawa (M-KO95 hereinafter) model developed in Liu et al. (2023). We also include in our comparison MNLS simulations with no breaking model (labelled 'NBM'). The MNLS is able to integrate the equations even breaking would have occurred.

Kato and Oikawa (1995) (KO95) model breaking by modifying the return-current term. We use a spectral dissipation strength parameter $\hat{\beta}(k)$, which is a function

of wavenumber k, to model the contribution to the dissipation term D on different wavenumbers. This model takes the form:

$$D = k_0 B \mathcal{F}^{-1} \left\{ \hat{\beta}(k) \mathcal{F} \left\{ \frac{\partial \bar{\phi}}{\partial x} \right\} \right\} H, \tag{4.11}$$

where $\hat{\beta}(k)$ is obtained from fitting experimental measurements (see Liu et al. (2023)) and the heaviside function H depends on whether a breaking criterion is satisfied. A global kinematic criterion with a fixed-duration active breaking interval is implemented.

We will examine the local kinematic breaking criterion, $H(u/c > 0.855 \pm 0.05)$, and global kinematic breaking criterion. These criteria are reviewed in Chapter 3.

4.2.3 Initial Conditions for the MNLS Simulations

We perform simulations for 3 types of wave conditions: 1) focused wave group (for training and testing purpose), 2) modulated plane wave (for testing purpose only), 3) random waves (for testing purpose only). We take the same sets of parameters from laboratory experiments on wave breaking for all types of waves (Eeltink et al., 2022) and give a brief review as follows. All variables in this section are dimensional with primes omitted.

Focused Wave Groups and Random Waves

We generate focused wave groups and random waves using the dimensional form of the JONSWAP spectrum $S(\omega)$:

$$S(\omega) = \frac{K_s g^2}{\omega^5} \exp\left[-\frac{5}{4} \left(\frac{\omega_0}{\omega} \right)^4 \right] \gamma^r, \tag{4.12}$$

$$r = \exp\left[-\frac{(\omega - \omega_0)^2}{2\sigma^2 \omega_0^2} \right], \tag{4.13}$$

$$\sigma = \begin{cases} 0.07 & \omega \leq \omega_0, \\ 0.09 & \omega > \omega_0, \end{cases} \tag{4.14}$$

where K_s is a scaling parameter to obtain appropriate initial wave amplitude a_0. All variables in equation (4.14) are dimensional, but we omit primes for simplicity. For focused wave groups with JONSWAP spectrum, phases are assigned by computing a linear phase shift from a given focussing distance L_f based on linear theory. For random waves, the amplitudes are derived from the JONSWAP spectrum, and the phases are randomised by a fixed random number seed. As the final step, the surface elevation thus generated is made non-dimensional according to (4.3). The parameters for the focused wave group and random wave cases are drawn from the following ranges: $\gamma \in [2, 5]$, $a_0 \in [10, 60]$ mm, $f_0 \in [0.5, 1.25]$ Hz, $L_f \in [10, 24]$ m for the focused wave only.

Modulated Plane Wave

We initialise our modulated plane wave case according to Eeltink et al. (2022) as

$$\eta(x,0) = a_0\left[\sqrt{b_c}\sin(k_0 x) + \sqrt{b_+}\sin(k_+ x + \psi) + \sqrt{b_-}\sin(k_- x + \psi)\right], \tag{4.15}$$

where the upper and lower sideband frequencies are set according to $\omega_\pm = \omega_0 \pm \Delta\omega$ with $\Delta\omega$ the modulational frequency, and ψ is the phase shift of the sidebands compared to the carrier wave. Sideband wave numbers $k_\pm$ are calculated using the linear dispersion relationship $\omega_\pm^2 = g k_\pm \tanh(\mathrm{k_\pm d})$. The amplitudes of the carrier wave and the upper and lower sidebands are set according to $a_c = a_0\sqrt{b_c}$, $a_+ = a_0\sqrt{b_+}$, and $a_- = a_0\sqrt{b_-}$, where $b_c = 1 - b_F$, $b_+ = (1 - b_c - \alpha)/2$, and $b_- = (1 - b_c + \alpha)/2$, respectively, and b_F is the sideband fraction. All variables in equation (4.15) are dimensional, with all single quotes omitted. The parameters are drawn randomly from the following ranges: $f_0 = \omega_0/(2\pi) \in [1.30, 1.55]$ Hz, $a_0 k_0 \in [0.12, 0.25]$, $b_F \in [0.01, 0.1]$, $\Delta\omega \in [0.7, 1.55]$ rad/s, $\psi \in [0, 2\pi]$ and $\alpha \in [-0.16, 0.16]$.

4.2.4 Simulation Settings

We perform non-dimensional MNLS simulations to generate synthetic wave breaking data. We use a 1D uniform mesh as our computational domain. The length of the computing domain spans $[-40L_0,\ 40L_0]$ in the direction of wave propagation, and the resolution in space is $0.15625L_0$. The left- and right-hand sides of the domain are periodic boundaries. The duration of the simulation is $100T_0$, and the resolution in time is $\tau = 0.125T_0$. We set the water depth to 0.8 m for all the cases in this study.

4.3 Neural Network Model

We introduce a novel approach to predict breaking dissipation locally in MNLS simulations, which is based on a convolution-recurrent neural network structure (Shi et al., 2015). In Figure 4.1, we present the structure of the neural network model. It is composed of a ConvLSTM cell with tanh activation and a hard sigmoid for recurrent activation, a convolution layer, and an output layer, both with linear activation. We define the operators $\Phi : \mathbb{Z} \to \mathbb{Z}$ for the MNLS equation and the neural network model:

$$\Phi^{\tau}_{\mathrm{MNLS}}(B_0) = B(\tau), \tag{4.16}$$

$$\Phi^{\tau}_{\mathrm{M-KO95}}(B_0) = B(\tau), \tag{4.17}$$

$$\Phi^{\tau}_{\mathrm{NN}}\left(\xi(0);\beta\right) = \xi(\tau), \tag{4.18}$$

where $\Phi^{\tau}_{\mathrm{MNLS}}$ indicates the operator for the MNLS equation (4.4) without a breaking model (NBM), $\Phi^{\tau}_{\mathrm{M-KO95}}$ is the operator of the MNLS equation with the M-KO95 breaking model (hereafter MNLS+M-KO95) and $\Phi^{\tau}_{\mathrm{NN}}$ is the neural network operator. B_0 is the initial condition and $B(\tau)$ is the solution to the initial value problem of equation (4.4) for $t \in [0, \tau]$. $\Delta B(\tau) = \Phi^{\tau}_{\mathrm{M-KO95}}(B_0) - \Phi^{\tau}_{\mathrm{MNLS}}(B_0)$ is the 'per-step difference' of the complex envelope and τ is the time step. The 'per-step difference' is the change in the complex wave-envelope for each single time step. β is the set of

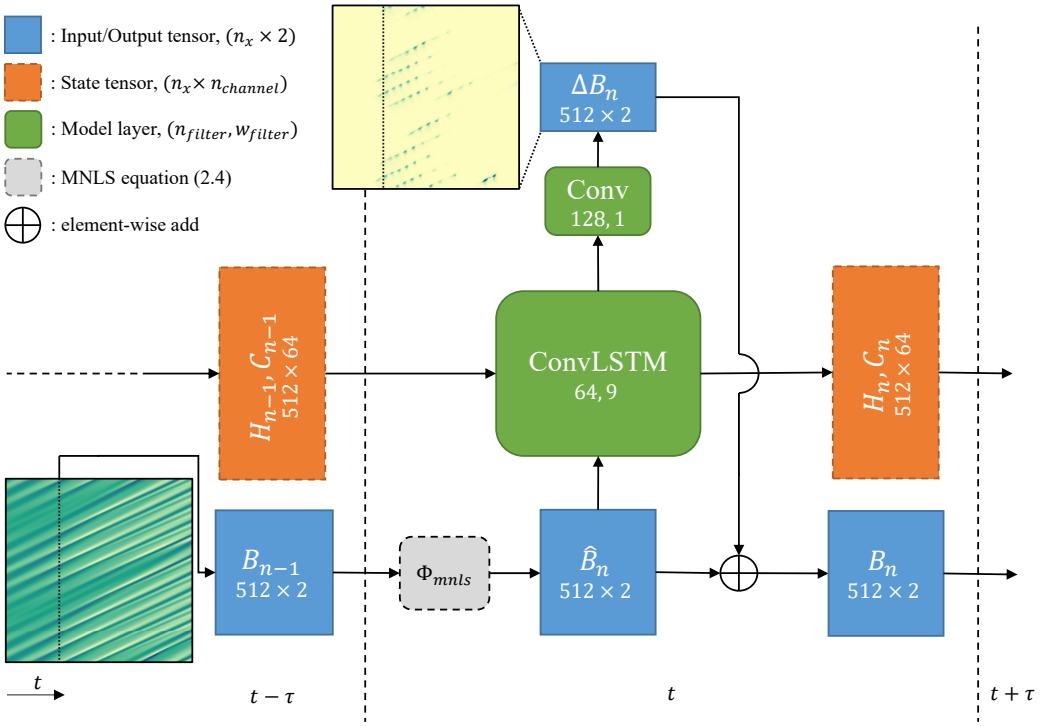


Figure 4.1: Schematic of the structure and computing diagram of a neural network model composed of four layers in vertical: an input layer accepting a pair of real numbers (the magnitudes of the real and imaginary part of the complex envelope), a ConvLSTM layer, a convolution layer, and an output layer. τ is the timestep. The model accepts input $\hat{B}_n$ and model states H_{n-1}, C_{n-1} from the previous timestep and predicts the change in ΔB_n and model states H_n, C_n between timesteps.

weights and biases of the neural network, ξ are the auxiliary states at time t:

$$\xi(t) = \left[\hat{B}(t), H(t), C(t)\right], \tag{4.19}$$

where $\hat{B}$ is the approximation of B by equation (4.4), H, C are the hidden states and cell states of the neural network, respectively. Thus, we are seeking to model breaking as an infinitesimal-domain ML correction occurring over the real duration of the event. This contrasts with the previous work of Eeltink et al. (2022) where breaking was lumped. Periodic boundary conditions in space are embedded into the input and hidden-state tensor.

The model is trained with a complex envelope B as input and a per-step differ-

ence ΔB as target. We use the Mean Squared Error (MSE) as loss function:

$$J(\beta) = \frac{1}{n_{\text{batch}} n_x n} \sum_{k=1}^{n_{\text{batch}}} \sum_{j=1}^{n} \sum_{i=1}^{n_x} \left(\Delta B_{ijk,\text{pred}} - \Delta B_{ijk,\text{true}}\right)^2, \tag{4.20}$$

where n_{batch}, n_x, n are the batch size, grid number in space and grid number in time, respectively. We minimise the MSE loss according to equation (4.20). Since B is complex valued, equation (4.20) is identical in physics space and fourier space. Once the model is trained, we deploy the model for the prediction task. The algorithm for the simulation of the machine learning-corrected MNLS equation (hereafter MNLS+ML) is given by Algorithm 1.

Algorithm 1 MNLS+ML

1: **for** n = 1, 2, ... **do**
2: $\quad \hat{B}_n \leftarrow \Phi^{\tau}_{\text{MNLS}}(B_{n-1})$
3: $\quad \begin{bmatrix} \Delta B_n \\ H_n \\ C_n \end{bmatrix} \leftarrow \Phi^{\tau}_{\text{NN}} \left(\begin{bmatrix} \hat{B}_n \\ H_{n-1} \\ C_{n-1} \end{bmatrix} \right)$
4: $\quad B_n \leftarrow \hat{B}_n + \Delta B_n$
5: **end for**

In Algorithm 1, we define several key variables that facilitate the execution of the MNLS+ML prediction:

1. B_n: This complex envelope evolves over iterations. It is calculated by applying the MNLS equation, denoted by Φ_{MNLS}, to the preceding state B_{n-1}. Subsequently, a machine learning (ML) correction term ΔB_n is incorporated into each iteration to adjust this state.

2. $\hat{B}_n$: This variable serves as aplaceholder, representing the tentative state of B_n before applying the ML correction. It is derived by applying the function $\Phi^{\tau}_{\text{MNLS}}$ to the preceding state B_{n-1}.

3. ΔB_n: This variable serves as the ML correction. It is added to $\hat{B}_n$ to obtain the updated state B_n. This correction is part of the output derived from the Φ^{τ}_{NN} function.

4. H_n and C_n: These auxiliary variables represent internal states that undergo updates at each iteration. They are associated with the $\Phi^{\tau}_{\mathrm{NN}}$ function, which updates these states simultaneously with ΔB_n.

4.4 Focused Wave Cases

In this section, we explain the methodology used to generate the synthetic focused wave cases for the training phase of our model. Concurrently, we undertake a grid search to identify the optimal hyperparameters for our model. Subsequently, we analyse the performance of the model in predictive tasks.

4.4.1 Synthetic Data Generation

For training and evaluation purposes, we have synthesised a wave breaking dataset using the MNLS+M-KO95 model, which we designate as the 'ground truth'. This dataset comprises 1000 breaking focused wave cases, partitioned into 80% used for training, 15% used for validation, and used 5% for testing. We have chosen 1000 as a moderate number of cases and the model can generate acceptable predictions with fewer training cases, such as 100. We have also generated 50 modulated plane wave cases and random wave cases to investigate the generalisability of the model (see relevant discussion in §4.5). The parameter selection adheres to a uniform distribution across a range of parameters pertinent to ocean waves introduced in §4.2.3. In addition, we incorporate a classifier during the generation process to exclude cases characterised by an excessively high or low initial steepness. Cases with an inordinately high initial steepness often trigger wave breaking at the beginning of the simulation or could cause the solver to blow up due to the non-physical steepness. Conversely, cases with an excessively low initial steepness never trigger wave breaking throughout the simulation, reducing their utility for training. Both scenarios could potentially impede the learning rate.

Our training dataset comprises input and output fields. Initially, we perform the MNLS+M-KO95 simulation to obtain synthetic ground truth, denoted as $B_{\mathrm{M-KO95}}(t) =$

$\Phi^t_{\text{M-KO95}}(B_0)$, at discrete time steps $t = 0, \tau, 2\tau, ..., n\tau$, where n represents the final time step's index and $\Phi^{n\tau} = \underbrace{\Phi^\tau \circ \ldots \circ \Phi^\tau}_{n}$, where $\circ$ is the composition of the operators. Subsequently, we engage a 'per-step' NBM simulation at each time step, generating the per-step prediction B_{MNLS} given by:

$$B_{\text{MNLS}}(t + \tau) = \Phi^\tau_{\text{MNLS}}(B_{\text{M-KO95}}(t)) \quad \text{for } t = 0, \tau, ..., (n-1)\tau. \tag{4.21}$$

Next, we compute the per-step difference between the ground truth and the estimated field, designated as $\Delta B(t) = B_{\text{MNLS}}(t) - B_{\text{M-KO95}}(t)$, for $t = \tau, 2\tau, ..., n\tau$. For training the neural network model, the input data consists of a time series of complex envelope $B_{\text{MNLS}}(t)$, at specific time steps $t = \tau, 2\tau, ..., n\tau$. The output data, on the other hand, is defined by the change in the complex envelope, represented as the per-step difference $\Delta B(t)$, at the same time steps.

4.4.2 Training History

Our model is trained for 50 epochs with an early stopping mechanism activated when there is no improvement in validation loss over 10 consecutive epochs. Moreover, we generate several models with different configurations to evaluate the impact of the choice of hyperparameters. The model is trained with data with time-steps of both $0.125T_0$ and $0.25T_0$, and we do not find a clear link between performance and time resolution. The number and width of filters in the ConvLSTM layer turns out to be a critical hyperparameter that influences the model's size and performance. A grid search for these two variables indicates that our state-of-the-art (SOTA) model (which minimises the prediction loss for focused wave cases) employs 64 filters, each with a width of 9 (hereafter referred to as the w9f64 model) and comprises 160898 trainable parameters. The training history of this SOTA model is illustrated in Table 4.1. Additionally, Table 4.1 shows the losses taken into account across all nine model configurations, revealing that the w9f64 model achieves the lowest prediction loss for the focused wave group cases. We also test a 'light' configuration—the w3f16 model—with a minimum of 16 filters of width 3 and a total of 5954 trainable

parameters. This lighter configuration may be preferred when striking a balance between model accuracy and model size. The lighter configuration also seems to generalise to unseen wave types well, such as modulated plane waves and random waves. We also explored some other simple variants that enable stable prediction for long-term simulations. However, for the sake of simplicity, our study focusses primarily on the SOTA model, with a brief discussion of the other variants given in Appendix C.1.

Model Name	**# Parameter**	**Training Loss**	**Validation Loss**	**Prediction Loss (Type I, focused)**	**Prediction Loss (Type II, plane wave)**	**Prediction Loss (Type III, random)**
NBM	-	-	-	0.3631	4.587	1.517
LSTM	722432	0.0205	0.0225	-	-	-
w3f16	5954	0.0233	0.0207	0.0141	**0.454**	**0.491**
w3f32	17666	0.0201	0.0167	0.0149	0.632	0.860
w3f64	59522	0.0159	0.0141	0.0116	0.849	0.775
w9f16	12866	0.0196	0.0166	0.0107	0.563	0.697
w9f32	43778	0.0153	0.0132	0.0214	0.645	1.041
w9f64	160898	0.0140	0.0123	**0.0105**	0.520	0.724
w15f16	19778	0.0176	0.0148	0.0135	0.915	0.718
w15f32	69890	0.0148	0.0131	0.0133	0.972	0.946
w15f64	262274	**0.0138**	**0.0118**	0.0120	0.995	0.932

Table 4.1: Overview of the training, validation and prediction losses of the models considered. The MNLS equation without a breaking model (NBM) and with a fully connected LSTM model (Hochreiter and Schmidhuber, 1997) are evaluated as baseline. All losses are computed by (4.20), divided by a universal upper bound of magnitude of ΔB, which is 0.04 for all types of waves considered in this study.

4.4.3 Model Analysis

In this section, we investigate the response of the neural network model to an arbitrarily selected case from the test dataset. Although we focus on this specific case, our conclusions generally apply to other scenarios. We specifically examine the cell states (Shi et al., 2015) of the ConvLSTM layer. In Figure 4.2 we plot the spatial-temporal evolution of cell state for each channel (each filter in the ConvLSTM layer creates a channel, see Figure 4.1). We find that some channels, especially the channels that maintain a high energy level throughout the duration, are activated over most of the simulation regardless of the state of the waves. Set against this, the other, 'weak', channels react to the input only during breaking. Interestingly, the cell states of some of the high-energy-level channels are blurred during breaking, which may be evidence that the model is switching between different states. This hints that the model has learnt to break the wave evolution problem into two processes—a classification process, which detects breaking, and a regression process, which occurs once breaking is detected—similar to how humans might tackle the breaking problem. The other evidence is obtained from the 'energy' of the cell state, defined as the mean squared sum over space: $E_{cell,i}(t,c) = (1/n_x)\sum_i^{n_x} C(t,x_i,c)^2$ of the ConvLSTM layer. In Figure 4.3 we plot the evolution of the 'energy' of the cell state C. The channel is sorted in descending order based on the cell energy at the last timestep. We find that the 'energies' of each channel are not equally distributed, and the 'energy' of some channels changes significantly during breaking.

4.4.4 Prediction for Focused Wave Groups

We apply our neural network model to a test dataset of 50 focused wave cases unseen during the training phase. To illustrate its performance, we present a specific test case before assessing the error across the entire test dataset. This model has limited capabilities and inherits bias from the synthesised dataset, which makes it unsuitable to compare with laboratory experiments. However, we expect that a model trained with high-fidelity simulation data or experiment data can be compared

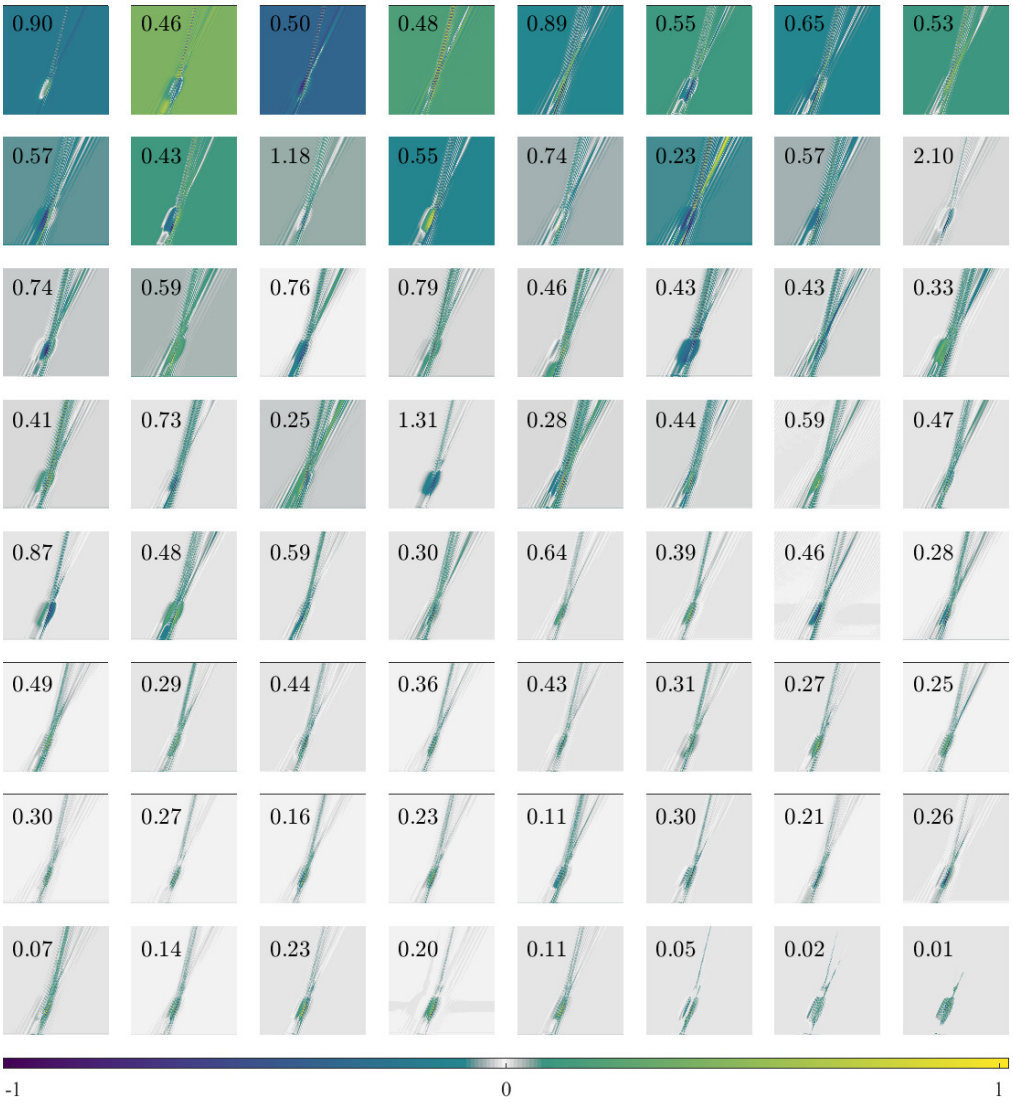


Figure 4.2: In this figure, the cell state C for each filter channel is represented in a spatial-temporal plot where space axis is horizontal and time axis is vertical, arranged in panels from top to bottom and left to right. The color scale of the plots is normalised to [-1, 1] for each panel, where brighter colors indicate higher values, darker colors represent lower values and color with decreased saturation for values close to zero. The scaling factor for the color range in each plot is denoted in the annotation at the top-left corner of each panel.

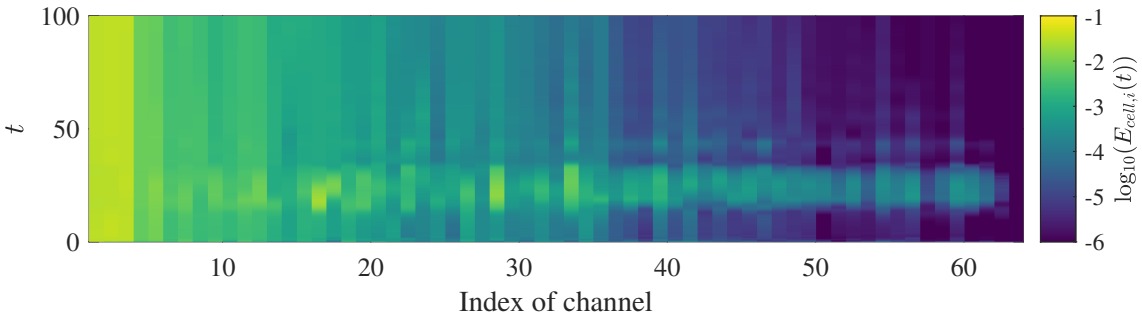


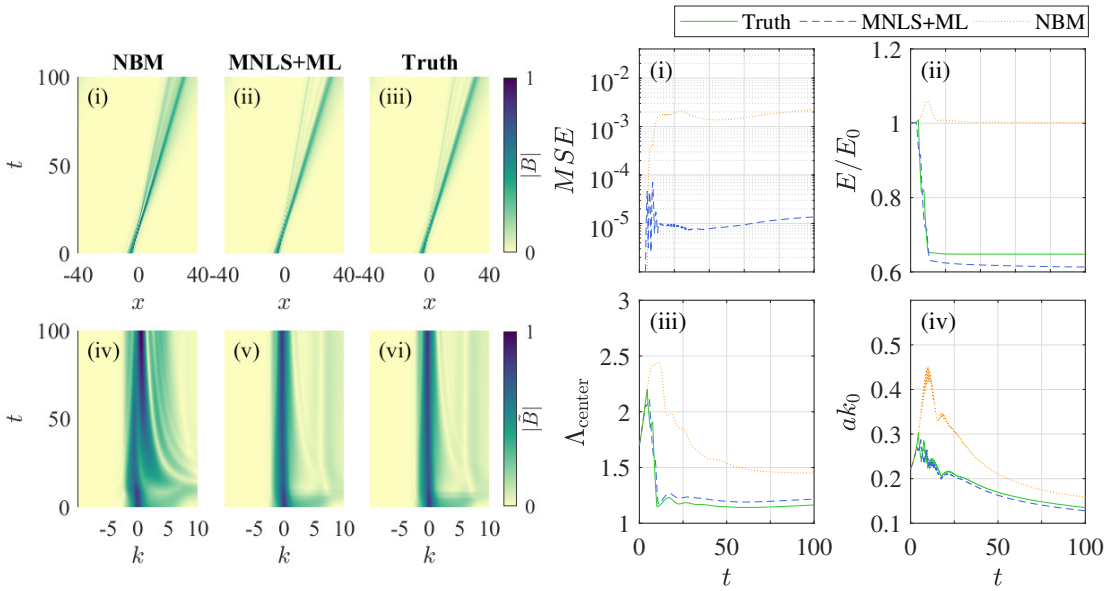
Figure 4.3: The evolution of the 'energy' (for each channel) of the cell state. The channels are sorted in descending order based on the energy level of the channel.

with experiment measurements directly.

Figure 4.4a compares the evolution of the complex envelope B in both the physical and wavenumber spaces for the NBM simulation, MNLS+ML simulation, and the ground truth. We note that the ground truth is synthetic data based on M-KO95 model, and for a thorough comparison among M-KO95 model, other reduced-order models, and laboratory data, can be found in Liu et al. (2023). Figure 4.4b depicts the evolution of energy ($\|B\|^2$), peak frequency, and steepness for all three simulations, and the evolution of the MSE compared to the ground truth for NBM simulations and MNLS+ML simulations. Our observations in Figure 4.4 suggest that the neural network model effectively predicts wave breaking dissipation and achieves a mean squared error (MSE) of the envelope approximately two orders of magnitude lower than that of the NBM simulation. The model also accurately reproduces the evolution of energy, peak frequency, and steepness.

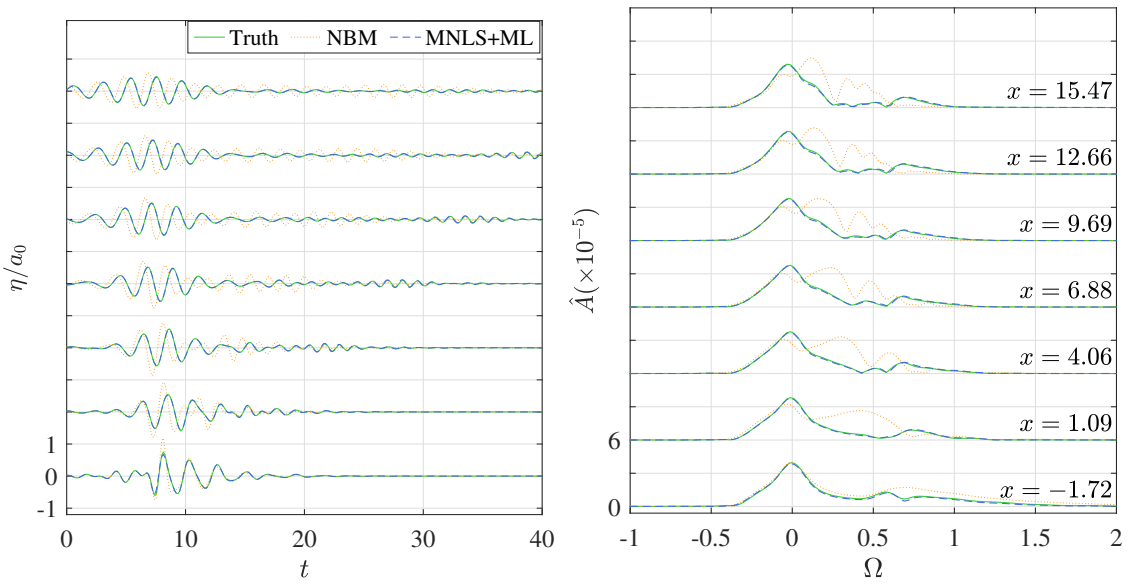
Figure 4.5 presents the time series of the surface elevation profile and the frequency spectrum recorded at seven gauges within the domain. The recorded time series is shifted by the group speed calculated using linear dispersion, and subsequently cropped to a fixed duration $t \in [0, 40]$. Our observations in Figure 4.5 indicate that the predicted time series aligns closely with the ground truth in both the time and frequency domains, while the NBM solution quickly diverges from the ground truth.

Broadening our focus beyond a single instance, we assess the performance of the neural network model across all 50 focused wave group test cases. Figure 4.6a



(a) Envelope and wavenumber spectrum (b) MSE, energy, spectral mean and steepness

Figure 4.4: The figures consists of two subplots. In subplot (a), panels (i), (ii) and (iii) show the evolution of the absolute value of the complex envelope using different models, while panels (iv), (v), and (vi) show the evolution of the absolute value of the wavenumber spectrum of the complex envelope. Specifically, panel (i) and (iv) show the NBM result, panel (ii) and (v) show the MNLS+ML result, and panel (iii) and (vi) show the ground truth generated by the M-KO95 model. In subplot (b), panel (i) plots the mean squared error (MSE) of the absolute value of the complex envelope. Panels (ii), (iii), and (iv) compare the energy evolution $E = \int \|B\|^2 \, \mathrm{d}t$ normalised by its value at the first time step E_0, wavenumber spectral mean or centroid, $\Lambda_{\text{center}} = \int k\tilde{B}(k)\mathrm{d}k / \int \tilde{B}(k)\mathrm{d}k$, and evolution of steepness. All panels share the same legend, which is placed on the top of subplot (b). In the legend, the green solid line represents the ground truth, the blue dashed line represents the MNLS+ML result or MSE of MNLS+ML compared to the ground truth, and the orange dotted line represents the NBM result or MSE of NBM result compared to the ground truth.



(a) Type I wave: surface elevation profile

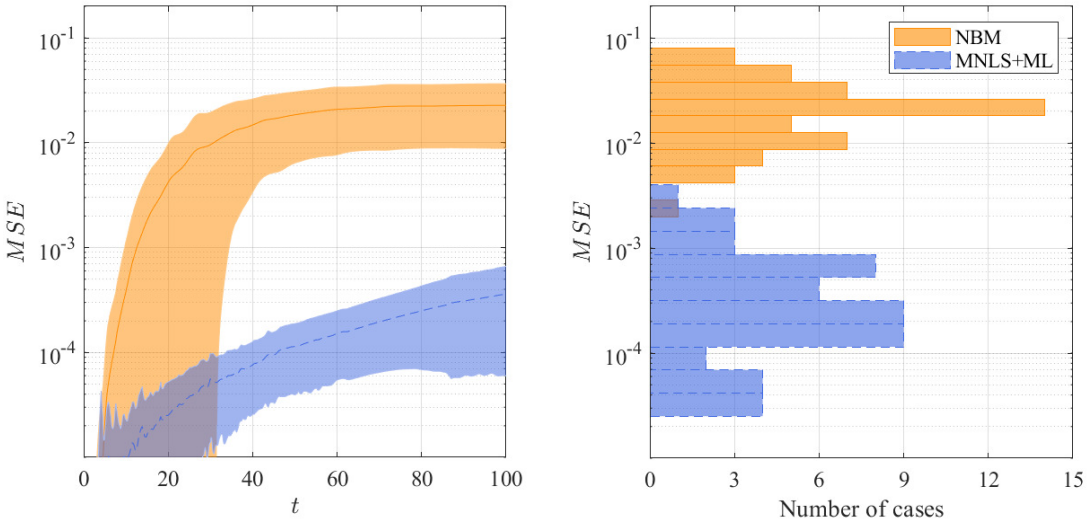
(b) Type I wave: frequency spectrum

Figure 4.5: The figure depicts profiles of a specific case from the test dataset at different gauge locations x. The case is randomly selected from the test dataset. The solid green line is ground truth, the blue dashed line is the MNLS+ML simulation and the orange dotted line is the NBM simulation. Panel (a) plots the surface elevation η normalised by the characteristic wave amplitude a_0 and panel (b) represents the frequency spectrum of normalised surface elevation, where $\Omega = \omega/\omega_0 - 1$ is the normalised modulational frequency.

presents the evolution of the mean squared error (MSE) for both the MNLS+ML simulations and the NBM simulations with respect to time. Further, Figure 4.6b displays a histogram of the MSE at the final time step of the simulation. We observe that significant MSE errors arise from inaccurate predictions concerning both the onset and strength of the breaking event.

4.5 Modulated Plane and Random Waves

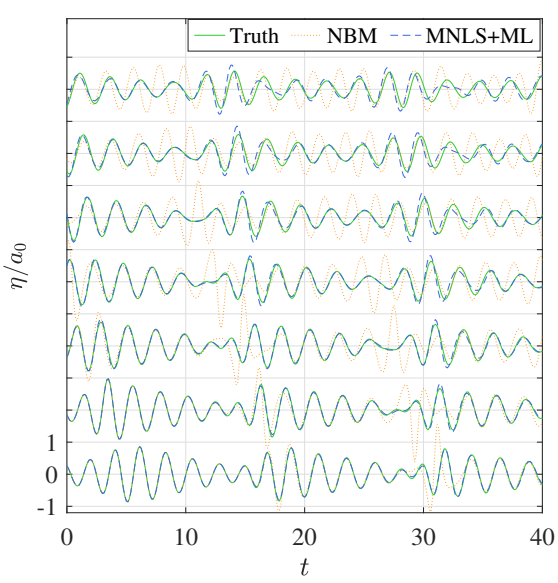
To examine the model's generalisability beyond wave groups, we apply the trained model to predict breaking dissipation in modulated plane wave and random wave scenarios. We generate 50 modulated plane wave cases and 50 random wave cases for testing, the latter characterised by a JONSWAP spectrum. It is important to note that the performance of the M-KO95 model tends to deteriorate when applied to waves other than focused wave groups, owing to its non-local breaking dissipation. Consequently, given that the scenarios under consideration here are modulated



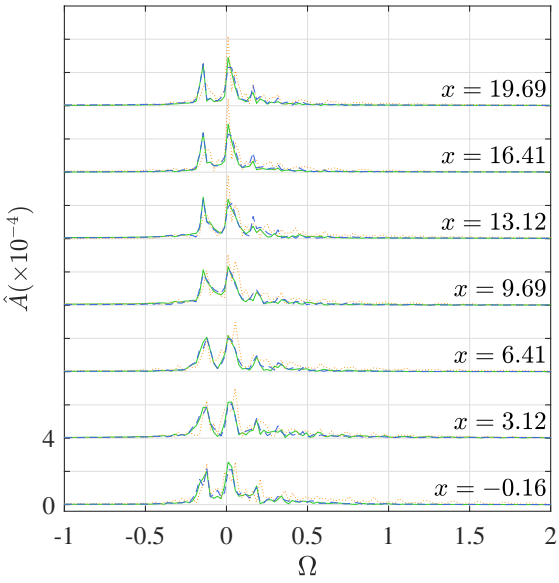
(a) Evolution of MSE for the MNLS+ML simulations and the NBM simulations as a function of time averaged over the 50 test cases.

(b) Histogram of the MSE for the MNLS+ML simulations and the NBM simulations at the last time step.

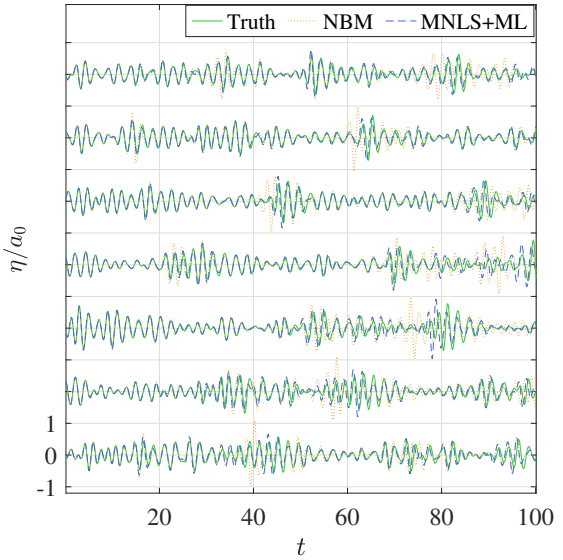
Figure 4.6: This figure plots the MSE error distribution across the test dataset. Panel (a) shows the evolution of MSE of MNLS+ML and NBM simulations as a function of time, where the blue line with the shaded region corresponding to $\pm 1\sigma$ indicates the MSE of the MNLS+ML simulations and the orange line with the shaded region corresponding to $\pm 1\sigma$ indicates the MSE of the NBM simulations. Panel (b) illustrates the distribution of the MSE for the MNLS+ML and the NBM simulations at the final time step, where blue bars stand for MNLS+ML and orange bars for NBM.



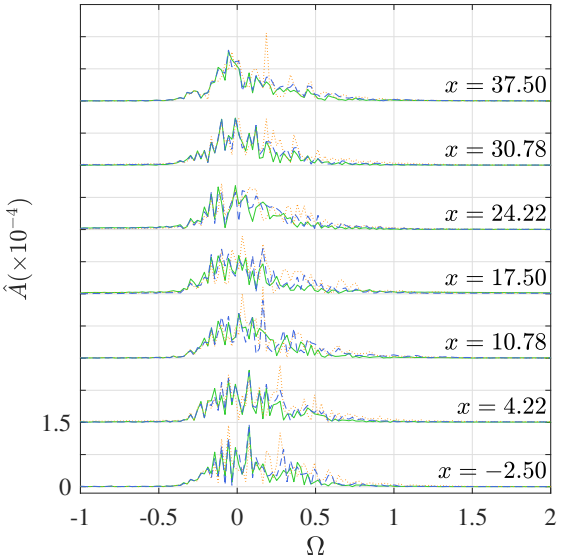
(a) Type II: surface elevation profile evolution



(b) Type II: frequency spectrum evolution



(c) Type III: surface elevation profile evolution



(d) Type III: frequency spectrum evolution

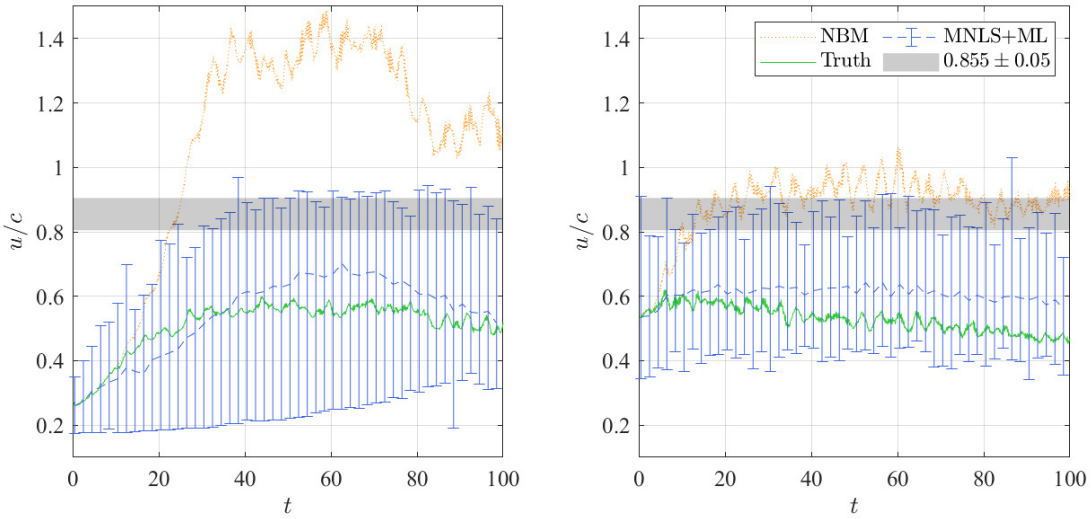
Figure 4.7: The figure depicts (a) the surface elevation profile of a modulational plane wave case;(b) the corresponding frequency spectrum; (c) the surface elevation profile of a random wave case and (d) the corresponding frequency spectrum. The case was randomly selected from the test dataset. Solid green line is ground truth, blue dashed line is MNLS+ML and orange dotted line is NBM simulation. The time series of random wave case is not shifted by group speed.

plane waves and random waves, we anticipate observing larger discrepancies when compared to the true evolution as predicted by the M-KO95 model.

Figures 4.7a and 4.7b plot the time series of surface elevation of a modulated plane wave and frequency spectrum. We find that the MNLS+ML simulation is much more accurate than the NBM simulations compared to ground truth. The error is, however, larger than for the focused wave cases presumably due to it being harder to localise the breaking event. Figures 4.7c and 4.7d plot the time series of surface elevation of a random wave case and corresponding frequency spectrum and we are able to draw the same conclusion from the figures. We find that the neural network model is able to predict surface elevation with little discrepancy. Furthermore, Figure 4.8 presents the evolution of the maximum breaking parameter, u/c, in the nonbreaking zone, averaged between test cases. We split nonbreaking and breaking zones in the MNLS+ML simulation by assessing whether the neural network output surpasses 3% of its total output range. Figures 4.8a and 4.8b compare the evolution of the mean breaking parameter, u/c, in MNLS+ML simulation with NBM and ground truth, for modulated plane wave and random waves respectively. The MNLS+ML and ground truth show similar u/c evolution, while the NBM simulation exhibits unbounded growth. Error bars for the MNLS+ML series denote extremes of the breaking parameters in the test cases, with most maxima aligning or falling below the threshold value of 0.855 ± 0.05, validating that the MNLS+ML simulation adheres to the breaking criterion. As such, we can say that the ML architecture developed herein appears to work for other wave breaking scenarios and not just for isolated wave groups. Additional results are given in Appendix C.2.

4.6 Conclusion

Machine learning the complexities of wave breaking is a promising way of capturing the key physics of breaking in computationally fast, reduced-form models such as the MNLS equation. As such, an MNLS+ML model promises greater fidelity than alternative reduced-form breaking models that have been implemented in the MNLS



(a) Type II: breaking parameter

(b) Type III: breaking parameter

Figure 4.8: The figure plots the evolution of maximum breaking parameter u/c (Barthelemy et al., 2018) in nonbreaking zone averaged over test cases for (a) modulated plane wave and (b) random waves. Solid green line is ground truth, blue dashed line with errorbars is MNLS+ML and orange dotted line is NBM simulation. The errorbars indicate maxima and minima of maximum breaking parameter throughout the test cases.

equation (see comparison of existing reduced-form breaking models in Liu et al. (2023)). This chapter extends the framework proposed in Eeltink et al. (2022). The model proposed here achieves similar or superior performance compared to Eeltink et al. (2022), with a scalable structure that allows one to use from thousands to hundred thousands of parameters. The model utilises a convolutional-recurrent structure that enables it to support simulations with arbitrary length in space and time.

The model assumes that wave breaking dissipation is local in space. We train the model with focused wave cases only and show that the model is able to generalise to breaking in very different wave fields. The ability of a neural network model to learn from a small set of canonical samples and generalise to arbitrary conditions is promising. This reduces the potential difficulty in preparing a dataset for such models as both computational fluid dynamics (CFD) simulations and wave tank experiments for focused waves are cheaper than similar such simulations or experiments for modulated plane wave or random wave datasets.

To improve the real-world accuracy of the model, integrating CFD data into the training process can be considered in future work, and the framework developed here is designed to enable this extension. This would enable the model to capture the complex dynamics of fluid flow and wave breaking. In addition, efforts should be made to establish a robust theoretical backbone for the model, incorporating insights from fluid dynamics, wave mechanics, and machine learning which the richer data from CFD might be able to provide. This would not only contribute to a deeper understanding of the underlying processes governing wave breaking and dissipation, but would also enable the development of more reliable and efficient models.

Chapter 5

Numerical simulation of wave breaking using RANS: comparison with experiments

Abstract

Wave breaking is a multifaceted physical phenomenon that is not fully understood and remains challenging to model. An effective method for investigating wave breaking involves utilising the two-phase Reynolds-averaged Navier–Stokes (RANS) equations to directly simulate breaking waves. In this study, we apply a RANS model with an adaptively refined mesh to simulate breaking waves on deep water using the stabilised RANS model proposed by Larsen and Fuhrman. This approach enables a more efficient simulation of the physics of breaking waves compared to Direct Numerical Simulations, as it places less stringent demands on grid resolution. Our findings demonstrate that the RANS model compares well with experimental data, including in terms of energy dissipation, and gives estimates of the breaking strength parameter that agree with existing parametrisations.

5.1 Introduction

Wave breaking is an important phenomenon in the ocean, yet many aspects of it remain poorly understood. Wave breaking dominates energy dissipation in the ocean (Babanin, 2011). Energy dissipation related to breaking involves a complex combination of energy transfer and energy dissipation mechanisms. In order to understand these mechanisms, many Computational Fluid Dynamics (CFD) methods including Direct Numerical Simulation (DNS), Large-Eddy Simulation (LES), and Reynolds-Averaged simulation (RANS) have been used to solve the two-phase Navier–Stokes equations. Although DNS and LES simulations have become feasible given increasing computing resources, it is still very expensive to perform parametric studies with these methods. Full-scale DNS simulation is difficult and resource-demanding even for systems at laboratory scale. Although wave-tank experiments are a high-fidelity data source that includes all the relevant physical processes albeit at scale, collecting a large ensemble of experimental data is expensive. Moreover, gauge measurements are almost always sparsely distributed in space, which poses inherent limitations on the spatial resolution of the data. Particle image velocimetry (PIV) could provide sufficient spatial resolution but is far more costly and time-consuming than gauge measurements. Therefore, with limited time and budget, Computational Fluid Dynamics simulations serve as our most reliable data source. We opted for RANS simulation due to its balance of efficiency and satisfactory precision. Hence, the focus of this chapter is on RANS simulation as a relatively cheap way to study wave breaking that can ultimately be used to generate a large ensemble of simulations, suitable, for example, for machine-learning applications.

RANS aims at solving the time-averaged or ensemble-averaged Navier–Stokes equation, with the Reynolds stresses being modelled by 'closure models'. Closure models can be roughly divided into two categories: turbulent-viscosity models and Reynolds-stress models. Turbulent-viscosity models are based on turbulent-viscosity hypothesis and gradient-diffusion hypothesis introduced by Boussinesq (1877). Mixing-length model, $\varkappa - \varepsilon$ model, $\varkappa - \omega$ model and Spalart–Allmaras model

are examples of representative turbulent-viscosity models. These models typically require 0 to 2 additional equations for turbulence variables, which makes these models very efficient to solve relative to DNS and the full Reynolds-stress RANS equations. However, the turbulent-viscosity hypothesis imposes intrinsic assumptions on the turbulence. These assumptions may be challenged in the context of wave breaking turbulence. Reynolds-stress models, such as the Launder–Reece–Rodi and stress-ω models, solve all individual Reynolds stress components and therefore do not rely on a turbulent-viscosity hypothesis. Reynolds-stress models can model anistropic turbulence. However, solving all individual Reynolds stresses components requires 6 additional equations to describe Reynolds stresses, and this is generally more expensive to solve than turbulent-viscosity models. Further discussion on closure models can be found in Pope (2000) or Wilcox (2006).

A well-known issue affecting RANS simulations is that all standard turbulence models, such as $\varkappa - \varepsilon$ or $\varkappa - \omega$, overestimate the generation of turbulent kinetic energy (TKE) in the near-potential flow region. The overproduction of TKE can cause an underestimation of wave height at the onset of or during breaking. This underestimation has been reported in existing studies (Lin and Liu, 1998; Bradford, 2000; Xie, 2013). Many numerical studies of breaking waves have adopted the non-stabilised $\varkappa - \varepsilon$ or $\varkappa - \omega$ model (Zhang et al., 2014; López et al., 2014; Colombo and Fairweather, 2015; Devolder et al., 2018). However, in recent years, this issue has been successfully addressed by switching to a modified $\varkappa - \omega$ model or to a Reynolds Stress Equation Model (RSM) (Larsen and Fuhrman, 2018; Li et al., 2022). Specifically, the unbounded growth of TKE leads to unphysical damping of surface waves. This issue appears due to the incorrect prediction of the generation of turbulence from the potential-flow motion. The conditional stability of $\varkappa - \omega$ models was shown by Mayer and Madsen (2001). Wilcox (2006) proposed a revised $\varkappa - \omega$ model with a stress limiter to improve the prediction of TKE in anisotropic regions such as shock-wave boundary layers and stagnation points. Following their work, Larsen and Fuhrman (2018) investigated the stability of several RANS models including the revised models (Mayer and Madsen, 2001; Wilcox, 2006) under (potential-flow)

gravity-wave perturbations, leading to the proposal of a new ω-limiter to stabilise the $\varkappa - \omega$ model of Wilcox (2006, 2008).

Several studies of breaking waves (Larsen et al., 2020; Fuhrman and Li, 2020; Gruwez et al., 2020; Ahmad et al., 2019) have been performed with the revised turbulence model of Larsen and Fuhrman (2018) and report close agreement between experiments and simulations for shallow-water breaking waves. In very recent work, simulations with Wilcox's stress-ω model (Li and Fuhrman, 2021) have been performed for modulated plane waves in deep water. These simulations compare well with experimental measurements in terms of spectral downshifting. To my knowledge, deep water wave breaking has not been successfully studied.

The goal of this chapter is to introduce an implementation of the RANS model for the purpose of near-energy-conserving (in the absence of breaking) simulation of breaking surface gravity waves on deep water with Adaptive Mesh Refinement (AMR) to enable relatively cheap computation of large ensembles of 2D simulations of breaking waves. Our aim is to enable simulation of large ensembles for machine-learning purposes. We show that the stabilised $\varkappa - \omega$ model proposed by Larsen and Fuhrman (2018) works well with AMR, and the result agrees satisfactorily with experimental measurements by Eeltink et al. (2022). Estimates of the breaking parameter (Drazen et al., 2008) obtained from our RANS simulations are in reasonable agreement with the parametrisation by Romero et al. (2012). Moreover, we show that the total energy loss outside of the breaking phase is less than 2% in most cases and that viscous dissipation has a negligible contribution.

This chapter will be organised as follows. In §5.2 we introduce the numerical model that we use to perform the RANS simulations. In §5.3 we discuss the convergence of the simulation for Stokes waves and a focused wave group case. In §5.4 we will analyse the results we obtained from the model and compare to experimental measurements from Eeltink et al. (2022) for three different types of waves (modulated plane waves, focussed wave groups and random waves). We conclude and discuss the validity of the model in §5.5.

5.2 Methodology

5.2.1 Navier–Stokes Equations

We use the open-source numerical package 'Basilisk' (Popinet, 2015) to solve two-phase Reynolds-Averaged Navier–Stokes (RANS) equations on a 2D grid that uses AMR. Momentum conservation is achieved by applying the momentum-conserving volume-of-fluid (VOF) scheme. Mass, momentum and volume conservation are described by:

$$\frac{\partial \rho}{\partial t} + \frac{\partial (\rho u_i)}{\partial x_j} = 0, \tag{5.1}$$

$$\frac{\partial (\rho u_i)}{\partial t} + \frac{\partial (\rho u_j u_i)}{\partial x_j} = -\frac{\partial p}{\partial x_i} + \frac{\partial \sigma_{ij}}{\partial x_i} + \frac{\partial \tau_{ij}}{\partial x_j} + \rho g_i, \tag{5.2}$$

$$\frac{\partial u_i}{\partial x_i} = 0, \tag{5.3}$$

where u is the mean velocity field, ρ is the fluid density, p is the pressure, g is gravity force vector, σ is the viscous stress tensor in incompressible flow that is defined as $\sigma_{ij} = 2\mu S_{ij}$, μ is the fluid dynamic viscosity, $S_{ij} = (\partial u_j/\partial x_i + \partial u_i/\partial x_j)/2$ (as defined in eqn. (5.7)), τ_{ij} is the Reynolds stress tensor. In this study, the effect of surface tension is ignored.

5.2.2 The $\varkappa - \omega$ Turbulence Model

This subsection sets out the equations for the turbulence model we consider in this chapter. More details and theoretical background can be found in Wilcox (2006). We implement a RANS turbulence model to approximate the Reynolds stress tensor τ_{ij} in eqn. (5.2) based on the $\varkappa - \omega$ Two-Equation Model (Wilcox, 2006). Using the Boussinesq approximation (Schmitt, 2007) for incompressible flow, we define $\tau_{ij} = 2\rho\nu_t \left[S_{ij} - 1/3 \left(\partial u_k/\partial x_k\right) \delta_{ij}\right] - 2/3\rho\varkappa\delta_{ij}$, where ν_t is the turbulent eddy viscosity and $\varkappa$ is the turbulence kinetic energy. The $-1/3\partial u_k/\partial x_k$ term vanishes in incompressible flow. In practice, the turbulent normal stress ($2/3\rho\varkappa\delta_{ij}$ term) can be either absorbed by the pressure term in the momentum equation (5.2), or

neglected in linear two-equation turbulence models. Following practical notes of Rumsey (2023), we choose to neglect the turbulent normal stress in the momentum equation. Therefore, only the deviatoric anisotropic stress components are involved in the simulation.

It has been shown by Larsen and Fuhrman (2018) that the 'standard' version of the $\varkappa-\omega$ model (Wilcox, 2006) is unstable to perturbations in the near-potential-flow region. The turbulence kinetic energy (TKE) is subject to unbounded growth under the influence of a Stokes wave. Hence, we adopt a modified version of this model with a specific stress limiter that has been introduced to solve this problem (Larsen and Fuhrman, 2018). The conservative form of $\varkappa-\omega$ model in incompressible flow with buoyancy correction is written as follows (Larsen and Fuhrman, 2018), given that $\varkappa$ is the modelled TKE and ω is the modelled turbulence dissipation rate:

$$\frac{\partial(\rho\varkappa)}{\partial t}+\frac{\partial(\rho u_j\varkappa)}{\partial x_j}=P-\rho\alpha_b^* N^2-\beta^*\rho\omega\varkappa+\frac{\partial}{\partial x_j}\left[\left(\mu+\sigma_\varkappa\frac{\rho\varkappa}{\omega}\right)\frac{\partial\varkappa}{\partial x_j}\right], \tag{5.4}$$

$$\frac{\partial(\rho\omega)}{\partial t}+\frac{\partial(\rho u_j\omega)}{\partial x_j}=\frac{\bar{\gamma}\omega}{\varkappa}P-\beta\rho\omega^2+\frac{\partial}{\partial x_j}\left[\left(\mu+\sigma_\omega\frac{\rho\varkappa}{\omega}\right)\frac{\partial\omega}{\partial x_j}\right]+\frac{\rho\sigma_d}{\omega}\frac{\partial\varkappa}{\partial x_j}\frac{\partial\omega}{\partial x_j}, \tag{5.5}$$

where

$$P=2\mu_t S_{ij}\frac{\partial u_i}{\partial x_j}, \tag{5.6}$$

$$S_{ij}=\frac{1}{2}\left(\frac{\partial u_i}{\partial x_j}+\frac{\partial u_j}{\partial x_i}\right), \tag{5.7}$$

$$\mu_t=\frac{\rho\varkappa}{\tilde{\omega}}, \tag{5.8}$$

$$\tilde{\tilde{\omega}}=\max\left[\tilde{\omega},\quad \lambda_1\sqrt{\frac{2S_{ij}S_{ij}-\alpha_b^* N^2}{\beta^*}}\right], \tag{5.9}$$

$$\tilde{\omega}=\max\left[\tilde{\tilde{\omega}},\quad \lambda_2\frac{\beta}{\beta^*\bar{\gamma}}\frac{S_{ij}S_{ij}}{\Omega_{ij}\Omega_{ij}}\omega\right], \tag{5.10}$$

$$N^2=\frac{g_i}{\rho}\frac{\partial\rho}{\partial x_i}, \tag{5.11}$$

and the constants and other parameters are:

$$\sigma_\varkappa = 0.6, \quad \sigma_\omega = 0.5, \quad \beta^* = 0.09, \tag{5.12}$$

$$\bar{\gamma} = \frac{13}{25}, \quad \beta_0 = 0.0708, \quad \beta = \beta_0 f_\beta, \tag{5.13}$$

$$\lambda_1 = 0.875, \quad \lambda_2 = 0.05, \quad \alpha_b^* = 1.36, \tag{5.14}$$

$$f_\beta = \frac{1 + 85\chi_\omega}{1 + 100\chi_\omega}, \quad \chi_\omega = \left| \frac{\Omega_{ij}\Omega_{jl}\hat{S}_{li}}{(\beta^*\omega)^3} \right|, \tag{5.15}$$

$$\hat{S}_{li} = S_{li} - \frac{1}{2}\frac{\partial u_m}{\partial x_m}\delta_{li}, \quad \Omega_{ij} = \frac{1}{2}\left(\frac{\partial u_i}{\partial x_j} - \frac{\partial u_j}{\partial x_i}\right), \tag{5.16}$$

$$\sigma_d = \begin{cases} 0 & \text{for} \quad \dfrac{\partial \varkappa}{\partial x_j}\dfrac{\partial \omega}{\partial x_j} \le 0, \\ 0.125 & \text{for} \quad \dfrac{\partial \varkappa}{\partial x_j}\dfrac{\partial \omega}{\partial x_j} > 0. \end{cases} \tag{5.17}$$

For the 2D problem we examine, we turn off the 'Pope Correction' (Pope, 1978; Oumrani et al., 2015) and set $\chi_\omega = 0$.

5.2.3 Adaptive Mesh Refinement

We solve the above mentioned Navier–Stokes equations in conjunction with the RANS model with an adaptively refined mesh. An adaptively refined mesh refines or coarsens elements in different regions according to specific criteria, such as the error estimates of the solution or the presence of steep gradients. Basilisk adopted a quadtree data structure to efficiently traverse the 2D mesh at different resolution levels. A quadtree is a tree data structure in which each node has exactly four children. In the context of 2D adaptive mesh refinement, a quadtree divides a 2D domain into four quadrants recursively. Each node in the quadtree represents a square region of the domain, and each division into four children corresponds to a refinement of that region. Further details of the mesh refinement scheme used are given in Popinet (2009).

An error estimator assesses the local error in the solution across the mesh. Based on the error estimates, the quadtree structure is refined by subdividing nodes into regions with high error and potentially coarsened by merging nodes in regions with

low error. This results in a new, adaptively refined mesh. The process iterates, solving the partial differential equations on the refined mesh, reestimating the error, and further refining the mesh until the solution meets the desired accuracy criteria. In this study, we evaluated the local error of the velocity and volume fraction. In addition, we enforce the grid resolution near the air-water interface and the bottom boundary to the maximum (Figure 5.1). We also performed a validation study to help determine the appropriate maximum grid resolution.

Prolongation and restriction of field variables are required when coarsening and refining the mesh. Prolongation transfers information from a coarse mesh to a fine mesh, and restriction is its complementary process. They must be processed with care to ensure that the adapted solution still satisfies the conservation of mass and momentum. We adopt default settings of Basilisk for velocity and volume fraction field (Popinet, 2009). For the turbulence variables $\varkappa$ and ω, we use the bilinear interpolation method for prolongation and the volume average method for restriction.

5.2.4 Wave Parameters

We perform simulations for three types of wave conditions:

1. Modulated plane waves;
2. Focused wave groups;
3. Random waves.

We compare our numerical simulation with the experiments of Eeltink et al. (2022). We choose 4 modulated plane wave cases, 2 focused wave group cases, and 4 random wave cases to investigate. Then, we study 300 random simulations generated by the same sets of parameter ranges for these three wave types used in laboratory experiments in (Eeltink et al., 2022), and a brief summary is given as follows.

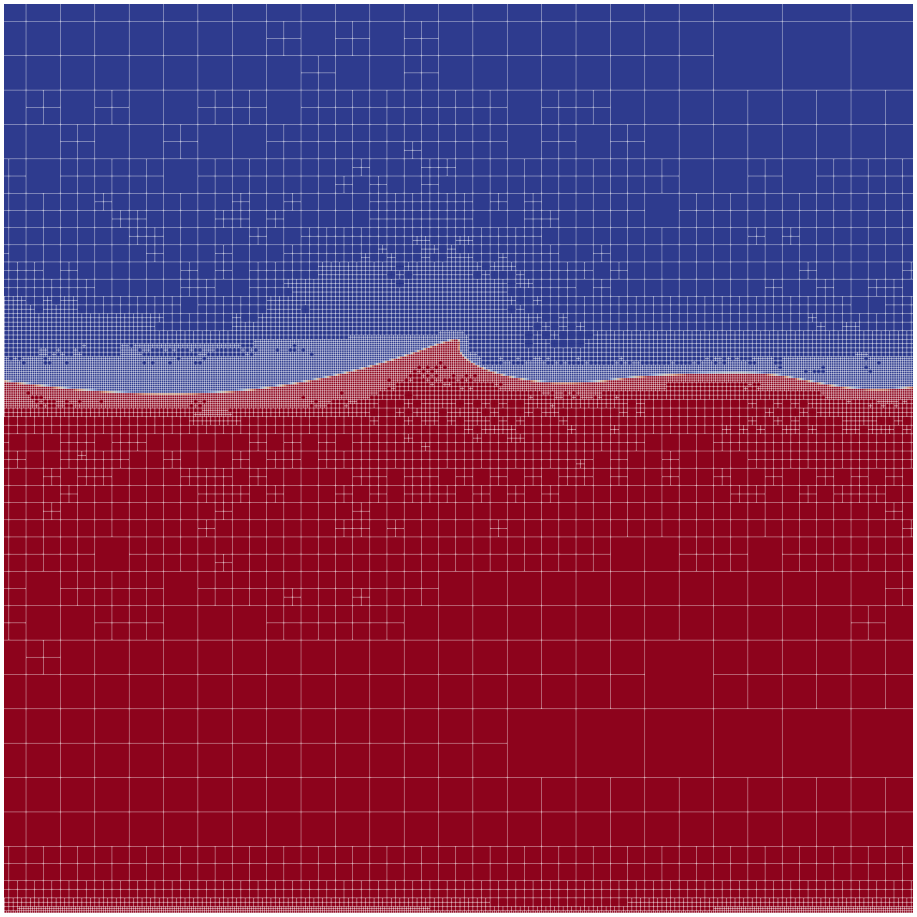


Figure 5.1: A snapshot of the mesh during breaking. The mesh is refined adaptively based on the local error of the velocity and volume fractions. The interface and the bottom boundary is enforced to be at maximum resolution at all time. The maximum resolution of this simulation is $0.0032\lambda_0$, where λ_0 is the carrier wave length.

Case	f_0 **[Hz]**	a_0 **[m]**	$\Delta\omega$ **[rad/s]**	b_F	ψ	ϵ	**Breaking?**
MPW1	1.4	0.051	0.98	0.09	π	0.20	Yes
MPW2	1.5	0.031	1.05	0.06	π	0.14	No
MPW3	1.5	0.055	1.05	0.01	π	0.25	Yes
MPW4	1.6	0.039	1.60	0.05	π	0.20	Yes

Table 5.1: Input parameters for the modulated plane wave cases.

Modulated Plane Waves

We initialise our modulated plane wave case following Eeltink et al. (2022) as

$$\eta(x,0) = a_0\left[\sqrt{b_c}\sin(k_0 x) + \sqrt{b_+}\sin(k_+ x + \psi) + \sqrt{b_-}\sin(k_- x + \psi)\right], \tag{5.18}$$

where the upper and lower sideband frequencies are set according to $\omega_\pm = \omega_0 \pm \Delta\omega$ with $\Delta\omega$ the modulational frequency, and ψ is the phase shift of the sidebands compared to the carrier wave. The sideband wavenumbers $k_\pm$ are calculated using the linear dispersion relationship $\omega_\pm^2 = gk_\pm\tanh(\mathrm{k_\pm d})$. The amplitudes of the carrier wave and the upper and lower sidebands are set according to $a_c = a_0\sqrt{b_c}$, $a_+ = a_0\sqrt{b_+}$ and $a_- = a_0\sqrt{b_-}$, where $b_c = 1 - b_F$, $b_+ = (1 - b_c)/2$, and $b_- = (1 - b_c)/2$, respectively, and b_F is the sideband fraction. The water depth $d = 0.8$ m. In Table 5.1 we list the specific cases we investigate in §5.4.1.

Focused Wave Groups and Random Waves

Focused wave groups and random waves were generated from the JONSWAP (Hasselmann et al., 1973) spectral density $S(\omega)$:

$$S(\omega) = \frac{K_0 g^2}{\omega^5}\exp\left[-\frac{5}{4}\left(\frac{\omega_0}{\omega}\right)^4\right]\gamma^{\mathrm{r}}, \tag{5.19}$$

$$r = \exp\left[-\frac{(\omega-\omega_0)^2}{2\sigma^2\omega_0^2}\right], \tag{5.20}$$

$$\sigma = \begin{cases} 0.07 & \omega \le \omega_0, \\ 0.09 & \omega > \omega_0, \end{cases} \tag{5.21}$$

Case	f_0 [Hz]	H_0 [m]	γ	x_f [m]	Breaking?
FGW1	0.91	0.01	3.30	18	No
FGW2	0.91	0.02	3.30	20	Yes
RDW1	1.11	0.02	3.30	-	No
RDW2	1.11	0.04	3.30	-	Rare
RDW3	1.11	0.06	3.30	-	Mild
RDW4	1.11	0.10	3.30	-	Extreme

Table 5.2: Input parameters for the focused wave groups and random waves based on the JONSWAP spectrum. Cases for which a focussing distance x_f is given correspond to focused wave groups, others to random waves.

where K_0 is a scaling parameter to obtain appropriate wave height by the characteristic height H_0 and g (m/s^2) is the gravitational constant. For focused wave groups, phases are assigned by computing a linear phase shift from a given focussing distance x_f based on linear theory. For random waves, phases are randomised by a fixed random number seed and we follow the approach of Tucker et al. (1984). We recommend Eeltink et al. (2022)'s article for further details. In Table 5.2 we list the focused wave group and the random wave cases that we investigate in §5.4.1.

The parameters for the randomly sampled focused wave group cases in §5.4.2 are drawn from the following ranges: $\gamma \in [2, 5]$, $H_0 \in [0.01, 0.06]$ m, $f_0 \in [0.5, 1.25]$ Hz, and $x_f \in [10, 24]$ m.

5.2.5 Numerical Configuration

Numerical Domain

We use two types of domains:

1. a non-periodic domain with wave inlet and zero-gradient outlet for comparison to experimental measurements in §5.4.1, the depth of the water is 0.8 m;

2. a periodic domain for focused wave group simulations with randomly sampled parameters in §5.4.2.

We keep all parameters the same between domains in order to maintain consistency between periodic and non-periodic simulations. The non-periodic simulation is for

validation purposes only, and wherever a non-periodic domain is applied instead of its periodic counterpart, we will highlight this.

The periodic domain spans [-26, 26]λ_0 horizontally, where λ_0 is the length of the carrier wave or the spectral peak calculated by the linear dispersion relation $\omega_0^2 = k_0 g \tanh(k_0 d)$. The depth of the water d is determined by $k_0 d = 5$, so that the water is considered to be deep. We use a square 2D domain, spanning $[-d, 52\lambda_0 - d]$ vertically. We only perform 2D simulations. By default, we restrict the Courant–Friedrichs–Lewy (CFL) number of the simulation to 0.1.

For the non-periodic domain, we use linear wave theory to determine the surface elevation η and the velocity vector $\mathbf{u}$ at the input boundary. We apply a Fourier Transform to decompose the measured surface elevation profile $\eta(t)$ at the first gauge in the experiment to obtain the amplitude and phase of the wave components. Then we compute the surface elevation and velocity vector using linear wave theory. We note that the error of linear wave theory increases rapidly when the input wave becomes steeper, and such a wave inlet boundary should be used with care. The non-periodic domain spans $52\lambda_0$ in the horizontal direction, and the wave inlet boundary aligns with the first gauge in the experiment.

We apply a zero-gradient condition for the top boundary and a no-slip condition for the bottom boundary. For the bottom boundary, we apply the Dirichlet condition for both $\varkappa$ and ω on a wall recommended in Menter (1993):

$$\varkappa_{\text{wall}} = 0, \tag{5.22}$$

$$\omega_{\text{wall}} = 10\frac{6\mu}{\rho\beta_0(\Delta x)^2}. \tag{5.23}$$

To properly resolve ω near the bottom boundary, we enforce the resolution at the bottom boundary to the maximum (see Figure 5.1).

The computational domain is always mapped via an affine transformation to the unit square $[0,1] \times [0,1]$ in $\mathcal{R}^2$. The refinement level L is defined as the number of subdivisions needed to reach the given cell starting from the unit square. By default, we set the grid refinement level in all simulations to $L = 14$, and we use

three levels of refinement $L = 14, 15, 16$ to verify the convergence of the simulation. The corresponding grid width is calculated as $\Delta x = L_0/2^L$ where L_0 is the width of the computation domain. The impact of the maximum refinement level to the solution will be examined in §5.3. Through a validation study, we find the minimum resolution required for our breaking wave study is $L = 14$. This will be a default setting in §5.4.

Characterising Wave Breaking

In order to perform simulations for which energy dissipation has converged (and numerical dissipation is thus negligible), the minimum length and time scales that need to be resolved must be determined in advance. Energy dissipation can be thought of as having two components: the effect of viscosity outside of wave breaking and dissipation during wave breaking. We aim at minimising viscous dissipation outside of wave breaking, because even in the laboratory-scale system, dissipation due to viscosity is insignificant as the Reynolds number of the system is of the order of 10^7. We do not model side-wall dissipation. To align with the experimental data, we will run the RANS simulations with Reynolds numbers as high as possible. In doing so, the aim is for viscous dissipation to be negligible outside of wave breaking, and dissipation due to breaking to dominate the energy evolution.

Wave-breaking dissipation is a highly non-linear process with different physical mechanisms coupled strongly with each other. To simplify the discussion, we follow Babanin (2011) and split the process into two effects that contribute to the energy dissipation involved in breaking:

1. instant, transient (occuring within one wave period) breaking dissipation due to the mechanical failure of the breaking crest and bubble dynamics, and;

2. delayed, persistent dissipation (spans several wave periods) due to the turbulence formed during breaking.

To resolve the first effect, we choose the finest grid resolution near the wave surface to be close to the settings of the Mostert et al. (2022)'s DNS simulation in order

to resolve the evolution of the breaking crest, and we verify the convergence of our simulation by comparing the crest shape at breaking onset under different resolutions. To resolve the second effect, we use the RANS model to approximate the dissipation caused by the underwater turbulence formed during breaking.

The Reynolds number of the simulation is bounded by the maximum resolution that can be achieved with the available computational resources. Wave Reynolds number is defined as (e.g., Mostert et al. (2022)):

$$\mathrm{Re} = \frac{\sqrt{g\lambda_0^3}}{\nu}, \tag{5.24}$$

where $g = 9.81\mathrm{m/s}^2$ is gravitational constant, λ_0 is carrier wavelength and ν is molecular viscosity. In previous studies, values of the wave Reynolds number of $\mathrm{Re} = 4 \times 10^4, 1 \times 10^5$ have been achieved in DNS simulations (Iafrati, 2009; Deike et al., 2017; Mostert et al., 2022). In this study, we run Stokes wave simulations with multiple Re numbers in §5.3 and we fix Re = 1,000,000 for all the simulations discussed in §5.4. We emphasise that such a range of Reynolds numbers is not reachable with fully resolved DNS at the present time.

We approximate the thickness of the viscous boundary layer to be $\delta = \sqrt{2\nu/\omega_0}$ where ω_0 is the angular velocity of the carrier wave (Longuet-Higgins, 1953).

The wave energy budget is made up of kinetic energy E_k and potential energy E_p. The energy budget together with its energy dissipation over time $E_d(t)$ due to molecular viscousity are obtained by integrating over the water phase (e.g., Mostert and Deike (2020)):

$$E_k = \frac{1}{2}\int_\Omega \rho_w(\mathbf{u}\cdot\mathbf{u}/2)\mathrm{d}\Omega, \tag{5.25}$$

$$E_p = \int_\Omega \rho_w g h \mathrm{d}\Omega - E_{p,0}, \tag{5.26}$$

$$E_d(t) = \int_0^t \int_\Omega \mu \frac{\partial u_i}{\partial x_j}\frac{\partial u_j}{\partial x_i}\mathrm{d}\Omega\mathrm{d}t', \tag{5.27}$$

where Ω indicates the water domain, u, v are horizontal and vertical velocity, ρ_w is the water density, h is the height of a water element with respect to a reference

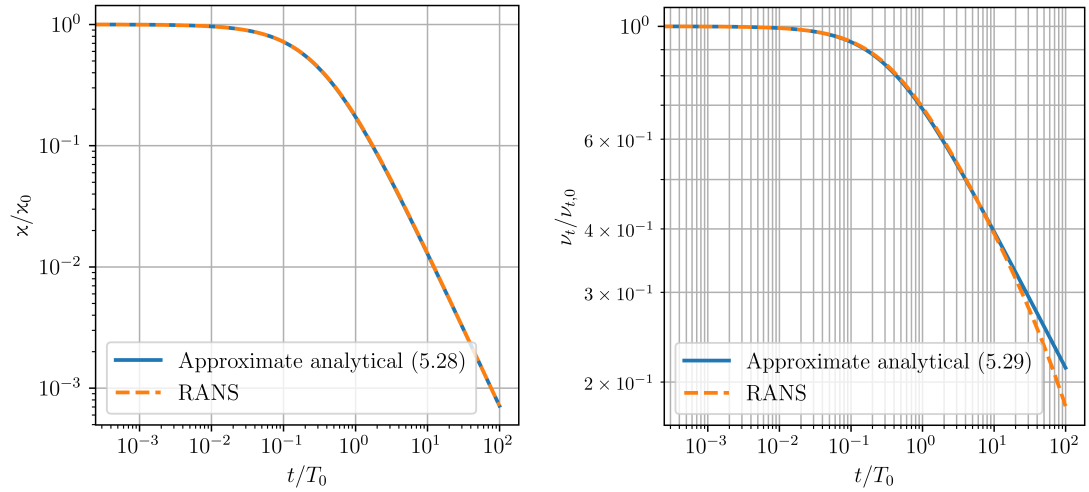


Figure 5.2: Validation of the RANS turbulence model, showing the evolution of TKE and turbulent eddy viscosity of a Stokes wave and comparing the approximate analytical solution of decaying turbulence, eqns. (5.28) and (5.29), in still water and RANS simulations.

level, and $E_{p,0}$ is the potential energy of still water with respect to the same level. The total energy budget $E_t = E_k + E_p + E_d$.

5.3 Validation of the RANS Turbulence Model

5.3.1 Non-Breaking Stokes Waves

To validate the model, we perform simulations of a non-breaking Stokes wave with different Reynolds numbers and examine energy conservation. We initialise the wave field with a third-order Stokes wave of amplitude a_0 and wavenumber k_0, setting the wave length $\lambda_0 = 2\pi/k_0 = 1.56$ m, the period $T_0 = 1$ s and steepness $\epsilon = a_0 k_0 = 0.02$. The domain spans $[-\lambda_0, \lambda_0]$ in both horizontal and vertical directions. The simulation lasts $100T_0$. We set Re = 60,000, CFL = 0.1 and $\Delta x/\delta = 4$, where $\delta = \sqrt{2\nu/\omega_0}$.

In Figure 5.2 we plot the integrated TKE and the turbulent eddy viscosity ν_t in the water phase and compare them to an approximate analytical solution for the decaying turbulence in still water. In still water, a reduced $\varkappa-\omega$ model with only the unsteady, production and dissipation terms preserved leads to following analytical

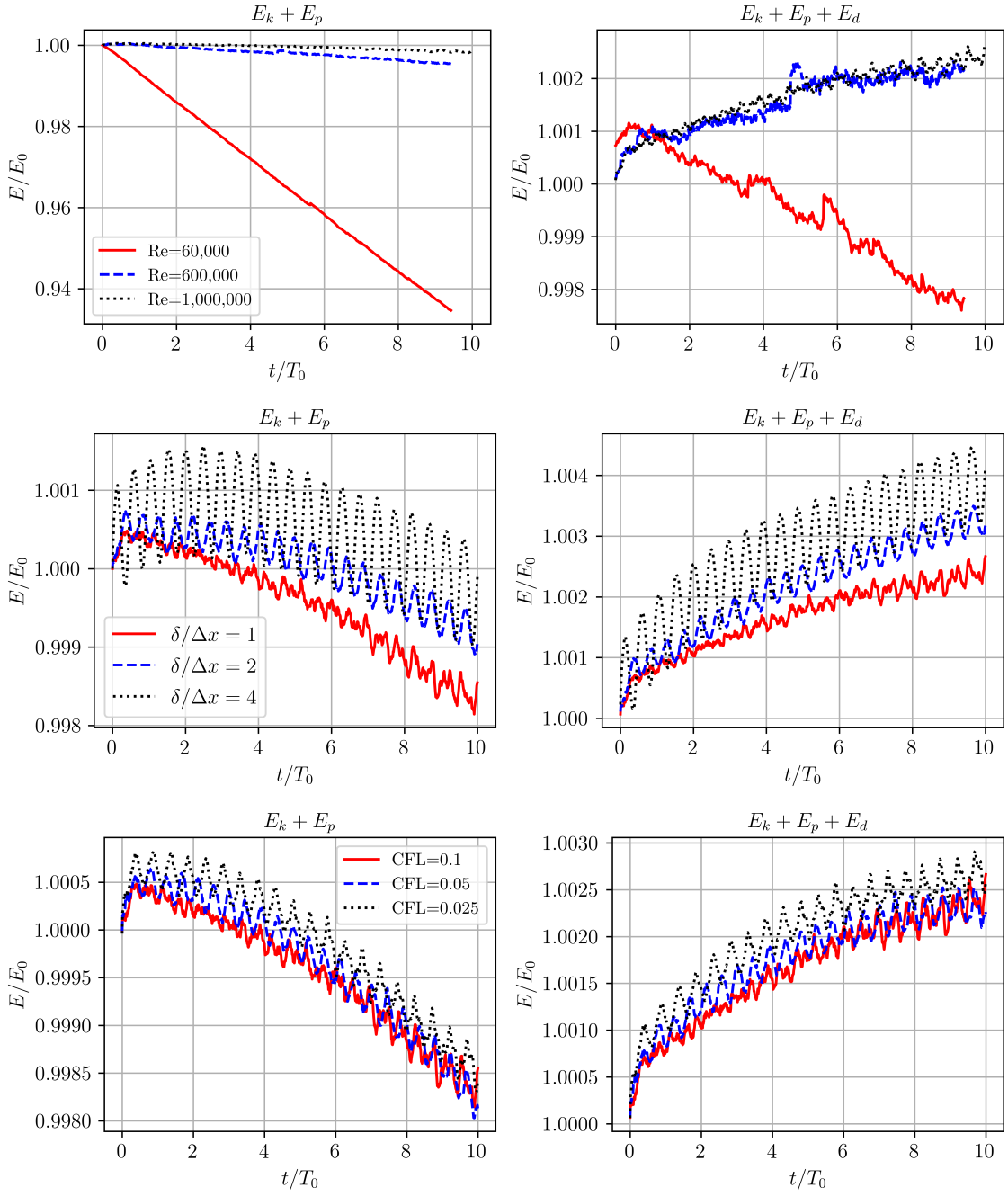


Figure 5.3: Validation of the RANS turbulence model, showing the energy budget for a Stokes wave. Top panels compare the energy budget for three different Reynolds numbers, Re = 60,000, 600,000, 1,000,000. Middle panels display the energy budget for Re = 1,000,000 with different grid resolutions, $\delta/\Delta x = 1, 2, 4$, where δ is the boundary layer thickness. Bottom panels plot the energy budget for Re = 1,000,000 with CFL numbers CFL = 0.025, 0.05 and 0.1. In all panels, E_k, E_p and $E_d(t)$ are kinetic energy, potential energy and viscous dissipation integrated over the water phase and the time, respectively.

solution (Pope, 2000):

$$\varkappa = \varkappa_0 \left(1 + \beta\omega_0 t\right)^{-\frac{\beta^*}{\beta}}, \tag{5.28}$$

$$\nu_t = \frac{\varkappa_0}{\omega_0} \left(1 + \beta\omega_0 t\right)^{1-\frac{\beta^*}{\beta}}, \tag{5.29}$$

where $\varkappa_0$, ω_0 are the initial condition for $\varkappa$ and ω. For the standard $\varkappa - \omega$ model, the TKE grows to become unbounded under the perturbation of potential-flow surface waves (Larsen et al., 2020), but for the stabilised $\varkappa - \omega$ model, no unbounded TKE growth is observed. The decaying TKE and ν_t match the analytical solution in Figure 5.2.

In Figure 5.3 we study the convergence of the wave energy budget by comparing different Reynolds numbers, maximum resolutions, and CFL numbers. In the top left panel we compare the energy budget for different Reynolds numbers. For Re = 60,000, 5% of the total energy is dissipated throughout the simulation. When an estimate of how much energy should have been dissipated is added back (top right panel), only 0.2% of the total energy is lost due to numerical dissipation, showing good convergence of the energy budget. For Re = 600,000, the energy dissipation shows a similar trend, but the amount of dissipation is much smaller. Adding an estimate of viscous dissipation leads to convergence at the level of 0.2%. For Re = 1,000,000, energy is nearly conserved. The descrease in energy remains as low as 0.2% over around 10 wave periods.

In the middle panels of Figure 5.3, we compare the energy budget for different grid resolutions. The energy budget for $\delta/\Delta x$ = 1, 2 and 4 agrees well at the level of 0.2%, demonstrating that the energy budget is approximately converged for different resolutions of the viscous boundary layer. Oscillations in the energy budget for $\delta/\Delta x$ = 2 and 4 are caused by the imperfect initial condition and the lack of viscosity. We believe that the oscillations are numerical artefacts that only have marginal influence on convergence. Large ensembles of simulation for machine learning purposes are bounded to the lowest acceptable resolution because of the limited computational resources. Due to the insufficient resolution on wall bound-

ary layer, a wall model for the RANS simulation could perhaps improve the results, but we do not pursue this in current study. In fact, our method should be applied cautiously when training machine learning models that aim to predict the influence of the boundary layer.

In the bottom panels of Figure 5.3, we investigate the influence of the CFL number. We note that the CFL number has a limited impact on the energy convergence at Re = 1,000,000. In the bottom right panel, it becomes evident that the CFL number affects the amount of numerical dissipation. The smaller the CFL number, the more numerical dissipation introduced into the simulation.

In general, we find that energy conservation is achieved to an acceptable level throughout the simulation; the numerical error can be controlled to be below 1%. We can thus conclude that our implementation of a RANS model in Basilisk should be able to perform high-fidelity simulations for a reasonably large range of Reynolds numbers, given sufficient time and space resolution.

5.3.2 Breaking Focused Wave Group

We also validate to breaking focused wave group cases and compare them to experiments. For non-periodic simulations, waves are introduced at the inlet boundary to reproduce wave-tank experiments. In this scenario, we do not examine volume-integrated energetics, as these quantities fluctuate with the wave group entering and exiting. The space-time plot (Figure 5.4) shows the details of the surface elevation evolution in a RANS simulation for case FGW2. The surface elevation profile $\eta(x,t)$ is shifted by its group speed. At $x \approx$19 m, the wave group experiences focusing and wave breaking event within a short time. On the right side, three distinct panels (5.4b, 5.4c and 5.4d) correspond to the three selected spatial positions (pre-breaking, post-breaking and near-breaking positions) marked on the contour plot. Comparisons on the grid refinement levels $L = 14$, 15 and 16 indicate a good agreement between RANS simulations with different grid resolutions. By default, we use $L = 14$ for all simulations in §5.4.1.

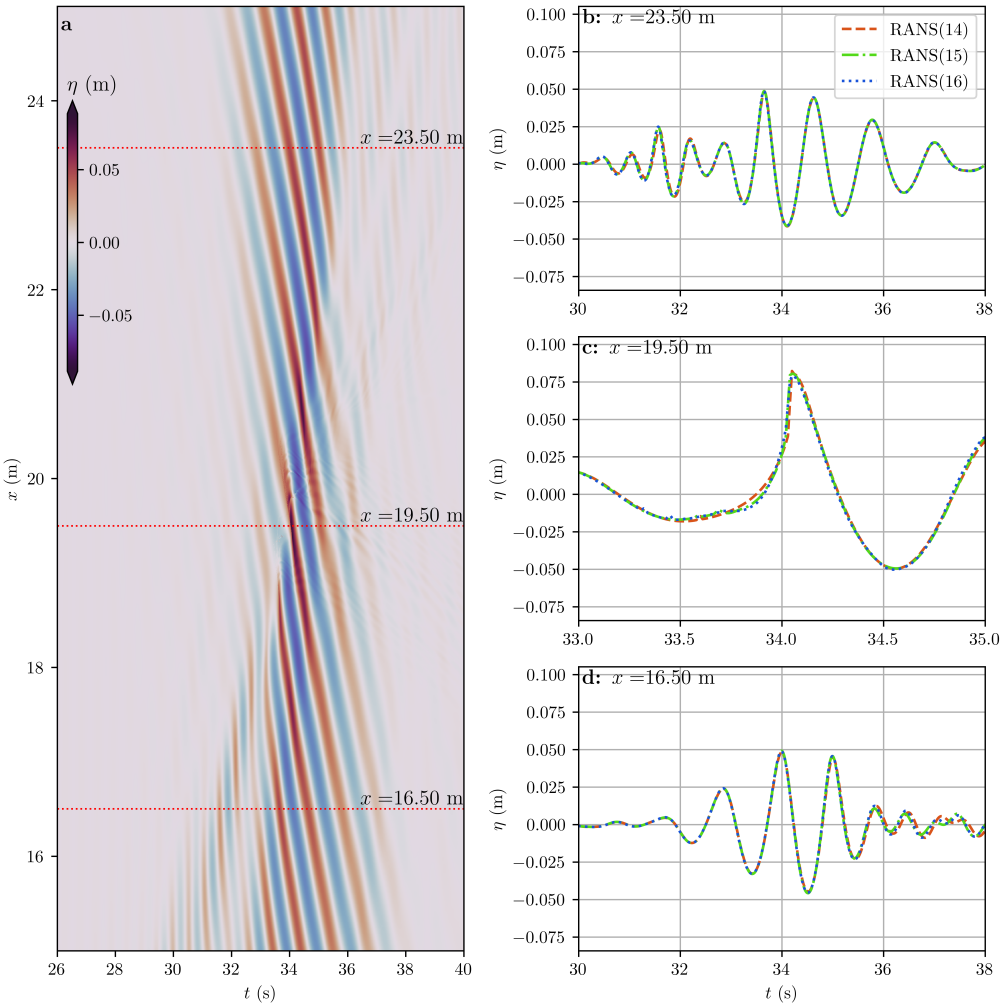


Figure 5.4: This figure contains a space-time plot and wave height profiles at different locations for case FGW2 in Table 5.2. On the left (a), a space-time plot displays the evolution of surface elevation for RANS simulation with maximum refine level L = 14. The red dotted lines indicate the positions of the gauges. The right side contains three separate plots (b–d) at specific x locations (23.50 m, 19.50 m, 16.50 m), comparing the surface elevation over time as predicted by RANS simulations with different maximum refine level. The red dashed line is RANS simulation with maximum refine level L = 14, L = 15 for the green dot-dashed line and L = 16 for the blue dotted line.

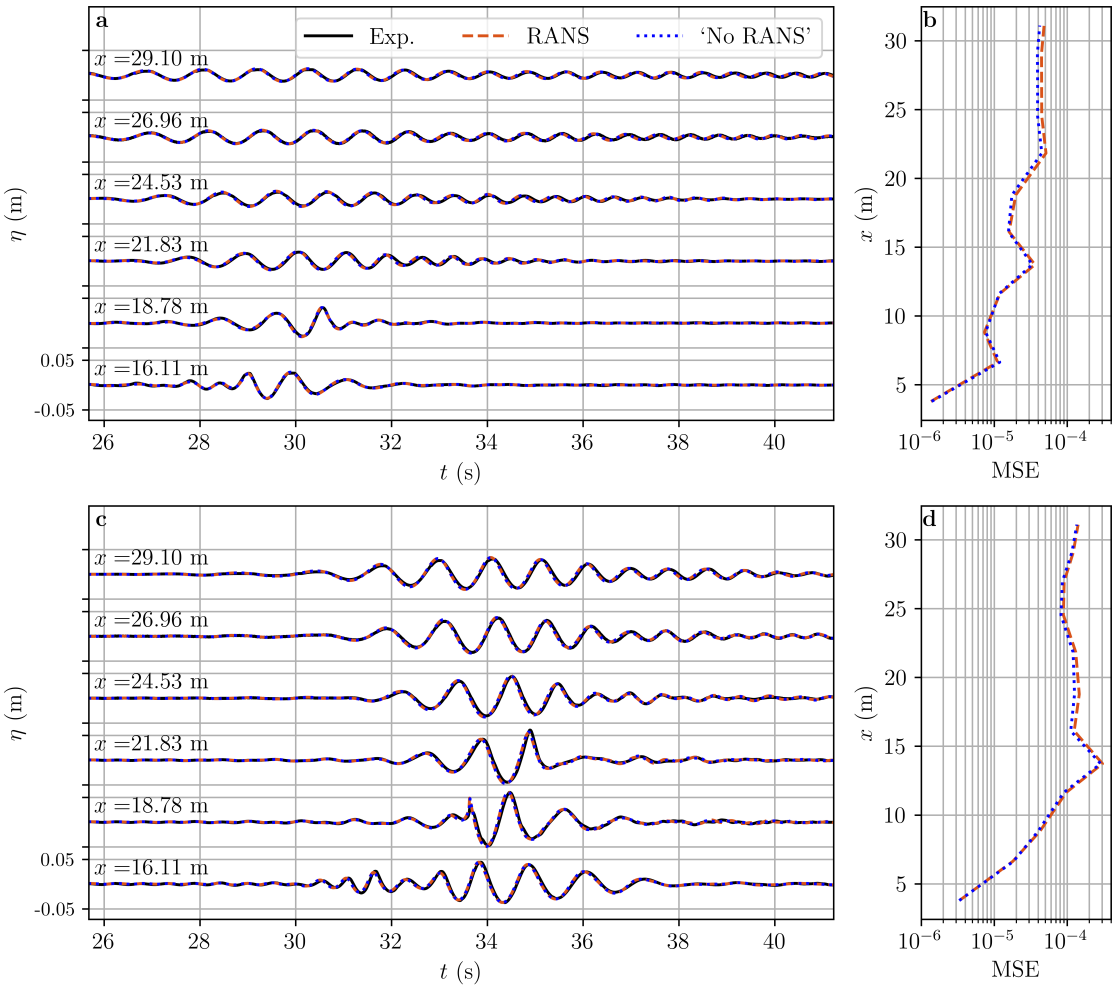


Figure 5.5: This figure plots the surface elevation profiles at multiple gauge positions for all focused wave cases in Table 5.2 and compares the experimental measurements, RANS simulation and 'No RANS' (simulation with turbulence model disabled) at different gauge positions. The top panels (a, b) are for case FGW1 and the bottom panels (c, d) are for case FGW2.

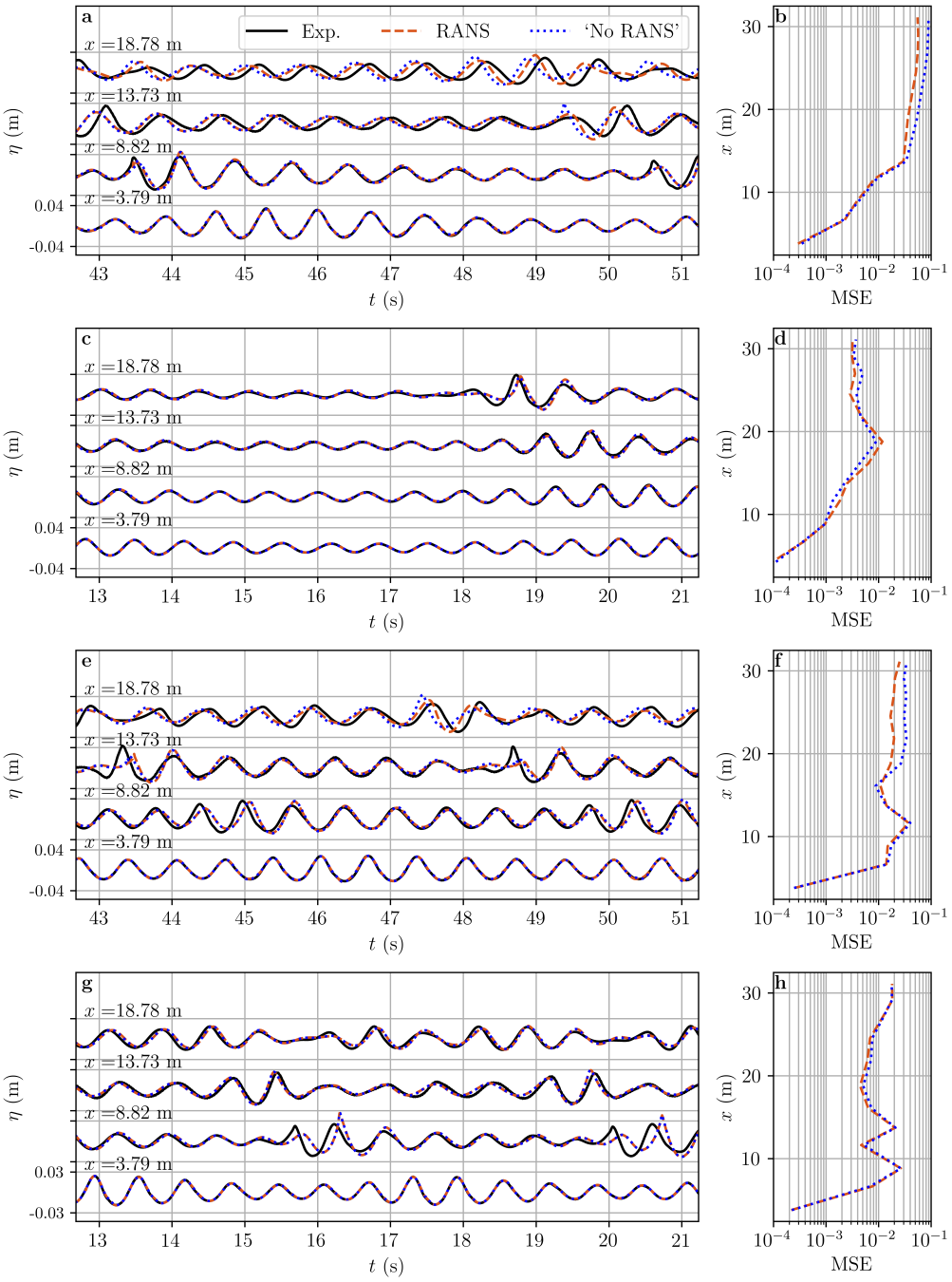


Figure 5.6: This figure plots the surface elevation profiles at multiple gauge positions for all modulated plane wave cases in Table 5.1 and compares the experimental measurements, RANS simulation and 'No RANS' (simulation with turbulence model disabled) at different gauge positions. Panels (a) and (b): case MPW1; Panels (c) and (d): case MPW2; Panels (e) and (f): case MPW3; Panels (g) and (h): case MPW4.

5.4 Numerical Results

In this section, we first reproduce the experiments of Eeltink et al. (2022) listed in Table 5.2. We then compare the RANS simulation and experimental measurements

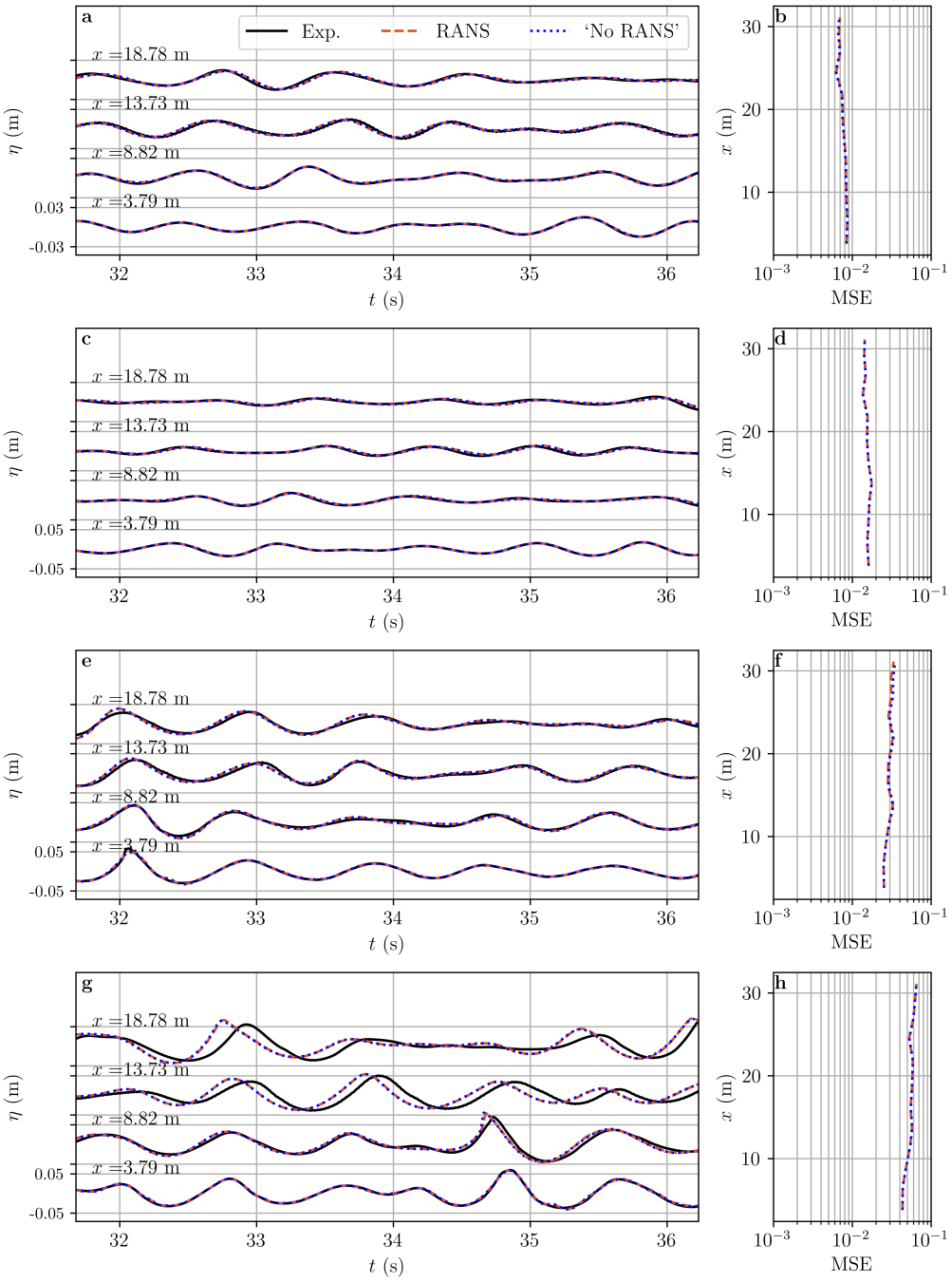


Figure 5.7: This figure plots the surface elevation profiles at multiple gauge positions for all random wave cases in Table 5.2 and compares the experimental measurements, RANS simulation and 'No RANS' (simulation with turbulence model disabled) at different gauge positions. Panels (a) and (b): case RDW1; Panels (c) and (d): case RDW2; Panels (e) and (f): case RDW3; Panels (g) and (h): case RDW4.

to study the confidence level of our RANS method. We also compare with simulation with no turbulence model to demonstrate the effect of RANS model.

5.4.1 Comparison to the Experiments of Eeltink et al. (2022)

To compare with experimental measurements, we apply nonperiodic simulations with wave input from experimental measurements of the elevation profile of the surface on the first gauge (x = 3.79 m). Then we compare the surface elevation profiles measured at gauges located at position 3.79 m, 6.64 m, 8.82 m, 11.63 m, 13.73 m, 16.11 m, 18.78 m, 21.83 m, 24.53 m, 26.96 m, 29.10 m and 31.10 m, with the corresponding experimental measurements.

In Figure 5.5, we compare the surface elevation profile of the RANS simulation with the gauge measurements of the experiment for the two focusing wave group cases listed in Table 5.2. The surface elevation profiles are shifted by its group speed. For case FGW1 (5.5a and 5.5b), there is no breaking event triggered. We find that the RANS simulation predicts surface elevation with satisfactory accuracy when compared to experimental measurements. The MSE is below 10^{-4}, suggesting a perfect match between experiment and RANS simulation. For case FGW2 (5.5c and 5.5d), a breaking event occurs around $x = 18.78$ m, where the surface elevation becomes very steep. The prediction of the RANS simulation for this breaking event is in good agreement with the experimental observation. Although we only show 6 gauges near the breaking position in Figure 5.5, in general we find that the RANS result agrees well with the experimental measurements at all gauges, and the RANS simulation is able to reproduce non-breaking wave evolution accurately. The MSE of case FGW2 starts from 10^{-6}, then grows rapidly during breaking, and ends up somewhere slightly above 10^{-4}. The 10^{-6} MSE level at the beginning indicates that our wave-inlet is able to reproduce the focused wave group input accurately. The rapidly rising MSE level, however, suggesting that the breaking events have potentially significant impact to the accuracy of the RANS simulation. Despite that, 10^{-4} is still a very low MSE level and the post-breaking surface elevation profiles (such as the measurement at x = 29.10 m in Figure 5.5) agrees well with the experimental measurements.

To investigate the performance of RANS simulation in more general scenarios, we further study the RANS simulation of modulated plane wave and random wave. In

Figure 5.6 we display the surface elevation profiles measured in 4 positions (x = 3.79 m, 8.82 m, 13.73 m, 18.78 m) for all 4 cases in Tables 5.1. The surface elevation profiles are shifted by its group speed. For all modulated plane wave cases, we note that the MSE starts from a relatively small value around $\mathcal{O}(10^{-4})$, however, rapidly increases to $\mathcal{O}(10^{-2})$. This is mainly due to the mismatch of the wave breaking events. For case MPW1 (Figure 5.6a), the breaking happens around x = 13.73 m, we find that the steepest crest in the surface elevation profile does not match to the experiment, indicating that the breaking happens in a different crest, or a different time in the simulation. Similar mismatches can be found in case MPW3 (Figure 5.6e) and MPW4 (Figure 5.6g) where the steepest crest does not match the experimental measurement. MSE of case MPW2 (Figure 5.6d) increases slower because waves are shallow and no breaking is triggered.

In Figure 5.6 we display the surface elevation profiles measured in 4 positions (same as the modulated plane wave cases) for all random wave cases listed in Table 5.2. For random wave cases, the MSE scales up quickly with the characteristic wave height H_0 (also the significant wave height for random wave cases). We also find that the MSE starts from $\mathcal{O}(10^{-2})$, indicating that the wave input error is large. For case RDW4 (Figure 5.6g), the simulation deviates a lot from the experimental measurement in the last 2 gauges. We believe this is due to the fact that case RDW4 has an exceedingly high H_0, resulting in frequent and intense breaking that deteriorates the quality of the simulation quickly.

5.4.2 Random Periodic Domain Simulations

Our aim is to perform high Reynolds number energy-resolving RANS simulations in a periodic domain for purpose of generating high quality training data for physics-based neural networks. We have built trust in our numerical setup by examining the Stokes wave simulation. We have shown that the simulation is in agreement with the experiment for cases with a few breaking events by studying the non-periodic wave simulations and comparing them to experimental data. In this section, we apply RANS to study focused wave breaking in the periodic domain.

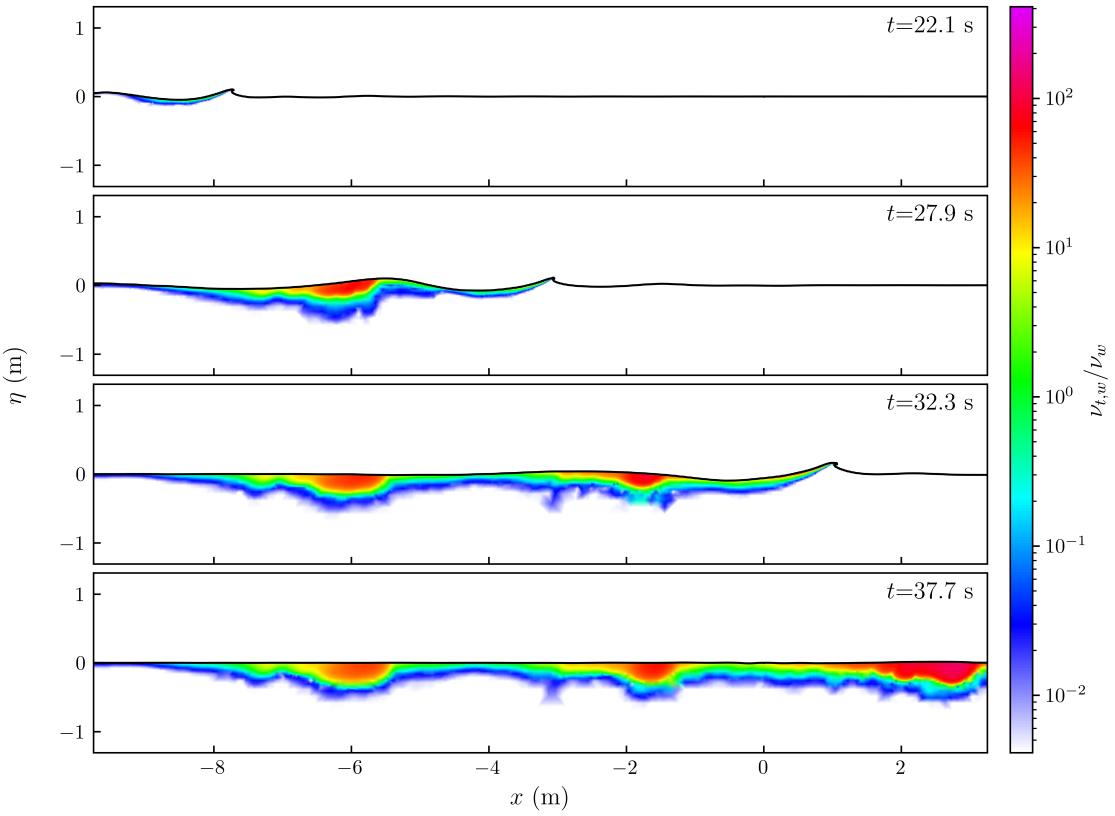


Figure 5.8: The evolution of interface and turbulent visocity $\nu_{t,w}$ in water domain. Waves propagate from left to right, with breakings occurring between snapshots, creating several slowly drifting patches of underwater turbulence.

In Figure 5.8 we plot 4 snapshots of the flow field in one of the periodic simulations of focused wave group cases, showing the evolution of the water-air interface and the turbulent eddy viscosity in the water domain. We find that coherent structures such as overturning crests, jet splashing, and bubble formation during breaking are resolved successfully. Turbulent cores with high turbulent eddy viscosity ($\geq 100\nu_w$) are produced during breaking events. The turbulent cores span around 1 carrier wavelength and have negligible drifting after settling down.

Figure 5.9 shows the evolution of the kinetic energy, the potential energy and the total energy of the simulation. We find that the total energy is well conserved in the nonbreaking interval. The total energy loss during the entire duration is around 2%. The potential energy oscillates slightly because there are subgrid-scale waves brought by the initial condition of surface elevation that interfere with each other.

Figure 5.10 displays the nondimensional energy dissipation parameter b as a

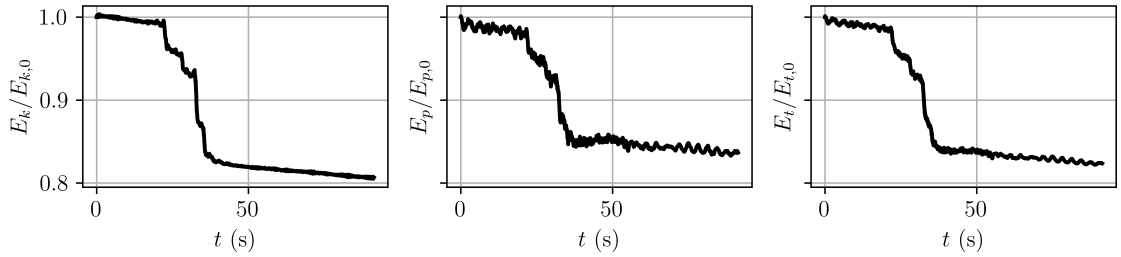


Figure 5.9: This figure plots the evolution of kinetic energy E_k, potential energy E_p and total energy E_t of the periodic RANS simulation of a focused group wave case.

result of breaking when plotted against ϵ, where in focused wave cases we define $\epsilon = \sum_i a_i k_i$ as the max linear slope. We plot randomly generated FGW cases with $\epsilon \in [0.28, 0.38]$ and other parameter ranges provided in §5.2.4. b is calculated with Drazen et al. (2008)'s approach:

$$b = \frac{g^2 c_g \int_{t_1}^{t_2} (\eta_1^2 - \eta_2^2) \mathrm{d}t}{T_b c_b^5}, \tag{5.30}$$

where g is gravitational constant, $c_g = \omega_0/2k_0$ is the carrier group speed, η_1 and η_2 is the surface elevation profile at far upstream and downstream of the breaking event where we assume the wave is not so steep and the equipartition of energy is valid. The control volume in time $t \in [t_1, t_2]$ wraps the wave group so that $\int_{t_1}^{t_2} (\eta_1^2 - \eta_2^2) dt \approx \int_{-\infty}^{+\infty} (\eta_1^2 - \eta_2^2) dt$. The breaking onset is defined as when the local slope η_x exceeds 0.5774 (Babanin, 2011; McAllister et al., 2023), and the active breaking interval T_b is estimated to be $0.5T_0$ (Derakhti et al., 2018). The breaking crest speed c_b is estimated to be 80% of the speed of the carrier phase speed ω_0/k_0 (Barthelemy et al., 2018).

We find that all the present RANS data fall within the range of ±1 standard deviation, giving confidence to the energy dissipation resolved in the RANS simulations. We note that in most cases the measured breaking parameter b is slightly lower than the empirical curve, but the deviation is lower than the uncertainties reported in the previous study of Mostert et al. (2022).

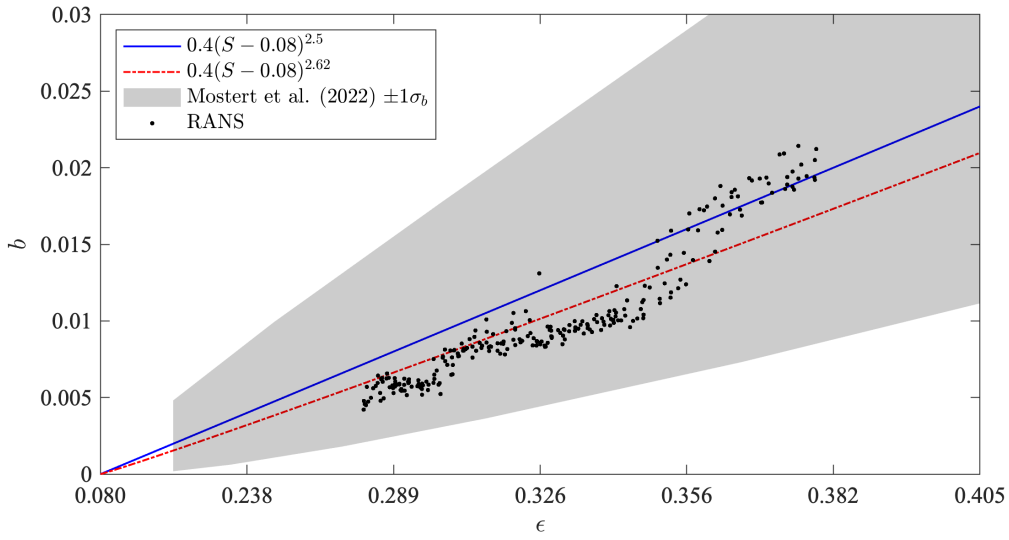


Figure 5.10: This figure plots breaking parameter b against the max linear slope ϵ. Blue solid line is a semi-empirical formula (Romero et al., 2012). Red dot-dashed line is an exponential fit $b = 0.4(\epsilon - 0.08)^q$ to the RANS data where $q = 2.62$. Grey shaded region is standard deviation $\pm 1\sigma_b$ on the scaling for b. Black dots indicates calculated parameter b of RANS data.

5.5 Conclusions

This chapter utilised RANS simulation with Basilisk to study the deep water wave breaking problem. We validated the numerical configurations with Stokes wave simulation. We then used the RANS model to simulate wave breaking in focused wave groups, modulated plane waves, and random waves with JONSWAP spectrum. The RANS simulation was found to be in agreement with the gauge measurements from the experiment. Additionally, we applied the RANS simulation to perform a large number of focused wave group simulations in the periodic domain. We discovered that the energy was nearly conserved in the nonbreaking region. We also studied the breaking parameter b, showing that the breaking parameter in our simulation agrees well with previous studies.

By verifying the RANS model, we can take advantage of the limitation of the Reynolds number. Compared to the traditional DNS approach used in Basilisk, which is limited to a Reynolds number of $\mathcal{O}(10^4)$, RANS simulations can be conducted in a much broader range, from $\mathcal{O}(10^4)$ to $\mathcal{O}(10^7)$. This enables us to simulate a system on a laboratory scale with reasonable computational resources. Our sim-

ulations are sufficiently computationally efficient to be used for the generation of large ensembles for machine-learning purposes in future work.

Chapter 6

Using machine learning based on RANS to model deep-water wave breaking in envelope-type wave models

Abstract

Wave breaking is a complex turbulent process that will remain too computationally demanding to resolve routinely in numerical simulations of ocean waves for the foreseeable future. Including breaking effects in phase-resolved envelope-based wave models, such as those based on the nonlinear Schrödinger equation, is crucial for certain applications, including forecasting. A potential strategy is to employ machine learning to capture these effects. In this study, we have trained a neural network to provide dense spatial predictions of breaking waves by utilising a dataset based on Reynolds-Averaged Numerical Simulation (RANS) as the reference. Our results demonstrate that the model, integrated into a fast NLS equation-based framework, achieves accurate and efficient results in forecasting both the phase and the amplitude of the breaking waves. The model also generalises to unseen wave conditions, paving the way towards a universal wave-breaking surrogate model in NLS-based

wave equations.

6.1 Introduction

Wave breaking has garnered significant attention from scientists and engineers due to its complex dynamics in the ocean. This phenomenon is crucial for shaping the surface properties of ocean (Babanin, 2011), regulating wave height, steepness and energy (Hasselmann, 1974). It also supports essential processes such as the dispersion of pollutants (Van Sebille et al., 2020), air-sea interactions (Melville, 1996; Banner and Peirson, 2007; Deike, 2022), ocean mixing (Melville et al., 1998), and the evolution of short-term wave statistics (Toffoli et al., 2010b). Despite its importance, the complex and unpredictable nature of wave breaking continues to challenge our ability to model and predict these interactions, revealing significant gaps in our scientific knowledge (Duncan, 2001).

Traditional approaches to modelling wave dynamics, notably potential-flow models and, in particular, envelope-type apporoximations of potential flow, such as the nonlinear Schrödinger equation (NLS) (Zakharov, 1972), the modified nonlinear Schrödinger equation (MNLS) (Dysthe, 1979) or its variants (Trulsen and Dysthe, 1996; Trulsen et al., 2000; Dysthe and Trulsen, 2001) are accurate models of non-breaking waves. However, these do not capture wave breaking. Various models have been considered, as discussed in Liu et al. (2023), to model wave breaking in envelope models. Our aim in the present chapter is to improve on these.

Direct numerical simulation of the breaking wave evolution is typically limited by computational demands. Resolving all the scales from energy-containing eddies, down to the viscous dissipation range, requires very high mesh resolution. Direct numerical simulation can only operate with a low Reynolds number to constrain the range of the physical scales (Deike, 2022; Mostert et al., 2022). Reynolds-averaged numerical simulation (RANS) can, to some extent, model turbulence induced by breaking waves. However, two equation RANS models like $\varkappa - \varepsilon$ or $\varkappa - \omega$ (Wilcox, 2006) have been shown by researchers to be subject to unphysical behaviour in the

near potential flow (Mayer and Madsen, 2001; Larsen and Fuhrman, 2018), resulting in an overpredict of the production of turbulence kinetic energy (Lin and Liu, 1998; Bradford, 2000; Xie, 2013; Zhang et al., 2014; López et al., 2014; Derakhti and Kirby, 2014; Colombo and Fairweather, 2015). Larsen and Fuhrman (2018) proposed a stabilised $\varkappa-\omega$ model and applied it to the surf zone wave breaking study (Ting and Kirby, 1994).

In this study, we integrate machine learning (ML) techniques into the MNLS to model wave breaking. We use a neural network model to capture the highly nonlinear process. Researchers have applied neural network models to accelerate fluid simulation (Kochkov et al., 2021; Deo et al., 2023) and predict nonlinear wave evolution (Qi and Majda, 2020; Eeltink et al., 2022) or ocean wave field statistics (Fan et al., 2020; Choi et al., 2020; Manucharyan et al., 2021). Building on the successful application of ML in wave breaking by Eeltink et al. (2022) we seek to generalise their results using a machine learning architecture which can handle the continuous wave breaking process rather than just capture the coarse influence of breaking which can be found in experiments.

To facilitate this, we have developed a methodical approach to generate relevant training data from high-fidelity (validated against experiments) RANS simulations of breaking waves, to collect dense space-time data required by the model (see Chapter 5). We do not use gauge measurements in experiments to train this model because they are sparsely distributed in space. We examine three types of wave conditions that cover a variety of spectral shapes, bandwidths, and phase alignments. The dataset is divided into training, cross-validation, and test subsets. The training and cross-validation subsets are solely composed of breaking focused wave group cases (Wave type I) which have been shown in a previous study to be sufficient to train models (Liu et al., 2024c). We include modulated plane waves (Wave type II) and random waves (Wave type III) in the testset to study the generalisability of the machine learning model.

We study wave parameter spaces for all types of waves that are similar to those adopted in Eeltink et al. (2022) because they are apposite to the real ocean con-

ditions (Shemer et al., 2010). We train the neural network using the RANS-based breaking focused wave group dataset mentioned above, that we designate as 'ground truth'. We then test the trained neural network model with breaking focused wave group cases (Wave type I), modulated plane waves (Wave type II) and random waves (Wave type III). Key to the framework developed is the convolutional-recurrent neural network architecture. Specifically, we employ a ConvLSTM (Shi et al., 2015) structure to build a convolutional model, enabling the model to learn and predict wave breaking process locally, instead of a fully-connected architecture as in Eeltink et al. (2022). In contrast to Eeltink et al. (2022) where models must be trained separately to predict each wave type, our model, by design, will be able to learn from a small set of breaking focused wave group cases and generalise better to unseen wave types. Our study implements 'Infinitesimal-Domain Machine Learning' by employing a recurrent architecture to apply correction per step, rather than 'Finite-Domain Machine Learning'—batch corrections for multiple steps at once—as was proposed in Eeltink et al. (2022).

6.2 Methods

The primary model utilised in this study is the MNLS equation as introduced by Trulsen et al. (2000). This equation accurately solves the linear component of the envelope evolution and provides an approximation of the weak nonlinearity, presuming that the waves are narrowbanded. In our investigation, we consider a fluid of significant depth, although not of infinite depth, thereby incorporating finite depth in the linear dispersion relation and in the return current. However, the coefficients of the nonlinear terms are minimally affected by depth within the specified range (Barratt et al., 2021).

6.2.1 Envelope-Based Evolution Equation

We solve the normalized MNLS equation introduced in Chapter 4, using the same normalization approach as described in Section 4.3.

The first-order surface elevation is obtained by shifting the complex envelope to the carrier frequency and taking the real part:

$$\eta = \mathrm{Re}\left(Be^{i(k_0x-\omega_0t)}\right). \tag{6.1}$$

The second-order super-harmonic wave is (Toffoli et al., 2010b; Adcock and Taylor, 2016a):

$$\eta_{2+} = \mathrm{Re}\left(\left[\frac{k_0B^2}{2} - \frac{iB}{2}\frac{\partial B}{\partial x}\right]e^{2i(k_0x-\omega_0t)}\right). \tag{6.2}$$

6.2.2 Initial Conditions for the MNLS Simulations

We perform simulations for 3 types of wave conditions:

- **Type I:** Focused wave group;
- **Type II:** Modulated plane wave;
- **Type III:** Random waves.

We take the similar sets of parameters from laboratory experiments on wave breaking for all types of waves (Eeltink et al., 2022) and give a brief review as follows:

- **Focused wave groups (Type I) and random waves (Type III):** We generate focused wave groups and random waves using the dimensional form of the Joint–North–Sea–Wave–Project (JONSWAP) spectrum $S(\omega)$ (Hasselmann et al., 1973):

$$S(\omega) = \frac{K_s g^2}{\omega^5}\exp\left[-\frac{5}{4}\left(\frac{\omega_0}{\omega}\right)^4\right]\gamma^r, \tag{6.3}$$

$$r = \exp\left[-\frac{(\omega-\omega_0)^2}{2\sigma^2\omega_0^2}\right], \tag{6.4}$$

$$\sigma = \begin{cases} 0.07 & \omega \le \omega_0, \\ 0.06\sigma_s & \omega > \omega_0, \end{cases} \tag{6.5}$$

  where K_s is a scaling parameter to obtain appropriate initial wave amplitude a_0. All variables in (6.3)–(6.5) are dimensional. For focused wave groups,

phases are assigned by computing a linear phase shifting from a given focussing distance L_f based on linear theory. For random waves, the amplitudes are derived from the JONSWAP spectrum, and the phases are randomised by a fixed random number seed (Tucker et al., 1984). As the final step, the generated surface elevation is non-dimensionalised. The parameters for the focused wave group and random wave cases are drawn from the following ranges: $\gamma \in [2, 5]$, $a_0 \in [10, 60]$ mm, $f_0 \in [0.5, 1.25]$ Hz, $L_f \in [10, 24]$ m and $\sigma_s \in [1.5, 4]$.

- **Modulated plane wave (Type II):** We initialise our modulated plane wave case according to Eeltink et al. (2022) as:

$$\eta(x,0) = a_0\left[\sqrt{b_c}\sin(k_0 x) + \sqrt{b_+}\sin(k_+ x + \psi) + \sqrt{b_-}\sin(k_- x + \psi)\right], \qquad (6.6)$$

where the upper and lower sideband frequencies are set according to $\omega_\pm = \omega_0 \pm \Delta\omega$ with $\Delta\omega$ the modulational frequency, and ψ is the phase shift of the sidebands compared to the carrier wave. Sideband wave numbers $k_\pm$ are calculated using the linear dispersion relationship $\omega_\pm^2 = gk_\pm \tanh(\mathrm{k_\pm d})$. The amplitudes of the carrier wave and the upper and lower sidebands are set according to $a_c = a_0\sqrt{b_c}$, $a_+ = a_0\sqrt{b_+}$, and $a_- = a_0\sqrt{b_-}$, where $b_c = 1 - b_F$, $b_+ = (1 - b_c - \alpha)/2$, and $b_- = (1 - b_c + \alpha)/2$, respectively, and b_F is the sideband fraction. All variables in (6.6) are dimensional. The parameters are drawn randomly from the following ranges: $f_0 = \omega_0/(2\pi) \in [1.30, 1.55]$ Hz, $a_0 k_0 \in [0.12, 0.20]$, $b_F \in [0.01, 0.1]$, $\Delta\omega \in [0.7, 1.55]$ rad/s, $\psi \in [0, 2\pi]$ and $\alpha \in$ [-0.16, 0.16].

6.2.3 Simulation Settings

We perform non-dimensional MNLS simulations to time-march the wave evolution. We use a 1D uniform mesh as our computational domain. The length of the computing domain spans $[-40L_0, 40L_0]$ in the direction of wave propagation, and the resolution in space is $0.15625L_0$. The computational domain is periodic in the hor-

izontal direction. The duration of the simulation is $100T_0$ and the time resolution is $\tau = 0.125T_0$. We set $k_0 d$ to 5 for all cases in this study. Different resolutions in space and time, as well as different configurations, do not lead to qualitative changes in the result.

6.2.4 Nerual Network Model

We introduce a convolution-recurrent neural network architecture (Shi et al., 2015) to approximate the breaking dissipation term D in MNLS simulation:

$$D \approx D_{\mathrm{NN}}(\xi; \theta), \tag{6.7}$$

where $\xi = [B(t), H(t), C(t)]$ is the auxiliary flow states at time t, θ is the trainable parameters, B is the complex envelope by (4.4), H, C are the hidden state and cell state of the neural network, respectively. Periodic boundary condition in space is embedded into the input B and hidden state tensor H. Figure 6.1 shows the diagram of the computation model. The model consists of a ConvLSTM layer with 64 filters, each having a width of 9, and two Conv1D layers with 128 and 2 filters, respectively, each having a width of 1. We adopt 'hard-sigmoid' ((6.8)) as the activation function and tanh function as the recurrent activation of the ConvLSTM layer. The definition of 'hard-sigmoid' function is:

$$\mathrm{Hardsigmoid}(x) = \begin{cases} 0 & \text{if } x \le -3, \\ 1 & \text{if } x \ge 3, \\ \frac{x}{6} + \frac{1}{2} & \text{otherwise.} \end{cases} \tag{6.8}$$

Therefore, our aim is to model breaking as a per-step correction that takes place throughout the actual duration of the event. This differs from the earlier study by Eeltink et al. (2022) in which the correction is applied to multiple time steps at once.

The model is trained with the complex envelope B as input and a per-step

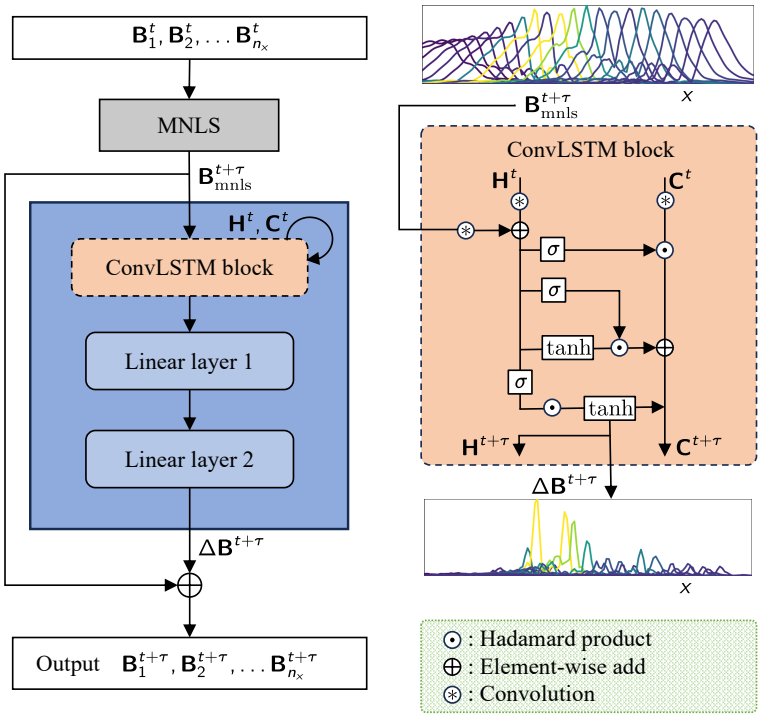


Figure 6.1: **Schematic of the structure and computing diagram of the neural network model.**

difference ΔB as target. We use Mean Squared Error (MSE) as loss function:

$$J(\beta) = \frac{1}{N n_x n_t} \sum_{k=1}^{N} \sum_{j=1}^{n_t} \sum_{i=1}^{n_x} (\Delta B_{pred} - \Delta B_{true})^2, \tag{6.9}$$

where N, n_x, n_t is the number of cases, grid number in space and time respectively. We minimise the MSE loss in physical space and Fourier space simultaneously. (In our case, the MSE loss in physical space and Fourier space is identical.) We use MSE, Normalised Mean Squared Error (NMSE) and Normalised Mean Absolute Error (NMAE) as metrics to evaluate the performance of the model:

$$\text{MSE}(t) = \frac{1}{N} \sum_{k=1}^{N} \left[\sum_{i=1}^{n_x} |\eta_{\text{pred}}(t) - \eta_{\text{true}}(t)|^2 \right], \tag{6.10}$$

$$\text{NMSE}(t) = \frac{1}{N} \sum_{k=1}^{N} \left[\sum_{i=1}^{n_x} |\eta_{\text{pred}}(t) - \eta_{\text{true}}(t)|^2 / \sum_{i=1}^{n_x} |\eta_{\text{true}}(t)|^2 \right], \tag{6.11}$$

$$\text{NMAE}(t) = \frac{1}{N} \sum_{k=1}^{N} \left[\sum_{i=1}^{n_x} |\eta_{\text{pred}}(t) - \eta_{\text{true}}(t)| / \sum_{i=1}^{n_x} |\eta_{\text{true}}(t)| \right]. \tag{6.12}$$

6.2.5 Data Preparation and Training Strategy

For training and evaluation purposes, we have built a RANS-based wave breaking dataset with 'Basilisk' (Popinet, 2015), which we designate as the 'ground truth'. This dataset comprises 993 focused wave cases, partitioned into 893 for training, 50 for validation, and 50 for testing. We have also simulated 20 modulated plane wave test cases and 20 random wave test cases to investigate the generalisability of the model. Modulated plane wave cases and random wave cases do not participate in the training and cross-validation stage. We do not follow strictly to the train-test-partition-ratio here because the RANS-based simulations are very expensive and we have limited computational resources. Parameter selection adheres to a uniform distribution in a range relevant to ocean waves introduced in §6.2.2. The 'wave Reynolds number' Re = $\sqrt{gk_0^3}/\nu$ (ν is molecular viscousity) (Mostert et al., 2022) is fixed to 10^6 to reduce the potential influence of viscous dissipation.

Our training dataset comprises input and output fields. Initially, we perform the RANS simulation to obtain fully nonlinear surface elevation profile $\eta_{\mathrm{nonl}}(x,t)$ as the ground truth. Subsequently, data preprocessing (see Appendix D.4) is applied to convert $\eta_{\mathrm{nonl}}(x,t)$ to the first-order envelope B as the compatible input for the MNLS equations. We then run a 'per-step' NBM simulation at each time step, generating the per-step difference ΔB.

We employ data augmentation and dedicated training strategy to reduce the overfitting issue during the training phase (see Appendix D.3 for details of data augmentation).

6.2.6 Aix-Marseille University Wave Tank Experiment

To perform an external assessment to the fidelity of the machine learning model, we have compared with laboratory experiments in the wave tank at Aix-Marseille University (Eeltink et al., 2022). For the wave tank experiment performed in AMU, the wave tank is 40 m long, 2.70 m wide, and 0.80 m deep. We have access to experimental data of 180 focused wave group (Type I) cases, 257 modulated plane

wave (Type II) cases, and 5 random wave (Type III) cases. In the experiment, the surface elevation profile is measured from 12 gauges at position 3.79 m, 6.64 m, 8.82 m, 11.63 m, 13.73 m, 16.11 m, 18.78 m, 21.83 m, 24.53 m, 26.96 m, 29.10 m and 31.10 m.

6.2.7 Reduced-Form Breaking Model

In this study, we will include MNLS simulations without a breaking model (referred to as NBM) for comparison. We will examine the five existing reduced-form breaking models with literature and optimised parameters, as well as the global kinematic breaking criterion being reviewed in Chapter 3.

6.3 Results

6.3.1 Wave Type I: Prediction for Focused Wave Groups

We apply our neural network model to a testset of 50 focused wave group cases (5% of the train dataset) characterised by a Joint–North–Sea–Wave–Project (JONSWAP) spectrum (Hasselmann et al., 1973). To illustrate its performance, we present a specific test case before assessing the error across the entire testset. Note that the bound waves are removed for all the results presented (see Appendix D.4 for data post-processing details) except for §6.3.4.

Figure 6.2 shows various comparisons among the Modified Nonlinear Schrödinger (MNLS) simulation without breaking model (NBM hereafter), the MNLS simulation with machine learning model (MNLS+ML hereafter), and the ground truth for a test case of the focused wave group. Analysis to the ground truth shows that the wave breaks multiple times in this case. In the NBM simulation (Fig. 6.2**a**, **d**), the main wave group splits into multiple wave groups due to strong nonlinear interactions during focus, and the spectrum remains broadbanded throughout the simulation. Our MNLS+ML simulation (Fig. 6.2**b**, **e**) predicts the wave evolution correctly when compared to the ground truth (Fig. 6.2**c**, **f**) where the wave group does

not split and the spectrum is downshifted after breaking. The bandwidth of the spectrum decreases after breaking.

Figure 6.2**g** plots the evolution of mean squared error (MSE) ((6.10)) over time for the NBM simulation and MNLS+ML simulation. The MSE of the MNLS+ML simulation reaches a peak during breaking and decreases afterwards. The MNLS+ML simulation achieves an MSE around one order of magnitude lower than the NBM simulation at the final timestep, showing that the MNLS+ML simulation effectively captures the wave-breaking process. Figure 6.2**h**–**j** depicts the evolution of various summary parameters. The evolution of energy ($\|B\|^2$) (Fig. 6.2**h**), peak frequency (Fig. 6.2**i**), and steepness (Fig. 6.2**j**) for all three simulations. Our observations suggest that the neural network model accurately reproduces the evolution of energy, peak frequency, and steepness.

Figure 6.3 presents the time series of the surface elevation profile and the frequency spectrum recorded in seven equally distributed gauges within the domain. The recorded time series is shifted by the group speed calculated using linear dispersion, and subsequently cropped to a fixed duration $t \in [0, 40]$. Similarly to the NBM envelope plots (Fig. 6.2**a**,**d**), we find that the NBM simulation also predicts multiple split wave groups in its surface elevation profile (Fig. 6.3**a**) and "upshifted" multimodal shape spectrum (Fig. 6.3**b**) which is far from the ground truth. The MNLS+ML results in Figure 6.3 indicate a close alignment for the predicted time series between the neural network model and the ground truth in both the time and frequency domains.

6.3.2 Wave Types II and III: Modulated Plane Wave and Random Waves

In order to assess the model's applicability beyond wave groups, we utilise the trained model to forecast dissipation during breaking in scenarios involving modulated plane waves and random waves. We generate 20 modulated plane wave cases and 20 random wave cases, the latter characterised by a JONSWAP spectrum with randomised

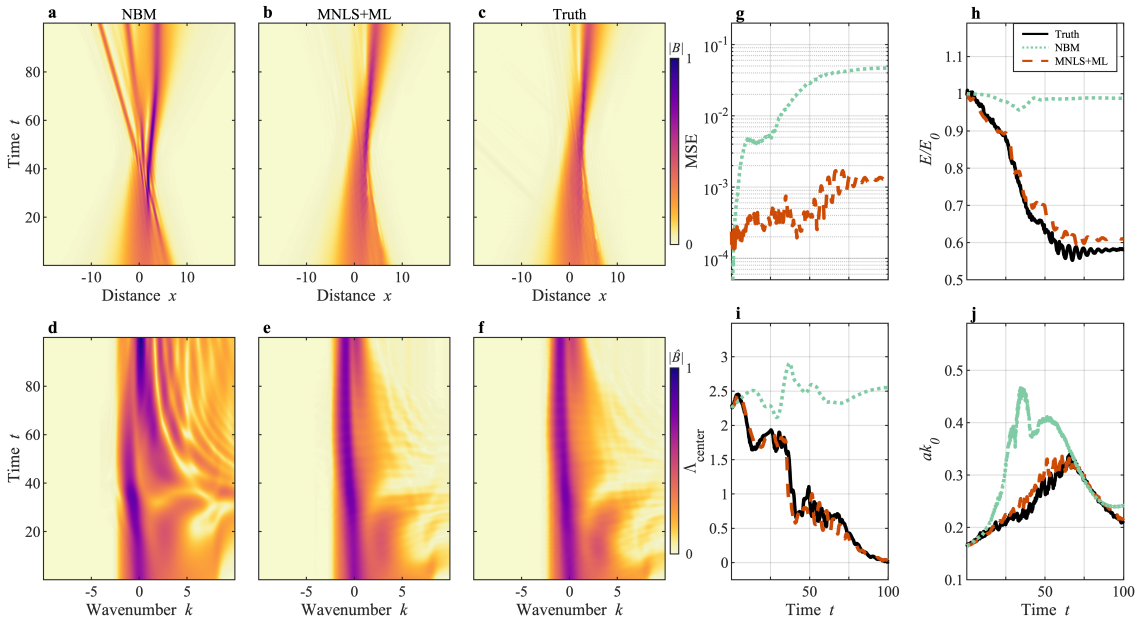


Figure 6.2: **Test result for the temporal evolution of a Type I (focused wave group) case. a–c** Space domain. Colorbar shows the absolute value of the wave envelope B. **d–f** Wavenumber domain. Colorbar shows the absolute value of the wavenumber spectrum $\hat{B}$. Specifically, **a** and **d** show the NBM result, **b** and **e** show the MNLS+ML result, and **c** and **f** show the ground truth which is RANS simulation. **g** Mean squared error (MSE) of the absolute value of the complex envelope. **h–j** Energy evolution $E = \int \|B\|^2 \,\mathrm{d}x$ normalised by its value in the first time step E_0, the spectral mean or centroid, $\Lambda_{\text{centre}} = \int k\tilde{B}(k)\mathrm{d}k / \int \tilde{B}(k)\mathrm{d}k$, and evolution of steepness. **g–j** share the same legend, the black solid line represents the ground truth, the orange dashed line represents the MNLS+ML result or MSE of MNLS+ML compared to the ground truth, and the green dotted line represents the NBM result or MSE of NBM result compared to the ground truth. The coordinates x, k and t are normalised by (4.3).

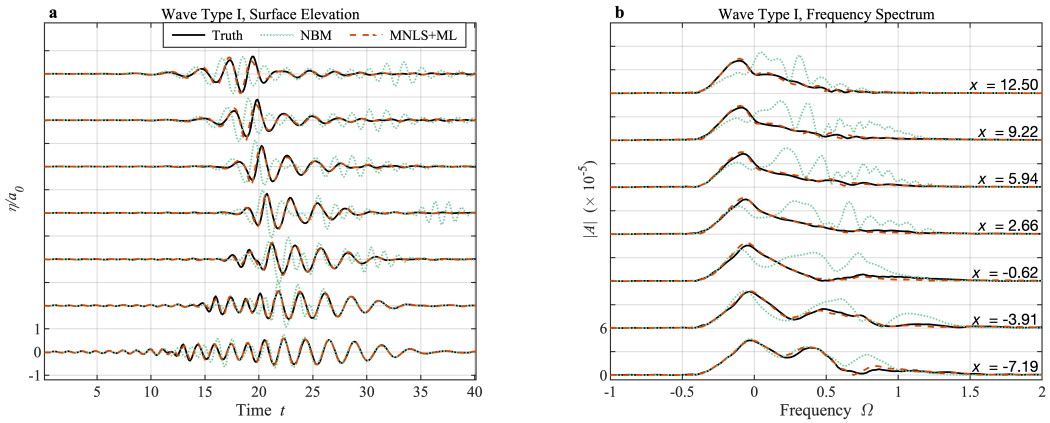


Figure 6.3: **The figure plots surface elevation profile of a focused wave group (Type I) case at equally distributed gauge locations.** **a** Surface elevation profile. The surface elevation η is normalised by the characteristic wave height a_0. **b** Frequency spectrum. The spectrum is normalised and $\Omega = \omega/\omega_0 - 1$ is the normalised modulational frequency. Solid black line is ground truth, orange dashed line is MNLS+ML and green dotted line is NBM simulation. The coordinates t and Ω are normalised by (4.3).

phase (Tucker et al., 1984).

Figure 6.4 shows various comparisons among the NBM simulation, the MNLS+ML simulation, and the ground truth for a test case of the modulated plane wave. In the NBM simulation (Fig. 6.4**a**,**d**), a Fermi–Pasta–Ulam–Tsingu recurrence (Fermi et al., 1955; Dauxois, 2008) occurs at $t = 70$ to 80 in the absence of breaking.

In contrast to Eeltink et al. (2022)'s approach to train and test on each wave category separately, we propose to train the model on focused wave group cases only, then test with other wave types. Our MNLS+ML simulation (Fig. 6.4**b**,**e**) predicts spectral downshifting correctly, and the evolution of the envelope and wavenumber spectrum agrees well with the ground truth (Fig. 6.4**c**,**f**). In Figure 6.4**g**, the MNLS+ML simulation achieves an MSE that is nearly one order of magnitude smaller than the NBM simulation.

The modulated plane wave breaks at $t \approx 40$ and the energy ($\|B\|^2$) (Fig. 6.4**h**) is conserved before the breaking onset, then followed by a rapid decrease due to wave breaking. The MNLS+ML simulation predicts the energy dissipation successfully but with a slight underestimation. The peak frequency (Fig. 6.4**i**) begins with an increase, then exhibits a downshifting. The steepness (Fig. 6.4**j**) increases rapidly

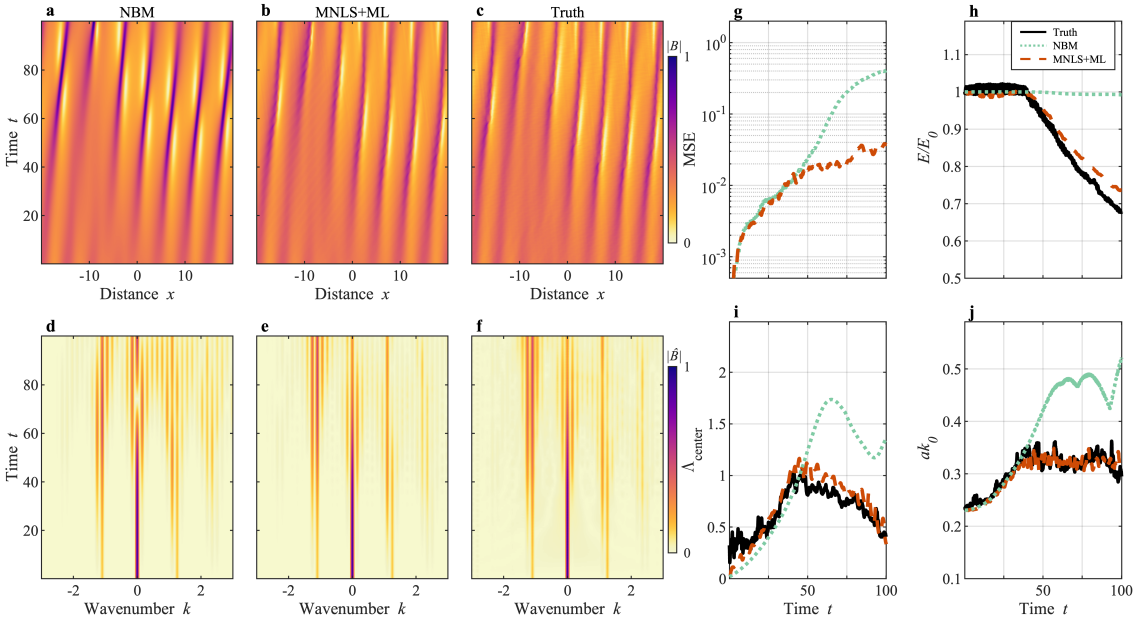


Figure 6.4: **Test result for the temporal evolution of a modulated plane wave (Type II) case. a–c** Space domain. Colorbar shows the absolute value of the wave envelope B. **d–f** Wavenumber domain. Colorbar shows the absolute value of the wavenumber spectrum $\hat{B}$. Specifically, **a** and **d** show the NBM result, **b** and **e** show the MNLS+ML result, and **c** and **f** show the ground truth which is RANS simulation. **g** Mean squared error (MSE) of the absolute value of the complex envelope. **h–j** Energy evolution, the spectral mean or centroid, and evolution of steepness. **g–j** share the same legend, the black solid line represents the ground truth, the orange dashed line represents the MNLS+ML result or MSE of MNLS+ML compared to the ground truth, and the green dotted line represents the NBM result or MSE of NBM result compared to the ground truth. The coordinates x, k and t are normalised by (4.3).

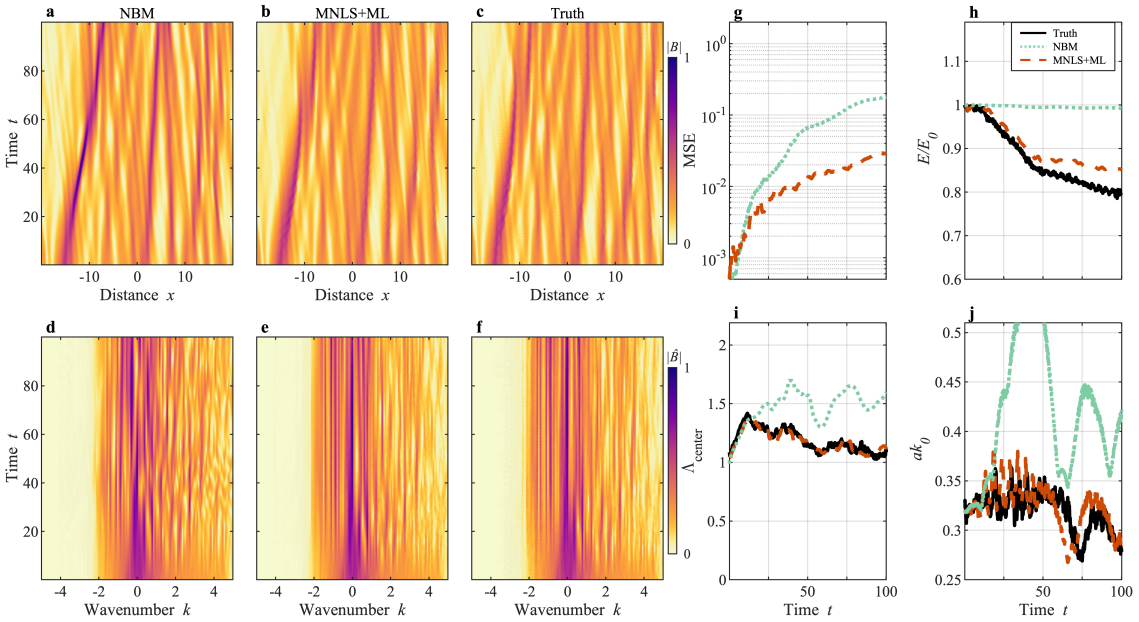


Figure 6.5: **Test result for the temporal evolution of a random wave (Type III) case.** **a–c** Space domain. Colorbar shows the absolute value of the wave envelope B. **d–f** Wavenumber domain. Colorbar shows the absolute value of the wavenumber spectrum $\hat{B}$. Specifically, **a** and **d** show the NBM result, **b** and **e** show the MNLS+ML result, and **c** and **f** show the ground truth which is RANS simulation. **g** Mean squared error (MSE) of the absolute value of the complex envelope. **h–j** Energy evolution, the spectral mean or centroid, and evolution of steepness. **g–j** share the same legend, the black solid line represents the ground truth, the orange dashed line represents the MNLS+ML result or MSE of MNLS+ML compared to the ground truth, and the green dotted line represents the NBM result or MSE of NBM result compared to the ground truth. The coordinates x, k and t are normalised by (4.3).

until it reaches the breaking limit, fluctuating around 0.35. The MNLS+ML predictions of the peak frequency and the wave steepness align closely to the ground truth, and the NBM simulation failed to predict all these summary variables.

Figure 6.5 shows similar comparisons among the NBM simulation, the MNLS+ML simulation, and the ground truth for a test case for random waves with an underlying JONSWAP spectrum. Figure 6.5**b**,**d** shows improvements in predicting the evolution of the envelope and wavenumber spectrum for MNLS+ML simulation. The MSE of the MNLS+ML simulation (Fig. 6.5**g**) is around 80% lower than the NBM simulation. The error, though, is greater than in the focused wave group cases, possibly because it is more challenging to localise the breaking event.

Figure 6.6 plots the time series of surface elevation and frequency spectrum of the modulated plane wave case and the random wave case. For the modulated plane wave (Fig. 6.6**a**,**b**), we find that the neural network model produces a phase-accurate prediction for the surface elevation profile. The neural network model also predicts the frequency spectrum very well. For random waves (Fig. 6.6**c**,**d**), the MNLS+ML simulation predicts multiple breaking events that occur at different positions and time points successfully, although the breakers are more irregular. For the MNLS+ML results, the surface elevation profile of the random waves closely agrees with the ground truth, indicating that our neural network model can make phase-accurate predictions in unseen wave types.

Figure 6.7 shows box plots of the mean squared error (MSE) for the MNLS+ML simulation, the M-KO simulation and the NBM simulation throughout the test cases. For the focused wave groups (Fig. 6.7**a**), the MSE rises quickly for both the NBM and the M-KO simulations, suggesting that the breaking effect in the focused wave group cases is not properly captured with the M-KO or the NBM simulation. The MNLS+ML model achieves a much lower MSE throughout the duration and outperforms both methods. The average MSE of the focused wave group cases in the last timestep is reduced by the MNLS+ML simulation for greater than an order of magnitude. For modulated plane waves (Fig. 6.7**b**), modulation takes place in the earlier time and most of the breaking events occur in the latter half of the duration.

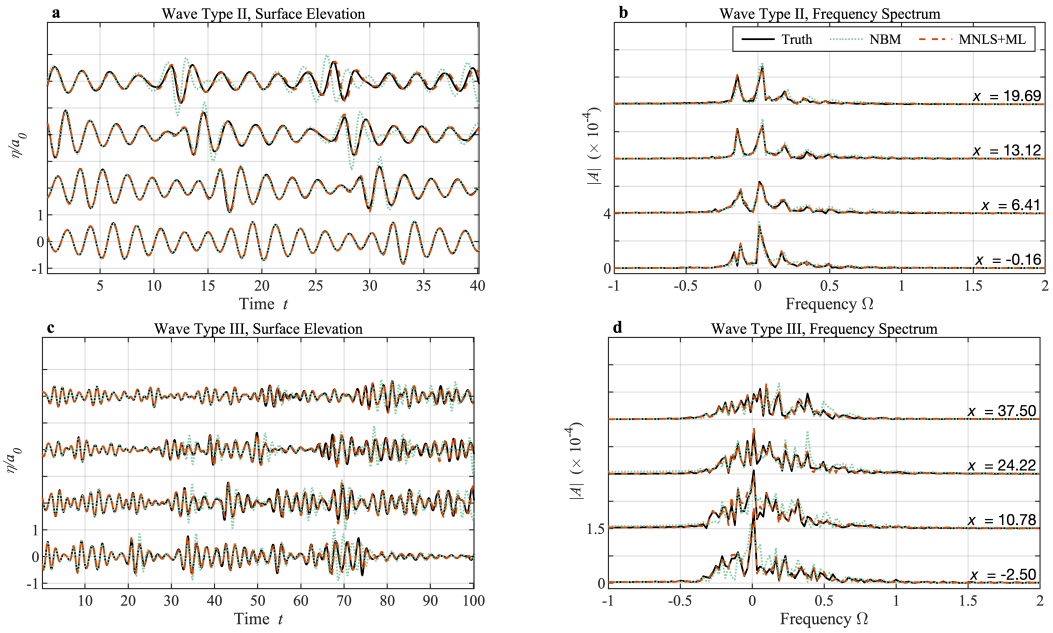


Figure 6.6: **The figure plots surface elevation profile of a modulated plane wave (Type II) and a random wave (Type III) case. a,c** Normalised surface elevation profile. **b,d** Normalised Frequency spectrum. $\Omega = \omega/\omega_0 - 1$ is the normalised modulational frequency. **a,b** Modulated plane wave case. **c,d** Random wave case. Solid black line is ground truth, orange dashed line is MNLS+ML and green dotted line is NBM simulation. The coordinates t and Ω are normalised by (4.3).

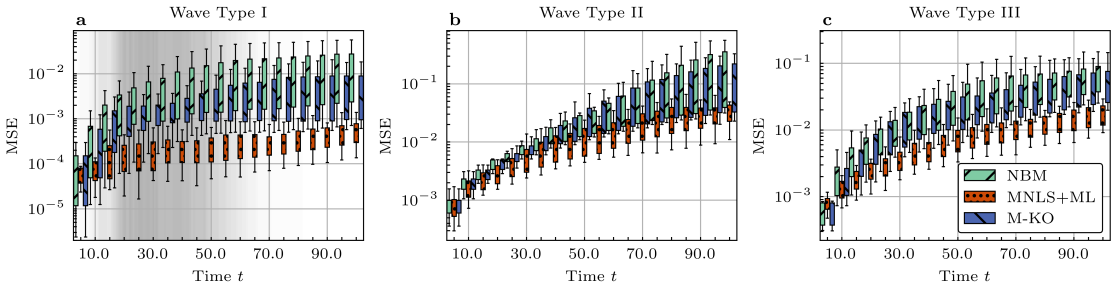


Figure 6.7: **This boxplot shows the MSE error distribution in the testset for all three wave types. a** Focused wave groups (Type I). The shaded region is composed of overlapping transparent gray intervals that indicate the breaking activities in each case. **b** Modulated plane wave (Type II). **c** Random waves (Type III). **a–c** Evolution of MSE of MNLS+ML prediction, M-KO prediction and NBM prediction with respect to time where minimums and maximums are indicated by caps, and the boxes indicate the interquartile ranges of the MSEs, where orange dotted boxes for MNLS+ML prediction, blue backslash boxes for M-KO prediction and green slash boxes for NBM prediction. t is normalised by (4.3).

We find that all of the MSEs grow rapidly at the beginning, and the MSEs of the M-KO simulation and the NBM simulation continue to increase afterward. The average MSE of the modulated plane wave cases in the last timestep is reduced approximately an order of magnitude by the MNLS+ML simulation. Breaking events spread more evenly in random wave cases (Fig. 6.7**c**) and therefore the MSEs evolve smoothly throughout the duration. The differences in MSEs among all three methods are smaller, with the MNLS+ML simulation taking a small advantage over the other two methods. The average MSE of the random wave cases in the last timestep is reduced 70% by the MNLS+ML simulation.

6.3.3 Comparision to Existing Breaking Models

We take five existing breaking models into comparison, to demonstrate the performance of our MNLS+ML model. The details of these existing models can be found in §6.2.

Table 6.1 shows the normalised mean squared error (NMSE) ((6.11)) and normalised mean absolute error (NMAE) ((6.12)) of the surface elevation profile averaged over the entire time span taken into account across all existing models, revealing that the MNLS+ML model achieves the lowest NMSE and NMAE for all types of waves, regardless of whether the wave type is seen (Type I) or unseen (Type II and Type III). The result demonstrates that our neural network model can make phase-accurate prediction of breaking waves, and its prediction generalises to unseen wave types well. (Also see Appendix D.5 for a comparison of the absolute magnitude of the envelope profile.) We note that the Selective Laplacian (SL) model performs well, often having the second lowest discrepancy in both tables, suggesting that the SL model can to some extent approximate breaking as a distributed dissipation effect. In this study, SL model outperforms all other models in terms of NMSE and NMAE, except for the MNLS+ML model. We believe the reason is that we evaluate the averaged MSE over multiple cases with different breaking scales, rather than a specific case as in Liu et al. (2023). The results of Tables 6.1 and D.1 demonstrate that SL model performs well in a statistical sense.

Model Name	Optimised (Y/N)	NMSE NMAE (Type I)	NMSE NMAE (Type II)	NMSE NMAE (Type III)
NBM		1.128	0.394	0.363
		0.799	0.415	0.427
TD90	Y	0.609	0.242	0.307
		0.640	0.354	0.411
TD90	N	0.500	0.247	0.299
		0.602	0.360	0.409
KO95	Y	0.917	0.360	0.327
		0.734	0.405	0.414
KO95	N	0.746	0.318	0.298
		0.673	0.390	0.403
SL	Y	0.701	0.327	0.278
		0.640	0.393	0.387
SL	N	0.291	0.236	0.247
		0.459	0.349	0.390
H11	Y	1.239	NaN	0.426
		0.854	NaN	0.447
H11	N	1.229	NaN	0.430
		0.854	NaN	0.449
M-KO95		0.333	0.285	0.265
		0.498	0.374	0.389
MNLS+ML		**0.063**	**0.123**	**0.105**
		0.240	**0.231**	**0.254**

Table 6.1: A comprehensive overview of the prediction losses of the models taken into consideration. MNLS without a breaking model (NBM) are evaluated as a baseline. All losses are calculated using (6.11) and (6.12) averaged over the entire time span $t \in [0, 100T_0]$ for the surface envelope η. The missing values marked by 'NaN' means the model encounter numerical issues and has failed to provide results in one or more test cases.

6.3.4 Comparison to Aix-Marseille University Wave Tank Experiment (Eeltink et al., 2022)

We make a direct comparison between the experimental data and the MNLS+ML predictions for Aix-Marseille University (AMU) wave tank experiment. We compare the MSE of measured time series among M-KO, MNLS+ML and NBM. We only test on cases with $k_0 d \geq 5$ for Type I, since the machine learning model is trained with fixed $k_0 d = 5$, leaving 24 cases to evaluate. We also exclude 66 Type II cases where $ak \leq 0.15$, as these cases are mostly non-breaking. The initial conditions for MNLS simulations are reconstructed from the measurements of the first gauge (x = 3.79 m) (Liu et al., 2023). The MSE is computed over the trimmed time series shifted by its group speed. For Type I, the time series is trimmed to [-$15T_p$, $15T_p$] s, centred around the wave group, and for Type II & Type III, the time series length is trimmed to $30T_p$ s, where T_p is the carrier wave period (Eeltink et al., 2022). To collect sufficiently long time series for all gauges, the durations of the

MNLS+ML simulation for AMU cases are $200T_0$, $300T_0$ and $400T_0$, and the space domain spans $80L_0$, $120L_0$ and $160L_0$, for Type I, II and III, respectively. The MSE is computed over fully nonlinear surface elevation profile, and for MNLS simulations we approximate it by $\eta_{\text{nonl, approx}} = \eta + \eta_{2+}$.

The results for Type I (Fig. 6.8**a**) demonstrate that the MNLS+ML simulation outperforms both the NBM and M-KO simulations in terms of MSE. For Type II (Fig. 6.8**b**), the MNLS+ML simulation performs only slightly better than M-KO due to multiple factors. On the one hand, a modulated plane wave with high steepness is likely to break multiple times at the same position, making wave evolution intractable. On the other hand, the result does not contrast with Figure 6.7**b** because the MNLS+ML model operates far beyond its train & test time series length. The performance of the model is expected to deteriorate when it exceeds $100T_0$.

We do not have enough Type III cases in the AMU wave tank experiment to perform an ensemble study. However, we evaluate two individual cases in Figure 6.8**c** with different significant wave heights. The case displayed with solid lines has a higher significant wave height, yielding frequent and intense breaking throughout the entire time span. The other case (plotted with dotted lines) has a lower significant wave height, leading to fewer and weaker breaking events. For the former case, the MNLS+ML simulation achieves a significantly lower MSE for the second half of the simulation. For the latter, the MNLS+ML simulation achieves lower MSE for the last gauge, but the overall performances among NBM, MNLS+ML and M-KO simulations are similar. We believe that this is due to the absence of breaking events, given that the MSEs of the latter case remain at a low level ($\mathcal{O}(10^{-5})$) for all time.

6.3.5 Model Efficiency

We study the efficiency of the models by comparing the average Simulation Efficiency Ratio (SER) for the focused wave group test cases (Type I). The definition of SER is given as follows:

$$\text{SER} = \frac{\text{Total simulated time}}{\text{Total simulation time}}. \tag{6.13}$$

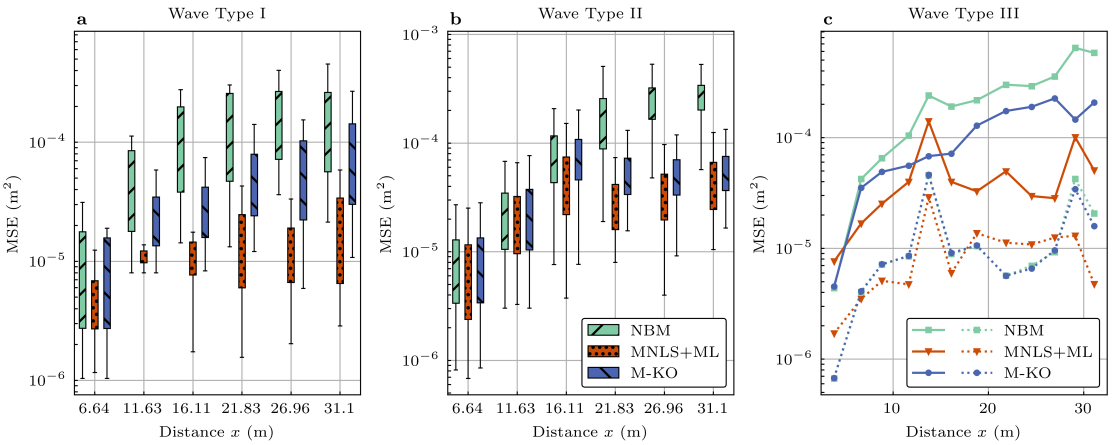


Figure 6.8: **Comparison to AMU wave tank experiment.** **a** MSE for focused wave group (Type I) cases. **b** MSE for modulated plane wave (Type II) cases. **c** MSE for random waves (Type III). The plots **a** and **b** include six gauges positioned in 6.64 m, 11.63 m, 16.11 m, 21.83 m, 26.96 m and 31.10 m. Minimums and maximums are indicated by caps, and the boxes indicate the interquartile ranges of the MSEs. Orange dotted boxes for MNLS+ML prediction, blue backslash boxes for M-KO prediction, and green slash boxes for NBM prediction. For the plot **c** the solid lines show a Type III case with a significant wave height of 80 mm, and the dotted lines display another Type III case with a significant wave height of 40 mm. Orange downward triangle marker for MNLS+ML prediction, blue circles for M-KO prediction, and green squares for NBM prediction.

The RANS simulation is the most time-consuming of all (SER = 0.0018), running on a 48 core Intel Xeon Platinum 8268 CPU @ 2.90GHz, in parallel. The MNLS simulation without breaking model is the fastest, having an SER = 70.0270 on an Apple M2 CPU. We find that the neural network model achieves an SER = 2.9487 (>1) on an Apple M2 CPU, allowing it to make predictions. Compared to the RANS simulation, the MNLS+ML simulation gains a 1638-times speedup for focused wave group cases. We do not include comparison for modulated plane wave and random wave cases because a different wave type does not impact efficiency for MNLS simulation, and the neural network model does not achieve an MSE low enough that allows us to make a fair comparison to the RANS simulation.

6.4 Discussion

The MNLS+ML framework has demonstrated its effectiveness in predicting wave evolution, including wave breaking and its subsequent effects on energy dissipation, steepness, and spectral changes. By combining the MNLS equation with the ConvLSTM model, the hybrid model captures the complexities of wave breaking more accurately than previous models. This study expands on the framework introduced in Eeltink et al. (2022). The use of a convolutional-recurrent architecture allows for handling arbitrary spatio-temporal lengths, showcasing the framework's advanced capabilities in simulating wave dynamics with clarity and technical precision. To the best of our knowledge, ConvLSTM is one of the simplest deep learning structures that has the ability to capture the nonlinear process of wave breaking. Therefore, ConvLSTM is more intuitive and easier to interpret compared to deeper structures.

This study represents a methodological shift by utilising RANS simulation data as ground truth. The approach contrasts with earlier models that might only use data from probe measurements in a wave tank experiment (which is only sparsely distributed in space) (Eeltink et al., 2022), indicating a significant expansion in the scale of the data in this field. Comparison to the AMU experiments provides further validation to the method taken in this study and reveals the importance of RANS simulation for generation of a high-quality wave breaking dataset.

Despite its innovative approach, the MNLS+ML framework has limitations, notably the inherent conditional stability of the recurrent neural network structure and the challenges in combating overfitting during the training phase. Moreover, an extra layer of bias is introduced when approximating the first-order wave envelope from the fully nonlinear surface elevation profiles of the RANS simulation. These limitations highlight the difficulties in developing a robust yet accurate framework for capturing wave breaking dynamics. The analysis provides a clear understanding of the hurdles that must be overcome to improve the applicability and performance of the model.

The incorporation of a neural network to capture wave breaking represents a

novel aspect of this research, especially in how it is validated against unseen wave types. This novel approach shows the framework's ability to extrapolate learning from focused wave groups to a broader range of types, indicating a significant advancement in modelling dynamic sea states. This work shows the possibility of capturing wave breaking dynamics as hidden states in a high-dimensional latent space, and parameterising the breaking term D in the MNLS equation with a neural network model, which is in line with a growing number of work on operator learning in partial differential equations (PDEs) (Raissi, 2018; Li et al., 2020; Lu et al., 2021; Boulle et al., 2020; Kochkov et al., 2021).

Looking ahead, the potential for more realistic sea state modelling is vast, with possibilities extending to both Finite-Domain and Infinitesimal-Domain approaches. Future research could enhance the accuracy and applicability of the MNLS+ML framework, exploring new frontiers in wave modelling. Replacing the current network structure with an unconditionally stable one is essential for long-term simulations. Running more accurate computational fluid dynamics simulations and scaling up the dataset will benefit the accuracy of neural network models in general. Improving the reconstruction of the first-order envelope from fully nonlinear surface elevation measurements will help eliminate the bias added to the training phase from the preprocessing stage (see Appendix D.4). To extend our method to directional seas, the current framework needs to adapt from 1D to 2D sea states. It will be challenging to arrange a sufficient amount of data as well as nontrivial efforts to build an accurate, efficient, and robust model. It is also of great interest to distill the model with, say, symbolic regression approach, to find interpretable insights. The model relies on dense spatial input, which may not be feasible in real-world settings. In such cases, the model can be integrated with methods that reconstruct a dense spatial field from probe observations (Blondel et al., 2008; Ehlers et al., 2024) or radar scans (Zinchenko et al., 2021; Ehlers et al., 2023).

In conclusion, the MNLS+ML framework offers a more accurate and efficient method for predicting wave evolution, including the complex process of wave breaking. The study's findings underscore the potential impact of the framework on future

research, advocating for its utility in advancing our understanding and prediction of wave dynamics. Reflecting on the broader implications, the MNLS+ML framework not only enhances current modelling capabilities but also sets a new standard for future developments in the field.

Chapter 7

Discussions and Conclusions

Fast prediction of wave breaking events is important for a wide range of offshore applications. Better prediction of breaking waves help us to understand the physical process of the ocean, design better offshore structures, and enhance safety of maritime activities. In this thesis, we developed reduced-order models with recent machine-learning methods, and contributed to the more accurate wave forecasting and simulation. This work explores new paths for capturing the wave-breaking mechanism as a strong nonlinearity in a reduced-order model.
In this study, we address 4 objectives listed in §1.1 which are:

Objective 1 *To improve existing breaking dissipation models for envelope-based wave equations using both conventional and machine-learning approachs.*

In Chapter 3 we found that a modified Kato and Oikawa (1995) model works well to approximate spectral dissipation in the 2 cases of the SJTU experiment and a small number of modulated plane wave cases. However, the model is non-local and unable to fit to more data. Although this model is not readily applicable to a general set of cases, we believe that this emphasises the selectively dissipative nature of the wave breaking and a possible way to model the breaking effect (namely, with a simple dissipation term).

In Chapter 4 we extended the framework proposed in Eeltink et al. (2022).

Eeltink et al. (2022) proposed using a fully-connected LSTM network, combined with the time-NLS equation, to predict the evolution of the breaking waves. The model proposed here achieves similar or superior performance compared to Eeltink et al. (2022), with a scalable structure that allows one to use between thousands and hundred thousands of parameters. The model utilises a convolutional-recurrent structure that enables it to support simulation with arbitrary length in space and time.

The model assumes that wave breaking dissipation is local in space. We train the model with focused wave cases only and show that the model is able to generalise to breaking in very different wave fields. This is a promising procedure exhibiting the ability of a neural network model to learn from a small set of canonical samples, then generalise to arbitrary conditions. This reduces the potential difficulty in preparing a dataset for such models, as both computational fluid dynamics simulations and wave tank experiments for focused wave groups are cheaper than creating modulated plane wave or random wave datasets.

Objective 2 *To explore the feasibility of generating large-scale synthetic training data for machine learning of wave breaking using envelope-based wave equations.*

In Chapter 4 we generated a large amount of synthetic data using the MNLS equation and the M-KO95 model developed in Chapter 3. We trained a machine learning model using synthetic data successfully and evaluted it on the test set that is also synthesised using MNLS+M-KO95. We demonstrated that a large volume of synthetic data can be generated efficiently, and this data can be effectively used to validate the model and assess its ability to capture the nonlinearity of wave breaking.

Objective 3 *To investigate the potential of using RANS simulations to produce higher-fidelity training data for machine learning models of wave breaking.*

In Chapter 5 we implemented RANS simulations with an open-source code package

'Basilisk'. We utilised RANS simulation with Basilisk to study the deep-water wave breaking problem. We validated the numerical configuration with a Stokes-wave simulation. We then used the RANS model to simulate wave breaking in focused wave groups, modulated plane waves, and random waves with an underlying JONSWAP spectrum. We found that the RANS simulations agree with the gauge measurements from the Eeltink et al. (2022)'s experiment. Additionally, we applied RANS simulation to perform an energy-converged simulation in the periodic domain. We discovered that the energy was conserved in the non-breaking region.

By verifying the RANS model, we can take advantage of the limitation of the Reynolds number. Compared to DNS approaches, which are limited to Reynolds numbers of $\mathcal{O}(10^4)$ (Mostert et al., 2022), RANS simulations can run in a much broader range of Reynolds number, from $\mathcal{O}(10^4)$ to $\mathcal{O}(10^7)$. This enables us to simulate a system on laboratory scale, without the need for enormous computational resources.

Objective 4 *To evaluate and compare the performance of conventional and deep-learning-based breaking dissipation models for envelope-based wave equations.*

In Chapter 3 we reviewed the existing models and discussed their performance in both perturbed plane waves and focused wave cases. We found that most existing models are able to produce correctly the recurrence cycle in perturbed plane waves but all failed to produce the correct spectral dissipation for focused wave cases.

By investigating the focused wave case, we noticed that wave breaking modifies 1 to 2 crests at the front of the wave group. The high-frequency part of the spectrum is selectively dissipated during breaking. It is interesting to note that the phase of the wave does not seem to be altered after wave breaking. However, we found that existing models struggle to reproduce the spectral dissipation caused by wave breaking.

In Chapter 6 we apply the framework proposed in Chapter 4 to the RANS dataset we built in Chapter 5. We made minor changes to the model architecture and the

training process to address the overfit issue and biases introduced during the preprocessing stage. The model achieves superior performance when compared to existing breaking models. The model can also generalise to unseen wave types, as we have conjectured in Chapter 4.

In this thesis, we proposed two reduced-order models to approximate wave breaking dissipation in envelope-based equations. One is the modified Kato & Oikawa model, and the other is the ConvLSTM-based model. We studied breaking dissipation in unidirectional deep-water waves. We showed that the existing models do not capture all the essence of the breaking dissipation, which is selective dissipation in the spectrum, locality in space, and intermittency in time. To satisfy these principles, we proposed modification to Kato & Oikawa model. We also introduced a nonlinear optimisation approach to fit the parameters from experimental measurements to avoid hand-crafting free parameters. We verified that the 1D wave breaking evolution represented by surface envelope can be learnt by a convolutional-recurrent neural network model such as ConvLSTM. While imperfection exists, neural network structures achieve state-of-the-art performance, showing substantial potential to approximate highly nonlinear wave breaking dissipation. We also discussed several ways to address the drawbacks of the neural network model exposed in the current study, yet this topic has not been fully explored. The model struggles to separate multiple physical processes, such as viscous dissipation, wave breaking, and nonlinear evolution of steep waves, leading to biases that accumulate and cause substantial divergence from the ground truth. The standard ConvLSTM model lacks the conserved quantity, raising the risk of the blow-up of the numerical solution. We have proposed an unconditionally stable variant of ConvLSTM model, yet training it with RANS-based data remains a challenge. Future studies should focus on enhancing neural network stability, and reducing the overfitting during the training phase. Introducing physics-based constraints, such as symmetries and invariants, could optimise the neural network model. Reducing the model's capacity to learn complex data patterns, for instance, by decreasing the number of trainable weights,

is also recommended to reduce overfitting or create a more scalable model.

References

Adcock, T. A. A. and Taylor, P. H. (2016a). Fast and local non-linear evolution of steep wave-groups on deep water: A comparison of approximate models to fully non-linear simulations. *Physics of Fluids*, 28(1):016601. Publisher: AIP Publishing.

Adcock, T. A. A. and Taylor, P. H. (2016b). Non-linear evolution of uni-directional focussed wave-groups on a deep water: A comparison of models. *Applied Ocean Research*, 59:147–152.

Agrawal, G. P. (2013). *Nonlinear fiber optics*. Elsevier/Academic Press, Amsterdam, fifth edition edition.

Ahmad, N., Bihs, H., Myrhaug, D., Kamath, A., and Arntsen, Ø. A. (2019). Numerical modelling of pipeline scour under the combined action of waves and current with free-surface capturing. *Coastal Engineering*, 148:19–35.

Amaechi, C. V., Reda, A., Butler, H. O., Ja'e, I. A., and An, C. (2022). Review on Fixed and Floating Offshore Structures. Part II: Sustainable Design Approaches and Project Management. *Journal of Marine Science and Engineering*, 10(7):973.

Ardhuin, F., Rogers, E., Babanin, A. V., Filipot, J.-F., Magne, R., Roland, A., Westhuysen, A. v. d., Queffeulou, P., Lefevre, J.-M., Aouf, L., and Collard, F. (2010). Semiempirical Dissipation Source Functions for Ocean Waves. Part I: Definition, Calibration, and Validation. *Journal of Physical Oceanography*, 40(9):1917 – 1941. Place: Boston MA, USA Publisher: American Meteorological Society.

Babanin, A. (2011). *Breaking and Dissipation of Ocean Surface Waves*. Cambridge University Press.

Banner, M. L. and Peirson, W. L. (2007). Wave breaking onset and strength for two-dimensional deep-water wave groups. *Journal of Fluid Mechanics*, 585:93–115.

Barratt, D., Van Den Bremer, T. S., and Adcock, T. A. A. (2021). MNLS simulations of surface wave groups with directional spreading in deep and finite depth waters. *Journal of Ocean Engineering and Marine Energy*, 7(3):261–275.

Barthelemy, X., Banner, M. L., Peirson, W. L., Fedele, F., Allis, M., and Dias, F. (2018). On a unified breaking onset threshold for gravity waves in deep and intermediate depth water. *Journal of Fluid Mechanics*, 841:463–488. Publisher: Cambridge University Press (CUP).

Bellman, R. (1957). Dynamic Programming. *Science*, 153:34 – 37.

Benjamin, T. B. and Feir, J. E. (1967). The disintegration of wave trains on deep water Part 1. Theory. *Journal of Fluid Mechanics*, 27(3):417–430.

Bihs, H., Wang, W., Pakozdi, C., and Kamath, A. (2020). REEF3D::FNPF—A Flexible Fully Nonlinear Potential Flow Solver. *Journal of Offshore Mechanics and Arctic Engineering*, 142(4):041902.

Blondel, E., Ducrozet, G., Bonnefoy, F., and Ferrant, P. (2008). Deterministic Reconstruction and Prediction of a Non-Linear Wave Field Using Probe Data. In *Volume 4: Ocean Engineering; Offshore Renewable Energy*, pages 379–386, Estoril, Portugal. ASMEDC.

Boffetta, G. and Ecke, R. E. (2012). Two-Dimensional Turbulence. *Annual Review of Fluid Mechanics*, 44(1):427–451.

Booij, N., Ris, R. C., and Holthuijsen, L. H. (1999). A third-generation wave model for coastal regions: 1. Model description and validation. *Journal of Geophysical Research: Oceans*, 104(C4):7649–7666.

Boulle, N., Nakatsukasa, Y., and Townsend, A. (2020). Rational neural networks. In Larochelle, H., Ranzato, M., Hadsell, R., Balcan, M. F., and Lin, H., editors, *Advances in Neural Information Processing Systems*, volume 33, pages 14243–14253. Curran Associates, Inc.

Boussinesq, J. (1877). *Essai sur la théorie des eaux courantes*. Imprimerie nationale.

Bradford, S. F. (2000). Numerical Simulation of Surf Zone Dynamics. *Journal of Waterway, Port, Coastal, and Ocean Engineering*, 126(1):1–13. Publisher: American Society of Civil Engineers (ASCE).

Brunton, S. L., Noack, B. R., and Koumoutsakos, P. (2020). Machine Learning for Fluid Mechanics. *Annual Review of Fluid Mechanics*, 52(1):477–508.

Brus, S. R., Wolfram, P. J., Van Roekel, L. P., and Meixner, J. D. (2021). Unstructured global to coastal wave modeling for the Energy Exascale Earth System Model using WAVEWATCH III version 6.07. *Geoscientific Model Development*, 14(5):2917–2938.

Campos, R. M., Costa, M. O., Almeida, F., and Guedes Soares, C. (2021). Operational Wave Forecast Selection in the Atlantic Ocean Using Random Forests. *Journal of Marine Science and Engineering*, 9(3):298.

Carter, J. D., Curtis, C. W., and Kalisch, H. (2019a). Particle Trajectories in Nonlinear Schrödinger Models. *Water Waves*, 2(1):31–57. Publisher: Springer Science and Business Media LLC.

Carter, J. D., Henderson, D., and Butterfield, I. (2019b). A comparison of frequency downshift models of wave trains on deep water. *Physics of Fluids*, 31(1):013103. Publisher: American Institute of Physics Inc.

Chao, X., Wang, Q., Wang, X., Chen, J., and Zhu, Y. (2024). Ocean-wave suppression for synthetic aperture radar images by depth counteraction method. *Remote Sensing of Environment*, 305:114086.

Chaplin, J. R. (1996). On Frequency-Focusing Unidirectional Waves. *International Journal of Offshore and Polar Engineering*, 6(02).

Chen, L. F., Zang, J., Taylor, P. H., Sun, L., Morgan, G. C. J., Grice, J., Orszaghova, J., and Tello Ruiz, M. (2018). An experimental decomposition of nonlinear forces on a surface-piercing column: Stokes-type expansions of the force harmonics. *Journal of Fluid Mechanics*, 848:42–77.

Chen, Q., Cai, C., Chen, Y., Zhou, X., Zhang, D., and Peng, Y. (2024). TemproNet: A transformer-based deep learning model for seawater temperature prediction. *Ocean Engineering*, 293:116651.

Choi, H., Park, M., Son, G., Jeong, J., Park, J., Mo, K., and Kang, P. (2020). Real-time significant wave height estimation from raw ocean images based on 2D and 3D deep neural networks. *Ocean Engineering*, 201:107129.

Clamond, D., Francius, M., Grue, J., and Kharif, C. (2006). Long time interaction of envelope solitons and freak wave formations. *European Journal of Mechanics - B/Fluids*, 25(5):536–553.

Colombo, M. and Fairweather, M. (2015). Multiphase turbulence in bubbly flows: RANS simulations. *International Journal of Multiphase Flow*, 77:222–243. Publisher: Elsevier Ltd.

Dauxois, T. (2008). Fermi, Pasta, Ulam and a mysterious lady. *arXiv preprint arXiv:0801.1590*.

Deike, L. (2022). Mass Transfer at the Ocean–Atmosphere Interface: The Role of Wave Breaking, Droplets, and Bubbles. *Annual Review of Fluid Mechanics*, 54(1):191–224.

Deike, L., Melville, W. K., and Popinet, S. (2016). Air entrainment and bubble statistics in breaking waves. *Journal of Fluid Mechanics*, 801:91–129.

Deike, L., Pizzo, N., and Melville, W. K. (2017). Lagrangian transport by breaking surface waves. *Journal of Fluid Mechanics*, 829:364–391. Publisher: Cambridge University Press.

Deike, L., Popinet, S., and Melville, W. (2015). Capillary effects on wave breaking. *Journal of Fluid Mechanics*, 769:541–569.

Deo, I. K., Gao, R., and Jaiman, R. (2023). Combined space–time reduced-order model with three-dimensional deep convolution for extrapolating fluid dynamics. *Physics of Fluids*, 35(4):043606.

Deo, M. and Jagdale, S. (2003). Prediction of breaking waves with neural networks. *Ocean Engineering*, 30(9):1163–1178.

Deo, M. and Sridhar Naidu, C. (1998). Real time wave forecasting using neural networks. *Ocean Engineering*, 26(3):191–203.

Derakhti, M., Banner, M. L., and Kirby, J. T. (2018). Predicting the breaking strength of gravity water waves in deep and intermediate depth. *Journal of Fluid Mechanics*, 848:R2. Publisher: Cambridge University Press.

Derakhti, M. and Kirby, J. T. (2014). Bubble entrainment and liquid–bubble interaction under unsteady breaking waves. *Journal of Fluid Mechanics*, 761:464–506. Publisher: Cambridge University Press.

Derakhti, M., Kirby, J. T., Banner, M. L., Grilli, S. T., and Thomson, J. (2020). A Unified Breaking Onset Criterion for Surface Gravity Water Waves in Arbitrary Depth. *Journal of Geophysical Research: Oceans*, 125(7).

Devolder, B., Troch, P., and Rauwoens, P. (2018). Performance of a buoyancy-modified k-ω and k-ω SST turbulence model for simulating wave breaking under regular waves using OpenFOAM®. *Coastal Engineering*, 138:49–65. Publisher: Elsevier B.V.

Dommermuth, D. G., Yue, D. K. P., Lin, W. M., Rapp, R. J., Chan, E. S., and Melville, W. K. (1988). Deep-water plunging breakers: a comparison between potential theory and experiments. *Journal of Fluid Mechanics*, 189:423–442.

Drazen, D. A., Melville, W. K., and Lenain, L. (2008). Inertial scaling of dissipation in unsteady breaking waves. *Journal of Fluid Mechanics*, 611:307–332. Publisher: Cambridge University Press.

Dudley, J. M., Genty, G., Mussot, A., Chabchoub, A., and Dias, F. (2019). Rogue waves and analogies in optics and oceanography. *Nature Reviews Physics*, 1(11):675–689. Publisher: Springer Science and Business Media LLC.

Duncan, J. H. (2001). Spilling breakers. *Annual Review of Fluid Mechanics*, 33(Volume 33, 2001):519–547.

Dysthe, K. B. (1979). Note on a modification to the nonlinear Schrödinger equation for application to deep water waves. *Proceedings of the Royal Society of London. A. Mathematical and Physical Sciences*, 369(1736):105–114. Publisher: The Royal Society.

Dysthe, K. B. and Trulsen, K. (2001). The evolution of an evolution equation. *Frontiers of Nonlinear Physics*, 2:125–138.

D'Agostino, D., Serani, A., Stern, F., and Diez, M. (2022). Time-series forecasting for ships maneuvering in waves via recurrent-type neural networks. *Journal of Ocean Engineering and Marine Energy*, 8(4):479–487.

Eeltink, D., Branger, H., Luneau, C., He, Y., Chabchoub, A., Kasparian, J., Bremer, T. S. v. d., and Sapsis, T. P. (2022). Nonlinear wave evolution with data-driven breaking. *Nature Communications*, 13(1):2343.

Ehlers, S., Klein, M., Heinlein, A., Wedler, M., Desmars, N., Hoffmann, N., and Stender, M. (2023). Machine learning for phase-resolved reconstruction of nonlinear ocean wave surface elevations from sparse remote sensing data. *Ocean Engineering*, 288:116059.

Ehlers, S., Stender, M., Klein, M., Hoffmann, N., Wagner, N. A., and Scherzl, A. (2024). Data assimilation and parameter identification for water waves using the nonlinear Schrödinger equation and physics-informed neural networks.

Engsig-Karup, A., Bingham, H., and Lindberg, O. (2009). An efficient flexible-order model for 3D nonlinear water waves. *Journal of Computational Physics*, 228:2100–2118.

Fan, S., Xiao, N., and Dong, S. (2020). A novel model to predict significant wave height based on long short-term memory network. *Ocean Engineering*, 205:107298.

Fermi, E., Pasta, P., Ulam, S., and Tsingou, M. (1955). Studies of the Nonlinear Problems. Technical report, Los Alamos National Laboratory (LANL).

Fuhrman, D. R. and Li, Y. (2020). Instability of the realizable k–ε turbulence model beneath surface waves. *Physics of Fluids*, 32(11):115108.

Gao, S., Yu, Z., Zhang, Z., Feng, C., Yan, T., He, B., and Zio, E. (2024). Physical model embedding-based generative adversarial networks for unsupervised fault detection of underwater thrusters. *Ocean Engineering*, 298:117190.

Gibson, R. S. and Swan, C. (2007). The evolution of large ocean waves: the role of local and rapid spectral changes. *Proceedings of the Royal Society A: Mathematical, Physical and Engineering Sciences*, 463(2077):21–48.

Goodfellow, I. J., Pouget-Abadie, J., Mirza, M., Xu, B., Warde-Farley, D., Ozair, S., Courville, A., and Bengio, Y. (2014). Generative adversarial networks.

Gramstad, O. and Trulsen, K. (2011). Hamiltonian form of the modified nonlinear Schrödinger equation for gravity waves on arbitrary depth. *Journal of Fluid Mechanics*, 670:404–426.

Grilli, S. T., Guérin, C.-A., and Goldstein, B. (2011). OceanWave Reconstruction Algorithms Based On Spatio-temporal Data Acquired By a Flash LIDAR Camera. pages ISOPE–I–11–508.

Gruwez, V., Altomare, C., Suzuki, T., Streicher, M., Cappietti, L., Kortenhaus, A., and Troch, P. (2020). Validation of RANS Modelling for Wave Interactions with Sea Dikes on Shallow Foreshores Using a Large-Scale Experimental Dataset. *Journal of Marine Science and Engineering*, 8(9):650.

Han, L., Ji, Q., Jia, X., Liu, Y., Han, G., and Lin, X. (2022). Significant Wave Height Prediction in the South China Sea Based on the ConvLSTM Algorithm. *Journal of Marine Science and Engineering*, 10(11):1683.

Hasselmann, K. (1974). On the spectral dissipation of ocean waves due to white capping. *Boundary-Layer Meteorology*, 6(1-2):107–127. Publisher: Springer Science and Business Media LLC.

Hasselmann, K., Barnett, T., Bouws, E., Carlson, H., Cartwright, D., Enke, K., Ewing, J., Gienapp, H., Hasselmann, D., Kruseman, P., Meerburg, A., Muller, P., Olbers, D., Richter, K., Sell, W., and Walden, H. (1973). Measurements of wind-wave growth and swell decay during the Joint North Sea Wave Project (JONSWAP). *Deut. Hydrogr. Z.*, 8:1–95.

Henderson, K., Peregrine, D., and Dold, J. (1999). Unsteady water wave modulations: fully nonlinear solutions and comparison with the nonlinear Schrödinger equation. *Wave Motion*, 29(4):341–361.

Hochreiter, S. and Schmidhuber, J. (1997). Long Short-Term Memory. *Neural Computation*, 9(8):1735–1780.

Hwung, H.-H., Chiang, W.-S., Yang, R.-Y., and Shugan, I. V. (2011). Threshold model on the evolution of Stokes wave side-band instability. *European Journal of Mechanics - B/Fluids*, 30(2):147–155. Publisher: Elsevier BV.

Iafrati, A. (2009). Numerical study of the effects of the breaking intensity on wave breaking flows. *Journal of Fluid Mechanics*, 622:371–411. Publisher: Cambridge University Press.

Infeld, E. and Rowlands, G. (2000). *Nonlinear Waves, Solitons and Chaos*. Cambridge University Press, 2 edition.

Kato, Y. and Oikawa, M. (1995). Wave Number Downshift in Modulated Wavetrain through a Nonlinear Damping Effect. *Journal of the Physical Society of Japan*, 64(12):4660–4669. Publisher: Physical Society of Japan.

Keulegan, G. H. (1950). Wave motion. *Engineering Hydraulics*, 11:711–768.

Kingma, D. P. and Welling, M. (2013). Auto-Encoding Variational Bayes. Version Number: 11.

Kochkov, D., Smith, J. A., Alieva, A., Wang, Q., Brenner, M. P., and Hoyer, S. (2021). Machine learning–accelerated computational fluid dynamics. *Proceedings of the National Academy of Sciences*, 118(21).

Kolmogorov, A. N. (1941). The local structure of turbulence in incompressible viscous fluid for very large reynolds. *Dokl. Akad. Nauk SSSR*, 30:301 – 305.

Komen, G. J., Cavaleri, L., Donelan, M., Hasselmann, K., Hasselmann, S., and Janssen, P. A. E. M. (1994). *Dynamics and Modelling of Ocean Waves*. Cambridge University Press, 1 edition.

Koza, J. R., Bennett, F. H., Andre, D., and Keane, M. A. (1996). Automated Design of Both the Topology and Sizing of Analog Electrical Circuits Using Genetic Programming. In Gero, J. S. and Sudweeks, F., editors, *Artificial Intelligence in Design '96*, pages 151–170. Springer Netherlands, Dordrecht.

Krige, D. (1951). A statistical approach to some basic mine valuation problems on the Witwatersrand, by D.G. Krige, published in the Journal, December 1951 : introduction by the author. *Journal of The South African Institute of Mining and Metallurgy*.

Kulkarni, R., Christensen, E. D., Troch, P., Breugem, W. A., Decrop, B., Song, Y., and Liu, X. (2023). Calibrating time development of scour and backfilling around

vertical pile using Immersed Boundary method. In Ugelvig Petersen, T. and Sassa, S., editors, *Proceedings of the 11th International Conference on Scour and Erosion*. International Society for Soil Mechanics and Geotechnical Engineering.

Kurnia, R. and Groesen, E. v. (2014). High order Hamiltonian water wave models with wave-breaking mechanism. *Coastal Engineering*, 93:55–70. Publisher: Elsevier BV.

Lake, B. M., Yuen, H. C., Rungaldier, H., and Ferguson, W. E. (1977). Nonlinear deep-water waves: theory and experiment. Part 2. Evolution of a continuous wave train. *Journal of Fluid Mechanics*, 83(1):49–74. Publisher: Cambridge University Press (CUP).

Larsen, B. E., A, D. A. v. d., Zanden, J. v. d., Ruessink, G., and Fuhrman, D. R. (2020). Stabilized RANS simulation of surf zone kinematics and boundary layer processes beneath large-scale plunging waves over a breaker bar. *Ocean Modelling*, 155:101705.

Larsen, B. E. and Fuhrman, D. R. (2018). On the over-production of turbulence beneath surface waves in Reynolds-averaged Navier–Stokes models. *Journal of Fluid Mechanics*, 853:419–460. Publisher: Cambridge University Press.

Le Méhauté, B. (1976). An Introduction to Water Waves. In *An Introduction to Hydrodynamics and Water Waves*, pages 197–211. Springer Berlin Heidelberg, Berlin, Heidelberg.

LeCun, Y., Bengio, Y., and Hinton, G. (2015). Deep learning. *Nature*, 521(7553):436–444.

Ley, J. and El Moctar, O. (2021). A Comparative Study of Computational Methods for Wave-Induced Motions and Loads. *Journal of Marine Science and Engineering*, 9(1):83.

Li, G., Weiss, G., Mueller, M., Townley, S., and Belmont, M. R. (2012). Wave en-

ergy converter control by wave prediction and dynamic programming. *Renewable Energy*, 48:392–403.

Li, Q., Luo, K., Kang, Q., He, Y., Chen, Q., and Liu, Q. (2016). Lattice Boltzmann methods for multiphase flow and phase-change heat transfer. *Progress in Energy and Combustion Science*, 52:62–105.

Li, Y., Draycott, S., Zheng, Y., Lin, Z., Adcock, T. A., and Van Den Bremer, T. S. (2021). Why rogue waves occur atop abrupt depth transitions. *Journal of Fluid Mechanics*, 919:R5.

Li, Y. and Fuhrman, D. R. (2021). CFD Simulation of Nonlinear Deep-Water Wave Instabilities Involving Wave Breaking. In *Volume 6: Ocean Engineering*. American Society of Mechanical Engineers.

Li, Y., Larsen, B. E., and Fuhrman, D. R. (2022). Reynolds stress turbulence modelling of surf zone breaking waves. *Journal of Fluid Mechanics*, 937:A7.

Li, Z., Kovachki, N., Azizzadenesheli, K., Liu, B., Bhattacharya, K., Stuart, A., and Anandkumar, A. (2020). Fourier Neural Operator for Parametric Partial Differential Equations.

Liao, B., Dong, G., Ma, Y., Ma, X., and Perlin, M. (2023). Modified nonlinear Schrödinger equation for gravity waves with the influence of wind, currents, and dissipation. *Physics of Fluids*, 35(3):037103.

Lim, H., Chang, K., Huang, Z., and Na, B. (2015). Experimental study on plunging breaking waves in deep water. *Journal of Geophysical Research: Oceans*, 120(3):2007–2049.

Lin, P. and Liu, P. L.-F. (1998). A numerical study of breaking waves in the surf zone. *Journal of Fluid Mechanics*, 359:239–264. Publisher: Cambridge University Press.

Liu, R. W., Yuan, W., Chen, X., and Lu, Y. (2021). An enhanced CNN-enabled learning method for promoting ship detection in maritime surveillance system. *Ocean Engineering*, 235:109435.

Liu, W., Chen, S., Hu, K., Guo, X., Wang, Q., Song, X., Liu, Z., and Li, Y. (2024a). Experimental and Numerical Investigation of the Hydroelastic Response of a Hinged Hexagon Enclosed Platform in Waves. *IEEE Journal of Oceanic Engineering*, 49(2):368–379.

Liu, W., Mo, Y., Xiong, L., Xu, H., Song, X., and Li, Y. (2024b). Hydroelasto-Plastic Response of a Ship Model in Freak Waves: An Experimental and Numerical Investigation. *Journal of Marine Science and Engineering*, 12(9):1555.

Liu, Y., Eeltink, D., Bremer, T. S. v. d., and Adcock, T. A. A. (2024c). A machine learning architecture for including wave breaking in envelope-type wave models. *Ocean Engineering*, 305:118009.

Liu, Y., Eeltink, D., Tang, T., Barratt, D., Li, Y., Adcock, T. A. A., and Bremer, T. S. v. d. (2023). Comparison of breaking models in envelope-based surface gravity wave evolution equations. *Physical Review Fluids*, 8(5):054803.

Lo, E. and Mei, C. C. (1985). A numerical study of water-wave modulation based on a higher-order nonlinear Schrödinger equation. *Journal of Fluid Mechanics*, 150:395–416. Publisher: Cambridge University Press (CUP).

Longuet-Higgins, M. S. (1953). Mass transport in water waves. *Philosophical Transactions of the Royal Society of London. Series A, Mathematical and Physical Sciences*, 245(903):535–581.

Lu, L., Jin, P., Pang, G., Zhang, Z., and Karniadakis, G. E. (2021). Learning nonlinear operators via DeepONet based on the universal approximation theorem of operators. *Nature Machine Intelligence*, 3(3):218–229.

Lubin, P. and Glockner, S. (2015). Numerical simulations of three-dimensional

plunging breaking waves: generation and evolution of aerated vortex filaments. *Journal of Fluid Mechanics*, 767:364–393. Publisher: Cambridge University Press.

López, I., Pereiras, B., Castro, F., and Iglesias, G. (2014). Optimisation of turbine-induced damping for an OWC wave energy converter using a RANS–VOF numerical model. *Applied Energy*, 127:105–114. Publisher: Elsevier Ltd.

Ma, Q. and Yan, S. (2006). Quasi ALE finite element method for nonlinear water waves. *Journal of Computational Physics*, 212(1):52–72.

Ma, Q. W., Zhou, Y., and Yan, S. (2016). A review on approaches to solving Poisson's equation in projection-based meshless methods for modelling strongly nonlinear water waves. *Journal of Ocean Engineering and Marine Energy*, 2(3):279–299.

Ma, Y., Sclavounos, P. D., Cross-Whiter, J., and Arora, D. (2018). Wave forecast and its application to the optimal control of offshore floating wind turbine for load mitigation. *Renewable Energy*, 128:163–176.

Mahjoobi, J. and Adeli Mosabbeb, E. (2009). Prediction of significant wave height using regressive support vector machines. *Ocean Engineering*, 36(5):339–347.

Majda, A. and Wang, X. (2001). The selective decay principle for barotropic geophysical flows. *Methods and Applications of Analysis*, 8(4):579–594. Publisher: International Press of Boston.

Manucharyan, G. E., Siegelman, L., and Klein, P. (2021). A Deep Learning Approach to Spatiotemporal Sea Surface Height Interpolation and Estimation of Deep Currents in Geostrophic Ocean Turbulence. *Journal of Advances in Modeling Earth Systems*, 13(1).

Mayer, S. and Madsen, P. A. (2001). Simulation of Breaking Waves in the Surf Zone using a Navier-Stokes Solver. In *Coastal Engineering 2000*, pages 928–941. American Society of Civil Engineers.

McAllister, M. L., Pizzo, N., Draycott, S., and Bremer, T. S. v. d. (2023). The influence of spectral bandwidth and shape on deep-water wave breaking onset. *Journal of Fluid Mechanics*, 974:A14.

Mei, C. C. (1989). *The applied dynamics of ocean surface waves*. Number 1 in Advanced series on ocean engineering. World Scientific, Singapore, 2. print. with corrections edition.

Melville, W. K. (1982). The instability and breaking of deep-water waves. *Journal of Fluid Mechanics*, 115(-1):165. Publisher: Cambridge University Press (CUP).

Melville, W. K. (1996). The role of surface-wave breaking in air-sea interaction. *Annual review of fluid mechanics*, 28(1):279–321. Publisher: Annual Reviews 4139 El Camino Way, PO Box 10139, Palo Alto, CA 94303-0139, USA.

Melville, W. K., Shear, R., and Veron, F. (1998). Laboratory measurements of the generation and evolution of Langmuir circulations. *Journal of Fluid Mechanics*, 364:31–58.

Menter, F. (1993). Zonal Two Equation k-w Turbulence Models For Aerodynamic Flows. In *23rd Fluid Dynamics, Plasmadynamics, and Lasers Conference*, Orlando,FL,U.S.A. American Institute of Aeronautics and Astronautics.

Mostert, W. and Deike, L. (2020). Inertial energy dissipation in shallow-water breaking waves. *Journal of Fluid Mechanics*, 890:A12. Publisher: Cambridge University Press.

Mostert, W., Popinet, S., and Deike, L. (2022). High-resolution direct simulation of deep water breaking waves: transition to turbulence, bubbles and droplets production. *Journal of Fluid Mechanics*, 942:A27. Publisher: Cambridge University Press.

Muis, S., Verlaan, M., Winsemius, H. C., Aerts, J. C. J. H., and Ward, P. J. (2016). A global reanalysis of storm surges and extreme sea levels. *Nature Communications*, 7(1):11969.

Neill, S. P., Angeloudis, A., Robins, P. E., Walkington, I., Ward, S. L., Masters, I., Lewis, M. J., Piano, M., Avdis, A., Piggott, M. D., Aggidis, G., Evans, P., Adcock, T. A., Židonis, A., Ahmadian, R., and Falconer, R. (2018). Tidal range energy resource and optimization – Past perspectives and future challenges. *Renewable Energy*, 127:763–778. Publisher: Elsevier BV.

Nouguier, F., Grilli, S. T., and Guérin, C.-A. (2014). Nonlinear Ocean Wave Reconstruction Algorithms Based on Simulated Spatiotemporal Data Acquired by a Flash LIDAR Camera. *IEEE Transactions on Geoscience and Remote Sensing*, 52(3):1761–1771. Conference Name: IEEE Transactions on Geoscience and Remote Sensing.

Oumrani, N., Aouissi, M., Bounif, A., Yssaad, B., Tabet, F., and Gokalp, I. (2015). A first- and second-order turbulence models in hydrogen non-premixed flame. *International Journal of Heat and Technology*, 33(3):27–34.

Peregrine, D. H. (2003). Water-wave impact on walls. *Annual review of fluid mechanics*, 35:23. Publisher: Annual Reviews, Inc.

Perlin, M., Choi, W., and Tian, Z. (2013). Breaking Waves in Deep and Intermediate Waters. *Annual Review of Fluid Mechanics*, 45(1):115–145.

Phillips, O. M. (1985). Spectral and statistical properties of the equilibrium range in wind-generated gravity waves. *Journal of Fluid Mechanics*, 156(-1):505.

Pope, S. B. (1978). An explanation of the turbulent round-jet/plane-jet anomaly. *AIAA Journal*, 16(3):279–281.

Pope, S. B. (2000). *Turbulent Flows*. Cambridge University Press.

Popinet, S. (2009). An accurate adaptive solver for surface-tension-driven interfacial flows. *Journal of Computational Physics*, 228(16):5838–5866.

Popinet, S. (2015). A quadtree-adaptive multigrid solver for the Serre–Green–Naghdi equations. *Journal of Computational Physics*, 302:336–358.

Portillo Juan, N. and Negro Valdecantos, V. (2022). Review of the application of Artificial Neural Networks in ocean engineering. *Ocean Engineering*, 259:111947.

Previsic, M., Karthikeyan, A., and Lyzenga, D. (2021). In-Ocean Validation of a Deterministic Sea Wave Prediction (DSWP) System leveraging X-Band Radar to Enable Optimal Control in Wave Energy Conversion Systems. *Applied Ocean Research*, 114:102784.

Qi, D. and Majda, A. J. (2020). Using machine learning to predict extreme events in complex systems. *Proceedings of the National Academy of Sciences*, 117(1):52–59.

Qiu, R., Huang, R., Xiao, Y., Wang, J., Zhang, Z., Yue, J., Zeng, Z., and Wang, Y. (2022). Physics-informed neural networks for phase-field method in two-phase flow. *Physics of Fluids*, 34(5):052109.

Raissi, M. (2018). Deep Hidden Physics Models: Deep Learning of Nonlinear Partial Differential Equations.

Raissi, M., Perdikaris, P., and Karniadakis, G. (2019). Physics-informed neural networks: A deep learning framework for solving forward and inverse problems involving nonlinear partial differential equations. *Journal of Computational Physics*, 378:686–707.

Rapp, R. J. and Melville, W. K. (1990). Laboratory measurements of deep-water breaking waves. *Philosophical Transactions of the Royal Society of London. Series A, Mathematical and Physical Sciences*, 331(1622):735–800.

Reeve, D. E., Chadwick, A., and Fleming, C. (2018). *Coastal engineering*. CRC Press, Boca Raton London New York, third edition edition.

Romero, L., Melville, W. K., and Kleiss, J. M. (2012). Spectral Energy Dissipation due to Surface Wave Breaking. *Journal of Physical Oceanography*, 42(9):1421–1444.

Rumsey, C. (2023). Notes on running the cases with CFD. Turbulence modeling resource. https://turbmodels.larc.nasa.gov/noteonrunning.html.

Samuel, A. L. (1959). Some Studies in Machine Learning Using the Game of Checkers. *IBM Journal of Research and Development*, 3(3):210–229.

Scarselli, F., Gori, M., Ah Chung Tsoi, Hagenbuchner, M., and Monfardini, G. (2009). The Graph Neural Network Model. *IEEE Transactions on Neural Networks*, 20(1):61–80.

Schmidhuber, J. (2022). Annotated History of Modern AI and Deep Learning.

Schmidt, R. M. (2019). Recurrent Neural Networks (RNNs): A gentle Introduction and Overview. Version Number: 1.

Schmitt, F. G. (2007). About Boussinesq's turbulent viscosity hypothesis: historical remarks and a direct evaluation of its validity. *Comptes Rendus Mécanique*, 335(9-10):617–627.

Semedo, A., Sušelj, K., Rutgersson, A., and Sterl, A. (2011). A Global View on the Wind Sea and Swell Climate and Variability from ERA-40. *Journal of Climate*, 24(5):1461–1479.

Shemer, L. and Dorfman, B. (2008). Experimental and numerical study of spatial and temporal evolution of nonlinear wave groups. *Nonlinear Processes in Geophysics*, 15(6):931–942.

Shemer, L., Kit, E., and Jiao, H. (2002). An experimental and numerical study of the spatial evolution of unidirectional nonlinear water-wave groups. *Physics of Fluids*, 14(10):3380–3390.

Shemer, L., Sergeeva, A., and Liberzon, D. (2010). Effect of the initial spectrum on the spatial evolution of statistics of unidirectional nonlinear random waves. *Journal of Geophysical Research: Oceans*, 115(C12).

Shi, F., Chen, Z., Wang, H., Yeung, D.-Y., Wong, W.-k., and WOO, W.-c. (2015). Convolutional LSTM Network: A Machine Learning Approach for Precipitation Nowcasting. In Cortes, C., Lawrence, N., Lee, D., Sugiyama, M., and Garnett, R.,

editors, *Advances in Neural Information Processing Systems*, volume 28. Curran Associates, Inc.

Solera-Rico, A., Sanmiguel Vila, C., Gómez-López, M., Wang, Y., Almashjary, A., Dawson, S. T. M., and Vinuesa, R. (2024). β-Variational autoencoders and transformers for reduced-order modelling of fluid flows. *Nature Communications*, 15(1):1361.

Song, T., Han, R., Meng, F., Wang, J., Wei, W., and Peng, S. (2022). A significant wave height prediction method based on deep learning combining the correlation between wind and wind waves. *Frontiers in Marine Science*, 9:983007.

Stokes, G. (1847). *On the Theory of Oscillatory Waves*. Transactions of the Cambridge Philosophical Society. Printed at the Pitt Press by John W. Parker.

Tian, Z., Perlin, M., and Choi, W. (2012). An eddy viscosity model for two-dimensional breaking waves and its validation with laboratory experiments. *Physics of Fluids*, 24(3):036601. Publisher: American Institute of Physics Inc.

Ting, F. C. and Kirby, J. T. (1994). Observation of undertow and turbulence in a laboratory surf zone. *Coastal Engineering*, 24(1-2):51–80.

Toffoli, A., Babanin, A., Onorato, M., and Waseda, T. (2010a). Maximum steepness of oceanic waves: Field and laboratory experiments. *Geophysical Research Letters*, 37(5). Publisher: Wiley Online Library.

Toffoli, A., Gramstad, O., Trulsen, K., Monbaliu, J., Bitner-Gregersen, E., and Onorato, M. (2010b). Evolution of weakly nonlinear random directional waves: laboratory experiments and numerical simulations. *Journal of Fluid Mechanics*, 664:313–336. Publisher: Cambridge University Press.

Trulsen, K. and Dysthe, K. B. (1990). Frequency Down-Shift Through Self Modulation and Breaking. In *Water Wave Kinematics*, pages 561–572. Springer Netherlands.

Trulsen, K. and Dysthe, K. B. (1996). A modified nonlinear Schrödinger equation for broader bandwidth gravity waves on deep water. *Wave Motion*, 24(3):281–289. Publisher: Elsevier BV.

Trulsen, K., Kliakhandler, I., Dysthe, K. B., and Velarde, M. G. (2000). On weakly nonlinear modulation of waves on deep water. *Physics of Fluids*, 12(10):2432. Publisher: AIP Publishing.

Tucker, M., Challenor, P., and Carter, D. (1984). Numerical simulation of a random sea: a common error and its effect upon wave group statistics. *Applied Ocean Research*, 6(2):118–122.

Tulin, M. P. and Waseda, T. (1999). Laboratory observations of wave group evolution, including breaking effects. *Journal of Fluid Mechanics*, 378:197–232. Publisher: Cambridge University Press (CUP).

Van Sebille, E., Aliani, S., Law, K. L., Maximenko, N., Alsina, J. M., Bagaev, A., Bergmann, M., Chapron, B., Chubarenko, I., Cózar, A., Delandmeter, P., Egger, M., Fox-Kemper, B., Garaba, S. P., Goddijn-Murphy, L., Hardesty, B. D., Hoffman, M. J., Isobe, A., Jongedijk, C. E., Kaandorp, M. L. A., Khatmullina, L., Koelmans, A. A., Kukulka, T., Laufkötter, C., Lebreton, L., Lobelle, D., Maes, C., Martinez-Vicente, V., Morales Maqueda, M. A., Poulain-Zarcos, M., Rodríguez, E., Ryan, P. G., Shanks, A. L., Shim, W. J., Suaria, G., Thiel, M., Van Den Bremer, T. S., and Wichmann, D. (2020). The physical oceanography of the transport of floating marine debris. *Environmental Research Letters*, 15(2):023003.

Vaswani, A., Shazeer, N., Parmar, N., Uszkoreit, J., Jones, L., Gomez, A. N., Kaiser, L., and Polosukhin, I. (2017). Attention Is All You Need. Version Number: 7.

WAMDI (1988). The WAM Model—A Third Generation Ocean Wave Prediction Model. *Journal of Physical Oceanography*, 18(12):1775–1810.

Wilcox, D. (2006). *Turbulence Modeling for CFD*. DCW Industries, third edition.

Wilcox, D. C. (2008). Formulation of the k-ω Turbulence Model Revisited. *AIAA Journal*, 46(11):2823–2838.

Xie, Z. (2013). Two-phase flow modelling of spilling and plunging breaking waves. *Applied Mathematical Modelling*, 37(6):3698–3713.

Xu, F., Zou, Z.-J., Yin, J.-C., and Cao, J. (2013). Identification modeling of underwater vehicles' nonlinear dynamics based on support vector machines. *Ocean Engineering*, 67:68–76.

Xue, H., Wang, S., Xia, M., and Guo, S. (2024). G-Trans: A hierarchical approach to vessel trajectory prediction with GRU-based transformer. *Ocean Engineering*, 300:117431.

Zakharov, V. E. (1972). Stability of periodic waves of finite amplitude on the surface of a deep fluid. *Journal of Applied Mechanics and Technical Physics*, 9(2):190–194.

Zakharov, V. E. and Shabat, A. B. (1972). Exact Theory of Two-dimensional Self-focusing and One-dimensional Self-modulation of Waves in Nonlinear Media. *Soviet Journal of Experimental and Theoretical Physics*, 34:62.

Zhang, J.-S., Zhang, Y., Jeng, D.-S., Liu, P. L.-F., and Zhang, C. (2014). Numerical simulation of wave–current interaction using a RANS solver. *Ocean Engineering*, 75:157–164.

Zhang, L., Wen, J., Huo, Z., Li, Z., Xi, M., and Yang, J. (2024a). From land to ocean: bathymetric terrain reconstruction via conditional generative adversarial network. *Earth Science Informatics*.

Zhang, M., Yuan, Z.-M., Dai, S.-S., Chen, M.-L., and Incecik, A. (2024b). LSTM RNN-based excitation force prediction for the real-time control of wave energy converters. *Ocean Engineering*, 306:118023.

Zhang, M., Zhang, X., Fu, S., Dai, L., and Yu, Q. (2023). Recent Developments and Knowledge in Intelligent and Safe Marine Navigation. *Journal of Marine Science and Engineering*, 11(12):2303.

Zhang, N., Yan, S., Ma, Q., and Li, Q. (2024c). Numerical simulation of wave-floater interactions using ISPH_gnn trained on data for wave-only cases. *Ocean Engineering*, 306:118041.

Zhao, M., Zheng, Y., and Lin, Z. (2023). Sea surface reconstruction from marine radar images using deep convolutional neural networks. *Journal of Ocean Engineering and Science*, 8(6):647–661.

Zheng, Y., Lin, Z., Li, Y., Adcock, T. A. A., Li, Y., and Van Den Bremer, T. S. (2020). Fully nonlinear simulations of unidirectional extreme waves provoked by strong depth transitions: The effect of slope. *Physical Review Fluids*, 5(6):064804.

Zinchenko, V., Vasilyev, L., Halstensen, S. O., and Liu, Y. (2021). An improved algorithm for phase-resolved sea surface reconstruction from X-band marine radar images. *Journal of Ocean Engineering and Marine Energy*, 7(1):97–114.

Appendix A

ConvLSTM neural network architecture

The ConvLSTM network replaces all matrix multiplication operations with convolutions, making it suitable for tasks related to image sequence prediction. The modified equations are written as follows:

$$i_t = \sigma(W_{xi} * X_t + W_{hi} * H_{t-1} + W_{ci} \circ C_{t-1} + b_i), \tag{A.1}$$

$$f_t = \sigma(W_{xf} * X_t + W_{hf} * H_{t-1} + W_{cf} \circ C_{t-1} + b_f), \tag{A.2}$$

$$C_t = f_t \circ C_{t-1} + i_t \circ \tanh(W_{xc} * X_t + W_{hc} * H_{t-1} + b_c), \tag{A.3}$$

$$o_t = \sigma(W_{xo} * X_t + W_{ho} * H_{t-1} + W_{co} \circ C_t + b_o), \tag{A.4}$$

$$H_t = o_t \circ \tanh(C_t), \tag{A.5}$$

where

- i_t, f_t, o_t, C_t, and H_t represent the input gate, forget gate, output gate, cell state, and hidden state at time step t, respectively.
- σ denotes the sigmoid function, which serves as an activation function.
- $*$ denotes convolution operation.
- $\circ$ denotes the Hadamard product (element-wise multiplication).

- W and b terms represent the weights and biases for different gates and states, with subscripts xi, xf, xc, xo, hi, hf, hc, ho, ci, and co indicating the specific gate or cell state with which they are associated.
- X_t is the input at time step t.
- H_{t-1} and C_{t-1} are the hidden state and cell state from the previous time step $t-1$, respectively.
- tanh is the hyperbolic tangent function, which serves as an activation function.

Appendix B

Appendices for Chapter 3

B.1 Comparison for Additional Perturbed Plane Wave Cases

Figures B.1, B.2, and B.3 show the comparison with experimental data for the additional three cases from Eeltink et al. (2022) in Table 3.2. Figure B.1 shows the non-breaking experiment (case 2). The breaking models that include a breaking criterion (TD90 and H11) are not turned on or only turned on briefly with only a weak breaking effect, and resulting predictions are equivalent (or very similar) to the case with no breaking model (NBM). No significant permanent downshift is observed, but we emphasise that considerable difference between experiments and MNLS predictions remains. Figure B.2 shows case 3, which has the largest steepness among the four cases. We find that the M-KO95 model achieves the best match of the amplitude of the carrier wave, while all the models underestimate the amplitude of the lower sideband. In Figure B.3, the M-KO95 and KO95 models match best to experimental data in terms of the carrier wave amplitude. All models can match the amplitudes of upper and lower sidebands reasonably well.

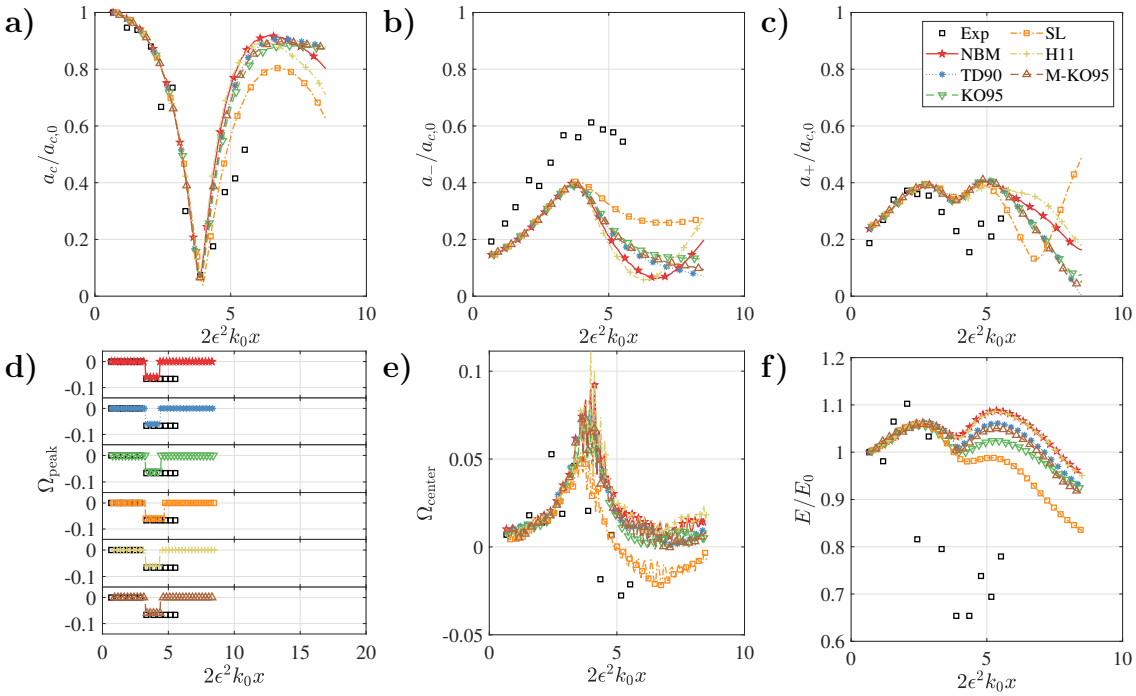


Figure B.1: Similar to Figure 3.3 but for case 2 from Table 3.2: spatial evolution of perturbed plane waves, showing a) the carrier wave normalised by its value at the first gauge, $a_c/a_{c,0}$; b) the normalised lower sideband $a_-/a_{c,0}$; c) the normalised upper sideband, $a_+/a_{c,0}$; d) the spectral peak, $\Omega_{\text{peak}} = \text{argmax}_\Omega \hat{A}$ with $\hat{A}$ the amplitude spectrum of η and $\Omega = \omega/\omega_0 - 1$; e) spectral mean or centroid, $\Omega_{\text{center}} = \sum \Omega_i \hat{A}_i / \sum \hat{A}_i$; f) the energy measure $E = \int |B|^2 \, \mathrm{d}t$ normalised by its value at the first gauge E_0. The black squares show the experimental data from Eeltink et al. (2022)).

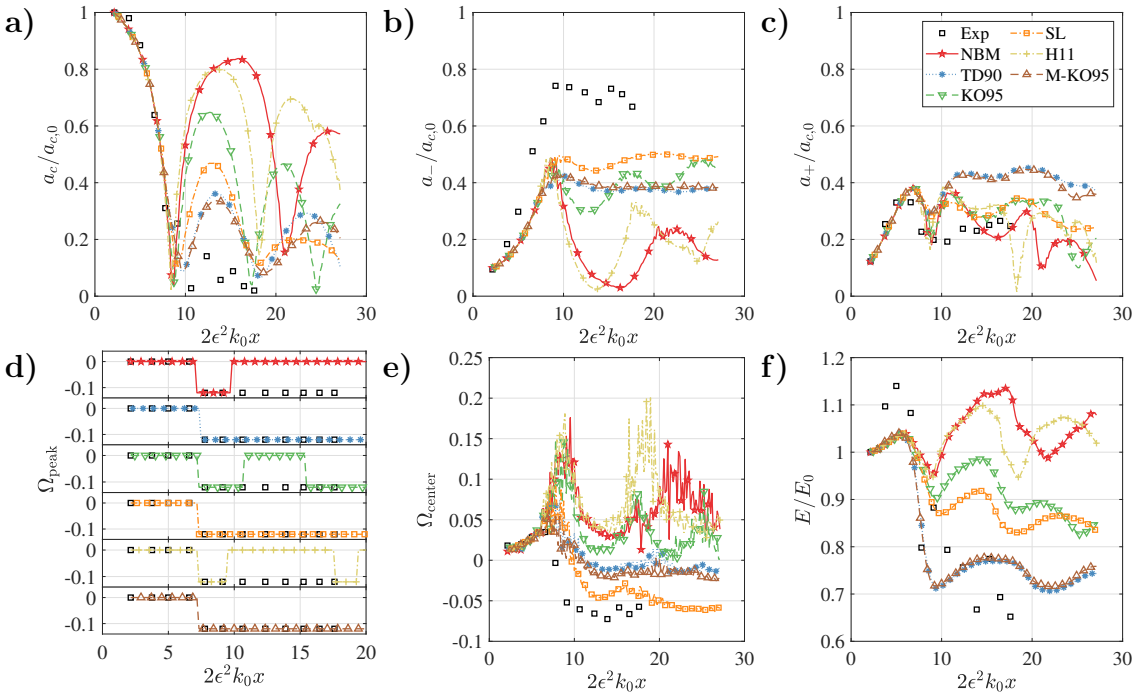


Figure B.2: Similar to Figures 3.3 and B.1 but for case 3 from Table 3.2.

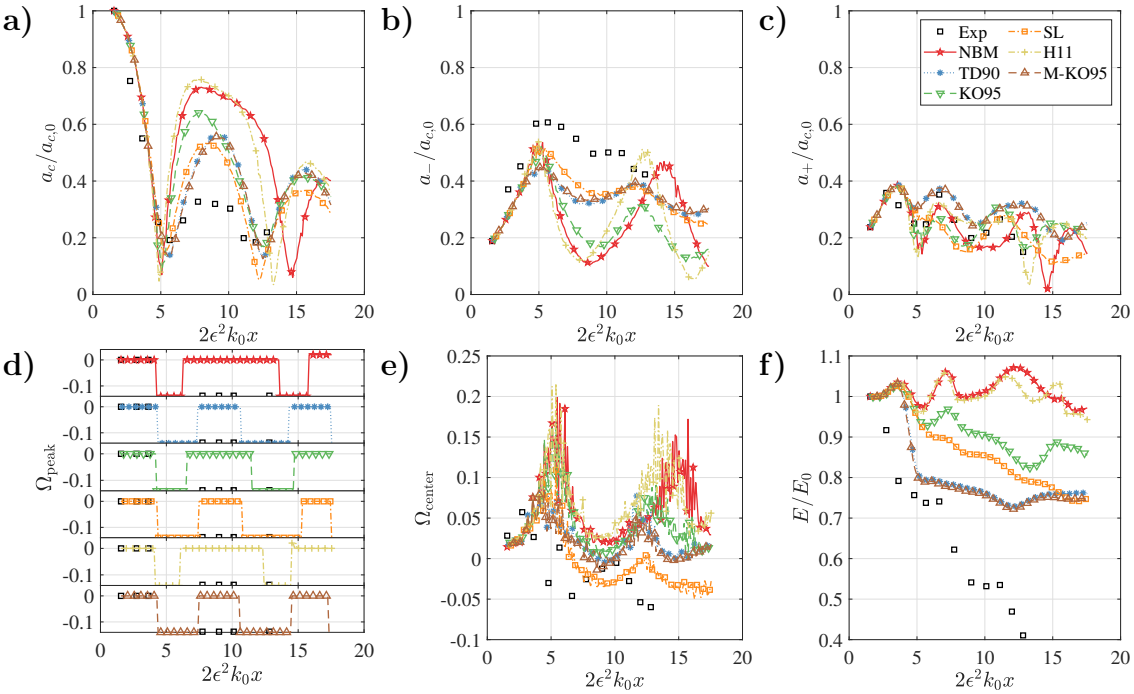


Figure B.3: Similar to Figures 3.3 and B.1 but for case 4 from Table 3.2.

B.2 Performance of Other Modified Models

In §3.5.3, we introduced a method to modify existing reduced-form breaking models by adding a spectrally weighted dissipation strength parameter as well different breaking criteria. In §3.5.4, we presented results for the M-KO95 model. In this section, we will examine modification of the other three models and evaluate their performance compared to our focused wave experiments.

Modified Trulsen & Dysthe (1990) Model (M-TD90)

The modified Trulsen & Dysthe (1990) (M-TD90) model has the form:

$$D = -\frac{1}{\tau} B \mathcal{F}^{-1}\left[\hat{\beta}(k)\mathcal{F}\left[\left(\frac{|B|}{B_0}\right)^r - 1\right]\right] H, \tag{B.1}$$

where H is the Heaviside function corresponding to one of the three breaking criteria in §3.5.1.

Modified Selective Laplacian Model (M-SL)

In Fourier space, the modified selective Laplacian (M-SL) model can be written as:

$$\hat{D} = \begin{cases} -\hat{\beta}(k)\frac{\omega_0}{k_0^2}\left(|k| - k^*\right)^2 \hat{B}(k)H & \text{for} \quad |k| > k^*, \\ 0 & \text{for} \quad |k| \leq k^*, \end{cases} \tag{B.2}$$

where $k^* = 1.2k_0$ as before.

Modified Hwung et al. (2011) Model (M-H11)

The modified Hwung et al. (2011) (M-H11) model has the form:

$$D = B\left(\frac{D_a}{g} + i4\gamma \int \frac{k_0 D_a}{g}\mathrm{d}x\right)H, \tag{B.3}$$

where $D_a = \omega_0 k_0^2/2\mathcal{F}^{-1}(\hat{\beta}(k)\mathcal{F}(|B|^2))$.

Comparison Between Modified Models

In Table B.1 we show the L2 loss for case 1, which is used in the optimisation, and case 2 for the three modified models above. We find that model modification reduces the L2 loss in general. The fact that the L2 loss is not improved as much for case 2 as for case 1 suggests the modified model we proposed cannot generally explain both cases; the good agreement for case 1 may be due to over-fitting. Among all the modified models, the M-KO95 model with a fixed-interval breaking criterion still achieves the lowest L2 loss for case 2 (not used for optimisation).

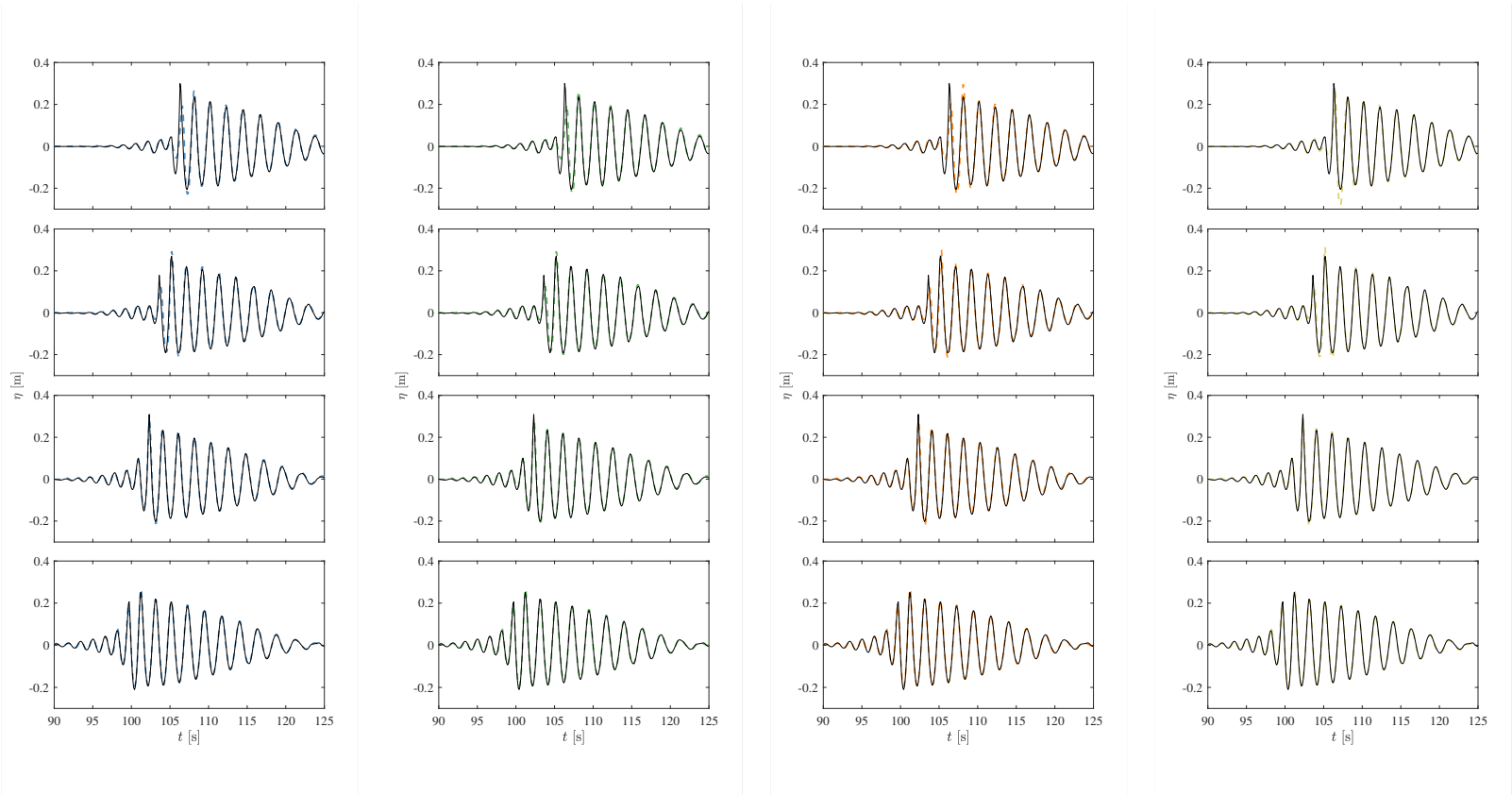
In Figure B.4 we show the surface elevation profiles for the optimised models. Compared to the case with values of the parameters from the literature, only modest improvements in the agreement of the surface elevation of the breaking crests with experiments is obtained with the optimised parameters.

In Figures B.5 and B.6 we examine the spectra for the optimised models and the modified models, respectively. Only the modified breaking models with a fixed-interval breaking criterion can reproduce the spectral dissipation of the 'shoulder'

correctly.

Model	**Breaking criterion**	**L2 loss (case 1)**	**L2 loss (case 2)**
NBM	None	1.00	1.00
M-KO95	Geometric	0.68	0.90
M-KO95	Kinetic	0.52	0.92
M-KO95	Fixed Interval	0.52	0.80
M-SL	Geometric	0.69	0.89
M-SL	Kinetic	0.56	0.89
M-SL	Fixed Interval	0.65	0.88
M-H11	Geometric	0.97	1.00
M-H11	Kinetic	0.66	1.00
M-H11	Fixed Interval	0.44	0.83
M-TD90	Geometric	0.65	0.91
M-TD90	Kinetic	0.33	0.92
M-TD90	Fixed Interval	0.49	0.86

Table B.1: Results from modification of the reduced-form breaking models (NBM denotes the case with no breaking model). The L2 loss is normalised by its value for the case with no breaking model.



(a) TD90 model, Geometric (b) KO95 model, Fixed Interval (c) SL model, Fixed Interval (d) H11 model, Kinematic

Figure B.4: For the reduced-form breaking models with optimised parameters, surface elevations at different gauge locations for focused wave groups (case 1 in Table 3.1). Black solid lines correspond to experimental data and coloured dashed lines to MNLS simulations with (a) the model of TD90; (b) the KO95 model with fixed-interval breaking criterion; (c) the SL model with fixed-interval breaking criterion; and (d) the H11 model with kinematic breaking criterion.

B.3 Dissipation Elements in Watertank Experiments

In this section we calculate the contribution from surface tension effect, internal friction and bottom&side-wall friction one by one to show the dissipation in watertank experiments. In this chapter, two experiments are introduced. One is performed in Shanghai JiaoTong University (SJTU) and the other is performed in Aix-Marseille University(AMU), France. For the watertank experiment in SJTU, the wave tank was 300 m long, 16 m wide, with a water depth of 7.33 m. The frequency of carrier wave modelled is f_0 = 0.5 Hz. For the other watertank experiment performed in AMU, the wave tank was 40 m long, 2.7 m wide, with a water depth of 0.80 m. The highest carrier frequency of modulated plane wave experiments is f_0 = 1.6 Hz.

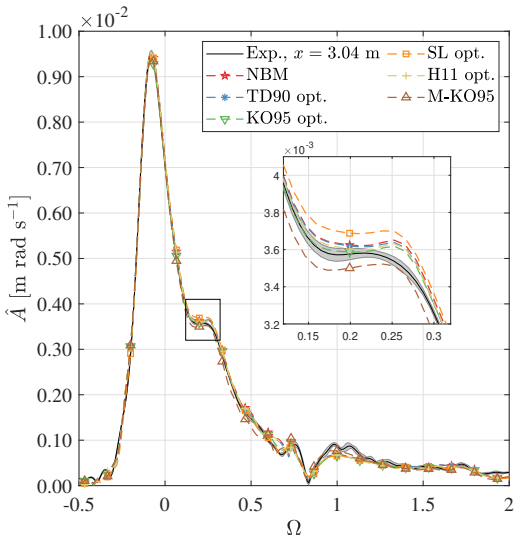
Based on "Rules of thumb" (Le Méhauté, 1976) we state that the surface tension contribution is negligible for both experiments as wave period is greater than 0.35 s and water depth is larger than 2 cm. In our case the wave period is no less than 0.625 s and water depth is 0.8 m. Hence the surface tension is negligible for all cases in this study.

Keulegan (1950) developed an expression to estimate the wave attenuation due to internal friction when boundary shear is negligible:

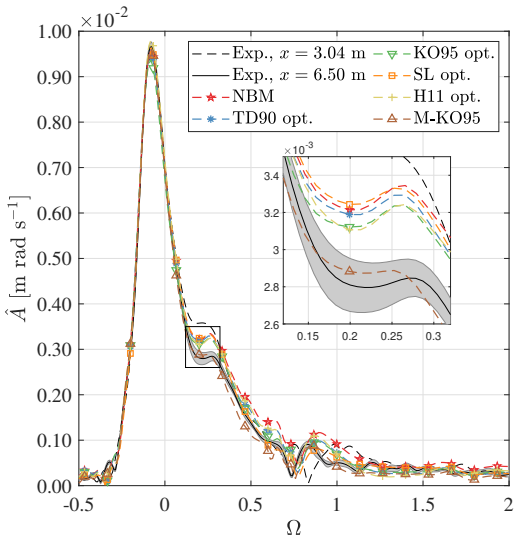
$$H(t) = H_0 e^{-8\pi\nu t/L^2}, \tag{B.4}$$

where H_0 is the wave amplitude at t = 0 and H is the wave amplitude at a given time t. $\nu = 10^{-6}\ m^2/s$ is the kinematic viscosity of water and L is the wave length. With (B.4) we found that the height loss due to internal friction is 0.03% with propagation time t = 155 s for SJTU experiment and 2.10% with propagation time t = 100 s for AMU experiment.

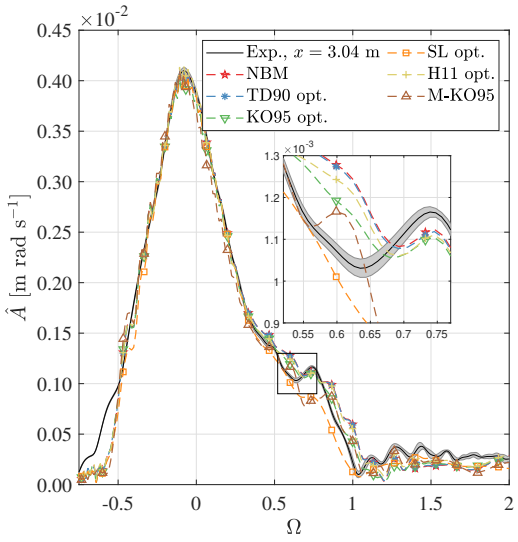
Keulegan (1950) developed another formula to estimate the wave attenuation of



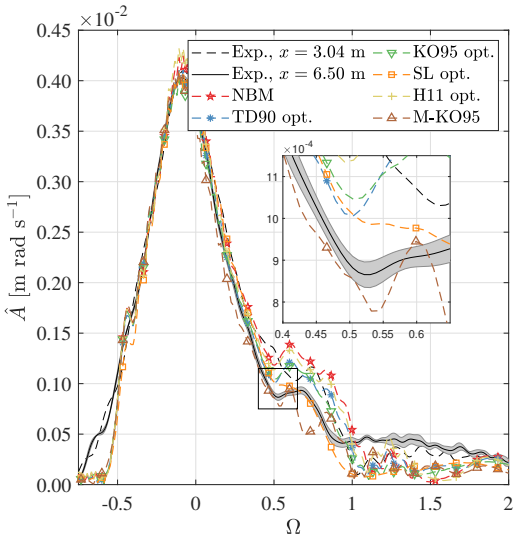
(a) Case 1, Before breaking (x = 3.04 m).



(b) Case 1, After breaking (x = 6.50 m).

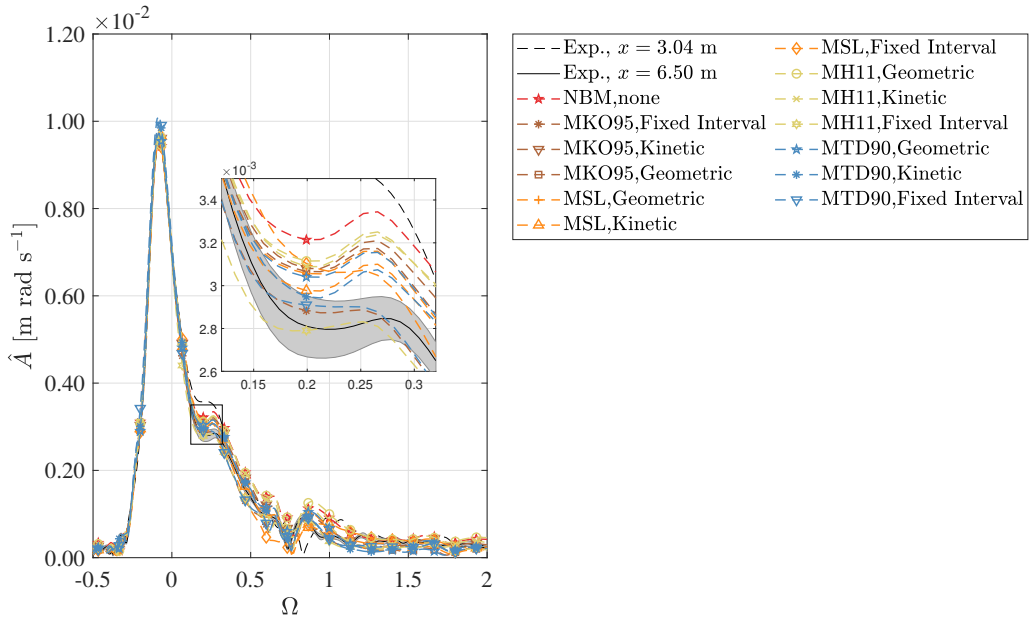


(c) Case 2, Before breaking (x = 3.04 m).

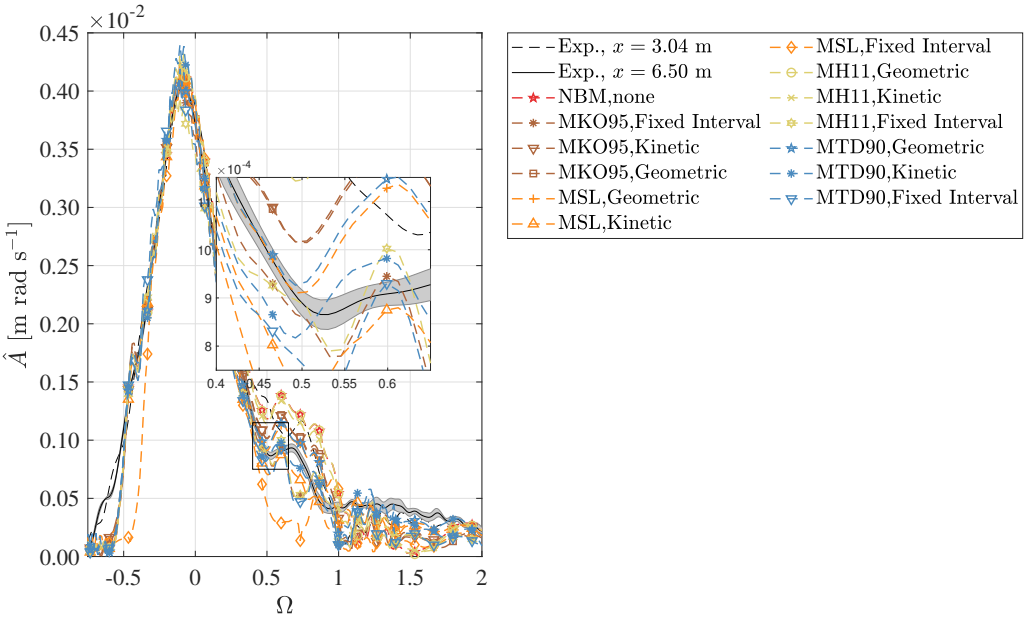


(d) Case 2, After breaking (x = 6.50 m).

Figure B.5: For the case with optimised parameters, comparison of amplitude spectra before and after breaking of a focused wave group (case 1 and case 2 in Table 3.1) for different reduced-form breaking models including no breaking model (NBM), showing experiments (black solid/dashed lines), with grey shaded region corresponding to ± 1 standard deviation from repeated experiments, and MNLS simulations with different breaking models (coloured dashed lines with markers).



(a) Case 1, After breaking (x = 6.50 m).



(b) Case 2, After breaking (x = 6.50 m).

Figure B.6: For the modified models, comparison of amplitude spectra after breaking of a focused wave group (case 1 and case 2 in Table 3.1) for different modified reduced-form breaking models with different breaking criteria and the case with no breaking model (NBM), showing experiments (black solid/dashed lines), with grey shaded region corresponding to ± 1 standard deviation from repeated experiments, and MNLS simulations with different modified breaking models and breaking criteria (coloured dashed lines with markers).

small amplitude linear wave in a wave flume with constant cross-section:

$$H_2/H_1 = e^{-\alpha x}, \tag{B.5}$$

where

$$\alpha = \frac{2}{BC}\sqrt{\frac{\pi\nu}{T}}\left[\frac{\sinh(\frac{4\pi h}{L}) + \frac{2\pi B}{L}}{\sinh(\frac{4\pi h}{L}) + \frac{4\pi h}{L}}\right], \tag{B.6}$$

and H_1 is the wave height at $x = 0$ and H_2 is the wave height at a given propagation distance x. B is the tank width, T is the wave period, $C = L/T$ is the wave celerity and h is the water depth. With (B.5) we found that the height loss due to bottom&side-wall friction is 0.75% with propagation distance $x = 150$ m for SJTU experiment and 6.58% with propagation distance $x = 40$ m for AMU experiment.

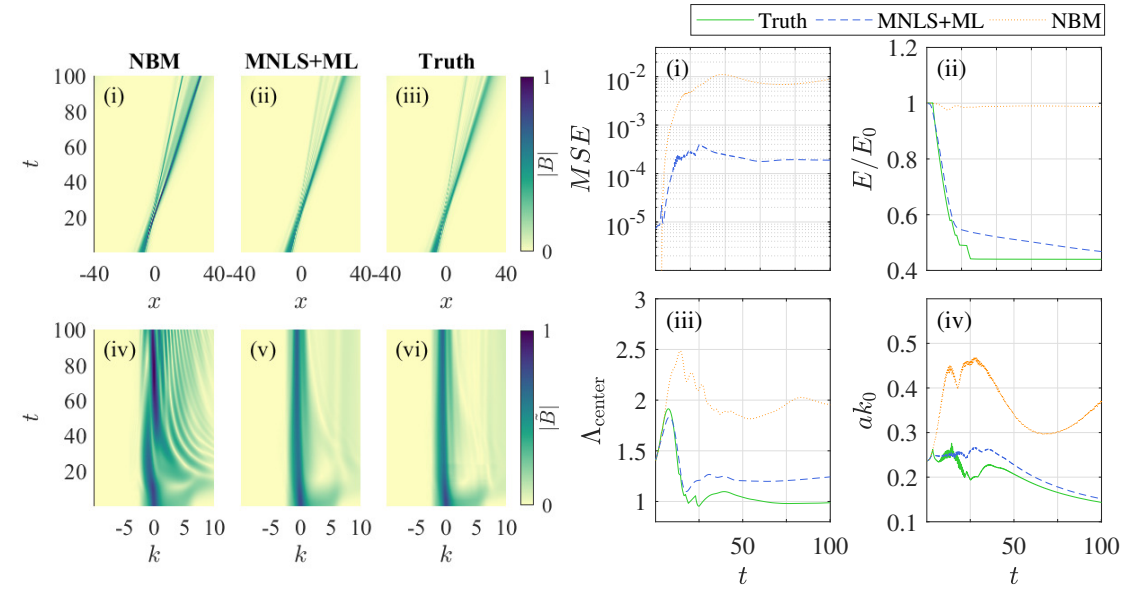
Appendix C

Appendices for Chapter 4

C.1 Simple Variants of the ConvLSTM Model

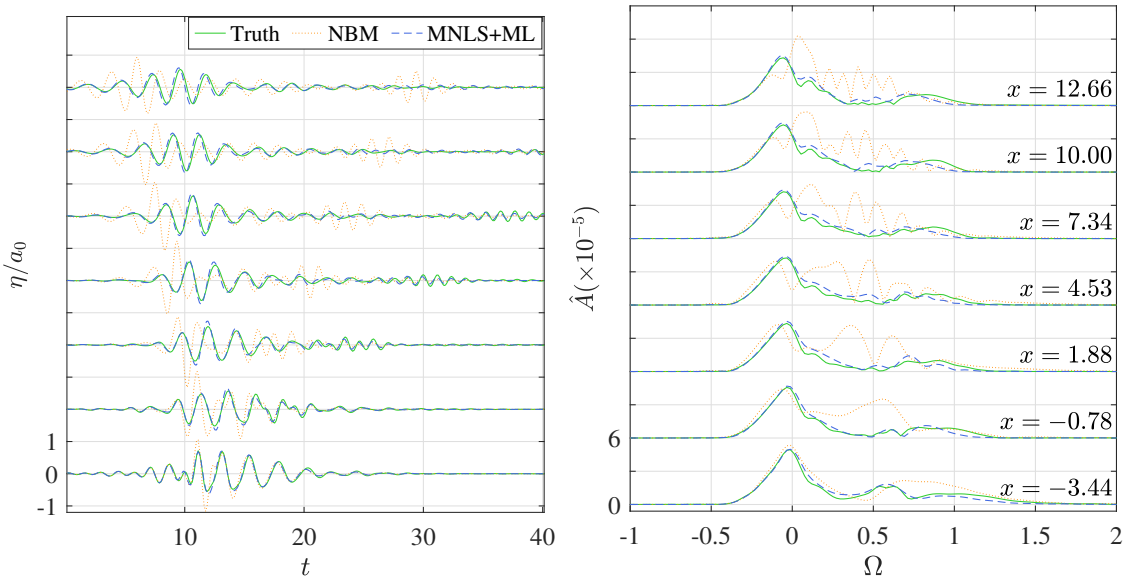
Figures C.1, C.2 and C.3 provides a comprehensive review on the performance of the w3f16 model. We can see that for all types of waves, the model is able to predict the evolution of the surface elevation reasonably well. It can also forecast the evolution of energy, spectral centroid and steepness of the wave field.

Figure C.4 plots the structure of four simple variants of the base model we have explored in this study. In this figure, the models accept an input $\hat{u}$ and provide an residual output z, where a shortcut is designed to build the final output by concatenating the input and the residual output in various ways. We find that after 200 epochs of training, the base model and variant V1 achieves a validation loss of 0.008, and variants V2, V3, V4 achieves a validation loss of 0.016. In addition, by utilizing ReLU activation function, variants V2, V3 and V4 is unconditionally stable as these models only dissipates energy, which is suitable for long-term predictions. Notice that these unconditionally stable variants impose an assumption that the wave breaking only dissipates the energy and/or modifies the phases.



(a) Envelope and wavenumber spectrum

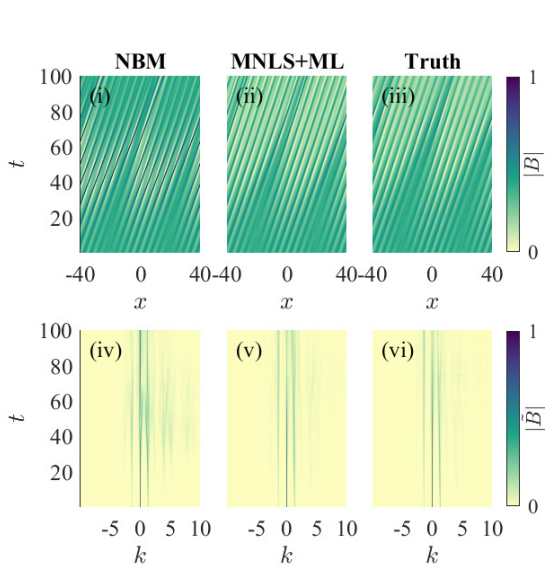
(b) MSE, energy, spectral mean and steepness



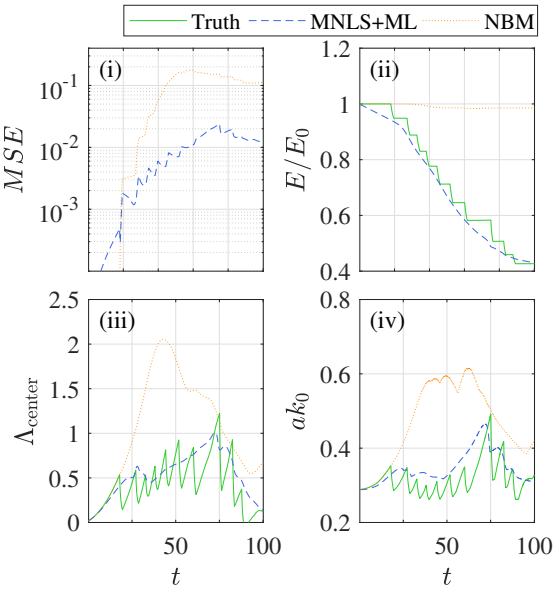
(c) Surface elevation

(d) Frequency spectrum

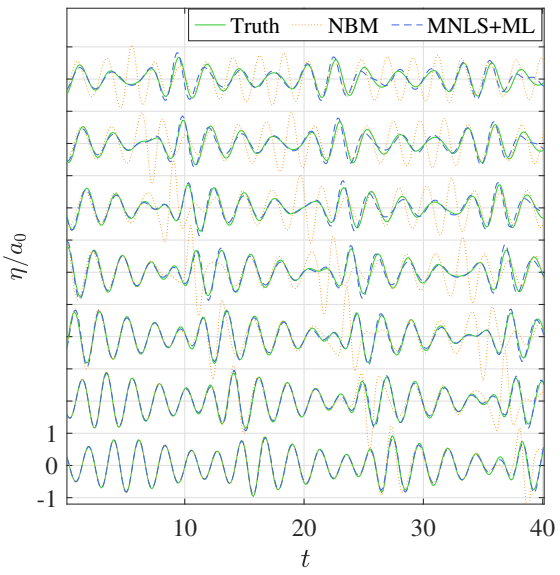
Figure C.1: Various measurements taken from a randomly selected test cases of focused wave, simulated by w3f16 model. The parameters for this case are $\gamma = 4.5027$, $a_0 = 0.0561$ m, $f_0 = 0.6100$ Hz, $L_f = 23.8265$ m and $\sigma_s = 1.2857$.



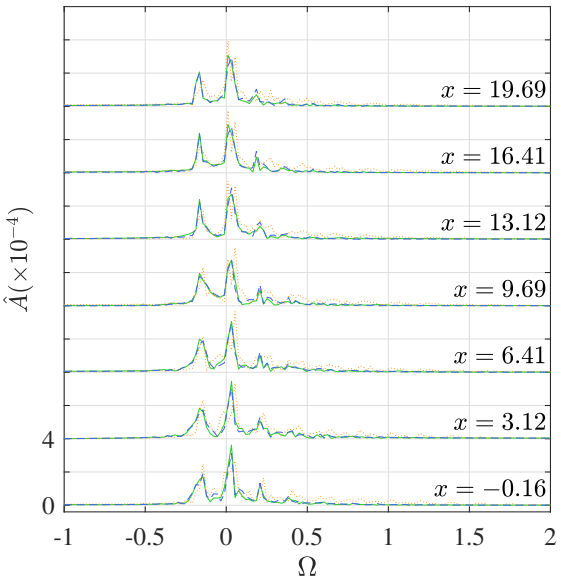
(a) Envelope and wavenumber spectrum



(b) MSE, energy, spectral mean and steepness

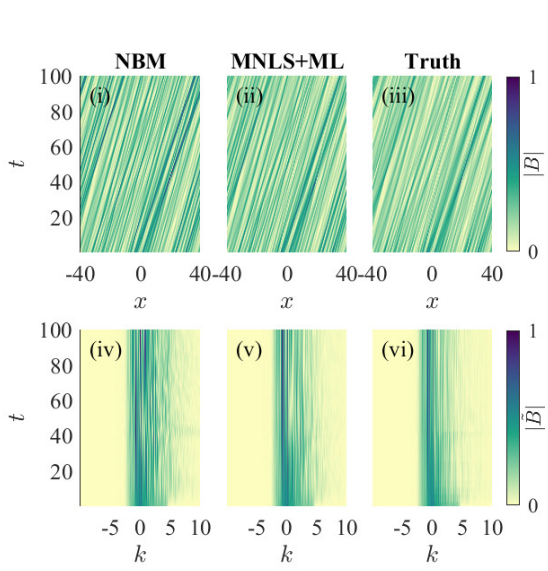


(c) Surface elevation

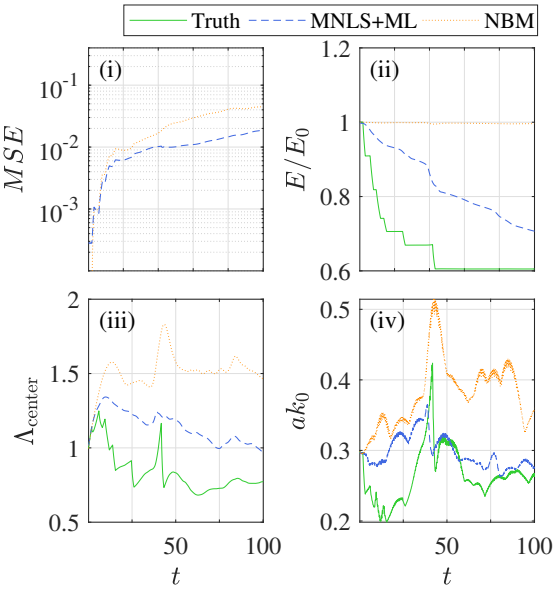


(d) Frequency spectrum

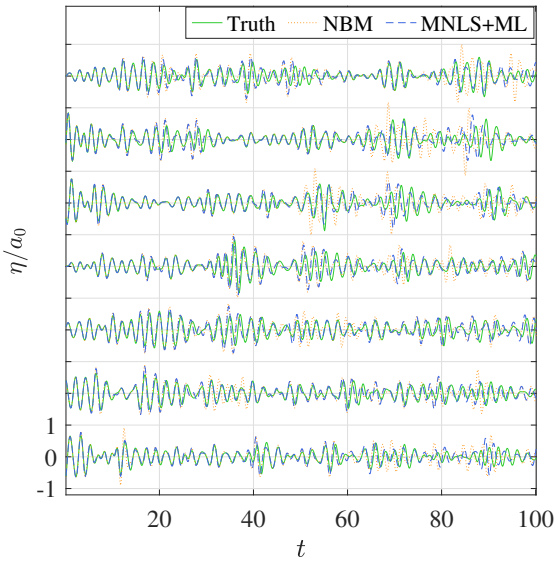
Figure C.2: Depictions of various measurements taken from a randomly selected test case of modulated plane wave, simulated by w3f16 model. The parameters for this case are $f_0 = 1.3769$ Hz, $a_0k_0 = 0.2322$, b_F= 0.0355, $\delta\omega = 0.9984$, $\psi = \pi$ and $\alpha = 0$.



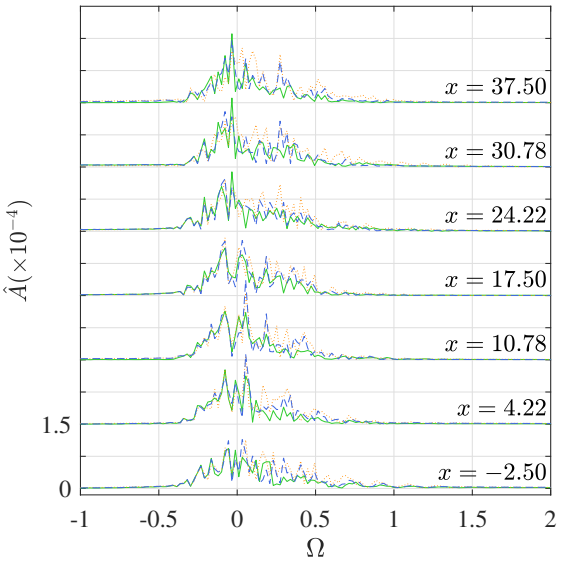
(a) Envelope and wavenumber spectrum



(b) MSE, energy, spectral mean and steepness



(c) Surface elevation



(d) Frequency spectrum

Figure C.3: Various measurements taken from a randomly selected test cases of random wave, simulated by w3f16 model. The parameters for this case are $\gamma = 2.5328$, $a_0 = 0.0383$ m, $f_0 = 1.2343$ Hz and $\sigma_s = 1.2857$.

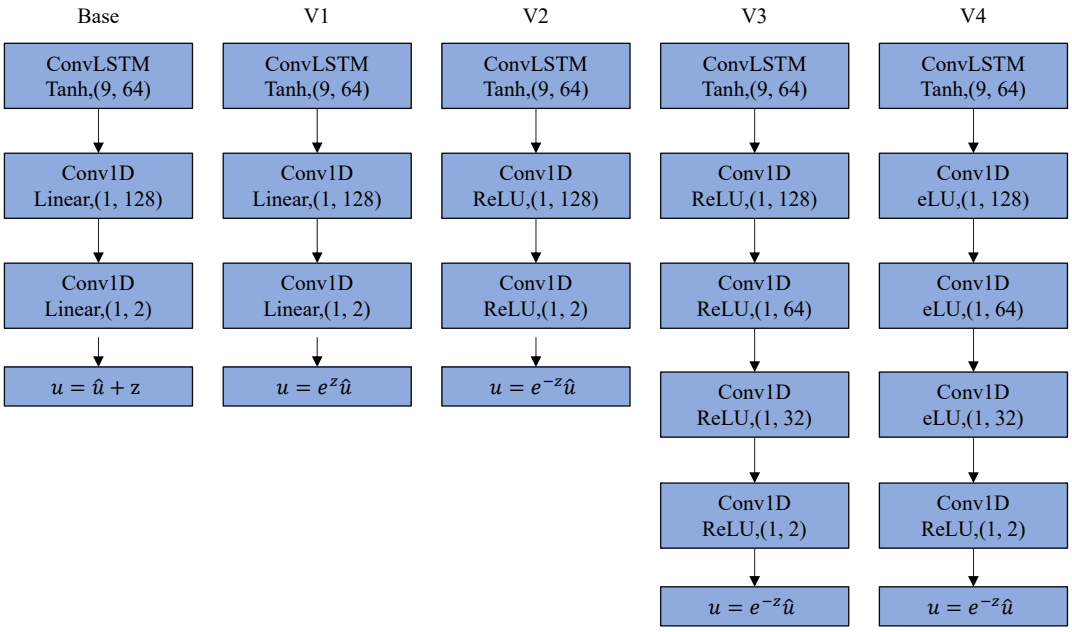
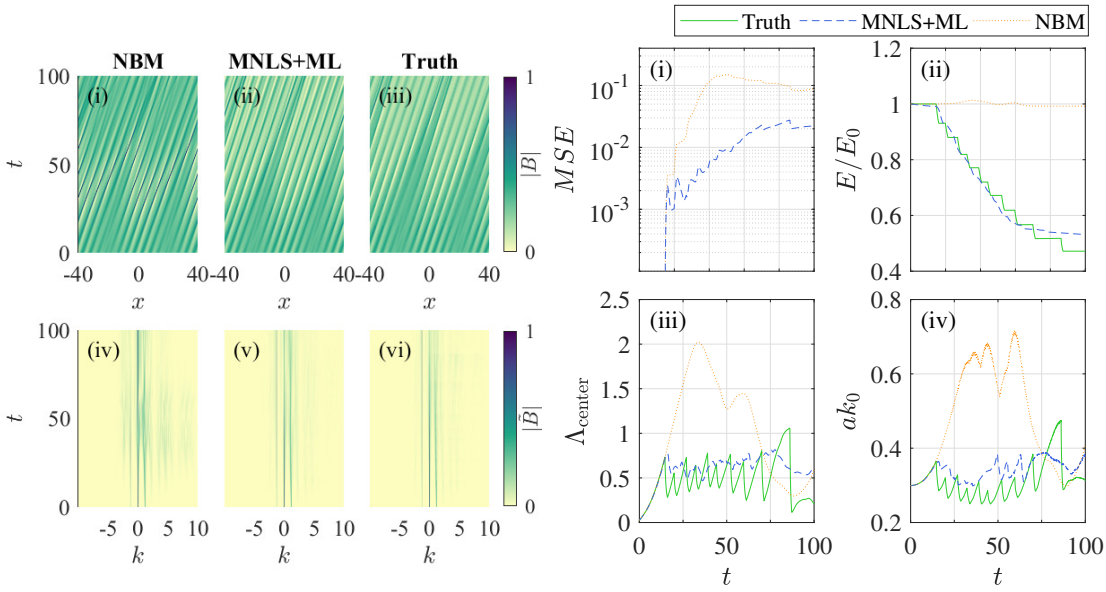


Figure C.4: This figure depicts four simple variants of the ConvLSTM model.

C.2 Additional Results for Plane Wave and Random Waves

Figure C.5a demonstrates the evolution of the complex envelope B in both physical and wavenumber spaces across the NBM, MNLS+ML simulations, and the ground truth. Energy progression, peak frequency, and steepness for all three simulations, along with the MSE evolution for the NBM and MNLS+ML simulations relative to the ground truth, are depicted in Figure C.5b. The neural network model, as inferred from Figure C.5, effectively predicts wave breaking dissipation, outperforming the NBM simulation by reducing the envelope's MSE by two orders of magnitude. This model accurately reproduces the energy evolution, peak frequency, and steepness. A similar conclusion can be drawn from Figures C.6a and C.6b for random waves, with the MSE, in this case, being 2.5 times lower than the NBM simulation.

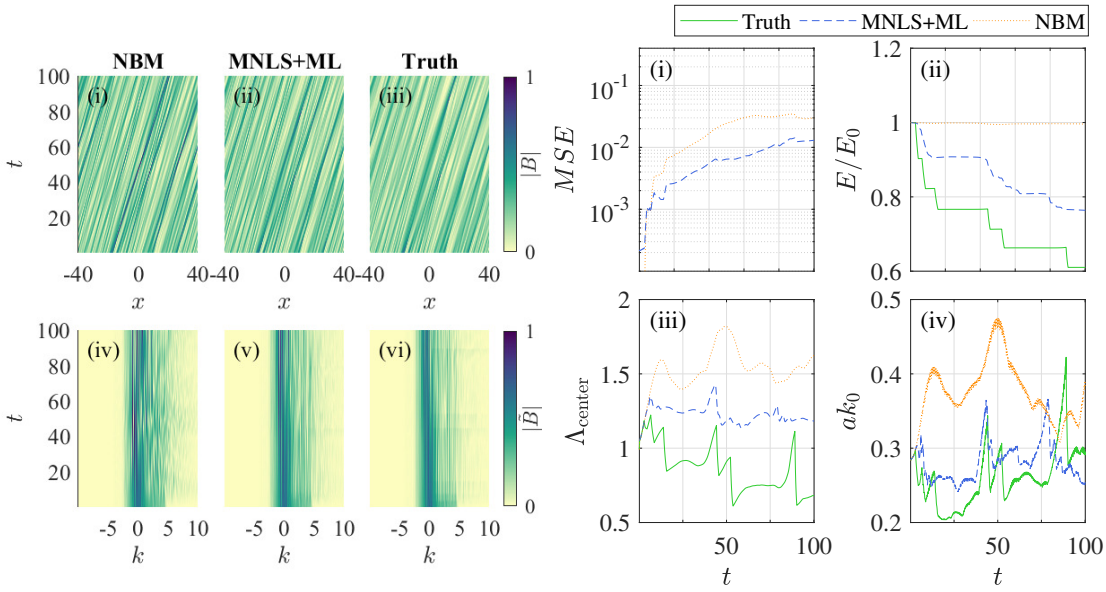
Figures C.7a and C.8a illustrates the temporal evolution of the mean squared error (MSE) for both the MNLS+ML simulation and the NBM simulation in the



(a) Envelope and wavenumber spectrum

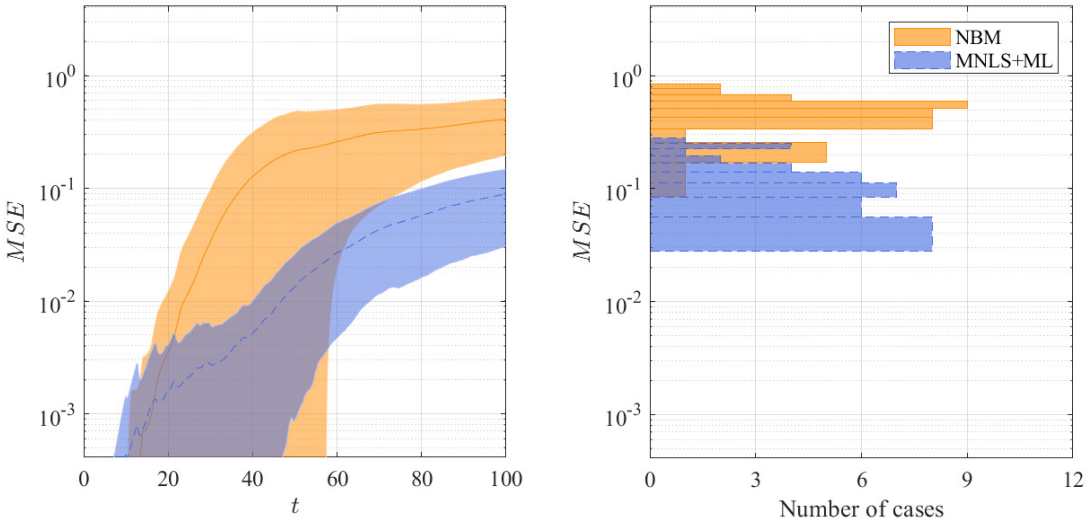
(b) MSE, energy, spectral mean and steepness

Figure C.5: The figure depicts various measurements taken from a randomly selected modulated plane wave case simulated by w9f64 model. In subplot (a), panels (i), (ii) and (iii) show the evolution of the absolute value of the complex envelope using different models, while panels (iv), (v), and (vi) show the evolution of the absolute value of the wavenumber spectrum. Specifically, panel (i) and (iv) show the NBM result, panel (ii) and (v) show the MNLS+ML result, and panel (iii) and (vi) show the ground truth generated by the M-KO95 model. In subplot (b), panel (i) plots the mean squared error (MSE) of the absolute value of the complex envelope.Panels (ii), (iii), and (iv) compare the energy evolution, wavenumber spectral mean or centroid, and evolution of steepness. All panels share the same legend, which is placed on the top of the subplot (b). In the legend, the green solid line represents the ground truth, the blue dashed line represents the MNLS+ML result or MSE of MNLS+ML compared to the ground truth, and the orange dotted line represents the NBM result or MSE of NBM result compared to the ground truth.



(a) Envelope and wavenumber spectrum (b) MSE, energy, spectral mean and steepness

Figure C.6: The figure depicts various measurements taken from a randomly selected random wave case simulated by w9f64 model. In subplot (a), panels (i), (ii) and (iii) show the evolution of the absolute value of the complex envelope using different models, while panels (iv), (v), and (vi) show the evolution of the absolute value of the wavenumber spectrum. Specifically, panel (i) and (iv) show the NBM result, panel (ii) and (v) show the MNLS+ML result, and panel (iii) and (vi) show the ground truth generated by the M-KO95 model. In subplot (b), panel (i) plots the mean squared error (MSE) of the absolute value of the complex envelope.Panels (ii), (iii), and (iv) compare the energy evolution, wavenumber spectral mean or centroid, and evolution of steepness. All panels share the same legend, which is placed on the top of the subplot (b). In the legend, the green solid line represents the ground truth, the blue dashed line represents the MNLS+ML result or MSE of MNLS+ML compared to the ground truth, and the orange dotted line represents the NBM result or MSE of NBM result compared to the ground truth.

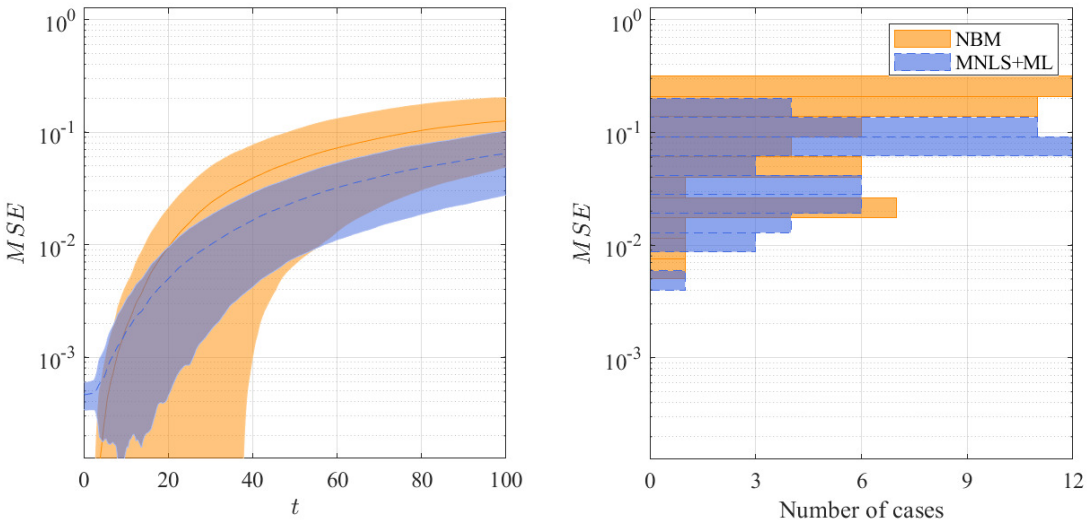


(a) Evolution of MSE of MNLS+ML model and NBM with respect to time averaged over 50 test cases.

(b) MSE of MNLS+ML model and NBM at the last time step.

Figure C.7: This figure plots the MSE error distribution across the modulated plane wave test cases. Panel (a) shows the evolution of MSE of MNLS+ML prediction and NBM with respect to time where blue line with $\pm 1\sigma$ error bar indicates the MSE of MNLS+ML prediction and orange line with $\pm 1\sigma$ error bar indicates the MSE of NBM prediction. Panel (b) illustrates the MSE of MNLS+ML prediction and NBM at the final time step where blue bar stands for MNLS+ML and orange bar for NBM.

case of modulated plane waves and random waves, respectively. Additionally, Figures C.7b and C.8b presents a histogram of the MSE at the final time step of the simulation. Notably, the MSE shows a significant reduction of approximately an order of magnitude for modulated plane wave cases and 2.5 times for random cases. It is intriguing to observe that the model's performance in random cases correlates with the tail strength of the wave spectrum, which is governed by the bandwidth parameter γ. As the γ decreases (i.e. the background spectrum becomes more broadbanded), the neural network prediction deteriorates rapidly.



(a) Evolution of MSE of MNLS+ML model and NBM with respect to time averaged over 50 test cases.

(b) MSE of MNLS+ML model and NBM at the last time step.

Figure C.8: This figure plots the MSE error distribution across the random wave test cases. Panel (a) shows the evolution of MSE of MNLS+ML prediction and NBM with respect to time where blue line with $\pm 1\sigma$ error bar indicates the MSE of MNLS+ML prediction and orange line with $\pm 1\sigma$ error bar indicates the MSE of NBM prediction. Panel (b) illustrates the MSE of MNLS+ML prediction and NBM at the final time step where blue bar stands for MNLS+ML and orange bar for NBM.

Appendix D

Appendices for Chapter 6

D.1 MNLS+ML Experiments on the Test Dataset

Figures D.1–D.3 show the MNLS+ML results for 8 test cases of Types I, II, and III, respectively. We find that the MNLS+ML simulations can predict spectral dissipation and the predictions are significantly improved when compared to the NBM simulation.

D.2 MNLS+ML Experiments on the Non-Breaking Cases

Figure D.4 demonstrates that the MNLS+ML simulation is able to cope with non-breaking waves. We can conclude that no false correction is applied to the non-breaking wave and the MSE remains very small for both NBM and MNLS+ML simulations. The MSEs of the NBM and MNLS+ML at the last timestep are close, centred around 2×10^{-6}.

D.3 Training History

We use an Adam optimiser to perform the backward propagation during the training procedure, with a number of data augmentation approaches and training strategies:

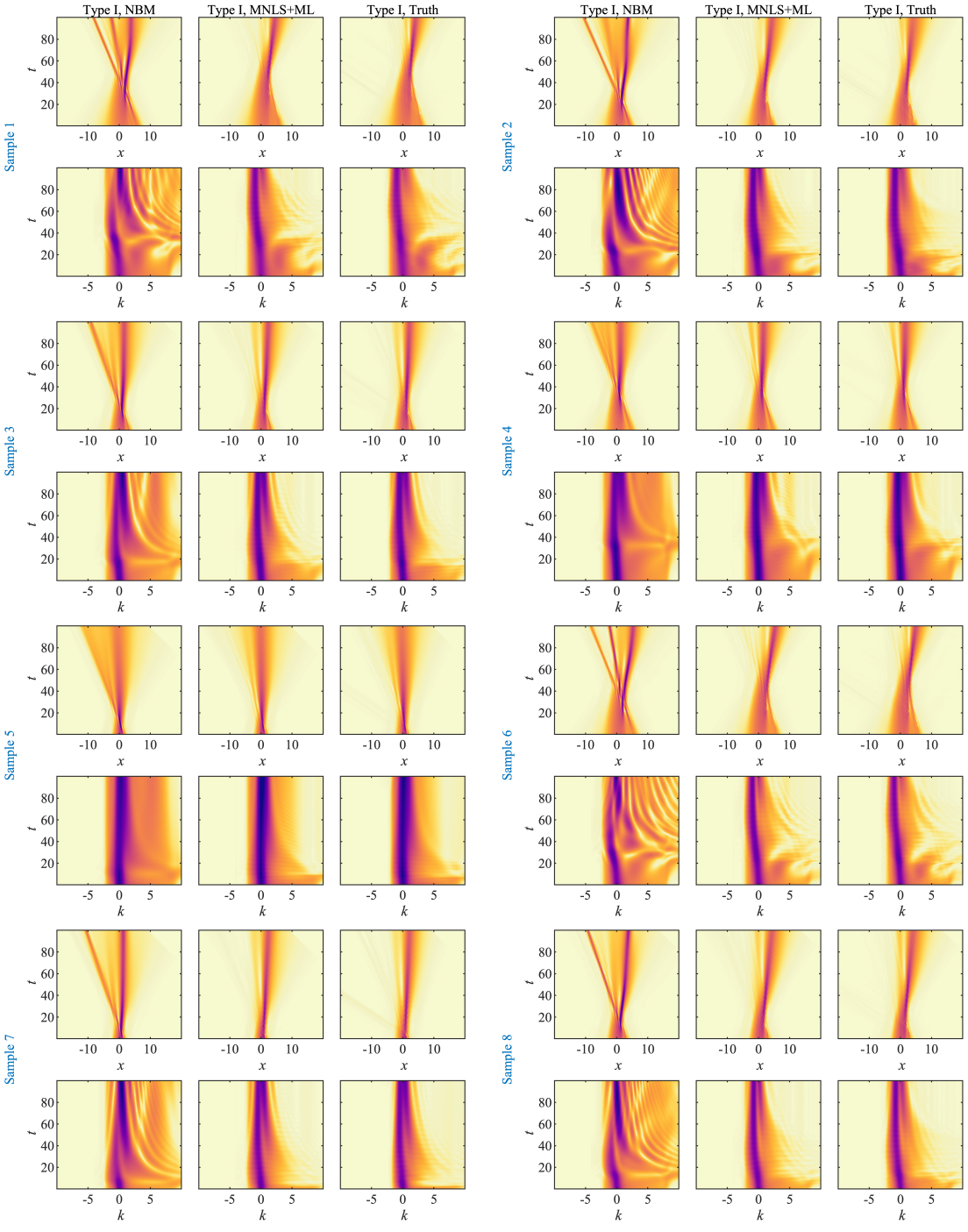


Figure D.1: **Test results for the temporal evolution of 8 test cases of focused wave group.**

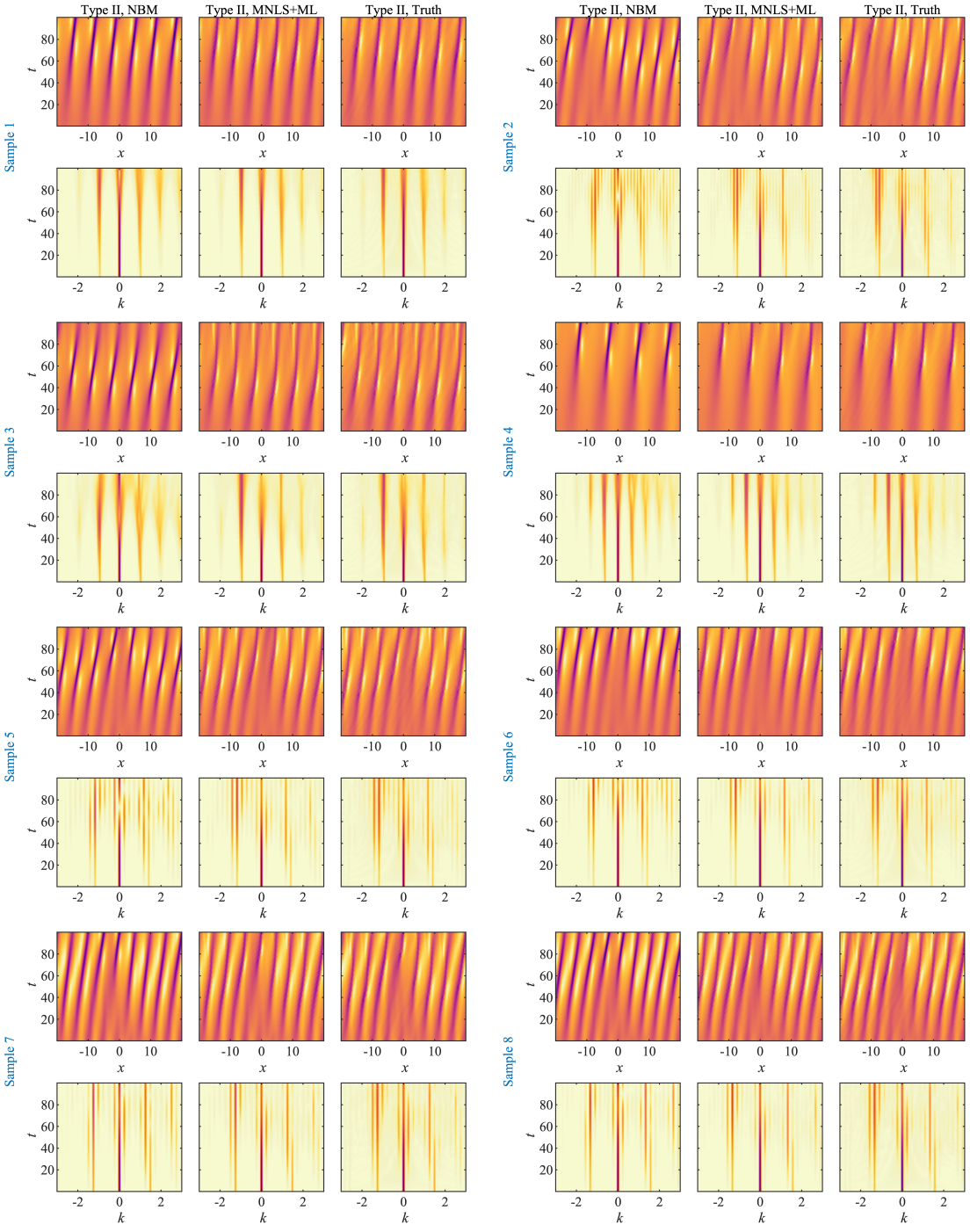


Figure D.2: **Test results for the temporal evolution of 8 test cases of modulated plane wave.**

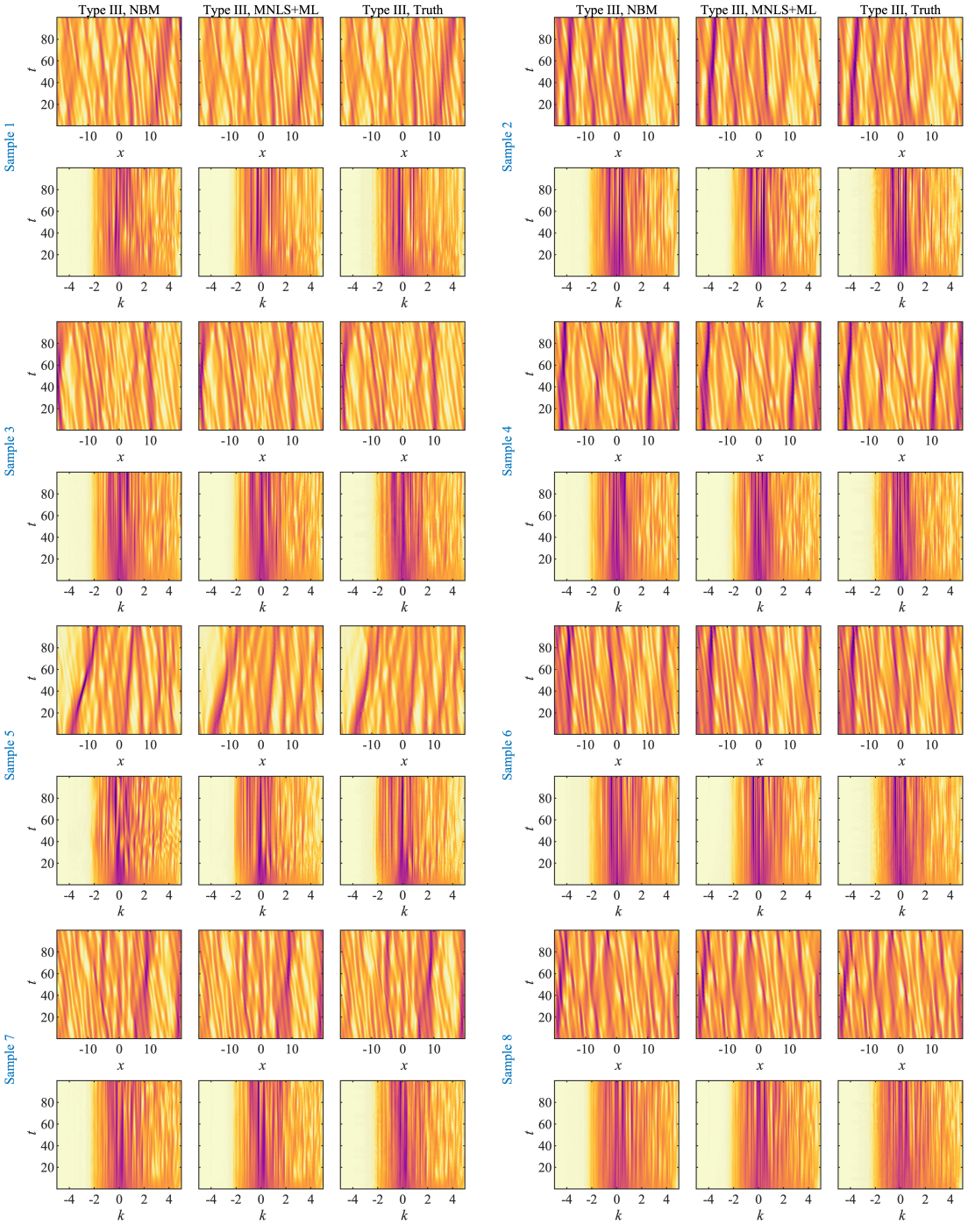


Figure D.3: **Test results for the temporal evolution of 8 test cases of random waves.**

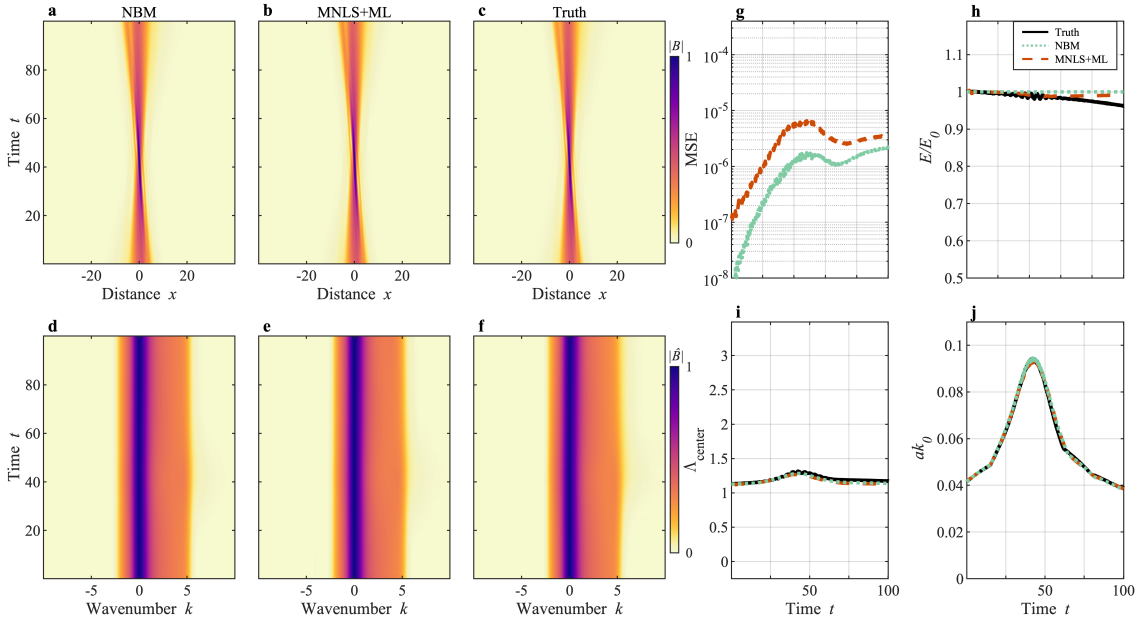


Figure D.4: **Test results for the temporal evolution of a non-breaking focused wave group.**

1. Normalisation: The input and output are normalised to [-1, 1] during the training phase. During the prediction phase, the inputs and outputs are also scaled accordingly.

2. Shuffling: For each epoch, the sequence of batches will be randomly shuffled.

3. Sliding: Instead of feeding the entire time series (which is too long for a recurrent neural network), we apply a sliding window along the time axis with a width of 400, and random shifting from the beginning of the time series.

4. Dropout: We add dropout layers (with dropout rate = 0.1) to the neural network structure (Fig. 6.1) in the training phase.

5. GradientLimiter: We clip the norm of the gradients in the Adam optimiser to 1.0 to prevent gradient explosion.

6. LRscheduler: We apply an exponentially decaying learning rate throughout the training process. For the first 10 epochs, the learning rate is fixed at 0.001, then decreases exponentially to 0.0001 in 50 epochs. After the first 60 epochs, the learning rate is fixed at 0.0001.

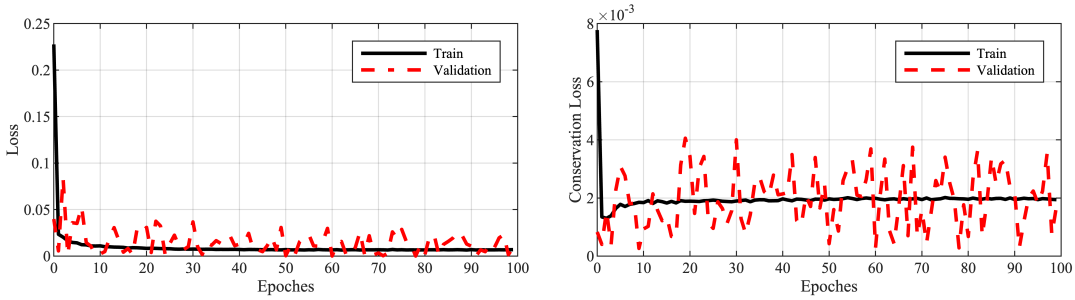


Figure D.5: **Training history of the neural network.**

7. Save-the-best: Only save the best model in terms of validation loss.

Convergence of the training procedure is verified by comparing models trained for 100 epochs and 200 epochs. Figure D.5 shows the training history of our neural network model trained for 100 epochs.

The conservation loss is defined as:

$$J_{\text{conservation}} = \frac{1}{N n_x n_t} \sum_{k=1}^{N} \sum_{j=1}^{n_t} \left| \sum_{i=1}^{n_x} |B_{pred}|^2 - \sum_{i=1}^{n_x} |B_{true}|^2 \right|. \tag{D.1}$$

Conservation loss does not enter the model training procedure; it is merely a metric on how well the neural network model predicts the integrated wave energy. We find that during the entire training procedure, the conservation loss remains at a constant level. There are multiple factors that prevent conservation loss down to zero. One major reason is that the bound wave removal procedure creates artefacts in the training data, causing oscillative behaviour in energy evolution, i.e., Figure 6.2**h** from $t = 50$ to $t = 70$.

D.4 Data-Processing Details

The only field that we obtain from the RANS simulations is the fully nonlinear surface elevation $\eta_{\text{nonl}}(x, t)$. The RANS data require several steps of preprocessing before being converted into a compatible format for MNLS equations and the neural network model. There are several procedures to prepare data for neural network training:

1. Collect the fully nonlinear surface elevation $\eta_{\text{nonl}}(x,t)$ from RANS simulation, where x and t are usually very dense.

2. Approximately remove the bound waves as the MNLS equations need a first-order envelope. We do it by extracting the approximated bound wave $\eta_{2+,\text{ approx}}$. We calculate a $\eta_{2+,\text{ approx}}$ from η_{nonl} using (6.2). The first-order surface elevation is approximated by $\eta \approx \eta_{\text{nonl}} - \eta_{2+,\text{ approx}}$.

3. Downsample the linearised surface elevation $\eta(x,t)$ into a coarser grid, approximately 1/8 of its original space and time resolution. The coarse grid is for the MNLS equations and the neural network model. We perform cubic interpolation in space and dispersion-accurate linear interpolation in time, in case of a misalignment of the low- and high-resolution grids at a particular position or time point.

4. Apply the Hilbert transform to convert the downsampled linearised surface elevation to a complex envelope. The carrier wave can be removed at this stage if necessary.

Given the linearised surface elevation $\eta(x, t = t_0)$ and $\eta(x, t = t_1)$, to obtain $\eta(x, t = t')$ where $t_0 \le t' \le t_1$, we perform the following dispersion-accurate linear interpolation operation:

1. We solve the linearised MNLS equation:

$$\frac{\partial B}{\partial t} + \mathcal{L}(\partial x) B = 0. \tag{D.2}$$

   We obtain solution $\eta_0(x, t = t')$ for the initial condition $\eta(x, t = t_0)$ and $t \in [t_0, t']$, and solution $\eta_1(x, t = t')$ for the other initial condition $\eta(x, t = t_1)$ and $t \in [t_1, t']$.

2. We perform a linear blending of the two solutions based on the time differences:

$$\eta(x, t = t') = \frac{t' - t_0}{t_1 - t_0} \eta_0(x, t = t') + \frac{t_1 - t'}{t_1 - t_0} \eta_1(x, t = t'), \tag{D.3}$$

and the error of the above operations is negligible when $t_1 - t_0$ is much smaller than the time scale of all the nonlinear processes.

D.5 NMSE and NMAE of the Absolute Magnitude of the Envelope

Table D.1 shows the NMSE and NMAE of the envelope profile averaged over the entire time span, and the MNLS+ML model achieves the lowest NMSE and NMAE for all metrics.

Model Name	**Optimized (Y/N)**	**NMSE NMAE (Type I)**	**NMSE NMAE (Type II)**	**NMSE NMAE (Type III)**
NBM		0.145	0.037	0.096
		0.337	0.103	0.203
TD90	Y	0.105	0.028	0.091
		0.296	0.095	0.200
TD90	N	0.098	0.034	0.092
		0.292	0.102	0.200
KO95	Y	0.135	0.033	0.094
		0.333	0.100	0.203
KO95	N	0.120	0.030	0.094
		0.320	0.097	0.203
SL	Y	0.081	0.033	0.085
		0.272	0.101	0.195
SL	N	0.054	0.026	0.084
		0.227	0.093	0.207
H11	Y	0.169	NaN	0.106
		0.360	NaN	0.209
H11	N	0.170	NaN	0.113
		0.361	NaN	0.212
M-KO95		0.067	0.029	0.080
		0.253	0.097	0.194
MNLS+ML		**0.014**	**0.011**	**0.021**
		0.132	**0.063**	**0.107**

Table D.1: A comprehensive overview of the prediction losses of the models taken into consideration. MNLS without a breaking model (NBM) are evaluated as a baseline. All losses are computed by (6.11) and (6.12) averaged over the entire time span $t \in [0, 100T_0]$ for magnitude of the envelope $|B|$. Missing values marked by 'NaN' means the model encounter numerical issues and has failed to provide results in one or more test cases.